NEUTRON SCATTERING STUDIES OF DISORDERED MAGNETIC SYSTEMS

Thesis

Submitted by

STEWART ANDERSON HIGGINS

For the degree of

DOCTOR OF PHILOSOPHY

University of Edinburgh,

OCTOBER, 1985.

ABSTRACT

The results of three projects on substitutionally disordered magnetic systems are reported in this thesis. The first project involved calculations by a computer simulation technique of magnetic excitation spectra in a diluted simple cubic ferromagnet with nearest neighbour Heisenberg exchange interactions. Spectra for low, intermediate and high levels of dilution-induced disorder are compared. A comparison has also been made between calculated spectra and experimental data for the metallic diluted ferromagnet system $Cr_{1-x}Fe_x$ with $x = 0.27$.

The second project involved an investigation of the magnetic phase transitions and magnetic excitations in the $d = 2$ mixed magnetic system with competing spin anisotropies $K_2Co_xFe_{1-x}F_4$. Neutron scattering experiments have been performed on samples with $x = 0.6$, $x = 0.27$ and $x = 0.2$. The $x = 0.6$ sample exhibits uniaxial antiferromagnetic long range order below a Néel temperature, T_N. The $x = 0.2$ and $x = 0.27$ both undergo two phase transitions. Below the higher temperature transition at T_N spin components order along the c-axis of the unit cell and below the lower phase transition at T_L, the spin components perpendicular to the c-axis acquire long range order so that below T_L the magnetic structure of both the $x = 0.2$ and the $x = 0.27$ samples corresponds to the Oblique Antiferromagnetic (OAF) phase. The magnetic excitation spectra for all three samples have been investigated by inelastic neutron scattering techniques at $T = 5K$. Computer simulation calculations have been used to calculate the ground state and the magnetic excitation spectra for the system and the results are compared with experimental

results.

In the third project neutron scattering measurements were made to investigate the magnetic phase transition and magnetic excitations in a sample of the mixed d = 2 system $Rb_2Mn_xCr_{1-x}Cl_4$ with nominally x = 0.754. The system is of interest because of competing ferromagnetic and antiferromagnetic exchange interactions and for a range of concentration values there is expected to be a spin glass phase. The sample with x = 0.754 was found to attain long-range antiferromagnetic order below $T_N \approx 32K$. Results are also reported from inelastic neutron scattering measurements on the magnetic excitations in this sample.

DECLARATION

I declare that the work and composition of this thesis is my own and that where there has been a contribution by others to the work presented, this has been duly acknowledged.

Values of Fundamental Constants and Relationships between Energy Units.

The values of fundamental constants which are used in this thesis are listed below:

Constant	Symbol	Value (S.I. Units)
Planck's Constant divided by 2π	$\hbar$	1.054×10^{-34} JS
Boltzmann's Constant	k_B	1.381×10^{-23} JK^{-1}
The Bohr Magneton	μ_B	9.274×10^{-24} JT^{-1}
The Mass of the Neutron	M_N	1.675×10^{-27} kg.
The Nuclear Magneton	μ_N	5.051×10^{-27} JT^{-1}
The Gyromagnetic ratio of the neutron	γ_N	- 1.91

In Chapters 3 and 5 the energy unit Terahertz (THz) is used. In Chapter 4 the energy values are given in millielectron volts (meV), except in Section (4.5) where they are quoted in THz units.

The relationships between millielectron volts, Terahertz and Joules (J) (the S.I. unit) are given below:

1 meV = 1.60219×10^{-22} J

1 THz = 4.13541 meV.

TO

JEAN, TOM,

SHEENA AND JOE.

ACKNOWLEDGEMENTS

I wish to thank Professor R.A. Cowley for his encouragement, experimental assistance and guidance during the course of this work.

Sincere thanks are due to Dr. M. Hagen for experimental assistance, useful discussions and his invaluable contribution to the computer simulation work reported in Chapter 4 which used the computing facilities of both Edinburgh University Physics Department and the Solid State Division at Oak Ridge National Laboratory.

I would also like to thank Dr. P.W. Mitchell and Dr. D. McK. Paul for valuable discussions and the inelastic neutron scattering data with which results from my calculations reported in Chapter 3, were compared.

Professor U. Dürr, Dr. K. Fendler and Dr. W.A.H.M. Vlak kindly supplied the samples for the experiments discussed in Chapter 4, while Professor R. Geick provided the sample for the experiments in Chapter 5. Thanks are extended to Dr. Vlak for experimental assistance and useful discussion during the course of the experiment on the $x = 0.27$ sample of $K_2Co_xFe_{1-x}F_4$, carried out at I.L.L., and to W. Kullmann and E. Neumann, who participated in the running of the experiment reported in Chapter 5, for which Dr. D. McK. Paul was the I.L.L. local contact.

The staff at A.E.R.E. Harwell, I.L.L. and E.U. Physics Department provided valuable technical support for which I am grateful.

I would also like to thank Mrs. R.W. Chester for her expert typing of the manuscript.

Finally I acknowledge the financial support of the S.E.R.C. in the form of a Research Studentship.

C O N T E N T S

C O N T E N T S (Contd.)

CHAPTER 1

INTRODUCTION

1.1 Introduction

This thesis presents the results of three effectively independent projects in which the magnetic phase transitions and collective magnetic excitations (spin waves) of different substitutionally disordered magnetic systems were investigated. Each project has been assigned a separate chapter with a specific introduction explaining the particular background, motivation and details of that work. This chapter and the next therefore introduce some theoretical and experimental background which is common to these projects.

The project reported in Chapter 3 utilised the "Equation-of-Motion" technique (Alben et al. (1977)) to compute the spin wave spectra in a simple cubic diluted ferromagnet with nearest neighbour Heisenberg exchange interactions. The results highlight features induced solely by the disorder and give some valuable information in interpreting data collected from neutron scattering experiments on metallic alloys such as Chromium-Iron.

Chapter 4 reports work on $K_2Co_xFe_{1-x}F_4$, a mixed magnetic system with competing spin anisotropies. Neutron scattering techniques have been used to investigate the magnetic phase transitions and spin waves in single crystal samples with concentrations $x = 0.6$ and $x = 0.2$. A further inelastic neutron scattering experiment to investigate the low temperature spin wave dispersion relation and the temperature dependence of the low energy, small reduced

wavevector spin waves in a sample with $x = 0.27$ is also featured. Comparison is made of the low temperature spin waves in all three samples with spectra calculated by the "Equation-of-Motion" technique.

The third project, reported in Chapter 5, concerns work on $Rb_2Mn_xCr_{1-x}C\ell_4$, a mixed magnetic system with competing ferromagnetic-antiferromagnetic exchange interactions. A "quasi-elastic" neutron scattering experiment was performed to study the magnetic phase transition and an inelastic neutron scattering experiment performed to investigate the spin wave dispersion relation close to the Brillouin zone centre for a sample with $x = 0.754$.

The remainder of this chapter and the next deals with the introductory material as follows. The next section describes the nature of the magnetic interactions and deals with some very general aspects of the disordered magnetic systems of interest. The second chapter reviews some background theory for thermal neutron scattering and also deals with the relevant experimental aspects, with particular emphasis being placed on the triple axis neutron spectrometer. The second chapter also introduces the idea of spectrometer resolution which is always important in interpreting the data from neutron scattering experiments and is vital in analysing some of the data presented in this thesis.

1.2 The Magnetic Systems: Some General Aspects

$K_2Co_xFe_{1-x}F_4$ and $Rb_2Mn_xCr_{1-x}Cl_4$ are discussed in Chapters 4 and 5 respectively. Both of these materials are isomorphous with crystalline K_2NiF_4 (Birgeneau et al. (1970)) which has the tetragonal unit cell in Figure (1.2.1). Ignoring the effect of spin-orbit coupling, the ground states of the free transition metal ions can be obtained from Hund's rules (Kittel (1976)). In a solid, the effect of the crystal field and spin-orbit coupling on the electronic levels can be treated by perturbation theory since the resulting energy levels are close together in energy compared with the gap between excited electronic states. The magnetic excitations considered in this thesis involve only the lowest lying of those energy levels and they can be considered in terms of energy levels of a pseudospin operator $\hat{\underline{s}}$ which is related to the total orbital angular momentum operator $\hat{\underline{L}}$, the total spin angular momentum operator $\hat{\underline{S}}$ and the magnetic moment $\underline{\mu}$ by the equations (1.2.1)

$$\hat{S}^\alpha = C_s^\alpha \hat{s}^\alpha \qquad (1.2.1a)$$

$$\hat{L}^\alpha = C_L^\alpha \hat{s}^\alpha \qquad (1.2.1b)$$

$$\mu^\alpha = \mu_B(\hat{L}^\alpha + 2\hat{S}^\alpha) = \mu_B g^\alpha \hat{s}^\alpha \; . \qquad (1.2.1c)$$

α labels cartesian components, C_s^α and C_L^α are proportionality constants and $g^\alpha = (C_L^\alpha + 2C_s^\alpha)$.

Whilst the crystal field and spin-orbit coupling determine the energy levels of individual transition metal ions in the solid, a third perturbing term couples the spins of the magnetic ions. This

is the magnetic exchange interaction given by equation (1.2.2).

$$\hat{H}_{exchange} = \sum_{ij} J_{ij} \hat{\underline{S}}_i \hat{\underline{S}}_j \qquad (1.2.2)$$

where this sum is over all pairs of sites, J_{ij} is the exchange interaction and $\hat{\underline{S}}_i$ and $\hat{\underline{S}}_j$ are the total spin operators at the sites $\underline{r}_i$ and $\underline{r}_j$ respectively. With suitable proportionality constants the exchange Hamiltonian can be related to the pseudospin operators. Discussion of the pseudospin values for Co^{2+}, Fe^{2+}, Cr^{2+} and Mn^{2+} in K_2NiF_4 isomorphs are left to the appropriate chapters.

In K_2NiF_4 isomorphs, the exchange interaction arises from overlap between the wavefunctions of the transition metal ions and the halide cations. Thus the transition metal ions are coupled via intermediate cations. This mechanism is called superexchange (Ziman (1971)). The larger the number of cations between the two magnetic ions, the smaller the energy of the interaction. Consequently, the predominant exchange energy is that between nearest neighbour magnetic ions in the basal $\underline{a}$ - $\underline{b}$ plane which are separated by one cation. Two cations separate the magnetic ions in neighbouring planes and, for example, in K_2CoF_4 the interplane exchange is a factor of about 1000 less than the intraplane exchange between nearest neighbour metal ions (Ikeda and Hirakawa (1974)). Additionally, with an exception of those systems in which the transition metal ion is Cr^{2+}, the magnetic exchange interactions lead to antiferromagnetic alignment below the Néel temperature, T_N. (In Rb_2CrCl_4 a ferromagnetic phase occurs below the critical temperature, T_c).

Since the late 1960's isomorphs of K_2NiF_4 have therefore been used as model systems in experiments designed to test the theory of cooperative phenomena in the spatial dimension $d = 2$, because of quasi two dimensional and predominantly nearest neighbour

FIGURE (1.2.1): The crystallographic unit cell of K_2NiF_4. The unit cell is tetragonal with a = b. M^{2+} corresponds to the divalent transition metal ion.

fig 1·2·1

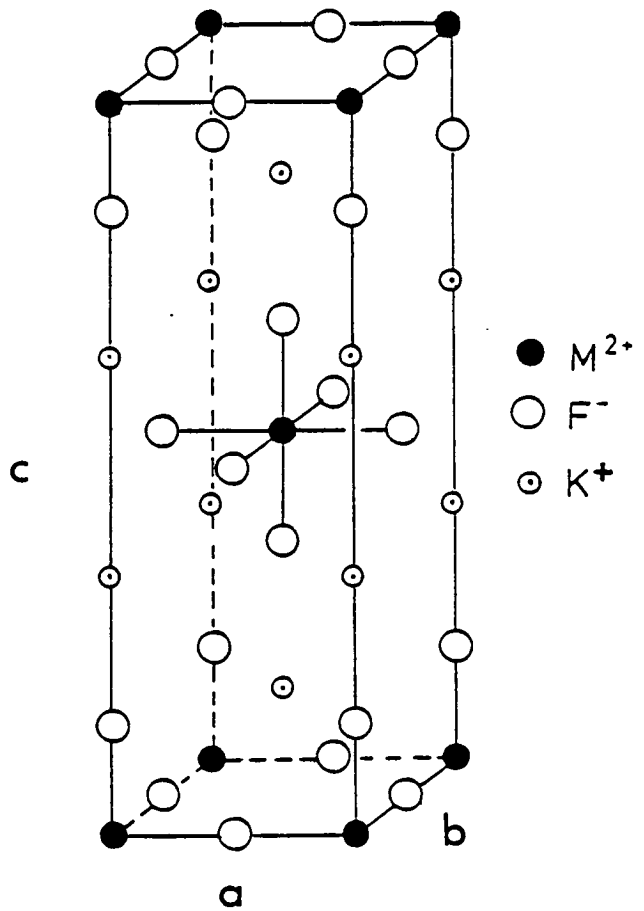

magnetic exchange interactions. Outstanding agreement has been obtained between theory and experiment in the case of pure systems (See, for example, Ikeda and Hirakawa (1974)), Cowley et al. (1984)). These types of system are also very suitable for studying cooperative phenomena in $d = 2$ disordered magnetic systems. The divalent transition metal ions differ only in the number of 3d level electrons and so, although the magnetic properties of each type of these transition metal ions are different, their masses and sizes are similar as are many of their chemical properties. Hence substitutional disorder in which some host transition metal ions have been replaced by defect ions of another transition metal species allow effects solely due to (magnetic) site substitutional disorder to be investigated experimentally. Effects such as mechanical stress which would be induced if the size difference between the host and defect ions was significant are thus avoided.

The specific properties of K_2CoF_4, K_2FeF_4, Rb_2MnCl_4 and $Rb_2Cr\ Cl_4$ which make mixtures of the former two systems of interest in studying mixed magnetic systems with competing spin anisotropy and mixtures of the latter two systems suitable for studying systems with competing ferromagnetic-antiferromagnetic exchange interactions are discussed in Chapters 4 and 5 respectively. However, a brief discussion of the different types of site substitutional disorder, in the magnetic context, is given here.

If, as in Chapter 2, the magnetic host sites are replaced by non-magnetic defect sites, the resulting random magnetic system is said to be diluted. In other systems the defects are also magnetic, leading to a mixed magnetic system. Single-ion anisotropy or

anisotropy in the exchange interaction usually determine the ordering direction of the magnetic moment in a pure system below the transition temperature, T_c. The phase transitions and magnetic excitations in diluted systems and in mixed magnetic systems, in which the favoured ordering directions for both magnetic species are the same, are fairly well understood. (A review of much of this work is given by Cowley (1982)). This understanding is possible because the magnetic ground state is, at least conceptually, known. However, in other systems such as those discussed in Chapters 4 and 5, the ground state is not obvious because of competing interactions and calculation of the ground state properties is in itself an interesting problem as well as a starting point for interpreting experimental data and modelling the spin waves in the systems.

In systems henceforth referred to as mixed magnetic systems with competing spin anisotropy the anisotropy of defect ions favours a different ordering direction from that of the host system. Three ordered phases exist in the temperature (T), defect concentration (x) plane. Two of these correspond to the favoured ordering directions of the host and defect spins respectively and the third intermediate phase corresponds to an ordering direction oblique to both end member systems. This is discussed in more detail in the context of $K_2Co_xFe_{1-x}F_4$ in Chapter 4. Finally, another type of mixed magnetic system occurs when, for example magnetic defects, between which ferromagnetic alignment is preferred, replace the magnetic ions in an antiferromagnetic host. This shall be referred to in this thesis as a mixed magnetic system with competing ferromagnetic-antiferromagnetic exchange interactions. As

discussed in Chapter 5, with respect to $Rb_2Mn_xCr_{1-x}C\ell_4$, the long range order can be ferromagnetic or antiferromagnetic below T_c depending on the concentrations of magnetic defects in the system. For intermediate concentrations there exists the possibility of a so-called spin-glass phase.

CHAPTER 2

NEUTRON SCATTERING BACKGROUND

2.1 Introduction

The experimental measurements on disordered magnetic systems which are discussed mainly in Chapters 4 and 5 of this thesis employed neutron scattering techniques. The purpose of this chapter is to review the relevant theoretical and experimental background of thermal neutron scattering and so specific details of experiments are left to the appropriate chapters.

Thermal neutrons are a very useful probe with which to investigate condensed matter systems for the following reasons. Firstly, the wavelength of the thermal neutrons is comparable to the interatomic spacing in the systems and so scattered neutrons can produce interference effects. Secondly, collective excitations such as phonons or magnons often have an energy which is the same order of magnitude as the initial energy of the neutron, so that the change in energy of the neutron, caused either by creation or annihilation of an excitation, is resolvable and the detection of scattered thermal neutrons can be used to obtain information about the excitations and dynamics on an atomic scale. Thirdly, the neutron is an uncharged particle and consequently thermal neutrons are able to penetrate deeply into solid materials, unlike charged particles such as electrons. Finally, the neutron has a magnetic moment enabling information about the magnetic structure and dynamics of magnetic systems to be deduced from the scattered neutrons. In general, the interactions between the neutron and the system of interest consist of an interaction between the neutron

and the nucleus by nuclear forces and an interaction between the magnetic moment of the neutron and the magnetic moment of the electrons in the scattering system. Any interaction between the magnetic moment of the nucleus and the Coulombic field generated by the charged electrons and nuclei can be neglected since it is very small in comparison with these purely nuclear and magnetic interactions.

The remainder of this chapter is set out as follows. In section (2.2), the theoretical background concerned mainly with thermal neutron scattering from magnetic systems is discussed, and the relationship between the spin-spin correlation function and the partial differential cross-section for scattered neutrons is arrived at. The experimental background with particular emphasis on the main features of the triple axis neutron spectrometer is given in section (2.3). Finally, in section (2.4), the resolution function of the triple-axis neutron spectrometer is discussed. Additionally two new developments, one of which I was involved in, which make resolution corrections more accessible, are briefly discussed.

2.2 Thermal Neutron Scattering: Theoretical Background

Consider a monochromatic neutron in a plane wave state with initial energy E_i, wavevector $\underline{k}_i$ and spin state σ_i, scattered by a sample into a plane wave state with energy E_f, wavevector $\underline{k}_f$ and spin state σ_f. Then in the Born Approximation, the partial differential cross-section, which defines the probability

of the neutron being scattered into a solid angle $d\Omega$ with energy in the range $E \rightarrow E + dE$ is given by: (Marshall and Lovesey (1971))

$$\frac{d^2\sigma}{d\Omega dE} = \frac{|\underline{k}_f|}{|\underline{k}_i|} \left(\frac{m_N}{2\pi\hbar}\right)^2 \sum_{m\sigma_i} \sum_{n\sigma_f} P_m P_{\sigma_i} |\langle k_f \sigma_f n | \hat{V} | k_i \sigma_i m \rangle|^2 \delta(\hbar\omega + E_m - E_n) \quad . \tag{2.2.1}$$

In equation (2.2.1), $|m\rangle$ is the initial state of the sample with energy E_m, $|n\rangle$ is the final state of the sample with energy E_n, P_m is the probability of the sample being in the state $|m\rangle$ and P_{σ_i} is the probability of the neutron being in the initial spin state σ_i. The Dirac delta function ensures conservation of energy in the overall system. $\hbar\omega$, the neutron energy transfer is then the difference between the energies of the initial and final states of the neutron and is given by:

$$\hbar\omega = E_i - E_f = \frac{\hbar^2}{2m_N} (k_i^2 - k_f^2) \quad . \tag{2.2.2}$$

For a magnetic sample, the potential operator $\hat{V}$, which represents the interaction between the neutron and the sample is given by:

$$\hat{V} = \sum_j \frac{2\pi\hbar^2}{m_N} b_j \, \delta(\underline{r} - \underline{R}_j) - \hat{\mu}_N \underline{H}_{eff}(\underline{r}) \quad . \tag{2.2.3}$$

The first term is the Fermi pseudopotential which models the interaction between the neutron and the nuclei in the sample as a sum of delta functions. The nuclei at positions $\underline{R}_j$ are assigned a nuclear scattering length b_j which governs the strength of the interaction and can be positive or negative. The magnitude of b_j

depends on the nucleus type and is different not only between nuclei of different elements but also between different isotopes of the same element. The size of b_j also depends on the relative spin states of the incident neutron and the nucleus. Since this thesis is concerned with the scattering of thermal neutrons from disordered magnetic systems and because, for unpolarised neutrons, the magnetic part of the partial differential cross-section can be considered separately, no further discussion of nuclear neutron scattering theory will be given here.

In equation (2.2.3), the second term gives that part of the potential operator which represents the interaction between the magnetic moment of the neutron $\hat{\underline{\mu}}_N$ and the effective magnetic field $\underline{H}_{eff}(\underline{r})$ at the position $\underline{r}$ in the sample. $\hat{\underline{\mu}}_N$ can be written as $\gamma_N \mu_N \hat{\underline{\sigma}}$, where γ_N is the gyromagnetic ratio of the neutron, μ_N is the nuclear magneton and vector $\hat{\underline{\sigma}}$ has the Pauli matrices $\hat{\sigma}^\alpha$ (α = x, y or z) as its elements. The effective magnetic field $\hat{\underline{H}}_{eff}(\underline{r})$ can be written as a sum of the magnetic fields due to unpaired electrons and it can be shown that (Marshall and Lovesey (1971)):

$$\langle \underline{k}_f | \hat{\underline{H}}_{eff}(\underline{r}) | \underline{k}_i \rangle = \int d^3r \, e^{i\underline{Q}\cdot\underline{r}} \{ \tilde{\underline{Q}} \times [\hat{\underline{M}}(\underline{r}) \times \tilde{\underline{Q}}] \} \quad . \qquad (2.2.4)$$

In equation (2.2.4), $\underline{Q} = \underline{k}_i - \underline{k}_f$ is the wavevector transferred to the sample by the neutron in the scattering process, $\tilde{\underline{Q}} = \underline{Q} / |\underline{Q}|$ and $\hat{\underline{M}}(\underline{r})$ is the magnetisation density operator. In magnetic samples which are also insulators, such as the materials mainly considered in this thesis, the magnetic electrons are localised at the magnetic ion sites and if $|\underline{Q}|^{-1}$ is much greater

than the mean electron orbital radius, then the following approximation can be made:

$$\int d^3r\, e^{i\underline{Q}\cdot\underline{r}}\, \tilde{\underline{Q}}\times[\hat{\underline{M}}(\underline{r})\times\tilde{\underline{Q}}] \simeq \sum_j e^{i\underline{Q}\cdot\underline{R}_j} f_j(\underline{Q})\tilde{\underline{Q}}\times[\hat{\underline{\mu}}_j\times\tilde{\underline{Q}}] \quad . \qquad (2.2.5)$$

In equation (2.2.5), the assumption has been made that the magnetisation in the vicinity of the magnetic ion can be represented by the total magnetic moment operator multiplied by the magnetic form factor $f_j(\underline{Q})$. The form factor $f_j(\underline{Q})$ is the Fourier transform of the magnetic moment density at the ion.

Using the approximation given in equation (2.2.5) and substituting with equations (2.2.4) and (2.2.3), the equation (2.2.1) can be rewritten to give the partial differential cross-section for the scattering of neutrons from localised magnetic ions as:

$$\frac{d^2\sigma}{d\Omega dE} = \frac{|\underline{k}_f|}{|\underline{k}_i|}\left(\frac{m_N}{2\pi\hbar}\right)^2 \gamma_N\mu_N \sum_{nm} P_m \sum_{\sigma_i\sigma_f} P_{\sigma_i} \Big|\sum_j e^{i\underline{Q}\cdot\underline{R}_j} f_j(\underline{Q})$$

$$<n\sigma_f|\hat{\underline{\sigma}}\cdot(\tilde{\underline{Q}}\times[\hat{\underline{\mu}}_j\times\tilde{\underline{Q}}])|m\sigma_i>|^2\delta(\hbar\omega + E_m - E_n) \qquad (2.2.6)$$

Expanding the matrix elements of equation (2.2.6) allows this equation to be written, for unpolarised neutrons, as:

$$\frac{d^2\sigma}{d\Omega dE} = \frac{|\underline{k}_f|}{|\underline{k}_i|}\left(\frac{m_N}{2\pi\hbar}\right)^2 \gamma_N\mu_N \sum_{\alpha\beta}(\delta_{\alpha\beta} - \tilde{Q}^\alpha\tilde{Q}^\beta)\sum_{j\ell} e^{i\underline{Q}\cdot(\underline{R}_j-\underline{R}_\ell)} f_j(\underline{Q}) f_\ell^*(\underline{Q})$$

$$\sum_{mn} P_m <m|\hat{\mu}_j^\alpha|n><n|\hat{\mu}_\ell^\beta|m>\delta(\hbar\omega + E_m - E_n) \quad . \qquad (2.2.7)$$

To get (2.2.7) from (2.2.6), the results that $\sum_{\sigma_f} |\sigma_f><\sigma_f|$ is a unit operator and that $\sum_{\sigma_i} P_{\sigma_i} <\sigma_i|\sigma^\alpha\sigma^\beta|\sigma_i> = \delta_{\alpha\beta}$ for unpolarised neutrons

have been used. If $\hat{s}^{\alpha}$ is the αth component of the pseudospin operator, then as shown in equation (1.2.1c) the magnetic moment operators can be replaced by $g^{\alpha}\mu_B\hat{s}^{\alpha}$. Equation (2.2.7) can be simplified even further by noting that

$$\langle n|\hat{s}_{\ell}^{\beta}|m\rangle\delta(\hbar\omega + E_m - E_n) = \int dt\, e^{-i\omega t}\langle n|\hat{s}_{\ell}^{\beta}(t)|m\rangle \qquad (2.2.8)$$

where $\hat{S}_{\ell}^{\beta}(t)$ is the Heisenberg operator given by

$\hat{s}_{\ell}^{\beta}(t) = \exp(\frac{i\hat{H}t}{\hbar})\,\hat{s}_{\ell}^{\beta}\exp(\frac{-i\hat{H}t}{\hbar})$ with $\hat{H}$ the Hamiltonian for the spins in the sample. Equation (2.2.8) then allows the partial differential cross-section to be written in the form:

$$\frac{d^2\sigma}{d\Omega dE} = \frac{|\underline{k}_f|}{|\underline{k}_i|}\left(\frac{m_N}{2\pi\hbar}\right)^2\gamma_N\mu_N\, S(\underline{Q},\omega) \qquad (2.2.9a)$$

where

$$S(\underline{Q},\omega) = \sum_{\alpha\beta}(\delta_{\alpha\beta} - \tilde{Q}^{\alpha}\tilde{Q}^{\beta})S^{\alpha\beta}(\underline{Q},\omega) \qquad (2.2.9b)$$

and

$$S^{\alpha\beta}(\underline{Q},\omega) = \sum_{j\ell} g_j^{\alpha}\, g_{\ell}^{\beta}\, f_j(\underline{Q})f_{\ell}^{*}(\underline{Q})e^{i\underline{Q}\cdot(\underline{R}_j-\underline{R}_{\ell})}\int dt\, e^{-i\omega t}\langle s_j^{\alpha}(0)s_{\ell}^{\beta}(t)\rangle \qquad (2.2.9c)$$

$S(\underline{Q},\omega)$ is the dynamical structure factor, which is the spatial and temporal Fourier transform of the spin-spin correlation function. The $S^{\alpha\beta}(\underline{Q},\omega)$ are called the partial dynamical structure factors. In uniaxial or isotropic magnetic systems, the number of partial dynamic structure factors is reduced by symmetry and $S(\underline{Q},\omega)$ is given by

$$S(\underline{Q},\omega) = (1 - \tilde{Q}_z^2)S^{zz}(\underline{Q},\omega) + (\frac{1 + \tilde{Q}_z^2}{2})[S^{xx}(\underline{Q},\omega) + S^{yy}(\underline{Q},\omega)]. \quad (2.2.10)$$

In equation (2.2.10) it has been explicitly assumed that z is the direction of ordering. The first term measures correlations between spin components along the ordering direction and the second term measures correlations between spin components transverse to the ordering direction. This second term therefore gives information about the spin waves.

2.3 Thermal Neutron Scattering: Experimental Background

The instruments used in performing the thermal neutron scattering experiments discussed in Chapters 4 and 5 were triple axis neutron spectrometers (Figure 2.3.1). This section sets out to discuss only the main features of that instrument and specific details of the way in which particular experiments were carried out are left to the appropriate chapters.

Fast neutrons, which are produced in the core of the nuclear reactor, pass through a moderating material where by collision processes, the neutrons come into equilibrium with the moderator. The outgoing neutrons have a distribution of energies which is mainly Maxwell-Boltzmann in character but which has additional weight at very high energies (which do not concern us here). As an example, the thermal neutron flux at the Institut Laue Langevin, Grenoble, France is in equilibrium with a D_2O (Heavy Water) moderator at T = 300K. The peak in the Maxwellian distribution corresponds to a neutron wavelength $\lambda = 1.2\text{Å}$. At the I.L.L.,

FIGURE (2.3.1): Plan view of the triple-axis neutron spectrometer (schematic). α, β are the horizontal and vertical collimations respectively. $2\theta_m$, $2\theta_s$ and $2\theta_A$ are the scattering angles at the monochromator, sample and analyser.

fig 2·3·1

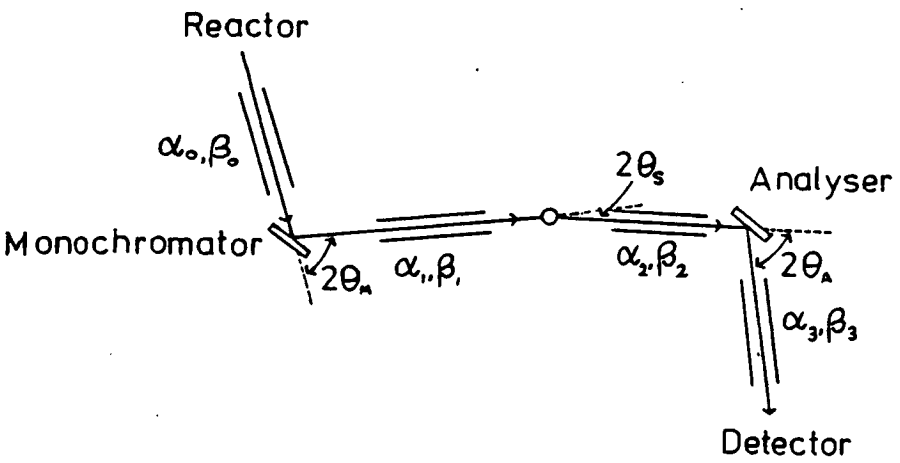
Reactor
α_0, β_0
$2\theta_S$
Analyser
Monochromator
$2\theta_M$
α_1, β_1
α_2, β_2
$2\theta_A$
α_3, β_3
Detector

the peak in the distribution is shifted in some of the beam and guide tubes by including a hot source or a cold source. The hot source consists of Graphite at a temperature T = 2000K and the cold source consists of liquid Deuterium at T = 25K. The hot source and the cold source give an enhancement of the neutron intensity in the wavelength ranges $0.4 < \lambda < 0.8\text{Å}$ and $\lambda < 4.0\text{Å}$ respectively. (Neutron Research Facilities at the I.L.L. High Flux Reactor (1983)).

On reaching the instrument, a monochomator crystal selects a nominal wavevector $\underline{k}_i$ for neutrons incident on the sample. If $2\theta_M$ is the angle through which the neutrons are scattered by the monochromator crystal and if d_M is the spacing between the appropriate scattering planes of that crystal, then by Bragg's Law:

$$|\underline{k}_i| = \frac{\pi}{d_M \sin \theta_M} \quad . \tag{2.3.1}$$

Similarly, an analyser crystal is used to define a normal wavevector $\underline{k}_f$ for neutrons reaching the detector where:

$$|\underline{k}_f| = \frac{\pi}{d_A \sin \theta_A} \quad . \tag{2.3.2}$$

Clearly, arm 1 of the spectrometer (cf. Figure 2.3.1) must be set at an angle $2\theta_M$ to the direction of the neutrons incident on the monochromator crystal and arm 3 of the spectrometer must be set at $2\theta_A$ to the direction of the neutrons incident on the analyser crystal. These spectrometer arms are fitted with collimators which restrict the divergence of the transmitted neutrons along the arms.

Neutrons which reach the detector have thus transferred a wavevector

$\underline{Q}_o$ and energy $\hbar\omega_o$ to the sample, where:

$$\underline{Q}_o = \underline{k}_i - \underline{k}_f \qquad (2.3.3)$$

and

$$\hbar\omega_o = \frac{\hbar^2}{2m_N}(k_i^2 - k_f^2) \quad . \qquad (2.3.4)$$

Clearly, arm 2 of the spectrometer has to be set an an angle of $2\theta_s$ to the direction of $\underline{k}_i$, where

$$2\theta_s = \cos^{-1}[(k_i^2 + k_f^2 - Q^2)/2k_ik_f] \qquad (2.3.5)$$

A computer sets the angles of the turntables on which the monochromator, sample and analyser are mounted and also the angles of the three arms of the spectrometer, allowing scans to be made in reciprocal space (i.e. $\underline{Q},\omega$ space). However, for a desired $\underline{Q}_o$ and ω_o, there are an infinite number of possible $\underline{k}_i$ and $\underline{k}_f$ and it is common to fix $\underline{k}_i$ or $\underline{k}_f$, so that the other can be uniquely determined.

Usually, a monitor is fitted on arm 1 of the spectrometer. The monitor is a fission chamber with a coating of metallic uranium on the counter wall. (Bacon (1975)). As the neutron beam passes through the monitor on its way along arm 1, the monitor produces electrical pulses, the number of which is proportional to the number of neutrons which pass through the monitor and thus the number of neutrons which reach the sample. The most practical way of performing a scan is to count the number of neutrons in the detector for a fixed number of neutrons hitting the sample at each point in the scan. If there were fluctuations in the incident neutron flux from the reactor, then counting for a fixed time at each point in

the scan would not guarantee that a fixed number of neutrons would have have been incident on the sample. Consequently it is most common to count the number of neutrons which reach the detector for a fixed number of monitor counts.

In performing elastic scans, defined by $\hbar\omega = 0$, $|\underline{k}_i|$ and $|\underline{k}_f|$ are fixed at the same value and from equation (2.2.9) it is obvious that the partial differential cross-section is a direct measure of $S(\underline{Q},\omega = 0)$. For inelastic scans, $\hbar\omega \neq 0$, and either $|\underline{k}_i|$ or $|\underline{k}_f|$ is fixed. For fixed $|\underline{k}_f|$, the number of counts in the detector is proportional to $S(\underline{Q},\omega)$ because the efficiency of the monitor is proportional to $1/k_i$ and this cancels the k_i factor in equation (2.2.9). When $|\underline{k}_i|$ is fixed the partial differential cross-section is $\partial^2\sigma/d\Omega d\theta_A$ instead of $\partial^2\sigma/d\Omega dE$. It can be shown that in this case the number of counts in the detector is proportional to $k_f{}^3 \cot\theta_A S(\underline{Q},\omega)$. Irrespective of whether it is $|k_i|$ or $|\underline{k}_f|$ which is fixed, inelastic scans are usually performed with either $\underline{Q}$ fixed and $\hbar\omega$ varied or $\hbar\omega$ fixed and $\underline{Q}$ varied.

Whilst the monochromator crystal reflects neutrons with wavevector $|\underline{k}_i|$ given by equation (2.3.1), it will also reflect neutrons with wavevector $|\underline{k}_i|$ multiplied by a positive integer n. To prevent these neutrons contributing to the number of counts measured by the detector, a filter can be fitted to arm 1 if $|\underline{k}_i|$ is fixed and to arm 2 if $|\underline{k}_f|$ is fixed. The type of filter used depends on the magnitude of the fixed neutron wavevector required. In the experiments discussed in Chapters 4 and 5 of this thesis, either a Pyrolytic Graphite filter or a cooled Beryllium filter was used as required. The Pyrolytic Graphite filter has a complicated transmission spectrum

with respect to the wavevector of thermal neutrons. However, if a fixed neutron wavevector $|\underline{k}_i|$ or $|\underline{k}_f|$ of 2.662Å^{-1} is required, then there are local minima in the transmission spectrum at twice and three times that wavevector. The Maxwellian distribution of the neutrons incident on the monochromator is such that the proportion of neutrons with wavevector greater than three times 2.662Å^{-1} is small and so the Pyrolytic Graphite filter is very effective indeed. A Beryllium filter consists of a block of polycrystalline Beryllium and utilises the Bragg cut-off. The Bragg cut-off wavelength is the wavelength at which the Bragg reflection angle is 90°. This occurs at $\lambda_c = 2d_c$, where d_c is the largest d-spacing in the material. For neutrons with wavelength greater than 2d, Bragg reflections cannot occur. For Beryllium, $\lambda_c = 3.97\text{Å}$ (Windsor (1981)), so the filter transmits neutrons with $\lambda > 3.97\text{Å}$, but neutrons of smaller wavelength are scattered by Bragg reflection. The scattered neutrons could be Bragg reflected many times within a single Beryllium block (multiple scattering) and some of these neutrons could end up travelling in the forward direction after leaving the filter, thus being transmitted. This multiple scattering can be almost completely removed by absorbing slits which are inserted into the Beryllium block along the beam direction. The absorber separation and the filter length determine how effective the absorbers are. Whilst the neutrons with wavelength larger than 3.97Å cannot be Bragg reflected, they can be scattered by phonons. This can be overcome by cooling the filter to T = 77K (liquid nitrogen temperature), removing the neutron energy gain scattering from the thermally excited phonons.

Further discussion of more detailed aspects of the actual experiments carried out will be given in Chapters 4 and 5.

2.4 Spectrometer Resolution

In the previous section, the triple axis neutron spectrometer was discussed, assuming that the wavevectors $\underline{k}_i$ and $\underline{k}_f$ of the neutrons could be selected exactly, by an appropriate setting of the spectrometer. However, due to finite collimations on the spectrometer arms and finite mosaic spreads on the monochromator and analyser crystals, neutrons are detected which have not transferred the nominal wavevector $\underline{Q}_o$ and energy $\hbar\omega_o$. These neutrons have transferred a wavevector $\underline{Q}$ and an energy $\hbar\omega$, where

$$\underline{Q} = \underline{Q}_o + \delta\underline{Q} \qquad (2.4.1)$$

and

$$\hbar\omega = \hbar\omega_o + \delta(\hbar\omega) \qquad (2.4.2)$$

with $|\delta\underline{Q}|$ and $\delta(\hbar\omega)$ small but non zero.

The resolution function of a triple axis neutron spectrometer is a function related to the probability of detecting neutrons which have transferred wavevector $\underline{Q}$ and energy $\hbar\omega$ when the spectrometer has been set to detect neutrons which have transferred wavevector $\underline{Q}_o$ and energy $\hbar\omega_o$. The 'single' crystals used for the monochromator and analyser really consist of many small crystallites, slightly misaligned with respect to an average orientation. It is generally accepted that the distribution of the misalignment angles can be approximated by a Gaussian function. Assuming Gaussian transmission functions for the collimators and a Gaussian mosaic for the monochromator and analyser crystals, a general formulation of the resolution function of a triple axis neutron spectrometer was derived by Cooper and Nathans

(1967). It was shown that the resolution function could be written as

$$R(\underline{X}) = R_o \exp\{-\tfrac{1}{2}\, \underline{X}\cdot\underline{\underline{M}}\cdot\underline{X}\} \qquad (2.4.3)$$

where

$$\underline{X} = (\delta\underline{Q},\ \delta(\hbar\omega)) \quad . \qquad (2.4.4)$$

The normalisation factor and the elements $M_{k\ell}$ of the matrix $\underline{\underline{M}}$ are functions of k_i, ω_o, $\underline{Q}_o$, the monochromator mosaic η_M, the analyser mosaic η_A, d_M, d_A, the horizontal collimations α_o, α_1, α_2, α_3 and the vertical collimations β_o, β_1, β_2, β_3.

For any straight line through the coordinates ω_o, $\underline{Q}_o$, the resolution function is Gaussian as a function of $\delta\omega$ and δQ. In order to visualise the resolution function, it is useful to consider the locus of points for which the resolution function has the value $R_o \exp(-p/2)$. This ellipsoid is defined by:

$$\sum_{k=1}^{4}\sum_{\ell=1}^{4} M_{k\ell}\, X_k\, X_\ell = p \quad . \qquad (2.4.5)$$

When $p = 1.386$, the surface of the ellipsoid defines the locus of points for which the resolution function has the value $\frac{1}{2}R_o$ and this is generally referred to as the resolution elipsoid.

The Cooper and Nathans formulation did not take into account the effect of the horizontal and vertical sample mosaic on the resolution function. Werner and Pynn (1971) showed how this could be incorporated. They relate modified matrix elements $M_{k\ell}'$ and normalisation factor R_o' to the matrix elements $M_{k\ell}$ and normalisation factor R_o of Cooper and Nathans. In addition, detailed treatment of the normalisation factor has been carried out by Dorner (1972) and by Chesser and Axe (1973).

Computer programs based on the above work are used to calculate the triple-axis neutron spectrometer resolution and, for most applications, provide a very good representation. The observed intensity at a nominal energy transfer $\hbar\omega_o$ and wavevector transfer $\underline{Q}_o$ can be obtained, in theory, by integrating the cross-section, σ, over the extent of the resolution function:

$$I(\underline{Q}_o,\omega_o) = \int R(\underline{Q}_o + \delta\underline{Q},\ \omega_o + \delta\omega)\sigma(\underline{Q}_o + \delta\underline{Q},\ \omega_o + \delta\omega)\delta\underline{Q}\delta\omega \quad . \tag{2.4.6}$$

In many applications it is essential to be able to fit the data collected in a scan to a model cross-section convoluted with the spectrometer resolution in order to interpret the data properly. A discussion of particular methods used to fit some of the experimental data in Chapters 4 and 5 will be given in the appropriate places within those chapters.

In the early stages of my research, I did some work on a project led by Dr. P.W. Mitchell, which solved a problem encountered in treating the resolution function of the triple-axis neutron spectrometer in the limit of small scattering angles at the sample. A published paper (Mitchell et al. (1983)), which is bound into the back of this thesis, describes the outcome of that work, which is only briefly discussed here. For sound technical reasons explained in that paper, it is sometimes necessary in making spin wave measurements, to collect the data at very small sample scattering angles. The most convenient way of performing an integration such as that in equation (2.4.6) is to first transform to a coordinate system in which the resolution matrix is diagonal. However, in the small

FIGURE (2.4.1): Pure spin wave scattering generated by the program discussed in Mitchell et al. (1983). (a), (b) and (c) differ only in configuration of the spectrometer with the vertical collimation the same for each, namely $\beta_o = \beta_1 = \beta_2 = \beta_3 = 4.0^o$. (a) and (d) differ in vertical collimations but have the same configuration [the intensity shown for (d) has been amplified by a factor of eight]. In labelling a configuration the three numbers ε_m, ε_s and ε_A, each of which can take the values +1 or -1, refer to the scattering sense at the monochromator, sample and analyser respectively. $\varepsilon = +1$ indicates scattering to the left and $\varepsilon = -1$ indicates scattering to the right. Note that the arrows point to the nominal spin wave energy. In each case $Q = 0.075 \text{Å}^{-1}$, $\varepsilon_g = 0$ and $D = 10$ THz Å^2. Horizontal collimation is (a) 30', (b) 20', (c) 20', and (d) 30'. $k_F = 1.55 \text{Å}^{-1}$, $2\theta_s \lesssim 2.8^o$.

fig 2·4·1

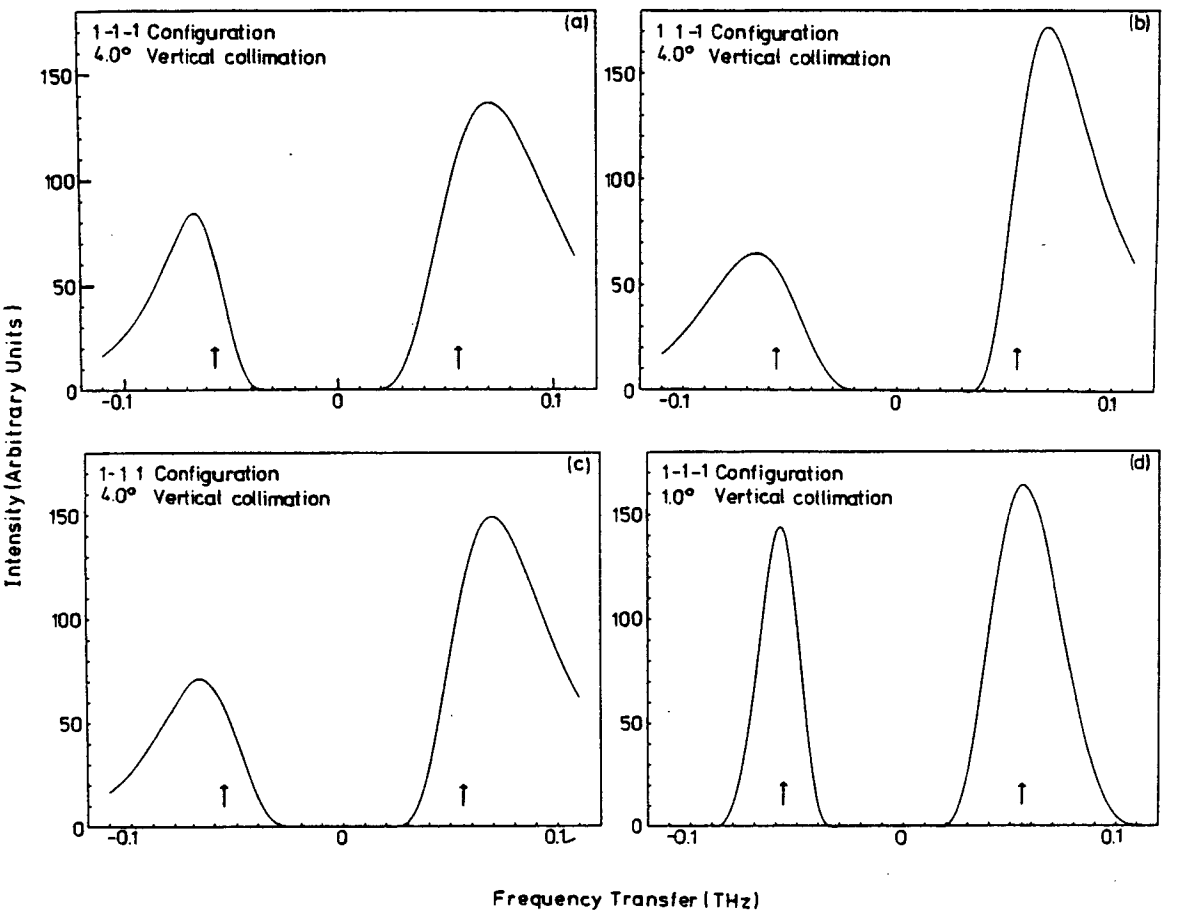
1-1-1 Configuration
4.0° Vertical collimation
(a)
1 1-1 Configuration
4.0° Vertical collimation
(b)
1-1 1 Configuration
4.0° Vertical collimation
(c)
1-1-1 Configuration
1.0° Vertical collimation
(d)
Intensity (Arbitrary Units)
Frequency Transfer (THz)
150
100
50
0
-0.1
0
0.1

angle limit, the Cooper Nathans formulation of the resolution function gives a singular resolution matrix. This singularity arises from the divergences of some of the elements of the resolution matrix because they contain terms in the reciprocal of the sine of the sample scattering angle. With the original program diagonalisation proved impossible. Using higher numerical precision (Double Precision in Fortran 77) diagonalisation could be achieved, but at the cost of additional computing time. In that standard program, the integration had to be carried out numerically with respect to three variables $\delta Q_x'$, $\delta Q_y'$ and $\delta\omega'$ (in the diagonal frame of reference). This is because the vertical resolution is not coupled to the horizontal resolution and if the scattering function in the vertical is replaced by a Dirac delta function in the variable δQ_z, the vertical resolution can be integrated out analytically. Recognising the origin of the singularity, an alternative derivation of the resolution matrix is given in the paper which avoids the difficulty of having to diagonalise a singular resolution matrix. In the new formalism, numerical integration over only two variables is required, so saving valuable computing time. The new formalism was incorporated into a program which could simply generate spin wave intensities and also into a fitting program which could be used to fit spin wave data. Figure (2.4.1) shows some purely spin wave scattering generated by the former of these two programs. The difference between the nominal spin wave energy, indicated by the arrows and the position of the peaks in the intensity illustrates the importance of taking the resolution into account if accurate

values for parameters such as the spin wave energy gap, ε_g, and the spin wave stiffness, D, are to be obtained.

Although in the small angle scattering limit, and with the vertical resolution integrated out analytically, numerical integration over only two variables is required, in a general case, numerical integration might have to be performed over all four variables Q_x', Q_y', Q_z' and $\delta\omega'$. To fit the data collected in a scan, using a non-linear regression fitting program, an integral such as that given in equation (2.4.6) would, in that case, have to be performed for each point in the scan, during each iteration of the program. On a time sharing computer, such as the ICL 2900 series computers available at the University of Edinburgh, which often have over 100 users, such a program could not feasibly be run interactively from a terminal. Attempts to fit the data would have to be run in background (i.e. by submission of computer batch jobs). The time interval between submitting large batch jobs and receiving the output can be up to several days, depending on the demand for computer C.P.U. (Central Processing Unit) time. In a successful attempt to overcome these problems, Mitchell and Dove (1985) have utilised the parallel architecture of the ICL DAP (Distributed Array Processor) computer in the program SHAMGAR'S OXGOAD. The DAP is a S.I.M.D (Single Instruction Multiple Data) computer with 4096 processing units, which is essentially capable of performing a given operation on 4096 sets of numbers simultaneously. In SHAMGAR'S OXGOAD, the integrals are performed numerically, several orders of magnitude faster than the speed which can be achieved on a serial computer such as the ICL 2976. The decrease

in C.P.U. time required is such that the data collected in spin wave scans can be fitted interactively. Further to this, if a model dispersion relation for the spin waves is used, as many scans as required, taken under similar resolution conditions, can be fitted at once, enabling resolution effects to be fully taken into account. SHAMGAR'S OXGOAD was used to fit some of the spin wave data presented in Chapter 4.

CHAPTER 3

CALCULATION OF MAGNETIC EXCITATION SPECTRA IN A DILUTED SIMPLE CUBIC FERROMAGNET

3.1 Introduction

In this chapter results are reported of calculations of the magnetic excitation spectra for a diluted simple cubic ferromagnetic system with nearest neighbour Heisenberg interactions. The calculations were made using the "Equation-of-Motion" method. This technique was used successfully by Thorpe and Alben (1976) to calculate $S(\underline{Q},E)$ spectra for the $d = 2$ mixed antiferromagnetic systems $Rb_2Mn_xNi_{1-x}F_4$ with $x = 0.5$ and the calculated spectra were in good agreement with the experimental results of Birgeneau et al. (1975) and Als-Nielsen et al. (1975). The results of calculations on $d = 2$ diluted antiferromagnetic systems also gave good agreement with experimental results (Cowley et al. (1977), Cowley et al. (1980d)).

Magnetic Excitation spectra in random $d = 3$ ferromagnets have previously been calculated by Alben et al. (1977). Their published work covered both mixed and diluted ferromagnetic systems but concentrated more on the calculation of density of states $\rho(E)$ than on calculation of $S(\underline{Q},E)$ spectra. The project discussed in this chapter involved calculation of $S(\underline{Q},E)$ spectra for the particular case of a diluted simple cubic ferromagnet. This was carried out in order to characterise the effects of dilution on the magnetic excitations from the point of view of what could be measured in

an inelastic neutron scattering experiment.

The remainder of this chapter is set out as follows. In Section (3.2) the equation-of-motion method is discussed and in Section (3.3) general details of how the technique is implemented are given. Section (3.4) describes some of the specific programming details and Section (3.5) discusses the results of tests which were made to ensure that the computer program performed correctly and gave correct results for known cases. In Section (3.6) results are presented and compared from calculations for magnetic site concentration x in what was expected to be three different concentration regimes. Finally, in Section (3.7) comparison is made between results generated by the computer program and some inelastic neutron scattering results.

3.2 The Equation-of-Motion Method

In this section it is shown how $S(\underline{Q},E)$ at $T = 0K$ for spin waves in a mixed magnetic system can be calculated numerically using the "Equation-of-Motion" method. This method will be developed specifically for a system with a simple cubic lattice randomly occupied by atoms labelled A and B. If A and B were both magnetic this would lead to a mixed system. The system of interest in this chapter is diluted and this corresponds to A being magnetic and B being non-magnetic. The mixed case will be described here since it is more general and the dilute case is easily obtained from it.

The spins in the system are assumed to have only nearest

neighbour Heisenberg interactions and the Hamiltonian for the spin system is given by

$$H = - \sum_{<ij>} J_{ij} \underline{S}_i \cdot \underline{S}_j \qquad (3.2.1)$$

where <ij> indicates a sum over nearest neighbour spins. J_{ij} is the exchange interaction between the neighbouring spins $\underline{S}_i$ and $\underline{S}_j$. The J_{ij} values are positive since the system is ferromagnetic. In the mixed system the exchange interaction between nearest neighbours of the same species is assumed to be the same as in the pure system and the exchange interaction between neighbours of different species is given by $J_{AB} = (J_{AA}J_{BB})^{\frac{1}{2}}$, which is known to be a good approximation for magnetic insulators (Cowley and Buyers (1972)). For a diluted system with nearest neighbour interactions there is clearly no interaction between two B neighbours or an A and a B neighbour, so that the only non-zero interaction is between two magnetic A-type neighbours. The Hamiltonian in equation (3.2.1) can be expanded in terms of the cartesian spin components S^x, S^y and S^z to give:

$$H = - \sum_{<ij>} J_{ij}(S_i^z S_j^z + S_i^x S_j^x + S_i^y S_j^y) \; . \qquad (3.2.2)$$

Explicitly assuming that the ordered spin is along the z-direction, the spin creation and annihilation operators S^+ and S^- are defined by:

$$S^+ = S^x + iS^y \qquad (3.2.3(a)$$

$$S^- = S^x - iS^y \qquad (3.2.3(b))$$

From equation (3.2.3), S^x and S^y can be written in terms of S^+ and S^- as:

$$S^x = \tfrac{1}{2}(S^+ + S^-) \qquad (3.2.4(a))$$

$$S^y = \frac{1}{2i}(S^+ - S^-) \quad . \qquad (3.2.4(b))$$

Substituting for S^x and S^y in equation (3.2.2) gives:

$$H = - \sum_{<ij>} J_{ij}(S_i^z S_j^z + \tfrac{1}{2}(S_i^+ S_j^- + S_i^- S_j^+)) \quad . \qquad (3.2.5)$$

Because the effects due to the disorder are of the most interest a linear spin wave approximation can be made which avoids the complication of non-linear spin wave interactions. The linear spin wave approximation can be made, using the lowest-order Holstein-Primakoff transformation given by equation (3.2.6).

$$S^+ \rightarrow (2S)^{\frac{1}{2}} a \qquad (3.2.6(a))$$

$$S^- \rightarrow (2S)^{\frac{1}{2}} a^* \qquad (3.2.6(b))$$

$$S^z \rightarrow S - a^* a \quad . \qquad (3.2.6(c))$$

In equation (3.2.6), S is the value of the spin and a and a^* are the Bose destruction and creation operators respectively. Replacing S^+, S^- and S^z in equation (3.2.5) by the expressions given in (3.2.6) gives:

$$H = - \sum_{<i,j>} J_{ij} S_i S_j + J_{ij}(S_j a_i^* a_i + S_i a_j^* a_j) - J_{ij}(S_i S_j)^{\frac{1}{2}}(a_i a_j^* + a_i^* a_j) \quad . \qquad (3.2.7)$$

In the diluted case all the magnetic sites have the same spin S and the non-magnetic sites do not have a spin so that (3.2.7) simplifies to

$$H = -\sum_{<ij>} J_{ij}S^2 + J_{ij}S(a_i^* a_i + a_j^* a_j - a_i a_j^* - a_i^* a_j) \quad . \qquad (3.2.8)$$

The first term in (3.2.8) is just the ground state Hamiltonian H_o: the second part is the spin wave part of the Hamiltonian and can for the diluted case be written:

$$H = \sum_{(i,j)} J_{ij}S(a_i^* a_i - a_i^* a_j) \qquad (3.2.9)$$

where (i,j) indicates a sum which includes all pairs of nearest neighbours twice.

A set of quantities $g_{iQ}(t)$ can be defined by (Alben et al. (1977)):

$$g_{iQ}(t) = <a_i(t)\sum_j a_j^*(0)e^{i\underline{Q}.\underline{R}_j}> \qquad (3.2.10)$$

where R_j is the position of the spin at site j and $\underline{Q}$ is the wavevector of interest. It can be shown (Alben et al. (1977)) that the g_{iQ} quantities obey the equation of motion

$$i\hbar \frac{dg_{iQ}}{dt} = \sum_j S J_{ij}(g_{iQ} - g_{jQ}) \quad . \qquad (3.2.11)$$

In the dilute case the g-factors (Chapter 1) and spin values can be set to 1 since the $S(\underline{Q},E)$ values calculated can be scaled for comparison with experimental data and the normalised form for the

scattering intensity is given by:

$$S(\underline{Q};E) = \frac{1}{2\pi N\hbar}\int_{-\infty}^{\infty} e^{iEt/\hbar} < (\sum_i a_i(t)e^{-i\underline{Q}.\underline{R}_i})(\sum_j a_j^*(0)e^{i\underline{Q}.\underline{R}_j}) > dt \quad . \tag{3.2.12}$$

Introducing a damping function $e^{-\lambda t^2}$ and with initial conditions $g_{iQ}(t=0) = e^{i\underline{Q}.\underline{R}_i}$ equation (3.2.12) can be written:

$$S(\underline{Q},E) = \lim_{\lambda\to 0}\lim_{T\to\infty} \frac{1}{\pi N\hbar} \mathrm{Re}\int_0^T \sum_i e^{-i\underline{Q}.\underline{R}_i} g_{iQ}(t)e^{\frac{iEt}{\hbar}} e^{-\lambda t^2} dt \quad . \tag{3.2.13}$$

The limits given correspond to infinitely good energy resolution. The effect of having a value $\lambda > 0$ is to introduce a broadened spectrum. Because the Fourier transform of a Gaussian envelope is another Gaussian, the value of λ can be chosen to give an energy resolution comparable or exactly matched with an instrumental energy resolution width, enabling comparison between calculated and experimentally obtained spectra. A finite value for λ also means that the integral need only be performed up to a limit in time of $T = T_{Max} < \infty$. The criteria for choosing λ and T_{Max} are discussed in the next section.

3.3 Implementation of the Equation-of-Motion Method

In the previous section (Section (3.2)) the mathematical details of the equation-of-motion method were set out (with final emphasis placed on the case of diluted systems) and an equation (equation (3.2.13)) was arrived at which related $S(\underline{Q},E)$ to the quantities $g_{iQ}(t)$. In practice, the implementation of the technique is as

follows. Initially, each magnetic site in the diluted system is assigned a g_{iQ} value given by equation (3.3.1).

$$g_{iQ}(t=0) = e^{i\underline{Q}.\underline{R}_i} \quad . \tag{3.3.1}$$

For each site, the equation-of-motion (equation (3.2.11)) is then used to calculate the derivative of g_{iQ} at time $t = 0$. If the time step for the numerical integration of equation (3.2.13) is given by Δt, then:

$$g_{iQ}(t = \Delta t) = g_{iQ}(t=0) + \frac{dg_{iQ}(t=0)}{dt} \cdot \Delta t \quad . \tag{3.3.2}$$

So equation (3.3.2) allows the g_{iQ} values to be calculated after the first time step. To calculate $g_{iQ}(t = n\Delta t)$ where $n \geq 2$, a more accurate method of calculating $g_{iQ}(t = n\Delta t)$ can be used because g_{iQ} is known at two or more previous time steps. The relationship between $g_{iQ}(t = n\Delta t)$ and the $g_{iQ}(t)$ at $t = (n-1)\Delta t$ and $(n-2)\Delta t$ is taken to be:

$$g_{iQ}(t=n\Delta t) = g_{iQ}(t=(n-2)\Delta t) + \frac{dg_{iQ}(t=(n-1)\Delta t)}{dt} \quad 2\Delta t \tag{3.3.3}$$

At successive time steps, $\frac{dg_{iQ}(t=(n-1)\Delta t)}{dt}$ is calculated from the equation-of-motion and then $g_{iQ}(t=n\Delta t)$ is calculated from equation (3.3.3). At each interaction, the $g_{iQ}(t=n\Delta t)$ are summed over all magnetic sites. Finally the time integration in equation (3.2.13) is performed numerically according to the Trapezium Rule (Stephenson (1973)).

As mentioned in Section (3.2), the time step, Δt, for the

numerical integration, the cut-off time T_{max} and the damping constant λ have to be chosen to meet various requirements. The time step is determined by the highest possible energy in the band. If E_{max} is expressed in Terahertz (THz), then Δt expressed in picoseconds (ps) is given by

$$\Delta t(ps) = \frac{1}{\alpha} \frac{1}{E_{max}(THz)} \qquad (3.3.4)$$

In the classical picture of precessing spins $\frac{1}{E_{max}}$ represents the minimum time period for precession of a spin. That is to say, all spins take at least $1/E_{max}$ picoseconds to precess once. The time step has to be small enough that the $g_{iQ}(t)$ vary smoothly on that scale and that the numerical calculations are a good approximation. The factor α ensures that the spins have made less than one revolution between successive time steps, $\alpha = 10$ gave a small enough time step for the calculations reported in this chapter.

In neutron scattering experiments the spectrum obtained in a fixed wavevector transfer scan to determine $S(\underline{Q},E)$ as a function of the energy transfer E $(= \hbar\omega)$ is broadened by the spectrometer resolution. It is therefore the broadened spectrum of $S(\underline{Q},E)$ which is of interest when comparing with experimental data. The damping function used for the calculations was a Gaussian $e^{-\lambda t^2}$. The effect of this in the calculations is to give a Gaussian shaped broadening to the $S(\underline{Q},E)$ spectrum, according to $e^{-E^2/4\hbar^2\lambda}$ (the Fourier transform of the Gaussian function $e^{-\lambda t^2}$ is $e^{-E^2/4\hbar^2\lambda}$). Comparing $e^{-E^2/4\hbar^2\lambda}$ with $e^{-E^2/2\sigma^2}$ then σ is related to λ by $\sigma^2 = 2\hbar^2\lambda$ and so the energy resolution requirement, given by the value of σ

determined the value of λ.

The value of T_{max} is determined by the acceptable noise level in the $S(\underline{Q},E)$ spectrum. If η is the acceptable noise level, then T_{max} is determined by:

$$e^{-\lambda T_{max}^2} = \eta \qquad (3.3.5)$$

where η is a fraction such that if 1% was the acceptable noise level then $\eta = 1/100$. Equation (3.3.5) can be rearranged to give T_{max} in terms of λ and η:

$$T_{max} = (\log_e(1/\eta)/\lambda)^{\frac{1}{2}} . \qquad (3.3.6)$$

The number of time steps in the calculation is then given by:

$$n_t = T_{max}/\Delta t . \qquad (3.3.7)$$

Computing details are given in the next section.

3.4 Computer Programming Details

The program used to calculate $S(\underline{Q},E)$ was written in Fortran 77 and called MASMEX. (This name is short for "MASter Magnetic EXcitations" program.) This program was compiled and run on the VAX 11/750 computer belonging to the University of Edinburgh Physics Department. For a given job, the VAX 11/750 uses more C.P.U. (Central Processing Unit) time than the ICL 2900 series computers (which are also available) of the ERCC (Edinburgh Regional Computing

Centre). As discussed later in this section MASMEX was run for a finite size simple cubic lattice with dimensions $L \times L \times L$. The value of L was chosen to be as large as possible to avoid finite size effects. One of the advantages of using the VAX was that the program could be compiled and run with $L = 35$ although this was later reduced to $L = 30$ after a new computer operating system was installed. (There seemed to be no discernible difference between the $L = 35$ and $L = 30$ spectra, so that $L = 30$ appeared to be above the limit below which finite size effects become more important.) A $30 \times 30 \times 30$ lattice was considerably larger than the largest finite sized system for which MASMEX could be compiled on the ICL 2988. Another advantage was that whilst the VAX uses around 4 times the amount of C.P.U. time used by the ICL 2988 to run the same program, the demand for C.P.U. time on the VAX is very much less. Consequently the actual time taken between submitting a batch job on the VAX and receiving the results is less and this is particularly true for large batch jobs. In addition, there is an upper limit in terms of C.P.U. time of 7200 seconds for batch jobs on the ICL 2988, so that some of the jobs which ran on the VAX could not have been run on the ICL 2988 since they required more C.P.U. time than that upper limit. (A typical batch job to calculate the spin wave spectrum for an $L = 30$ lattice with magnetic concentration $x = 0.34$, averaging over 5 configurations and with an energy resolution which was 1% of E_{max} took around $8\frac{1}{2}$ hours of VAX C.P.U. time.)

The program MASMEX sets up the model system on a finite size simple cubic lattice with the dimensions $L \times L \times L$. A random coordinate

(c_1, c_2, c_3) with $1 \leq c_i \leq L$ is generated and designated as a magnetic site. This procedure is repeated and if the random coordinate generated does not already correspond to a magnetic site, then it becomes a magnetic site. If x is the desired concentration of magnetic sites in the diluted system then the procedure continues until N_s sites have been occupied by magnetic species, where:

$$x = N_s/L^3 \quad . \tag{3.4.1}$$

Depending on the value of x, the model system can contain isolated clusters of spins. The question then arises as to whether these isolated clusters should be allowed to contribute to the calculated scattering. In a real system with only nearest neighbouring interactions, the clusters are completely isolated both from other clusters and from the infinite cluster. One would therefore expect the finite clusters to be randomly orientated so that no coherent scattering would be expected from them. It is therefore argued that only the scattering from the spin deviations on the "infinite cluster" (which consists of all the spins which are not in isolated clusters) is of interest in these calculations and a subroutine was written which eliminated the isolated clusters. After this subroutine has been called, only magnetic sites which were linked to all six sides of the finite cubic system (which has to satisfy periodic boundary conditions) are retained. Figure (3.4.1) illustrates the "infinite cluster" for a $d = 2$, 16×16 square lattice with the magnetic site concentration x close to but greater than the site percolation threshold x_p. (The "infinite cluster" does not exist for $x < x_p$ and the system

FIGURE (3.4.1): Illustration of the "infinite cluster" of magnetic sites for a 16×16 finite size system satisfying periodic boundary conditions. The filled circles indicate the magnetic sites and the lines link nearest neighbour magnetic sites.

Figure (3.4.1)

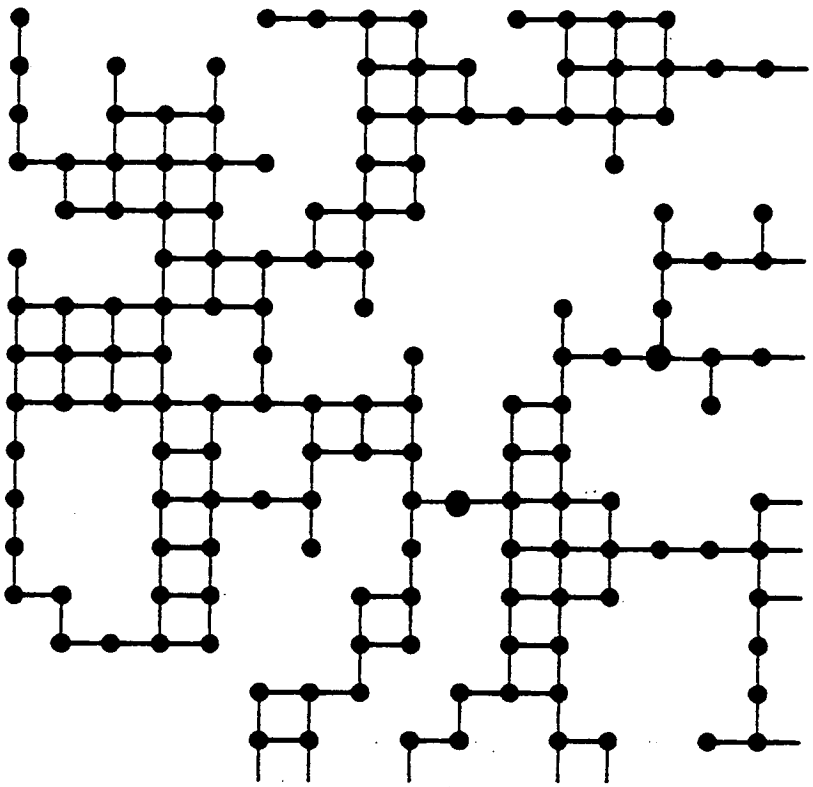

consists only of finite clusters of magnetic sites, i.e. there is no long range order. This chapter is not concerned with the excitations in that concentration regime.) Labelling the concentration of magnetic sites in the "infinite cluster" by x_{inf}, then there are N_{inf} magnetic sites left after this procedure, where:

$$x_{inf} = N_{inf}/L^3 \qquad (3.4.2)$$

Clearly $x_{inf} \leq x$ and when x is close to x_p, the percolation concentration, then x_{inf} is considerably less than x because a substantial number of finite clusters have to be thrown away.

After the random diluted system has been set up, the magnetic sites are labelled from 1 to N_{inf} and the non-magnetic sites are labelled from N_{inf} to L^3. The six nearest neighbours of each spin are identified and stored for use with the equation-of-motion. The "Equation of Motion" method as described in Sections (3.2) and (3.3) is then followed. In the diluted system g_{iQ} is only non zero for the magnetic sites and so the values of g_{iQ} at each time step only need be calculated for the magnetic sites. In the final sum over sites in the calculation of $S(\underline{Q},E)$ only the magnetic sites need be summed over so that the program requires progressively less C.P.U. time as x is reduced. In each calculation, $S(\underline{Q},E)$ is calculated as a function of E for a specified but fixed value of $\underline{Q}$. The range of E and the energy step ΔE were chosen according to where and how broad, as a function of energy, the interesting features were expected to be.

The motivation behind calculating $S(\underline{Q},E)$ in the diluted magnetic systems lies in being able to identify the features of real

systems which are truly associated with this kind of disorder. Any effects which occur purely because the model system is of finite size with periodic boundary conditions are of no physical interest because they would not be a feature of $S(\underline{Q},E)$ in an effectively infinite real system. To allow for these potential problems, several steps have been taken. Firstly, the system has been made as large as possible and to the best of my knowledge has been run for the largest ever model system. Alben et al. (1977) used lattices with typically 8000 (20^3) sites. In the calculations reported in this chapter lattices with 27000 (30^3) sites have mainly been used but lattices of up to 42875 (35^3) sites had also been used in program tests. Secondly, the program can generate $S(\underline{Q},E)$ for several different random configurations, all of which have the same concentration x. (Particular configurations are determined by the initial random number seed.) A program SPECAV (SPECTrum AVerage) was written to average a series of spectra which differ only in that they are generated by MASMEX for different random configurations. For each energy value, the program can calculate the standard deviation defined by equation (3.4.3), which is a measure of the spread of the distribution of $S(\underline{Q},E)$ values at that energy value.

$$\sigma(E) = \left(\frac{1}{n_c} \sum_{i=1}^{n_c} (S_i(\underline{Q},E) - \overline{S(\underline{Q},E)})^2\right)^{\frac{1}{2}} \qquad (3.4.3)$$

where $\overline{S(Q,E)}$ is the mean of $S(\underline{Q},E)$ obtained by averaging n_c configurations. If an uncertainty is to be attached to each $\overline{S(Q,E)}$ value then it can be argued (from the discussion about errors in

Squires (1976)) that this is given by the standard deviation in the mean defined by equation (3.4.4) and which is also calculated by program SPECAV.

$$\sigma_m(E) = \sigma/(n_c - 1)^{\frac{1}{2}} . \qquad (3.4.4)$$

Whereas σ is a measure of the spread in the values of $S(Q,E)$, σ_m gives the uncertainty in the mean value. $\sigma_m(E)$ can be reduced by averaging over progressively larger numbers of configurations.

Table (3.4.1) summarises the procedures carried out by programs MASMEX and SPECAV.

3.5 Program Tests

Before a new computer program is used to generate any new results, it is desirable to check that the program reproduces known results. It was straightforward to check MASMEX in two cases. Firstly, the program was used to generate $S(Q,E)$ spectra for a simple cubic Heisenberg ferromagnet. Secondly, in previous work by Alben et al. (1977) a few graphs of $S(Q,E)$ for the simple cubic diluted system were given, and the program was used to generate similar spectra for comparison.

Because the model system is finite with periodic boundary conditions $S(Q,E)$ was calculated for the pure system only at allowed wavevectors. The allowed wavevectors along the [1,0,0] direction are obtained from the following considerations. The periodic boundary conditions demand that:

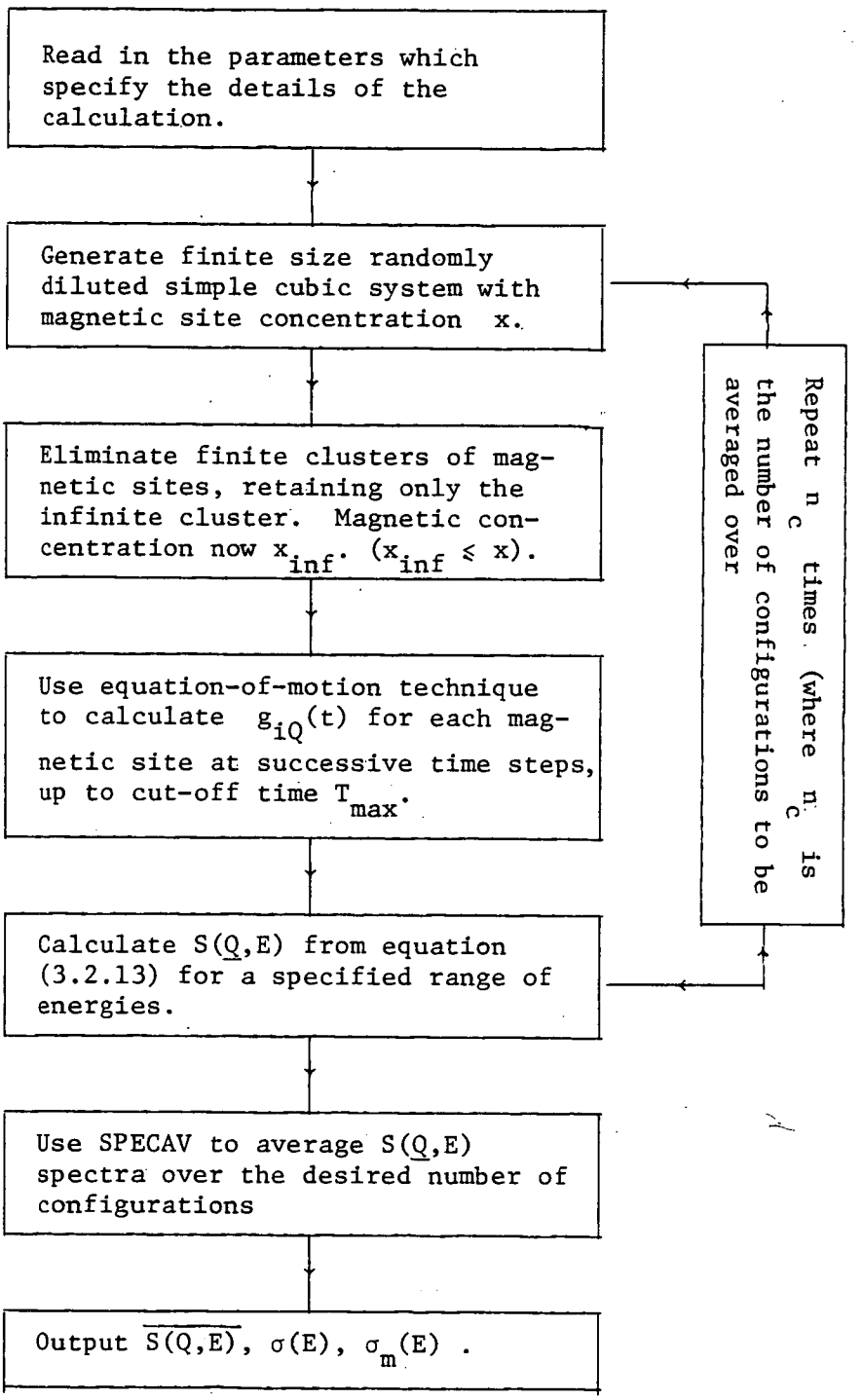

TABLE (3.4.1): Summary of the General Procedures carried out by MASMEX and SPECAV.

$$F((x+L)a) = F(xa) \tag{3.5.1}$$

where $F(X)$ is a function which needs to satisfy the periodic boundary conditions, a is the lattice parameter, L is the number of units along one side of the $L \times L \times L$ system and $x < L$. A possible solution to equation (3.5.1) is:

$$F(X) = e^{iqX} \quad . \tag{3.5.2}$$

For this solution to satisfy equation (3.5.1) then:

$$e^{iq(x+L)a} = e^{iqxa} \quad . \tag{3.5.3}$$

It follows that:

$$e^{iqLa} = 1 \quad . \tag{3.5.4}$$

Hence:

$$q = \frac{p}{L}\left(\frac{2\pi}{a}\right) \tag{3.5.5}$$

where, for wavevectors restricted to the first Brillouin zone:

$$-L/2 < p \leq L/2 \tag{3.5.6}$$

if L is even.

To test the program in the pure case, an $L \times L \times L$ lattice with $L = 10$ was chosen and $S(\underline{Q},E)$ generated as a function of E for $\underline{Q} = (Q_X,0,0)$ at $Q_X = 0$, 0.1, 0.2, 0.3, 0.4 and 0.5. At each $\underline{Q}$ Gaussian peaks were obtained, whose full width at half maximum height (FWHM) was in accordance with the width expected from the chosen value of λ. Figure (3.5.1) shows a typical peak. For a simple cubic ferromagnet with nearest neighbour Heisenberg interactions Kittel (1976) shows that the spin wave dispersion relation

FIGURE (3.5.1): Single resolution limited Gaussian peak obtained by running MASMEX for the pure case (x = 1) with Q = (0.3,0,0). The chosen energy resolution was 0.2 THz F.W.H.M. in this case.

fig 3·5·1

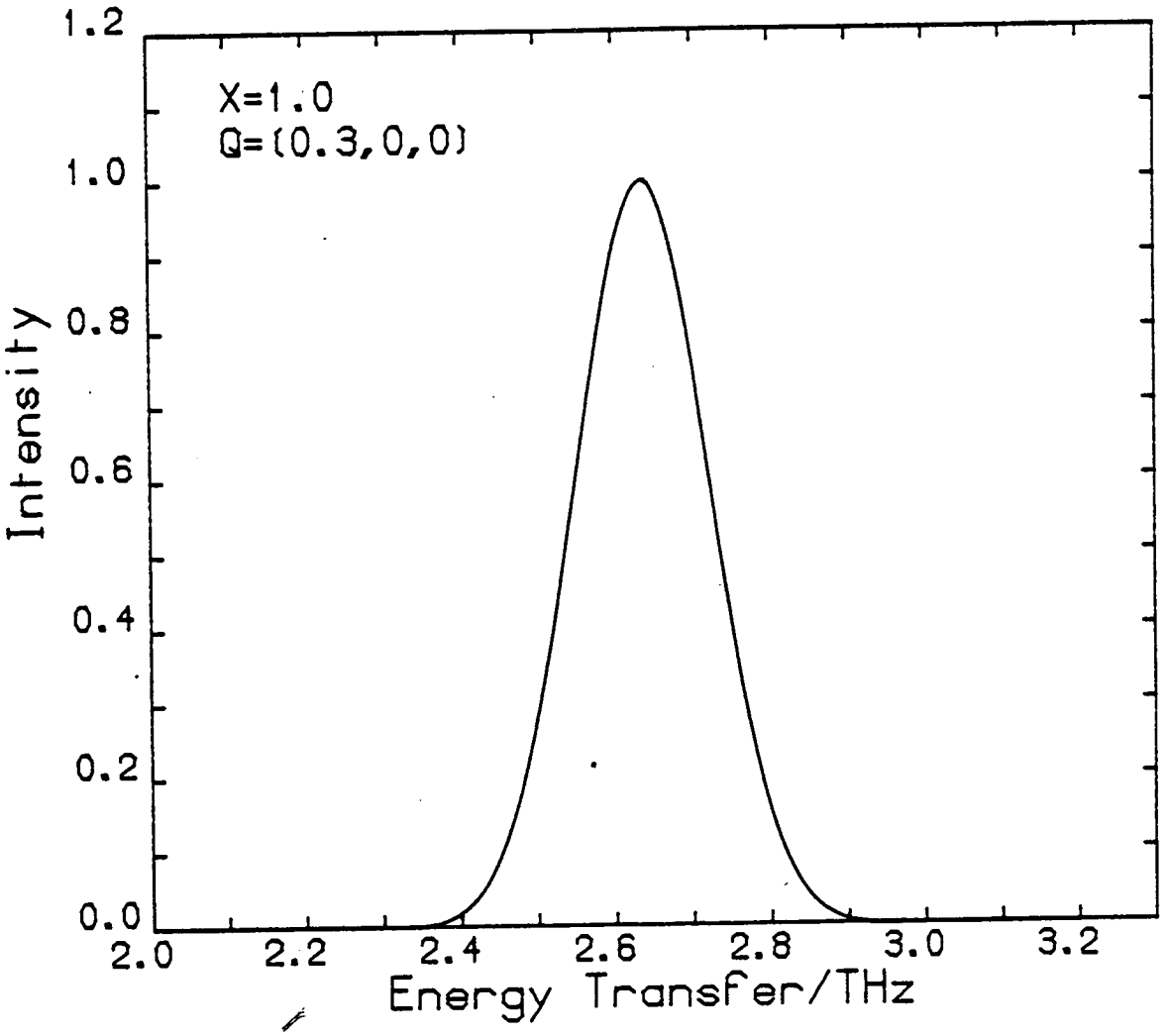
X=1.0
Q=(0.3,0,0)
Intensity
1.2
1.0
0.8
0.6
0.4
0.2
0.0
2.0
2.2
2.4
2.6
2.8
3.0
3.2
Energy Transfer/THz

is given by:

$$\hbar\omega = J S[z - \sum_{\delta} \cos(\underline{q}.\underline{\delta})] \qquad (3.5.7)$$

where J is the exchange interaction (a factor of 2 greater than the one given by Kittel due to a factor of 2 difference in the definition of the Hamiltonian), S is the spin, z is the number of nearest neighbours, $\underline{q}$ is the wavevector of the spin waves and the vectors $\underline{\delta}$ join any spin to its six nearest neighbour spins. In Figure (3.5.2(a)) comparison is made between the peak positions at the chosen wavevectors and the dispersion relation calculated from equation (3.5.7). The fact that the resolution limited peaks that were obtained were centred at the energies expected from theory, is strong evidence that the program worked in the pure system limit.

Alben et al. (1977) considered not only $S(\underline{Q},E)$ but also the density of states $\rho(E)$ for both mixed and diluted systems with the Heisenberg form of the Hamiltonian. Since the calculation of $S(\underline{Q},E)$ for diluted systems comprised only a fraction of that work the number of published $S(\underline{Q},E)$ spectra with which a comparison could be made was limited. Nevertheless, excellent agreement between spectra published by Alben et al. (1977) and those generated by MASMEX was found for the available wavevectors and concentrations. At $x = 0.25$ the spectra available had wavevectors at $Q = (Q_X, Q_X, Q_X)$ with $Q_X = 0.125, 0.25, 0.375, 0.5$. At $x = 0.5$ a comparison could only be made with a spectrum at $Q = (Q_X, Q_X, Q_X)$ with $Q_X = 0.5$. The agreement is very reassuring, especially when the fact that MASMEX generated the spectra for a larger (35^3 compared with 20^3) finite system is taken into account. Since these spectra

FIGURE (3.5.2): Comparison between energy values at the peak positions in spectra generated by MASMEX for x = 1 and the spin wave dispersion relation calculated from equation for wavevectors along the [1,0,0] direction.

fig 3·5·2

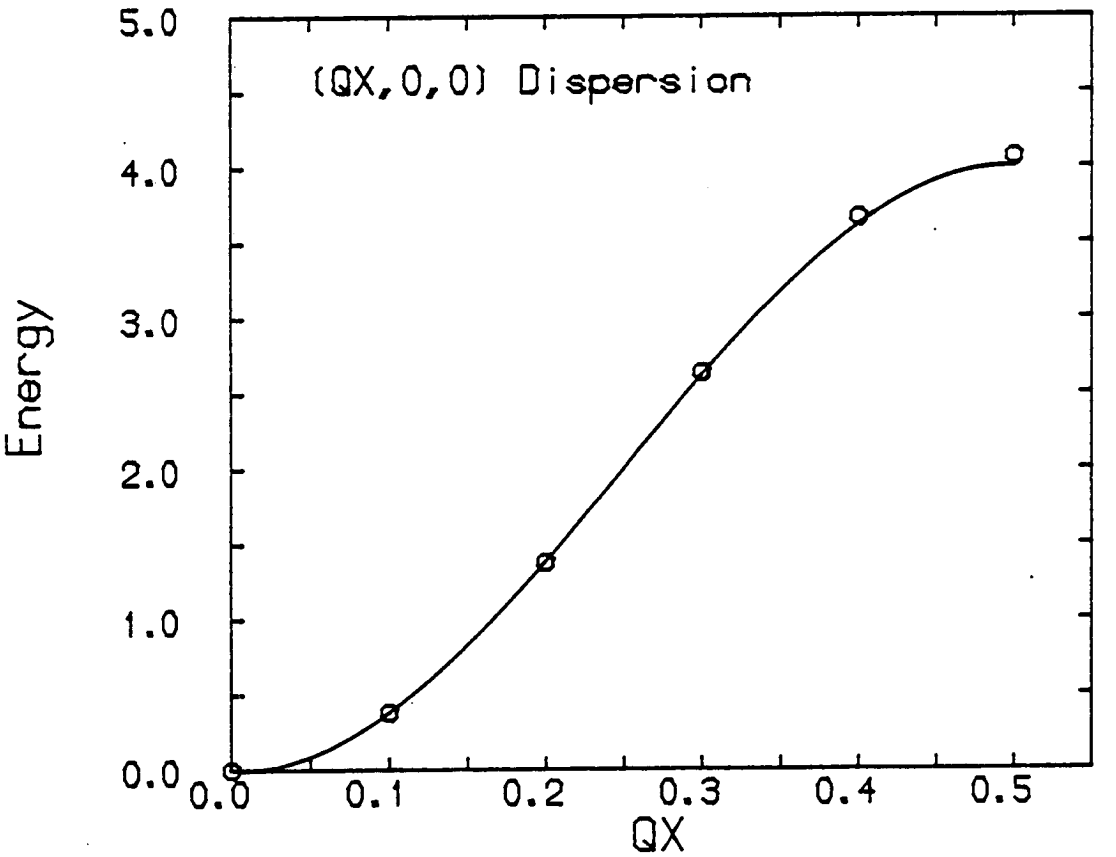

seem independent of the difference in lattice size, the spectra presented in the remainder of this chapter should not be dominated by intrinsic finite size effects, since they were obtained for $L = 30$.

3.6 Results

In this section spectra are presented which were calculated for model systems with magnetic site concentration x in three potentially different regimes. The motivation lies in being able to compare and contrast calculated spectra for what will be described as low, intermediate and high levels of magnetic site dilution. The three magnetic site concentrations for the calculated spectra were chosen to be $x = 0.9$, $x = 0.5$ and $x = 0.34$. Values of $S = 1$ and $J = 1$ were chosen and so the highest possible energy in the spin wave band would be $E_{max} = 12$ THz. The energy resolution was selected to be 0.12THz which is 1% of E_{max}. The spectra were generated for wavevector transfers along the [1,1,1] direction.

In a simple cubic system each site has six nearest neighbours and for $x = 0.9$ only 10% of magnetic sites have been replaced by non-magnetic sites so that many of the magnetic sites must be completely surrounded by other magnetic sites as in the pure system. The probability of any isolated clusters at this concentration is low enough to be negligible and so no isolated clusters are expected in the finite model system: in fact, for the calculations at $x = 0.9$, it was found that $x_{inf} = x = 0.9$. Since for $x_{inf} = 0.9$ each magnetic site has on average less than one non-

magnetic nearest neighbour, it was anticipated that this level of disorder would not have a particularly drastic effect on the spectra compared with those expected for the pure system and the spectra in Figure (3.6.1) support this view. At Q = (0,0,0), which corresponds to the centre of the first Brillouin zone, the spectrum consists of a single resolution limited Gaussian peak centred on zero energy with a F.W.H.M. of 0.12 THz. At Q = (0.1, 0.1, 0.1) the peak has moved to higher energies, has broadened slightly and there is a hint of the spectrum changing shape with more weight in the wings of the peak. At Q = (0.2, 0.2, 0.2) the peak has a width of around 0.8 THz, which is over 6 times the resolution width, so clearly as Q increases from the zone centre the peak width increases. However, this broadening does not continue indefinitely. At Q = (0.3, 0.3, 0.3) the peak has broadened a little bit more but there is obvious weight in the spectrum all the way from E = 0 up to $E = E_{max}$ = 12 THz. At Q = (0.4, 0.4, 0.4) and Q = (0.5, 0.5, 0.5) the effects of the disorder became even more obvious although there is still a peak close to the energy expected in the pure system. The spectra are asymmetric with long tails of intensity down to zero energy. No excitations can exist in the system with energy greater than E_{max} = 12 THz and this imposes an upper cut-off on the spectra. Figure (3.6.2) shows the spectra for all six wavevectors on one graph.

At x = 0.5 only half the sites are magnetic and when an average was made over 5 configurations, it was found that x_{inf} was 0.4894 so that just over 1% of magnetic sites had to be excluded from the calculation of the magnetic excitation spectra.

FIGURE (3.6.1): S(Q,E) spectra generated by MASMEX with x = 0.9 for

(a) Q = (0, 0, 0)

(b) Q = (0.1, 0.1, 0.1)

(c) Q = (0.2, 0.2, 0.2)

(d) Q = (0.3, 0.3, 0.3)

(e) Q = (0.4, 0.4, 0.4)

(f) Q = (0.5, 0.5, 0.5).

Fig (3.6.1(a))

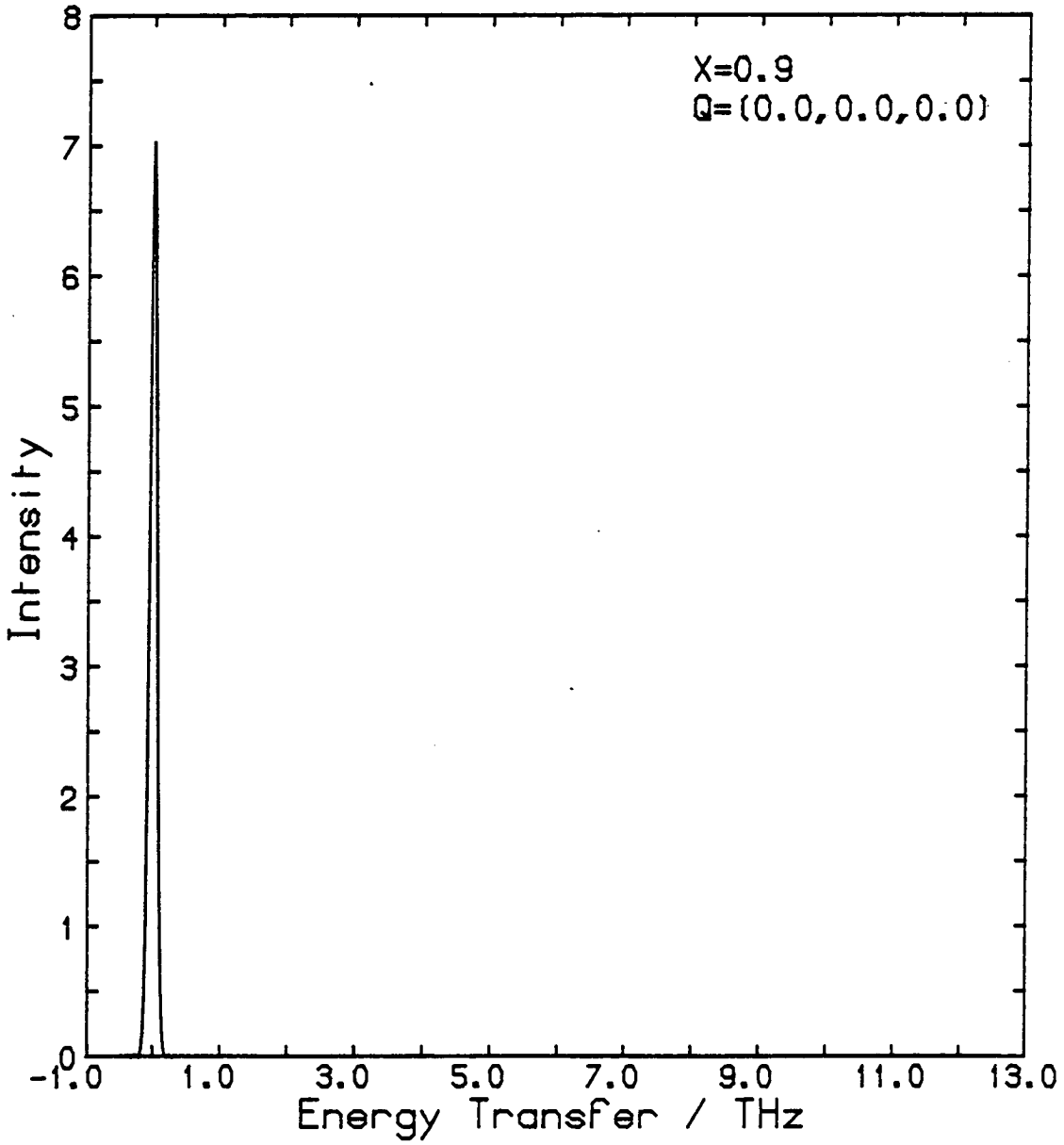
X=0.9
Q=(0.0,0.0,0.0)
Intensity
Energy Transfer / THz
8
7
6
5
4
3
2
1
0
-1.0
1.0
3.0
5.0
7.0
9.0
11.0
13.0

Fig (3.6.1(b))

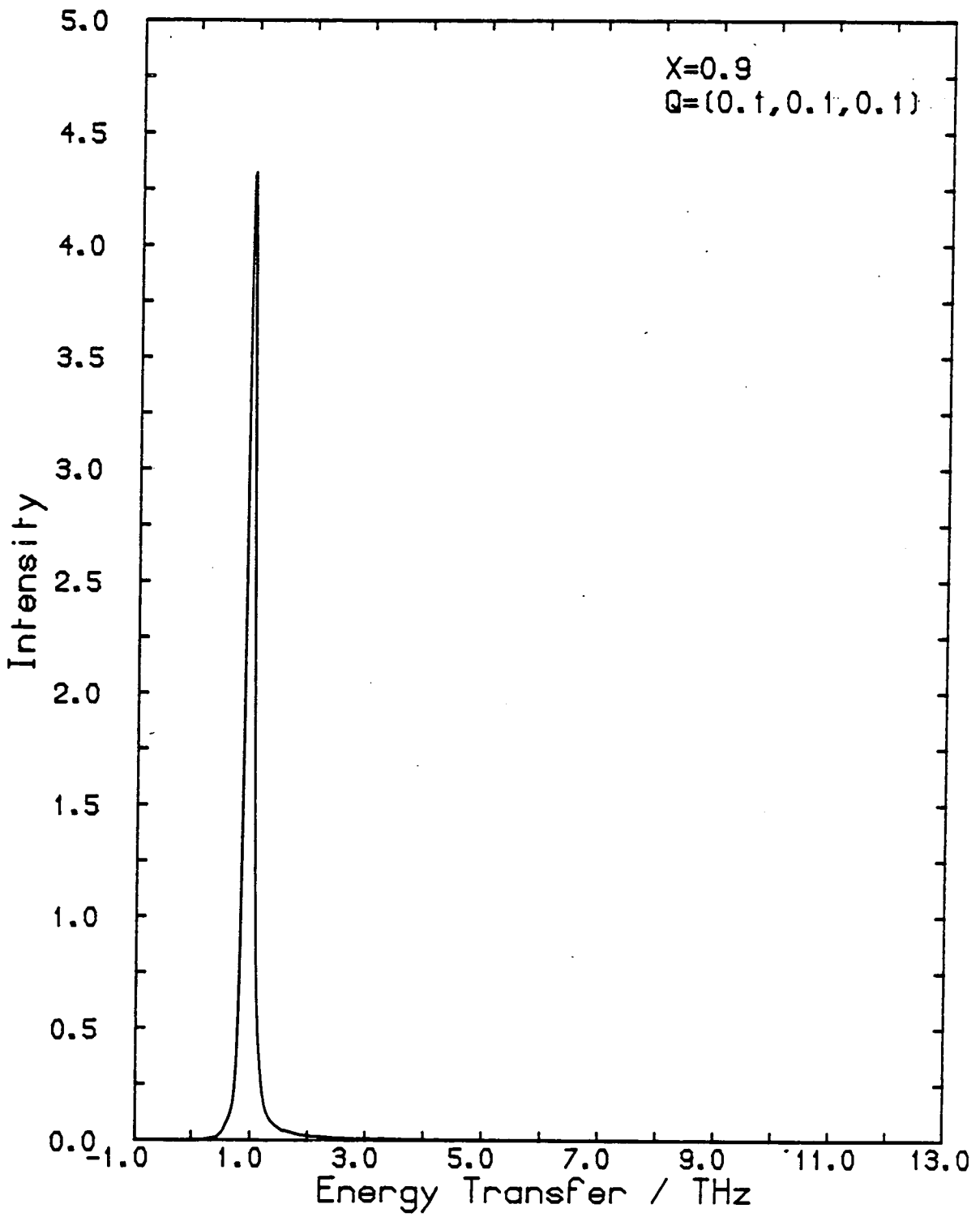
X=0.9
Q=(0.1,0.1,0.1)
Intensity
Energy Transfer / THz
5.0
4.5
4.0
3.5
3.0
2.5
2.0
1.5
1.0
0.5
0.0
-1.0
1.0
3.0
5.0
7.0
9.0
11.0
13.0

Fig (3.6.1(c))

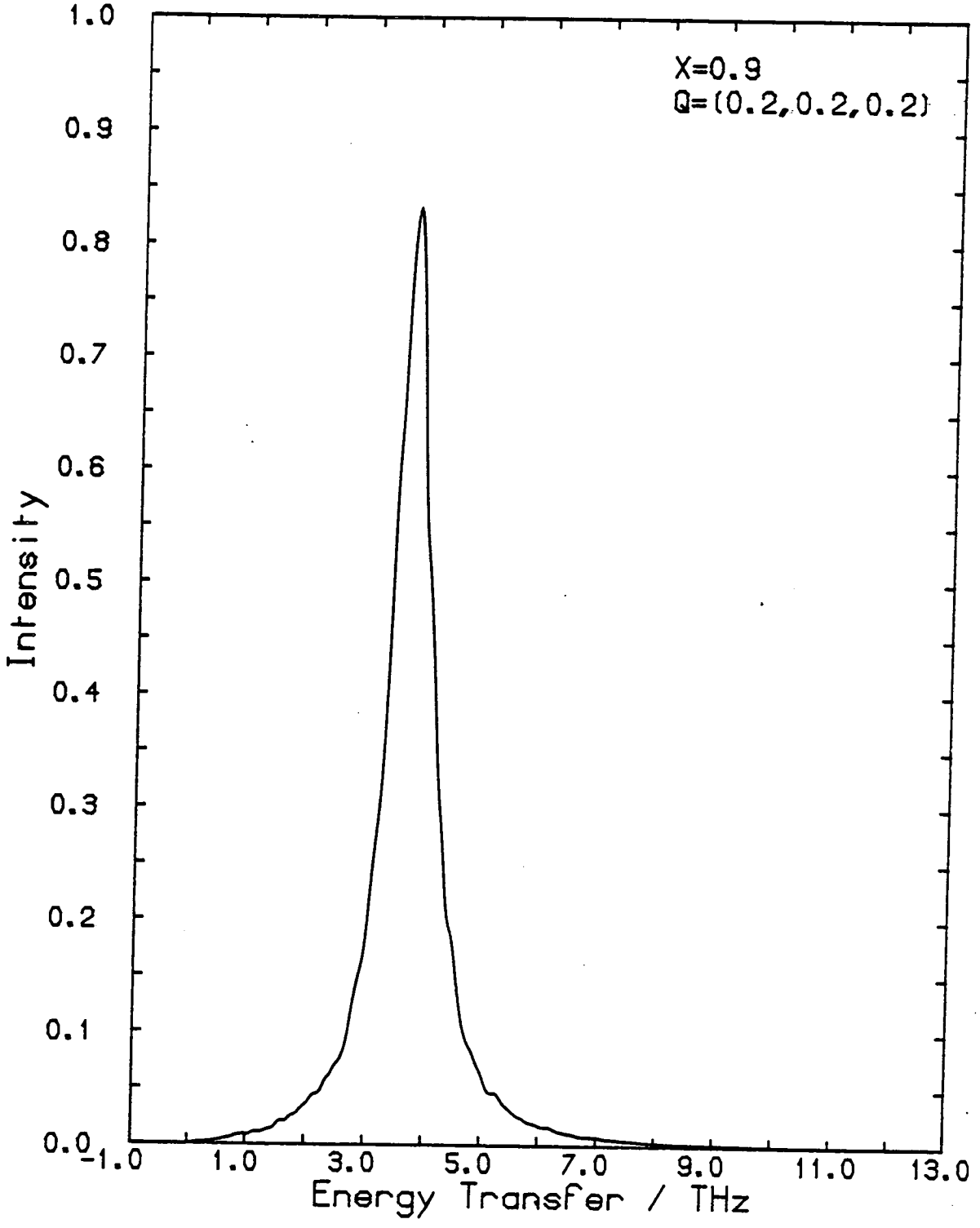
X=0.9
Q=(0.2,0.2,0.2)
Intensity
1.0
0.9
0.8
0.7
0.6
0.5
0.4
0.3
0.2
0.1
0.0
-1.0
1.0
3.0
5.0
7.0
9.0
11.0
13.0
Energy Transfer / THz

Fig (3.6.1(d))

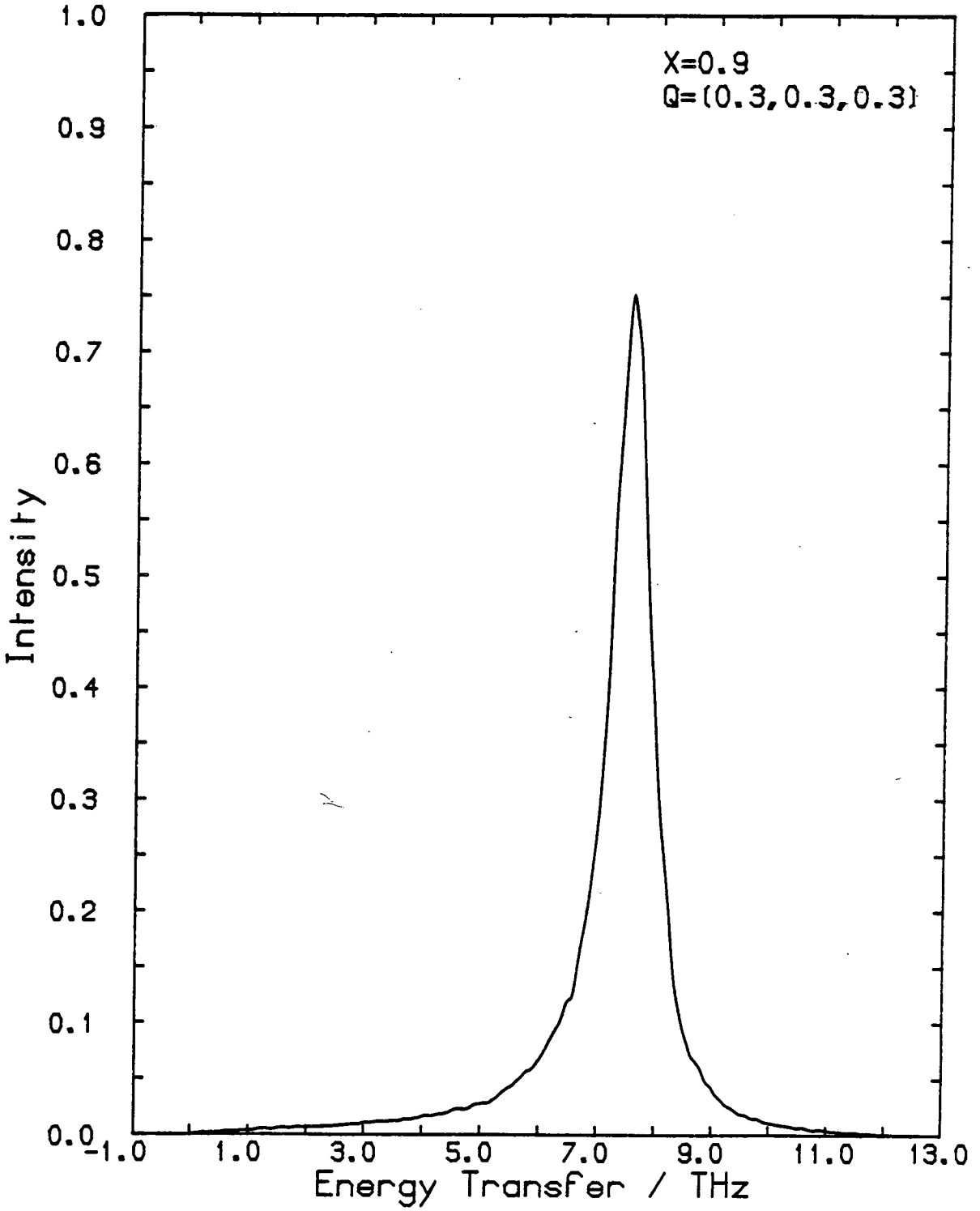
X=0.9
Q=(0.3,0.3,0.3)
Intensity
1.0
0.9
0.8
0.7
0.6
0.5
0.4
0.3
0.2
0.1
0.0
-1.0
1.0
3.0
5.0
7.0
9.0
11.0
13.0
Energy Transfer / THz

Fig (3.6.1(e))

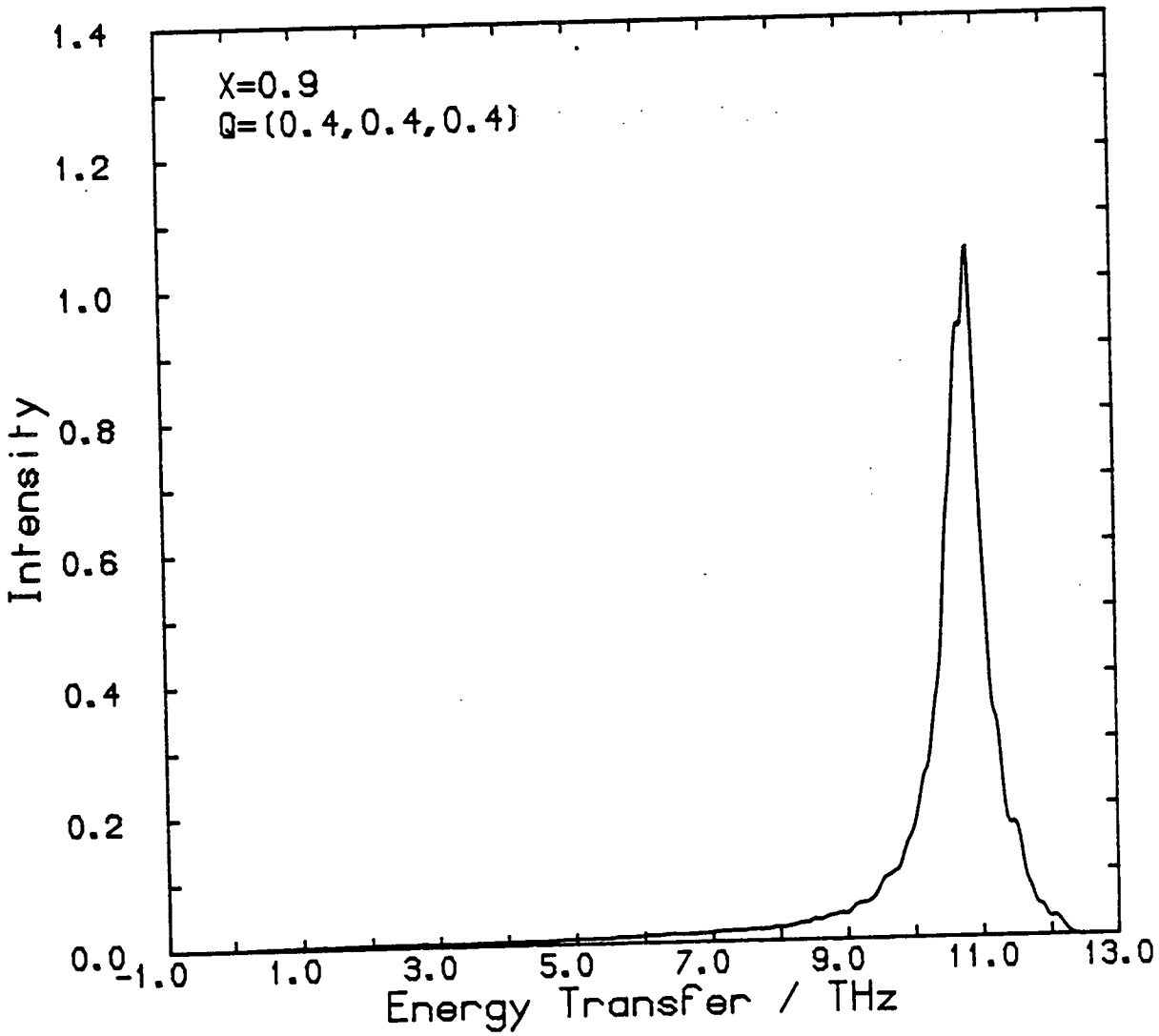
X=0.9
Q=(0.4,0.4,0.4)
Intensity
1.4
1.2
1.0
0.8
0.6
0.4
0.2
0.0
-1.0
1.0
3.0
5.0
7.0
9.0
11.0
13.0
Energy Transfer / THz

Fig (3.6.1(f))

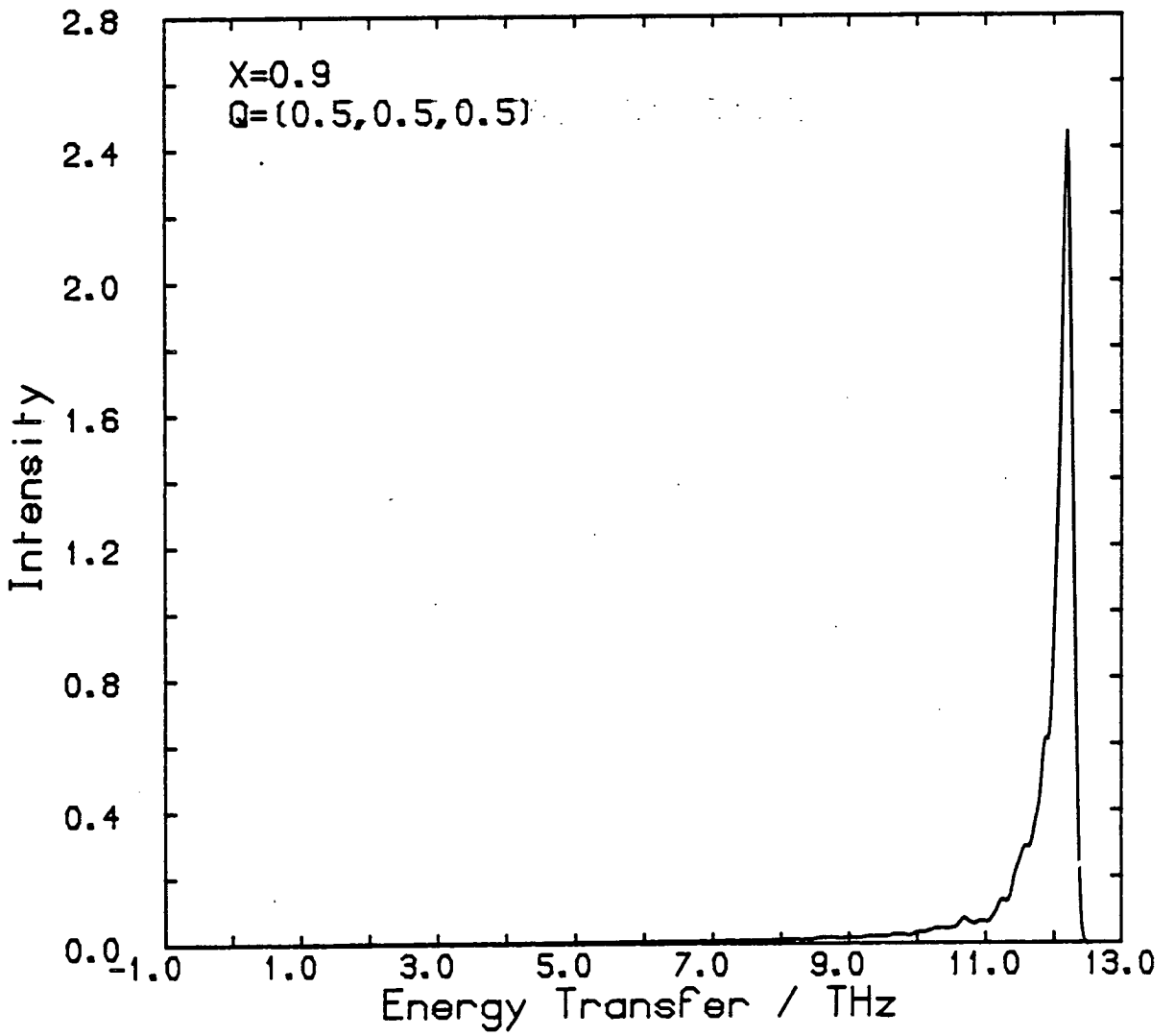
X=0.9
Q=(0.5,0.5,0.5)
Intensity
2.8
2.4
2.0
1.6
1.2
0.8
0.4
0.0
-1.0
1.0
3.0
5.0
7.0
9.0
11.0
13.0
Energy Transfer / THz

FIGURE (3.6.2): Comparison of the S(Q,E) spectra generated by MASMEX with x = 0.9 for

(a) Q = (0, 0, 0)

(b) Q = (0.1, 0.1, 0.1)

(c) Q = (0.2, 0.2, 0.2)

(d) Q = (0.3, 0.3, 0.3)

(e) Q = (0.4, 0.4, 0.4)

(f) Q = (0.5, 0.5, 0.5).

Fig (3.6.2)

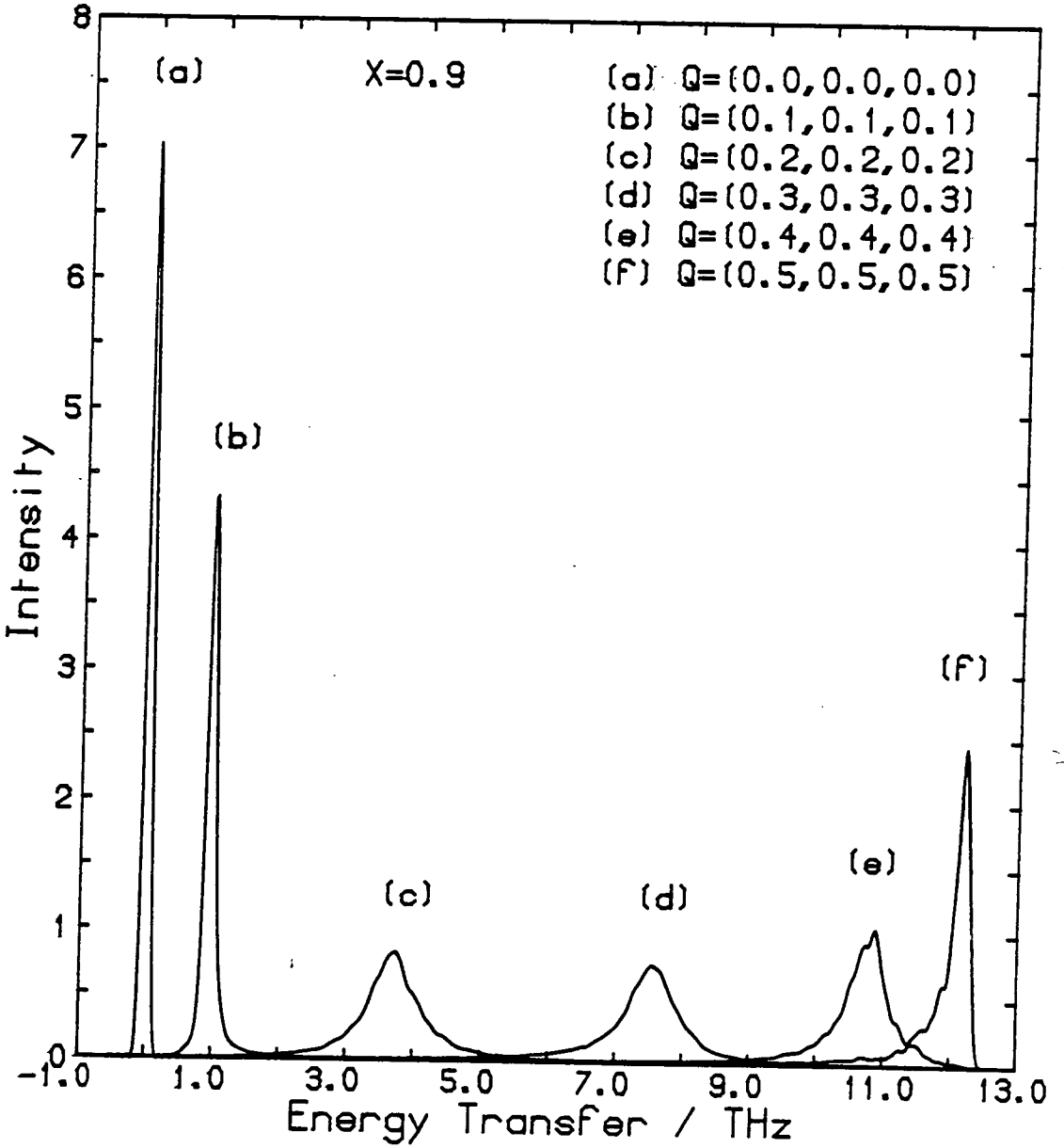
(a)
X=0.9
(a) Q=(0.0,0.0,0.0)
(b) Q=(0.1,0.1,0.1)
(c) Q=(0.2,0.2,0.2)
(d) Q=(0.3,0.3,0.3)
(e) Q=(0.4,0.4,0.4)
(f) Q=(0.5,0.5,0.5)
(b)
(c)
(d)
(e)
(f)
Intensity
Energy Transfer / THz
8
7
6
5
4
3
2
1
0
-1.0
1.0
3.0
5.0
7.0
9.0
11.0
13.0

The calculated spectra are shown in Figure (3.6.3).

As with x = 0.9, the spectrum at Q = (0,0,0) for x = 0.5 consisted of a resolution limited peak centred at zero energy. However the effects of disorder were far more pronounced as Q was increased from the zone centre value. At Q = (0.1, 0.1, 0.1) there was still a distinguishable peak with a width just over 4 times that of the resolution width and there was weight in a tail of intensity which extended towards higher energies. Beyond this the spectra did not consist so much of a single peak but more as a broad distribution of intensity. As Q increases, the bulk of the intensity moves through to higher energies but compared with x = 0.9, the peaks of the distributions have moved down in energy at any particular Q.

The third concentration chosen was x = 0.34, which is just over 3% above the magnetic site percolation threshold $x_p = 0.31$ for a simple cubic system. The number of finite clusters diverges as the percolation threshold is approached from above and for x = 0.34, calculations revealed that $x_{inf} = 0.2431$. This meant that only about two-thirds of the original magnetic sites generated in a configuration belonged to the "infinite cluster" and the one-third of magnetic sites belonging to the finite clusters were excluded from the calculations. Figure (3.6.4) shows spectra generated by MASMEX for x = 0.34. In common with the other two configurations chosen, the Q = (0,0,0) spectrum for x = 0.34 exhibited a resolution limited peak centred on zero energy. At larger Q, the spectrum consisted of broad distributions of intensity similar to the x = 0.5 case but with energy shifted downwards, at a given Q .

FIGURE (3.6.3): S(Q,E) spectra generated by MASMEX with x = 0.5 for

(a) Q = (0, 0, 0)

(b) Q = (0.1, 0.1, 0.1)

(c) Q = (0.2, 0.2, 0.2)

(d) Q = (0.3, 0.3, 0.3)

(e) Q = (0.4, 0.4, 0.4)

(f) Q = (0.5, 0.5, 0.5).

The spectra were obtained by averaging over 5 configurations.

Fig (3.6.3(a))

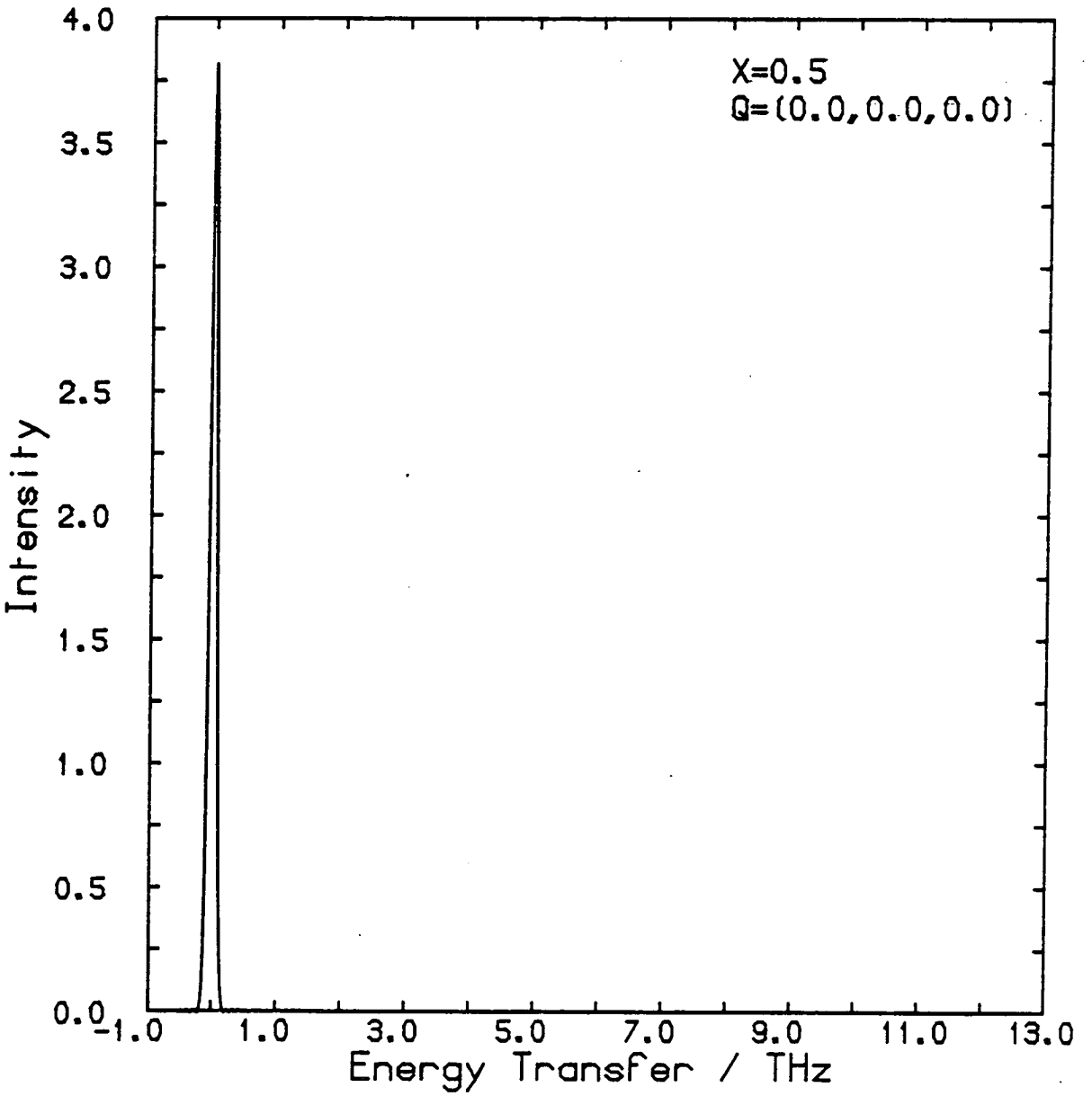
X=0.5
Q=(0.0,0.0,0.0)
Intensity
4.0
3.5
3.0
2.5
2.0
1.5
1.0
0.5
0.0
-1.0
1.0
3.0
5.0
7.0
9.0
11.0
13.0
Energy Transfer / THz

Fig (3.6.3(b))

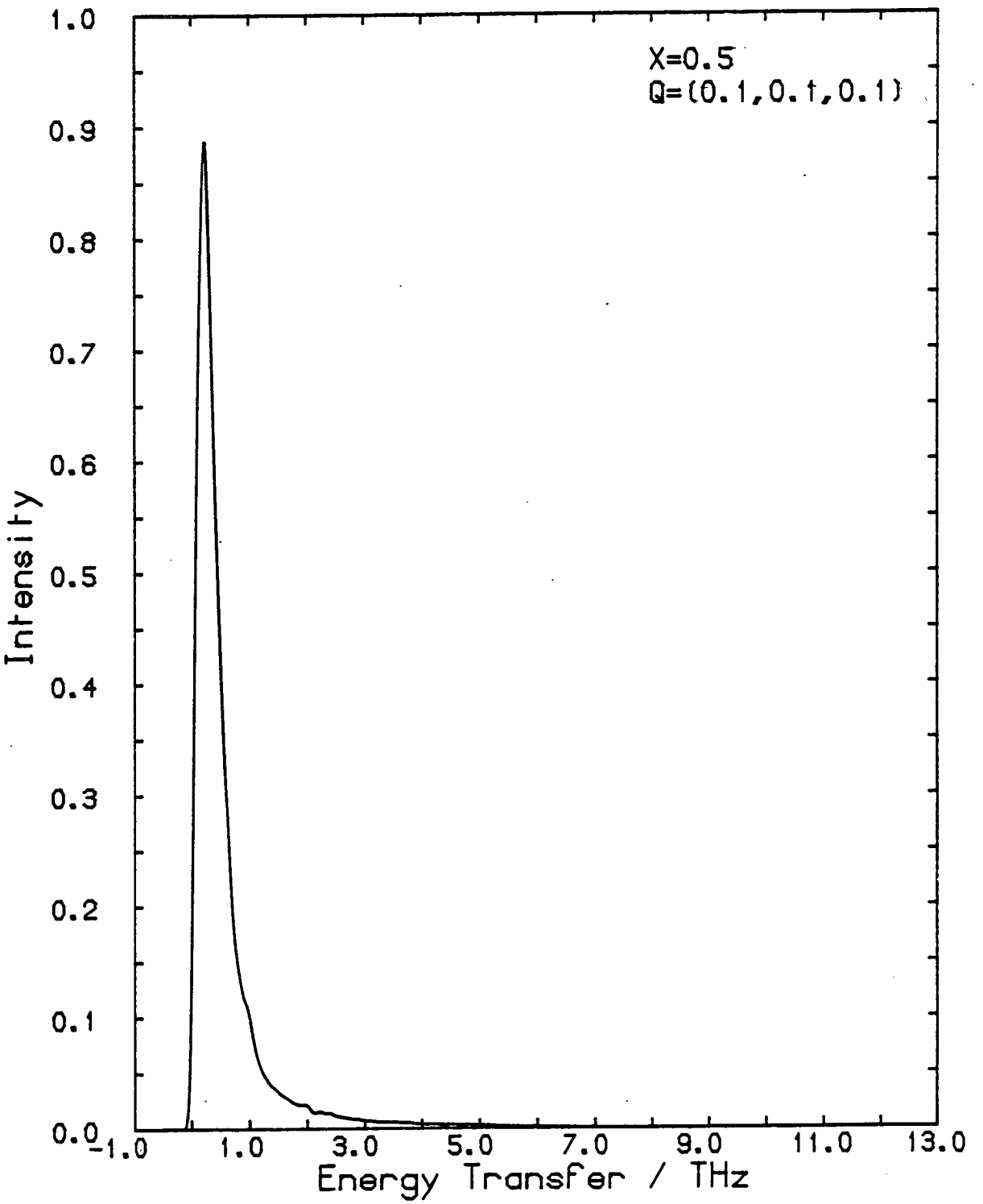
X=0.5
Q=(0.1,0.1,0.1)
Intensity
1.0
0.9
0.8
0.7
0.6
0.5
0.4
0.3
0.2
0.1
0.0
-1.0
1.0
3.0
5.0
7.0
9.0
11.0
13.0
Energy Transfer / THz

Fig (3.6.3(c))

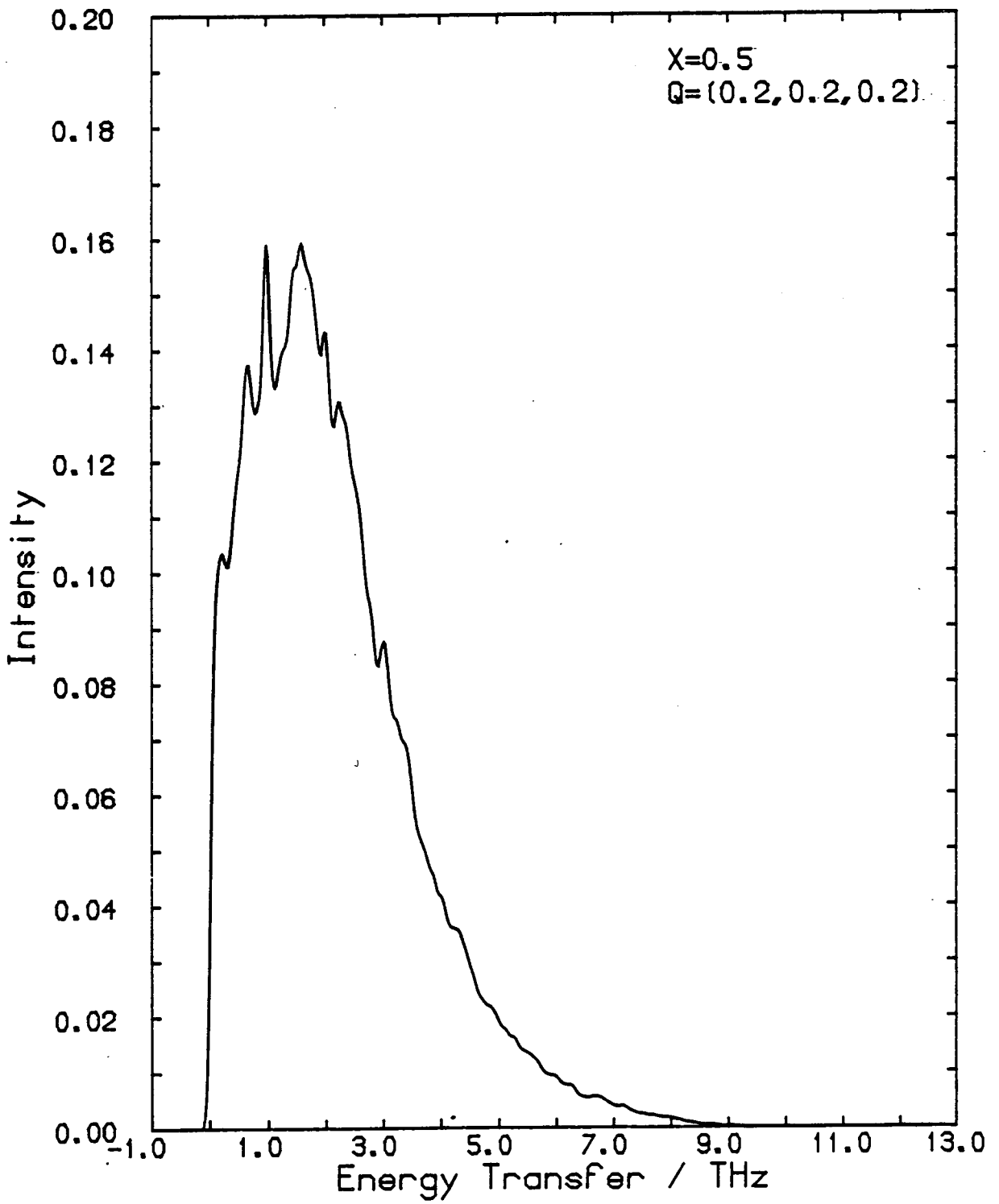
X=0.5
Q=(0.2,0.2,0.2)
Intensity
0.20
0.18
0.16
0.14
0.12
0.10
0.08
0.06
0.04
0.02
0.00
-1.0
1.0
3.0
5.0
7.0
9.0
11.0
13.0
Energy Transfer / THz

Fig (3.6.3(d))

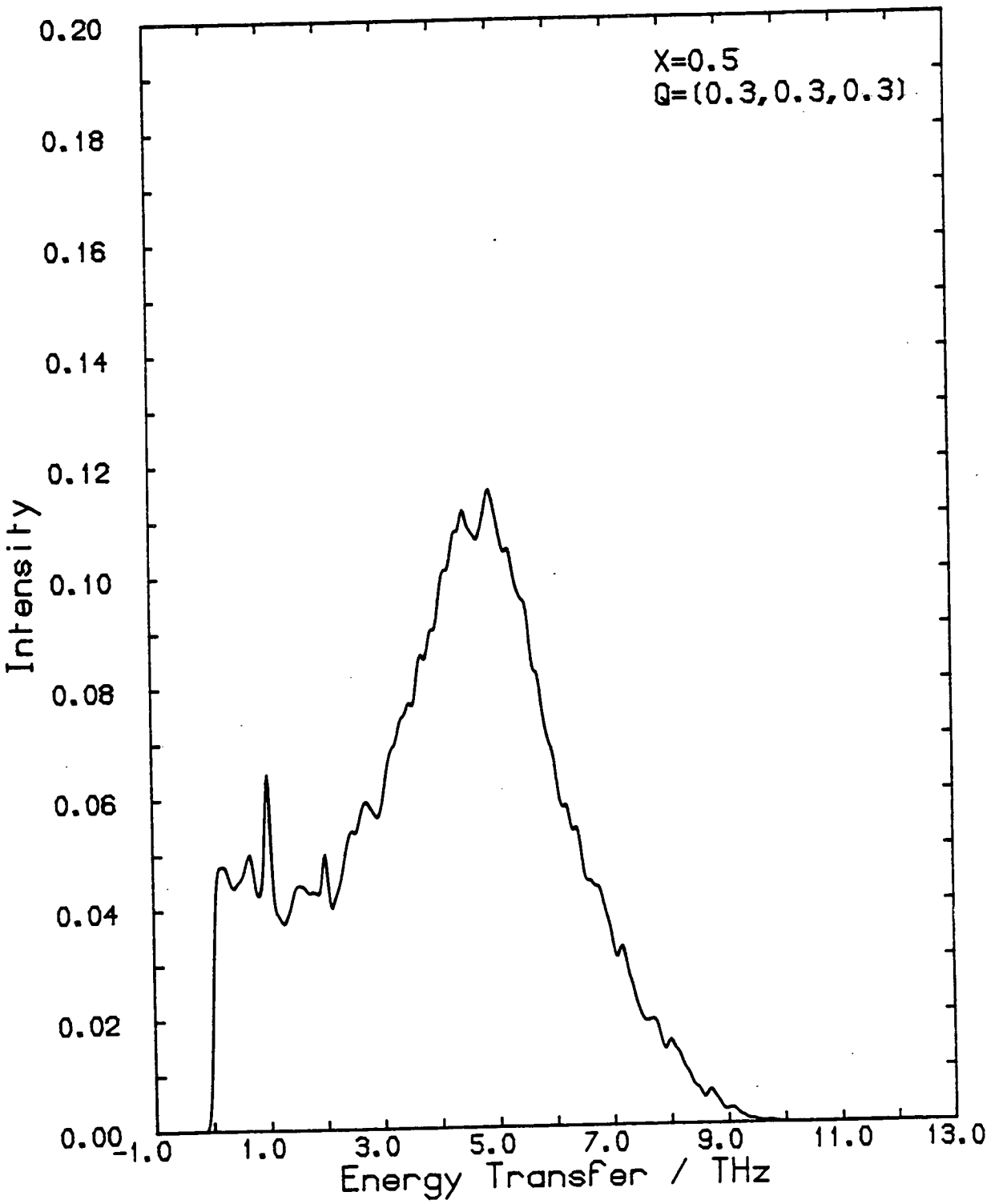
X=0.5
Q=(0.3,0.3,0.3)
0.20
0.18
0.16
0.14
0.12
0.10
0.08
0.06
0.04
0.02
0.00
Intensity
-1.0
1.0
3.0
5.0
7.0
9.0
11.0
13.0
Energy Transfer / THz

Fig (3.6.3(e))

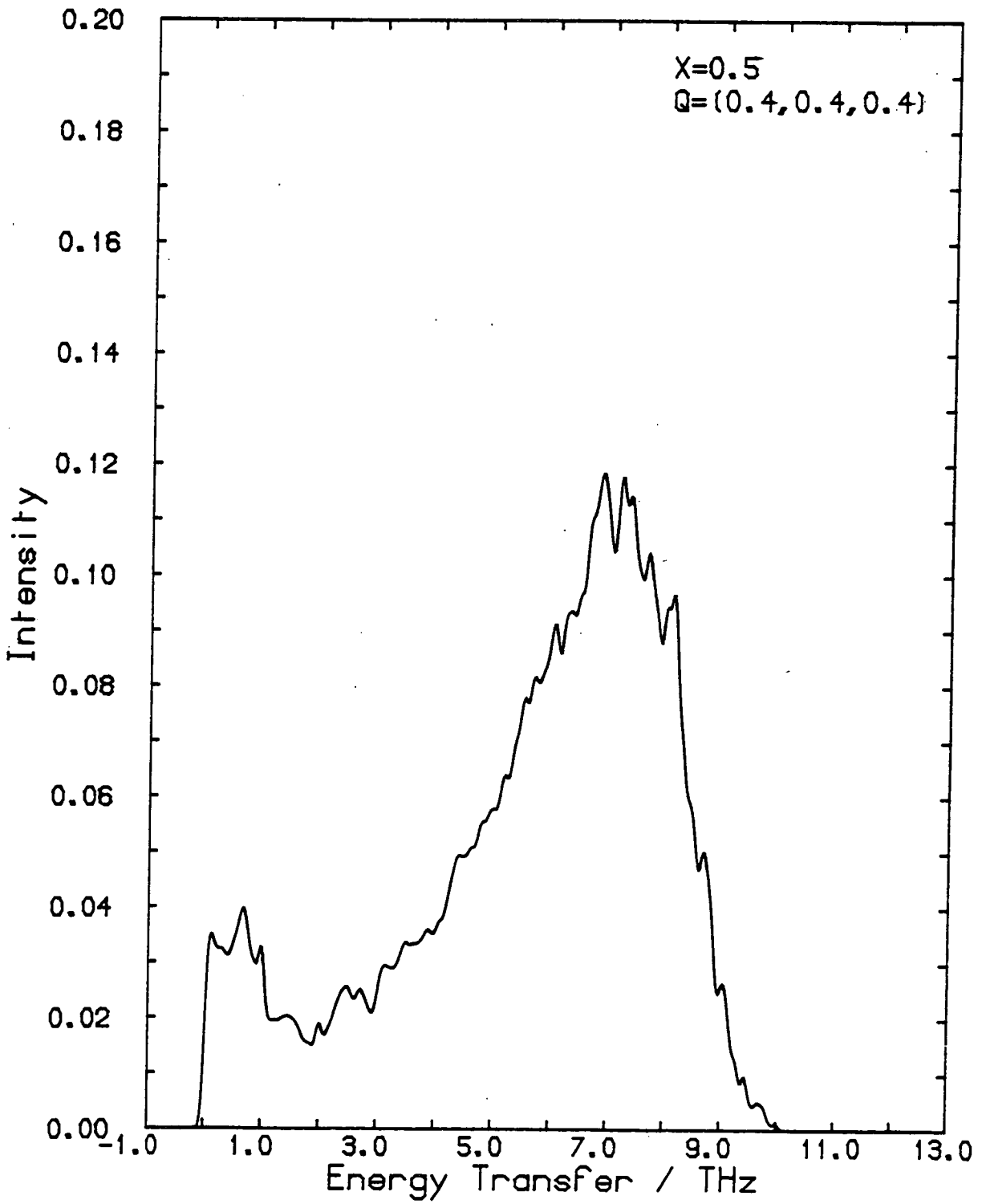
X=0.5
Q=(0.4,0.4,0.4)
Intensity
0.20
0.18
0.16
0.14
0.12
0.10
0.08
0.06
0.04
0.02
0.00
-1.0
1.0
3.0
5.0
7.0
9.0
11.0
13.0
Energy Transfer / THz

Fig (3.6.3(f))

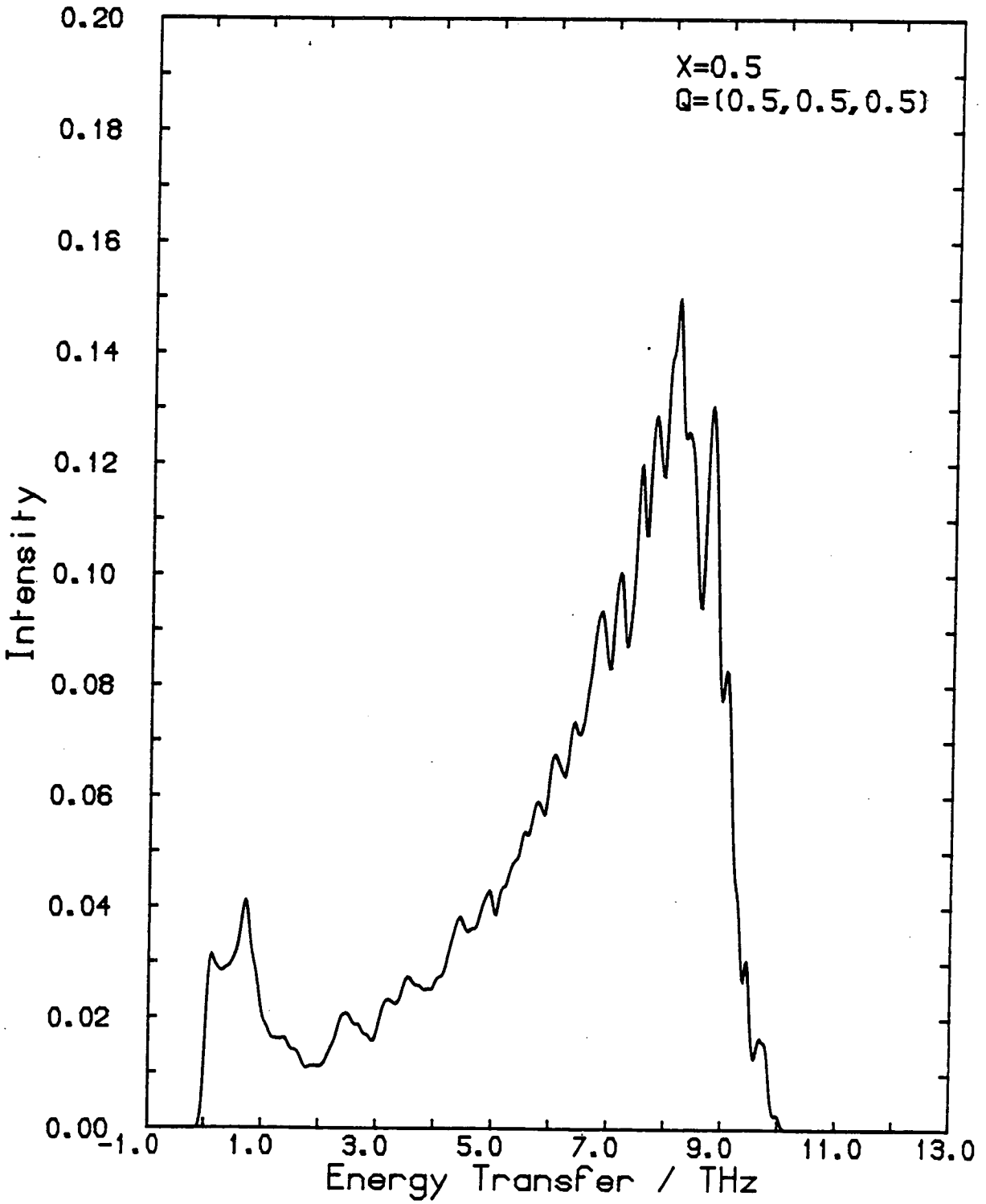
X=0.5
Q=(0.5,0.5,0.5)
Intensity
0.20
0.18
0.16
0.14
0.12
0.10
0.08
0.06
0.04
0.02
0.00
-1.0
1.0
3.0
5.0
7.0
9.0
11.0
13.0
Energy Transfer / THz

FIGURE (3.6.4): S(Q,E) spectra generated by MASMEX with 0.34 for

(a) Q = (0, 0, 0)

(b) Q = (0.1, 0.1, 0.1)

(c) Q = (0.2, 0.2, 0.2)

(d) Q = (0.3, 0.3, 0.3)

(e) Q = (0.4, 0.4, 0.4)

(f) Q = (0.5, 0.5, 0.5).

The spectra were obtained by averaging over 5 configurations.

Fig (3.6.4(a))

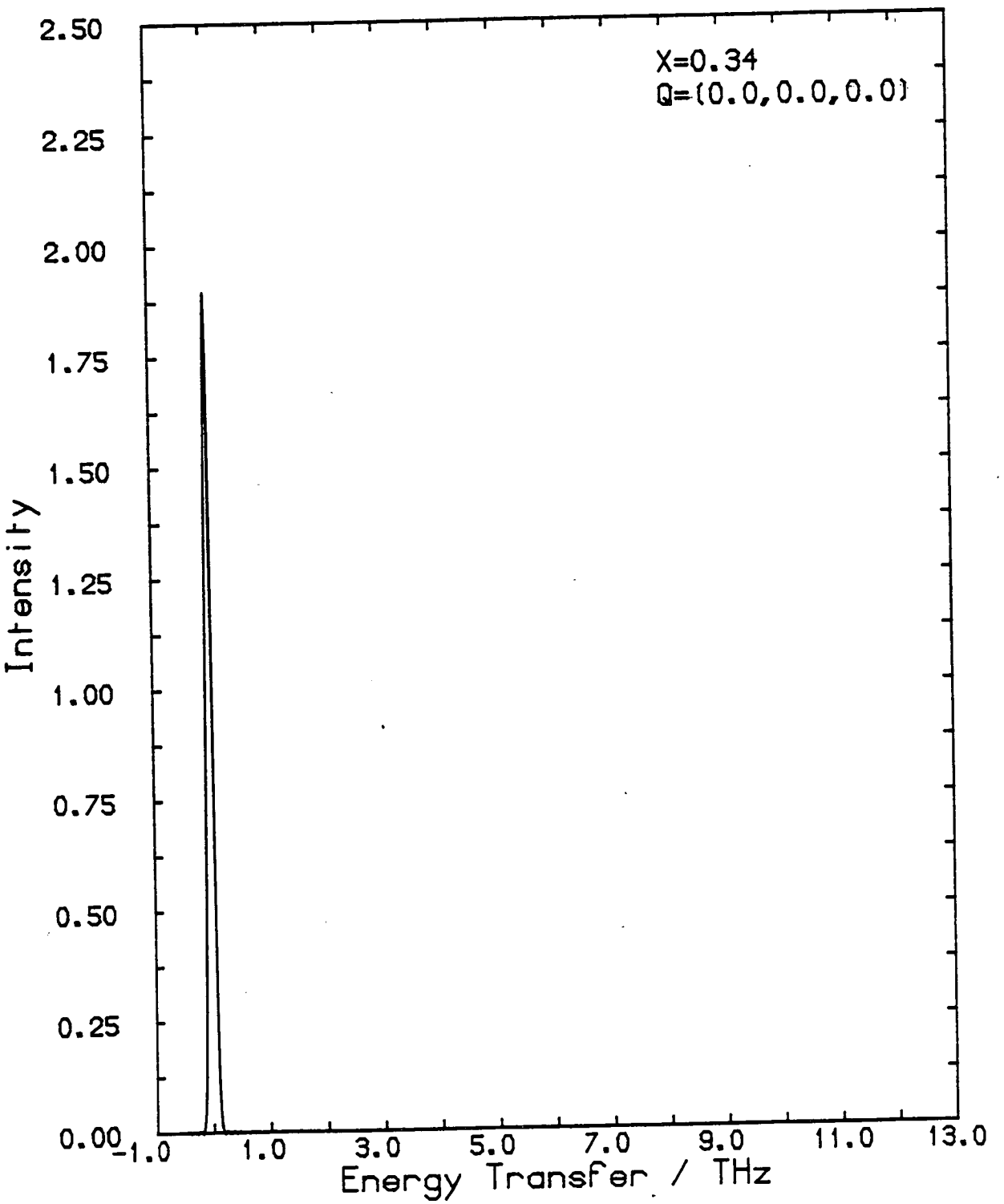
X=0.34
Q=(0.0,0.0,0.0)
Intensity
2.50
2.25
2.00
1.75
1.50
1.25
1.00
0.75
0.50
0.25
0.00
-1.0
1.0
3.0
5.0
7.0
9.0
11.0
13.0
Energy Transfer / THz

Fig (3.6.4(b))

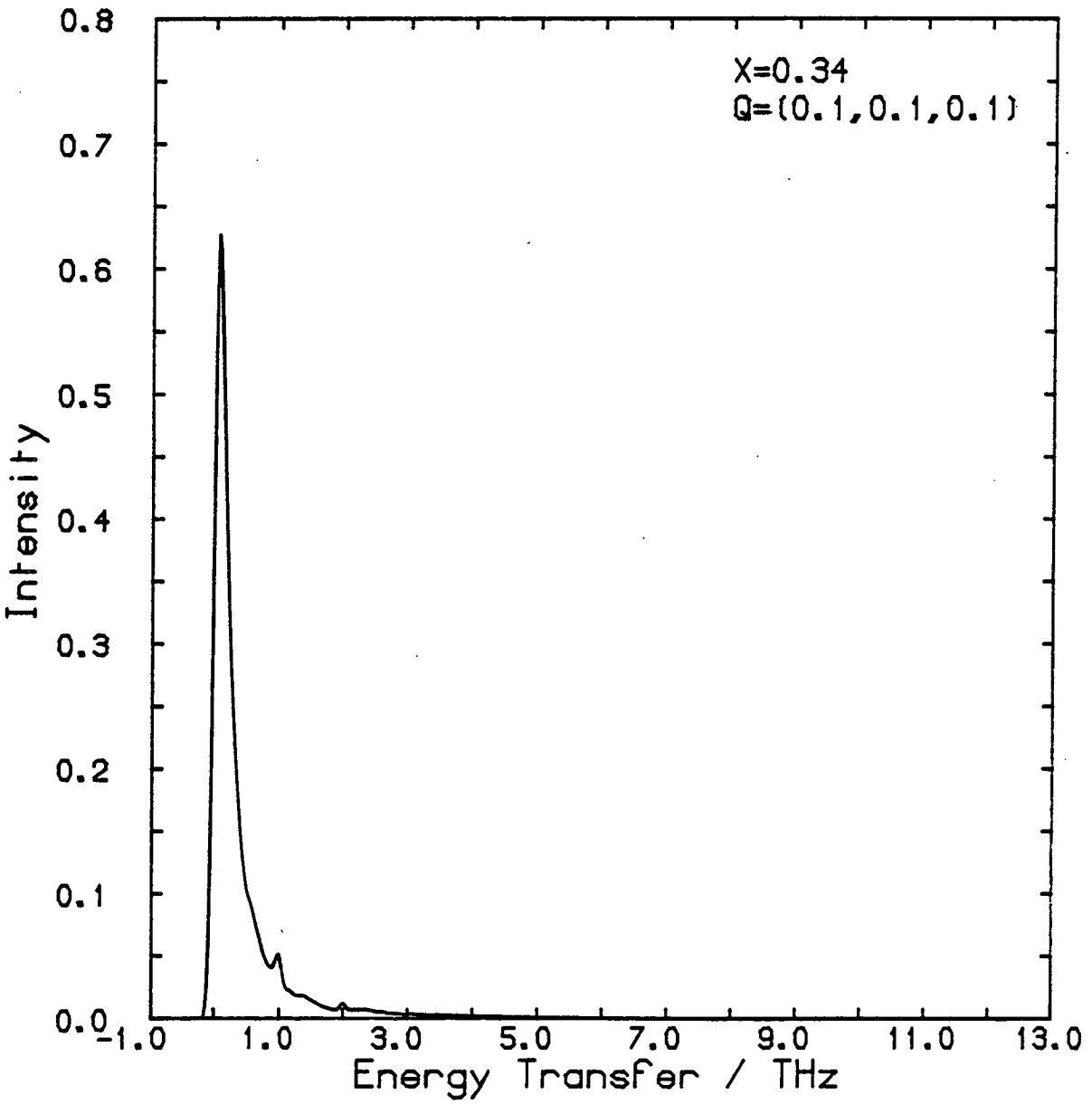
X=0.34
Q=(0.1,0.1,0.1)
Intensity
0.8
0.7
0.6
0.5
0.4
0.3
0.2
0.1
0.0
-1.0
1.0
3.0
5.0
7.0
9.0
11.0
13.0
Energy Transfer / THz

Fig (3.6.4(c))

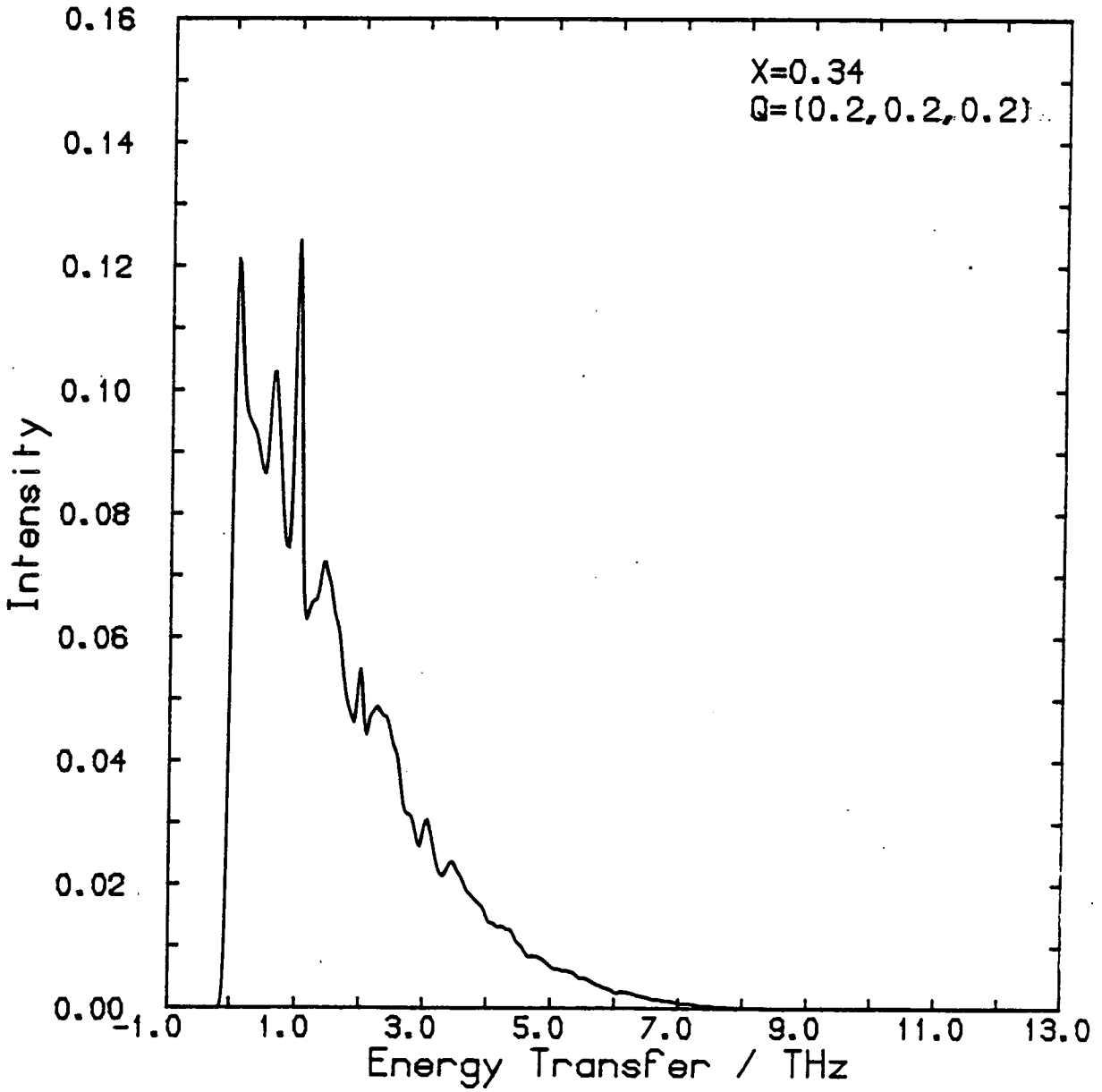
X=0.34
Q=(0.2,0.2,0.2)
Intensity
0.16
0.14
0.12
0.10
0.08
0.06
0.04
0.02
0.00
-1.0
1.0
3.0
5.0
7.0
9.0
11.0
13.0
Energy Transfer / THz

Fig (3.6.4(d))

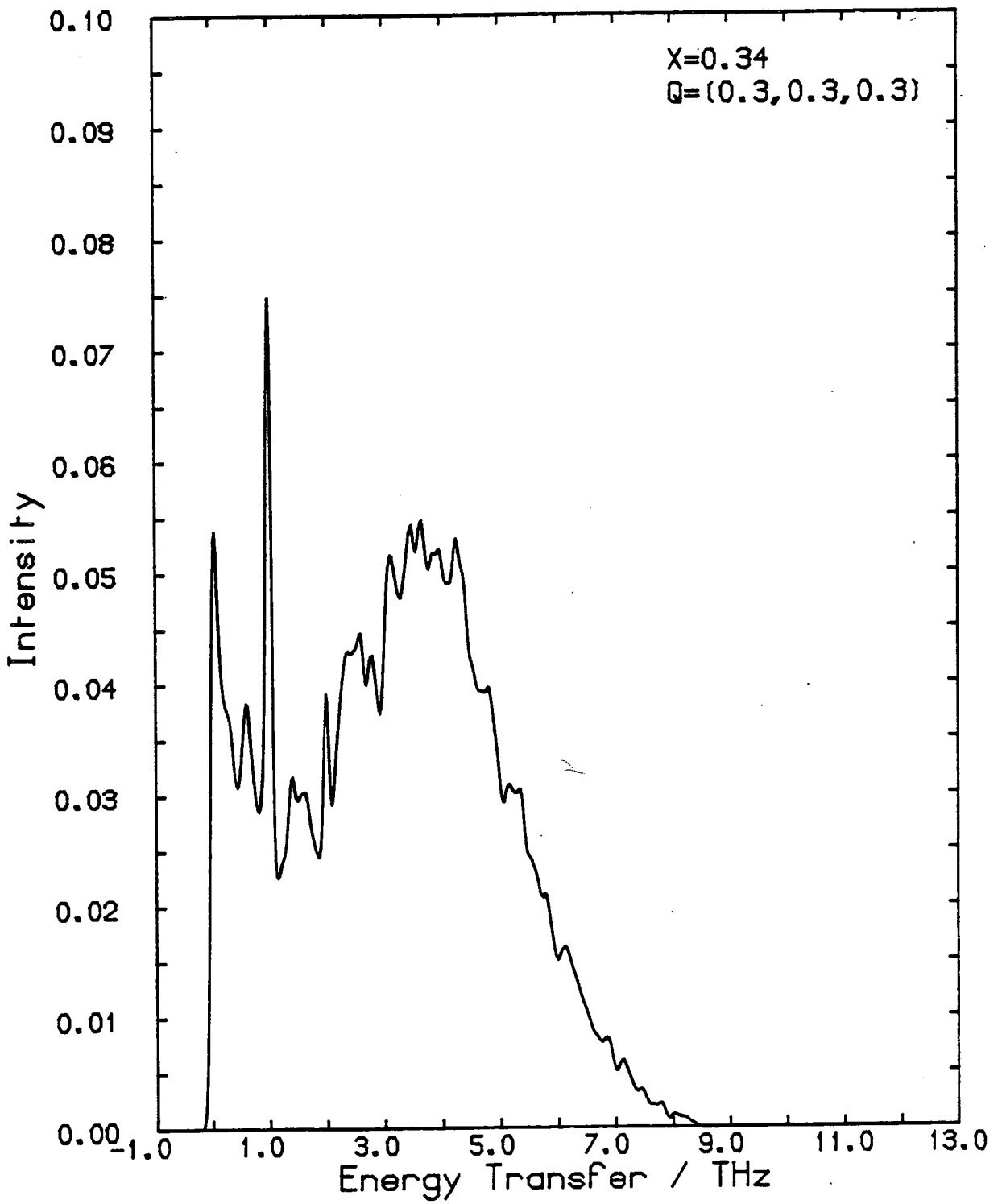
X=0.34
Q=(0.3,0.3,0.3)
Intensity
0.10
0.09
0.08
0.07
0.06
0.05
0.04
0.03
0.02
0.01
0.00
-1.0
1.0
3.0
5.0
7.0
9.0
11.0
13.0
Energy Transfer / THz

fig 3·6·4 e

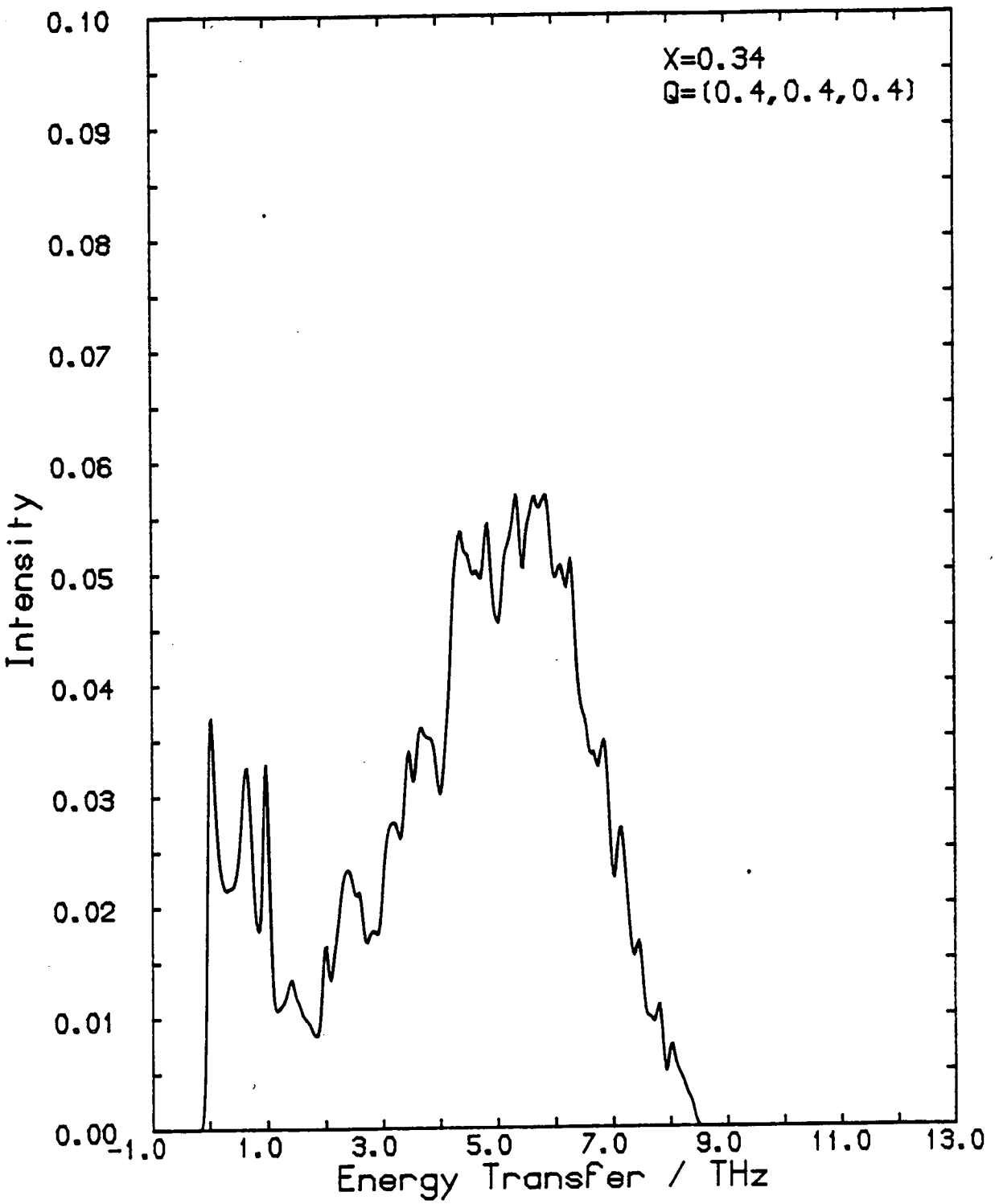
X=0.34
Q=(0.4,0.4,0.4)
Intensity
0.10
0.09
0.08
0.07
0.06
0.05
0.04
0.03
0.02
0.01
0.00
-1.0
1.0
3.0
5.0
7.0
9.0
11.0
13.0
Energy Transfer / THz

Fig (3.6.4(f))

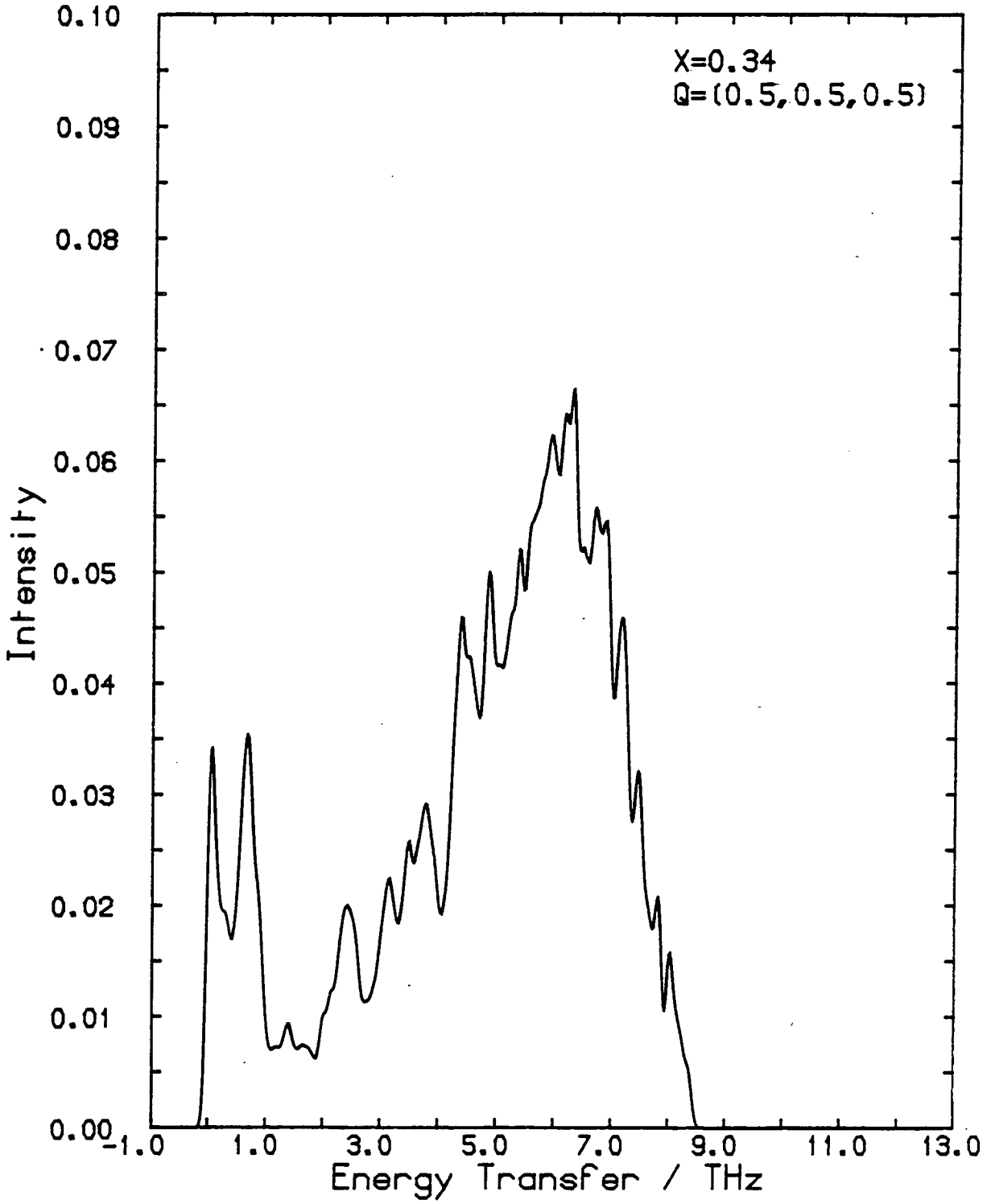
X=0.34
Q=(0.5,0.5,0.5)
Intensity
0.10
0.09
0.08
0.07
0.06
0.05
0.04
0.03
0.02
0.01
0.00
-1.0
1.0
3.0
5.0
7.0
9.0
11.0
13.0
Energy Transfer / THz

3.7 Comparison with Experimental Data

This section reports a comparison which was made between spectra generated by the computer program MASMEX and some experimental data, which was obtained from inelastic neutron scattering measurements on the system $Cr_{1-x}Fe_x$ with $x = 0.27$ (Mitchell et al. (1985)). Body Centred cubic (b.c.c) Chromium-Iron is a diluted magnetic system because the Iron ions have magnetic moments but the Chromium ions behave non-magnetically (Aldred et al. (1981)). The real system differs from the model system in several ways. Firstly, the real system is b.c.c. whereas the model system has a simple cubic (s.c.) lattice, but this is not considered a serious problem since disorder induced phenomenological features should not be affected. (Plans are afoot to extend MASMEX so that it can model b.c.c. systems.) Secondly, the real system is metallic and since the magnetic moment is associated with the conduction electrons, the excitations might be influenced by single particle or Stoner excitations as well as the disorder. In the model system, only the disorder can affect the excitations and so comparison of the spectra generated from the model system with the experimental data from the real system should show whether single particle excitations significantly affect the spectra.

The neutron inelastic scattering measurements were performed on a single crystal sample of $Cr_{1-x}Fe_x$ with $x = 0.27$ on the IN3 triple-axis neutron spectrometer at the I.L.L., Grenoble, France. This alloy composition is, in fact, just in the region where at low temperatures the small-wavevector spin waves appear to collapse (Shapiro et al. (1981)) and ferromagnetism gives way to a more

complicated structure. This is not of concern here since it seems unlikely that the large wavevector magnetic excitations would be effected by that transition.

The experiments had to be performed at around $\frac{1}{2}T_c$ (in fact at T = 100K compared with T_c = 195K) since at lower temperatures the intensity of the spin wave scattering was too weak to be distinguished from the background. Even at this temperature data was collected only in the range up to 2 THz because there appeared to be little intensity above background at higher energies.

Pyrolytic graphite (0,0,2) Bragg reflections were used in both the monochromator and analyser. The fixed final wavevector was fixed at $k_f = 2.662\text{Å}^{-1}$ and a pyrolytic graphite filter was used to eliminate higher order contamination.

The real crystal, being b.c.c., had a value of x = 0.27 which is around 8% above the minimum concentration where ferromagnetism is observed (Burke et al. (1983)).

Since only a qualitative comparison can be made between the experimental data for the b.c.c. system and the calculated spectra for the s.c. system, the magnetic site concentration was chosen to be x = 0.39 in the model system. That value of x is 8% above the magnetic site percolation threshold for a simple cubic lattice. With a spin S = 1 the exchange interaction was chosen to be J = 8.18 THz, corresponding to the observed spin wave stiffness in pure Iron. The energy resolution in the experiment was around 0.3 THz and λ was chosen so that the energy resolution in the calculated spectra matched this. As discussed previously, the calculated spectra are essentially a calculation of $S(\underline{Q},E)$ at

at $T = 0$. $S(\underline{Q},E)$ is related to the imaginary part of the magnetic transverse susceptibility by:

$$S(\underline{Q},E) = (n(E) + 1)\ \chi''(\underline{Q},E) \qquad (3.7.1)$$

where $n(E)$ is the Bose Einstein population factor, given by:

$$n(E) = [\exp(E/kT) - 1]^{-1} \quad . \qquad (3.7.2)$$

In this definition of the population factor, E is positive for neutron energy loss processes and negative for neutron energy gain processes. Hence, for excitations with finite energy, $n(E) = 1$ for neutron energy loss and $n(E) = 0$ for neutron energy gain at $T = 0$. (That makes physical sense because at $T = 0$ there are no excitations in the system from which the neutron could gain energy, but the neutrons can always lose energy by creating a magnetic excitation.) Consequently $\chi''(\underline{Q},E)$ is the neutron energy loss part of $S(\underline{Q},E)$ at $T = 0$. In comparing experimental data with calculated data then it was assumed that the only effect of increasing the temperature to T = 100K was to populate the excitations such that $S(\underline{Q},E)$ was given by equation (3.7.1) with $\chi''(\underline{Q},E)$ replaced by $S(\underline{Q},E)$ at $T = 0$. Hence to compare the spectra produced by MASMEX to the experimental data, $S(\underline{Q},E)$ at $T = 0$ was simply multiplied by the population factor.

Calculations were made for various wavevectors along the [1,0,0] direction. That direction was chosen because the experimental data was collected for wavevectors along the [1,1,0] direction: the [1,0,0] direction in s.c. systems and [1 1 0] direction in b.c.c. systems are the directions for which Brillouin

zone boundary is closest to the Brillouin zone centre. Comparisons are shown in Figure (3.7.1) between experimental and calculated spectra with the same values of Q/Q_{zB} (where Q_{zB} indicates the wavevector at the Brillouin zone boundary). Note that only a rough scaling has been performed on the intensity of the computer generated data and that the scale factor used was the same at each Q.

Bearing in mind the qualitative nature of the comparison between the experimental and computer generated data, the phenomenological agreement is good enough to suggest that the main features of the experimental spectra can be attributed to the random substitutional disorder. That is to say, there do not seem to be any features in the available experimental data which cannot be qualitatively explained in terms of the calculated spectra from the simple model system which takes only the disorder into account. The existence of single particle or Stoner modes do not seem necessary to explain the experimental data. However, a quantitative comparison between the experimental spectra and the computer generated spectra for a model b.c.c. system would be even more informative and in the next stage of this project it is intended to extent the program MASMEX to deal with b.c.c. systems.

The calculated spectra in Figure (3.7.1) are for energies up to around 2THz because that was the range of neutron energy transfers for which experimental data was collected. However the calculated spectra were generated for energies up to about 30THz. Figure (3.7.2) shows a calculated spectrum for $S(\underline{Q},E)$ at T = 0K and Figure (3.7.3) shows that spectrum multiplied by the population factor to give an $S(\underline{Q},E)$ at T = 100K. A striking feature of the

FIGURE (3.7.1): Experimental data for the system $Cr_{1-x}Fe_x$ with $x = 0.27$ at $T = 100K$ for

(a) $Q = (0.3, 0.3, 0)$

(b) $Q = (0.4, 0.4, 0)$

(c) $Q = (0.5, 0.5, 0)$

The solid line indicates calculated intensity obtained by the method described in the text.

fig 3·7·1a

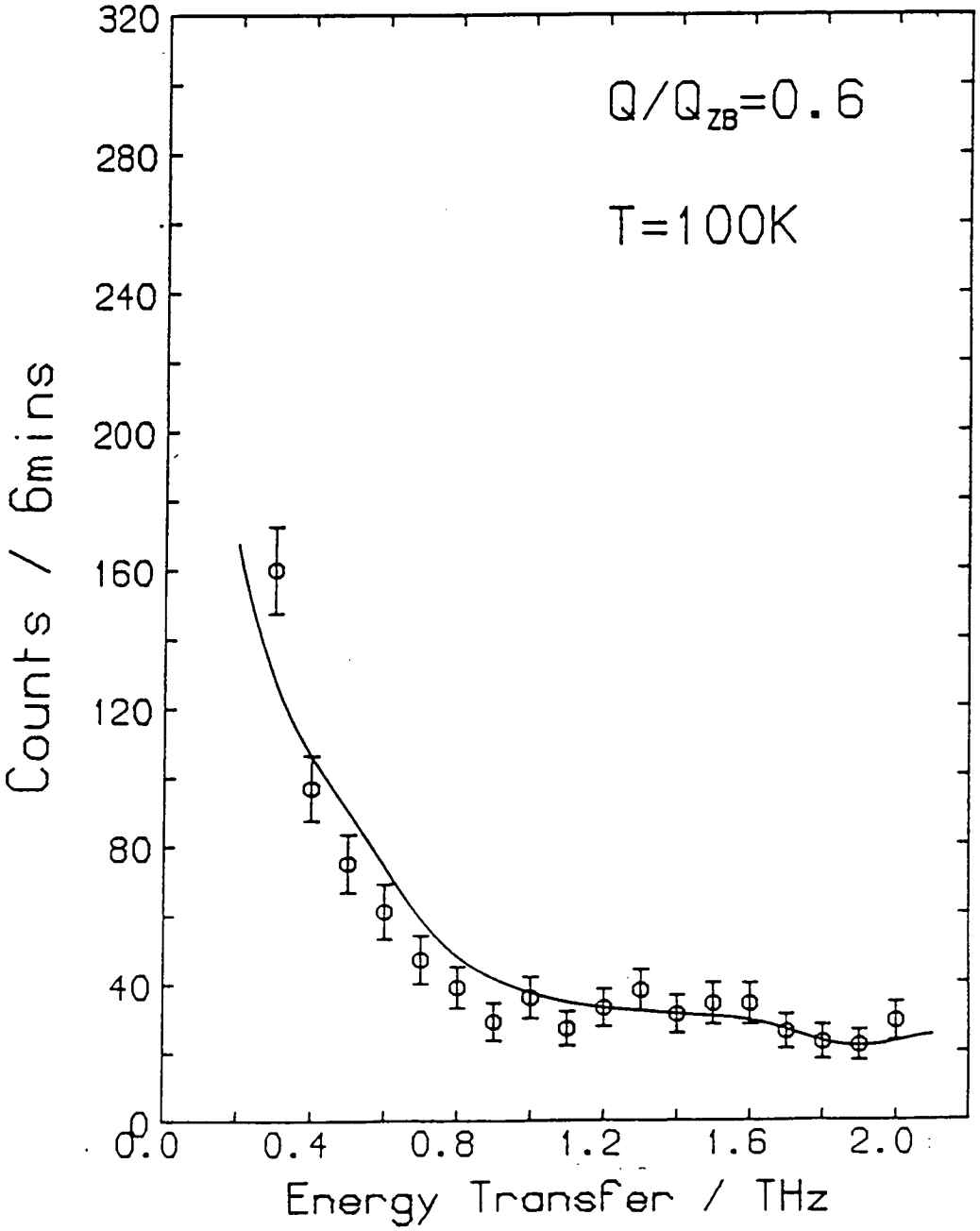
Q/Q_ZB=0.6
T=100K
Counts / 6mins
Energy Transfer / THz
0
40
80
120
160
200
240
280
320
0.0
0.4
0.8
1.2
1.6
2.0

fig 3·7·1 b

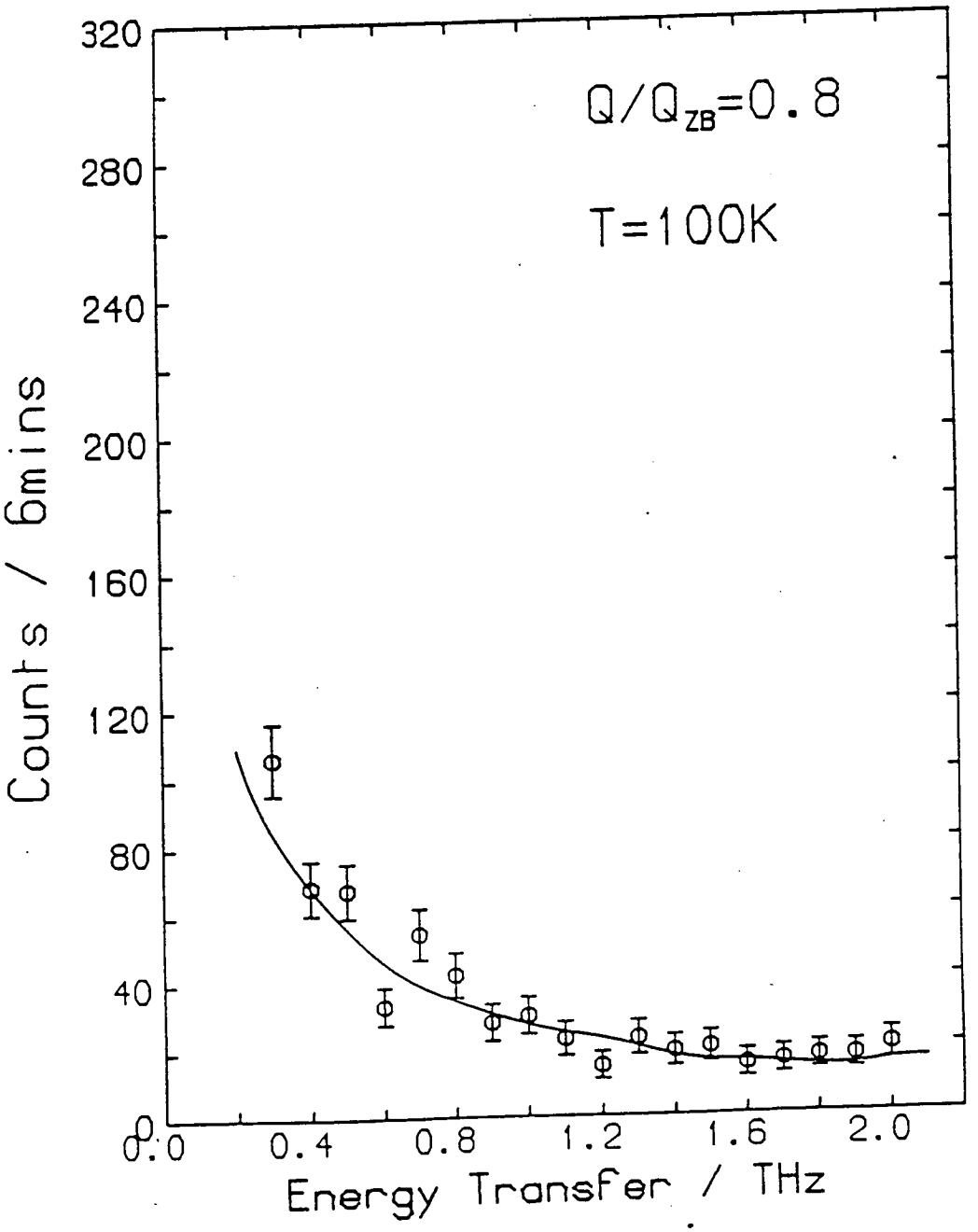
Q/Q_ZB=0.8
T=100K
Counts / 6mins
Energy Transfer / THz
0
40
80
120
160
200
240
280
320
0.0
0.4
0.8
1.2
1.6
2.0

fig 3·7·1 c

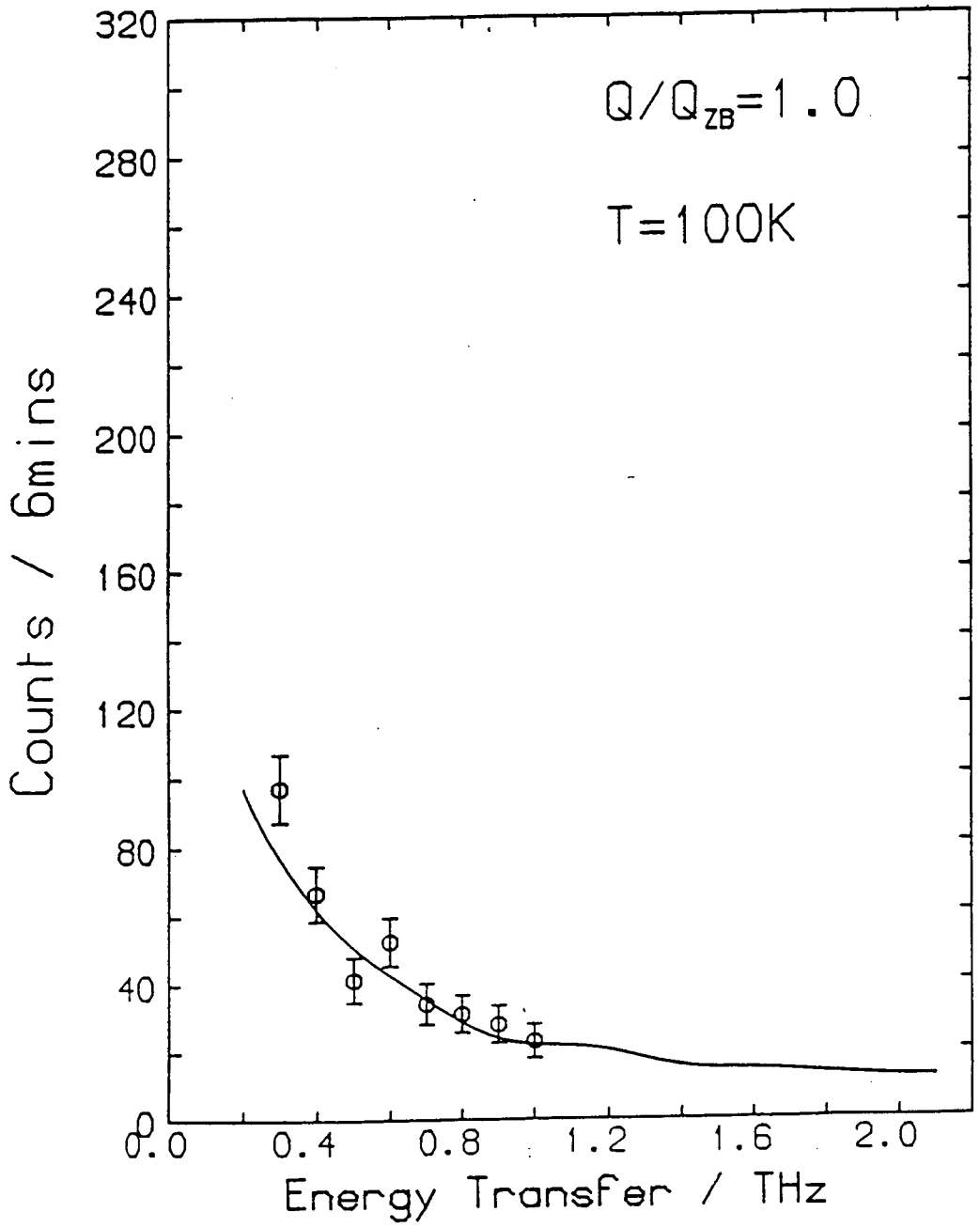
Q/Q_ZB=1.0
T=100K
Counts / 6mins
Energy Transfer / THz
0
40
80
120
160
200
240
280
320
0.0
0.4
0.8
1.2
1.6
2.0

FIGURE (3.7.2): Calculated S(Q,E) spectrum with x = 0.39 at T = 0K for Q = (0.5, 0 , 0).

fig 3·7·2

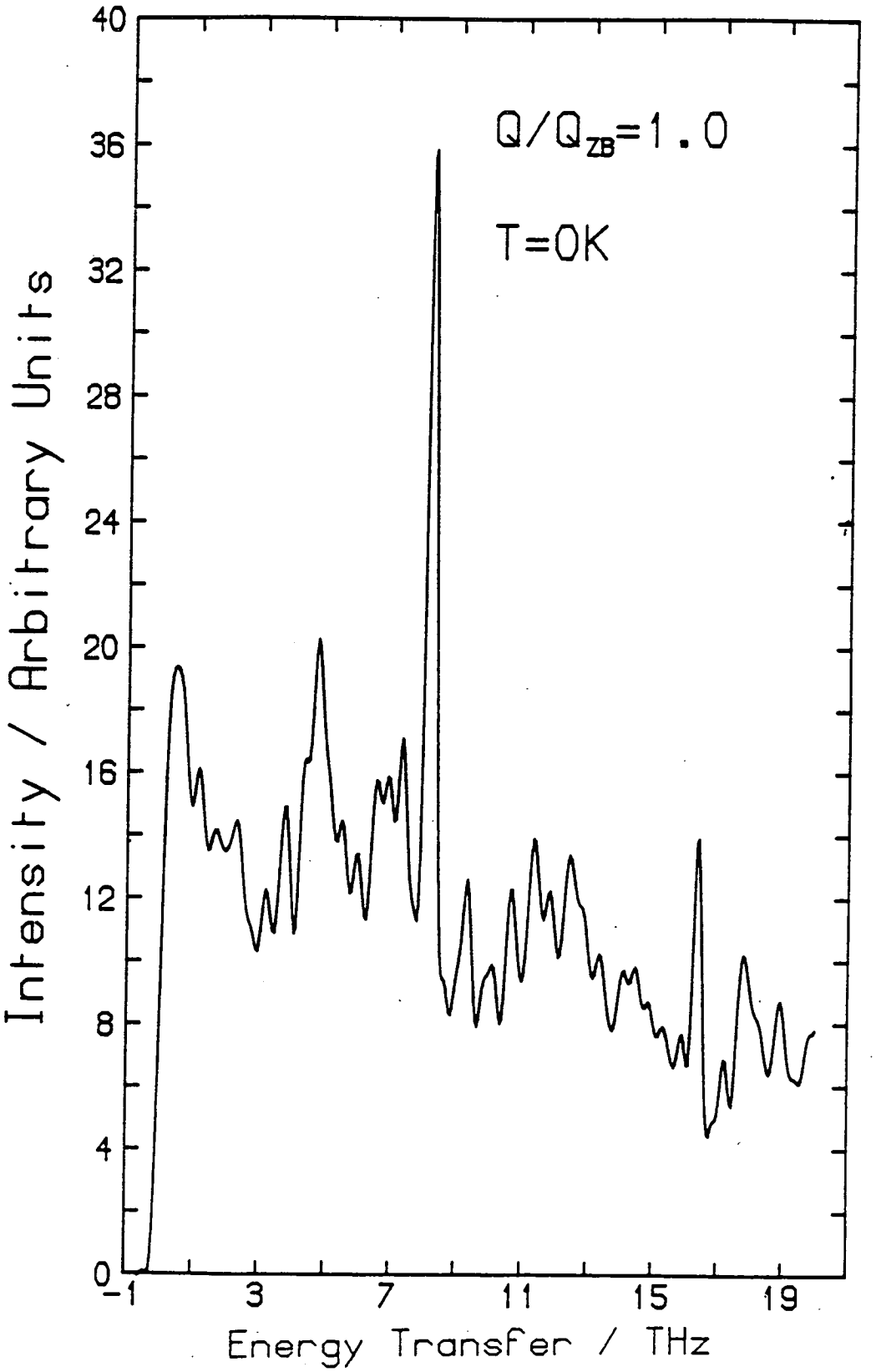
Q/Q_ZB=1.0
T=0K
Intensity / Arbitrary Units
Energy Transfer / THz
0
4
8
12
16
20
24
28
32
36
40
-1
3
7
11
15
19

FIGURE (3.7.3): Calculated S(Q,E) spectrum with x = 0.39 at T = 100K for Q = (0.5, 0 , 0).

fig 3·7·3

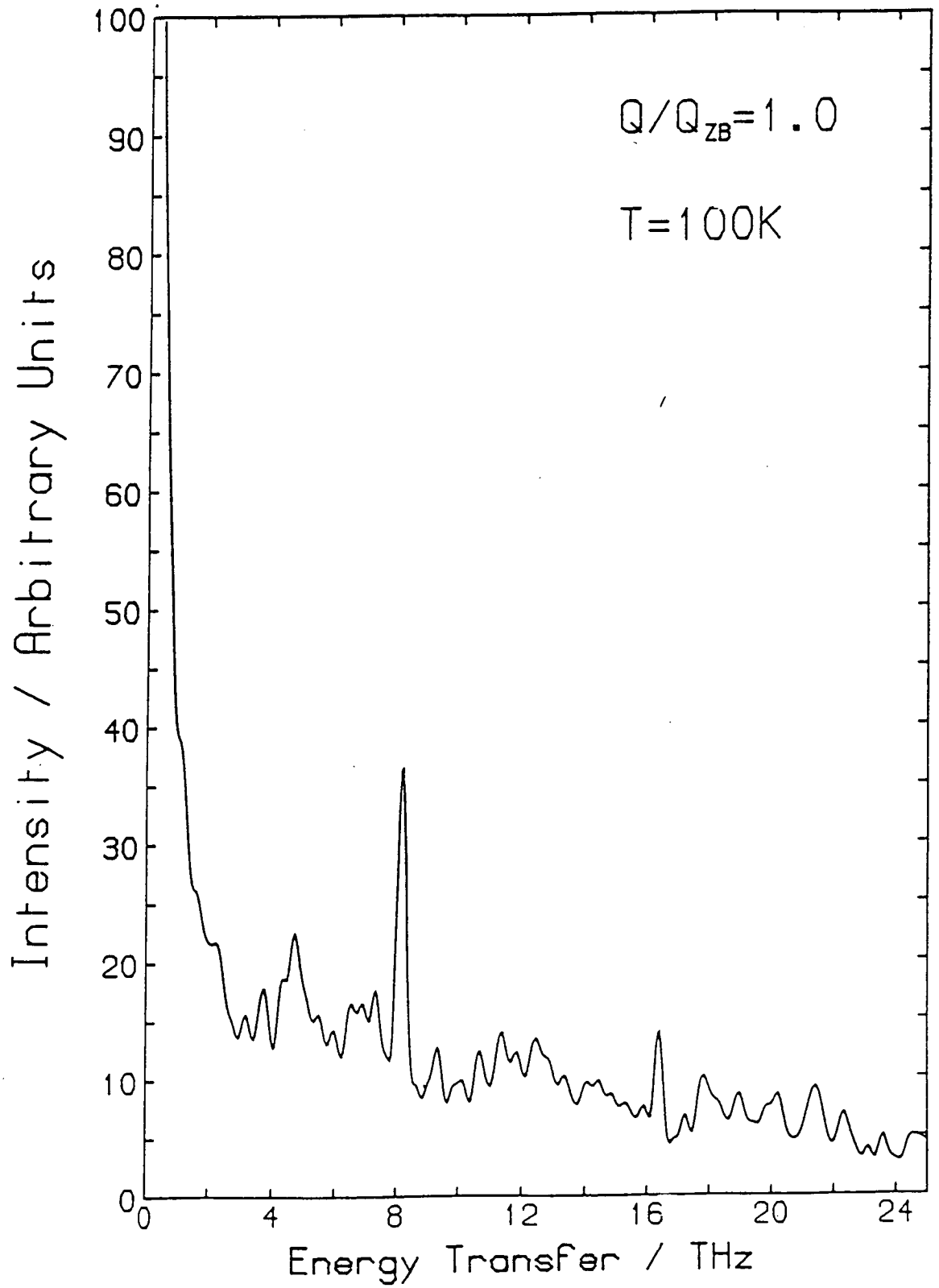
Q/Q_ZB=1.0
T=100K
Intensity / Arbitrary Units
Energy Transfer / THz
0
10
20
30
40
50
60
70
80
90
100
0
4
8
12
16
20
24

spectra is a resolution limited peak at 8.18 THz which is superimposed on the rest of the spectrum. This peak is also evident in spectra generated for other wavevectors and since $S = 1$ and $J = 8.18$ THz the peak may correspond to the lowest energy localised mode of the model system and is presumably a facet of the nearest neighbour interactions in the model system. However, the magnetic interactions in the real metallic alloy system $Cr_{1-x}\ Fe_x$ with $x = 0.27$ are expected to have the RKKY mechanism. With the RKKY mechanism, the conduction electron gas in the neighbourhood of a particular magnetic ion is magnetised with a spatial dependence shown on page 554 of Kittel (1976). Other magnetic ions are influenced by that magnetisation so that there is an indirect exchange interaction between pairs of magnetic ions in the system. Since the RKKY mechanism involves the conduction electrons, it would seem at first sight that the magnetic interactions in $Cr_{1-x}\ Fe_x$ with $x = 0.27$ would therefore not be explained satisfactorily by a nearest neighbour model. But the system is highly disordered and scattering of the conduction electrons due to that disorder in the system might reduce the mean free path to an extent that the magnetic interactions could be described as approximately nearest neighbour. To test this hypothesis a proposal has been submitted to the I.L.L., Grenoble (P.W. Mitchell (1985)) for an experiment to determine whether or not the localised mode exists in the real system.

CHAPTER 4

$K_2Co_xFe_{1-x}F_4$: A MIXED MAGNETIC SYSTEM WITH ORTHOGONAL COMPETING SPIN ANISOTROPIES

4.1 Introduction

In pure systems, the spin anisotropy determines the direction along which the magnetic moments of the constituent magnetic ions align below the magnetic phase transition temperature. The anisotropy can arise from dipole-dipole interactions, single ion crystal field effects or there can be anisotropy in the exchange interaction. In theory, a mixed magnetic system with orthogonal competing spin anisotropies can be formed by randomly mixing two pure systems which differ only in the type of magnetic ion and in that the favoured ordering directions are orthogonal. These systems here received considerable theoretical and experimental attention in recent years (a review of much of this work has been given by Katsumata (1983)). Mean field (Matsubara and Inawashiro (1977)) and renormalisation group (Fishman and Aharony (1978)) calculations for these systems predict three ordered phases in the concentration-temperature plane: two phases in which there is long range order of the spin components in the directions favoured by the two end members and an intermediate phase in which there is long range order in both spin components. For antiferromagnetic systems this phase is known as the Oblique Antiferromagnetic (OAF) phase (Matsubara and Inawashiro (1977)). A schematic phase diagram for such systems is shown in Figure (4.1.1).

FIGURE (4.1.1): Schematic temperature T against concentration x phase diagram for a mixed magnetic system with competing spin anisotropies.

P Indicates the paramagnetic phase.

L1 indicates a phase in which the spin ordering direction is that of one end member and L2 indicates that the spin ordering direction is that of the other end member.

M indicates the mixed phase which for antiferromagnetic systems is known as the Oblique Antiferromagnetic (OAF) phase.

fig 4·1·1

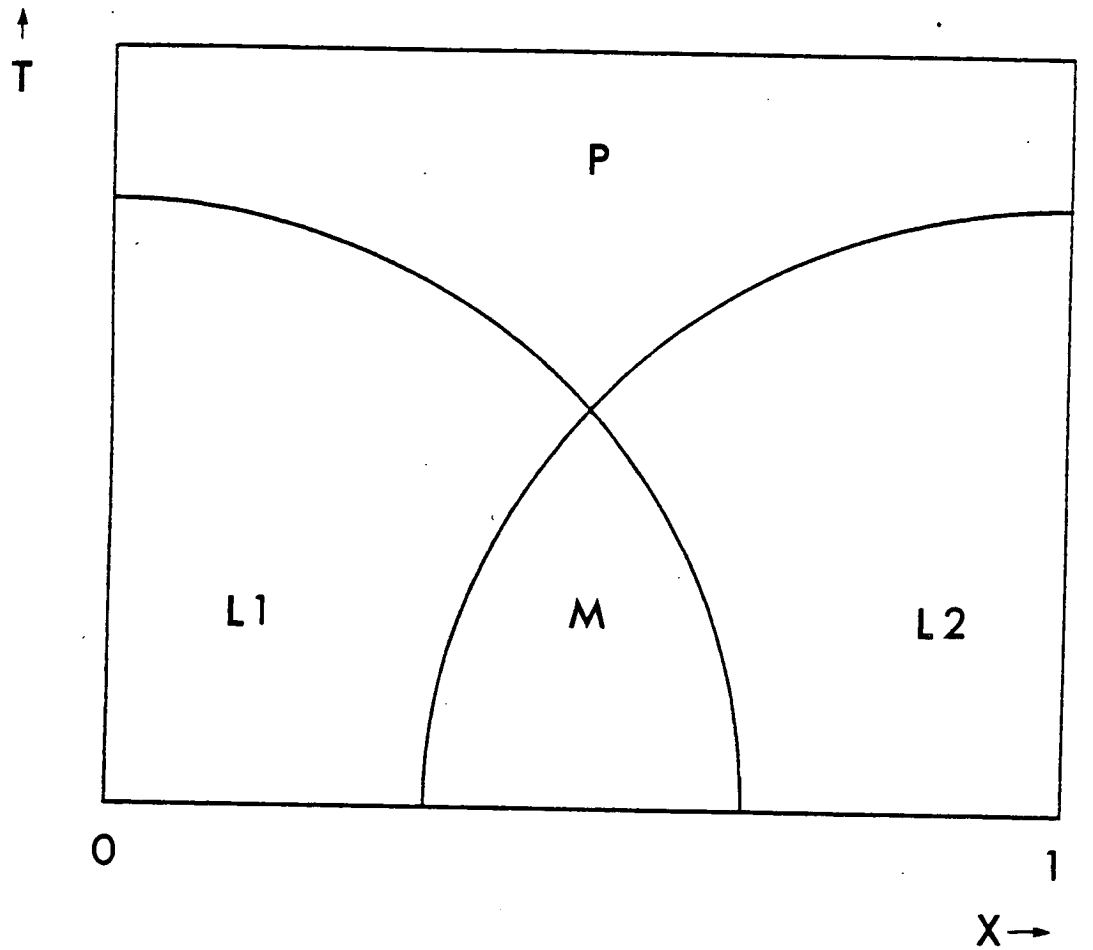

Both calculations predicted that the two phase boundaries (the boundary here being the locus of points in the concentration-temperature plane below which a particular spin component orders) cross at a tetracritical point and that all of the phase transitions will be second order. The mean-field calculations predict that the ordering of one spin component affects the ordering of the spin component orthogonal to it with the result that both phase boundaries change slope at the tetracritical point, whilst the renormalisation group calculations, which take spin fluctuations into account, suggest that each of the spin components order independently so that the phase boundaries pass through a decoupled tetracritical point without change of slope. Consequently the principal focus of theoretical and experimental attention has been the form of the phase diagram. Experiments on systems with the spatial dimension $d = 3$ (Ito et al. (1980), Ito et al. (1982), Someya et al. (1983) and Wong et al. (1983)) and $d = 2$ (Bevaart et al. (1978), Vlak et al. (1983) and Higgins et al. (1984)) have shown the existence of the OAF phase. Clearly, the experiments have to be performed on individual samples, each with a fixed concentration, and it is by investigating the order parameter and/or the response functions such as the specific heat and magnetic susceptibility as a function of temperature that the critical temperature and nature of the phase transition at that concentration can be found. If x_1 and x_2 define the position of the intersection of the phase boundaries with the zero temperature ($T = 0$) axis then samples with a concentration $x_1 < x < x_2$ should undergo two phase transitions on cooling from the paramagnetic phase. As the temperature

is lowered, there should be an onset of long range order in one of the spin components at T_N and at a lower temperature T_L, the other spin component should order so that below T_L the system attains the OAF magnetic structure. In a very detailed study of the mixed $d = 3$ antiferromagnet $Fe_{1-x}Co_xCl_2$ Wong et al. (1983) found that although the high temperature transition at T_N was well defined, the lower one at T_L was smeared. They suggested that this was because the ordering of one spin component generated a random field on the other, and that this random field inhibited the development of true long range order in the other spin component. The random fields were generated by off-diagonal coupling arising from the low local symmetry in the $FeCl_2$ structure. $K_2Co_xFe_{1-x}F_4$ has a significantly higher local symmetry and so the nature of the transition at T_L is of particular interest for this system.

The rest of this chapter is laid out as follows. In the next section (Section 4.2), the relevant properties of the pure systems (or 'end members') K_2CoF_4 and K_2FeF_4 will be discussed. In Section (4.3) the results of an investigation of the magnetic structure of a sample of $K_2Co_xFe_{1-x}F_4$ with $x = 0.6$ and a sample with $x = 0.2$ are reported. The $x = 0.6$ sample is shown to exist in the uniaxial antiferromagnetic phase below $T_N = 92.2 \pm 0.1K$. In the nominally $x = 0.2$ sample the uniaxial spin components order below $T_N = 66 \pm 1K$ and below a well-defined transition at $T_L = 32 \pm 2K$ the transverse components also order. In Section (4.4) measurements to determine the dispersion of the low temperature ($T \sim 5K$) spin waves in the $x = 0.6$ and $d = 0.2$ samples are discussed. The properties of the spin wave excitations in the OAF phase and the

role they play in the phase transitions to the other two ordered phases have only recently begun to receive attention and in Section (4.5) the results of inelastic neutron scattering measurements of the spin waves in the OAF phase of a sample with a nominal concentration $x = 0.27$ are reported. The magnetic structure of the sample had previously been investigated by Vlak et al. (1983), who found the transition temperatures to be $T_N = 64.4 \pm 0.6K$ and $T_L = 27 \pm 2K$. In Section (4.6), a computer program designed to calculate relevant parameters for the ground state ($T = 0$) magnetic structure in $K_2Co_xFe_{1-x}F_4$ across the complete range of concentrations (x) is discussed and some results presented with particular emphasis on the OAF phase which is of most interest. In Section (4.7) another computer program which calculates $S(\underline{Q},\omega)$ at $T = 0$, using the "Equation-of-Motion" technique (Alben and Thorpe (1976)) is discussed and results are compared with the low temperature spin wave measurements for the $x = 0.2$, $x = 0.6$ and $x = 0.27$ samples.

4.2 The Pure Systems

4.2 (i) The Pure Systems (Introductory Remarks)

The pure systems (or end members) K_2CoF_4 and K_2FeF_4 crystallise in the K_2NiF_4 structure (Birgeneau et al. (1970)). The magnetic ions are in antiferromagnetic quadratic layers separated by two layers of KF. As discussed by Lines (1967) and in Chapter 1 of this thesis, the exchange interactions between nearest neighbour magnetic ions within the quadratic layers is much stronger than that between magnetic ions in layers adjacent to each other, so that systems with the K_2NiF_4 structure are good $d = 2$ magnetic systems.

The crystallographic unit cell of K_2NiF_4 was shown in Figure (1.2.1) (Chapter 1). In discussing isomorphs of K_2NiF_4 it is common to define a magnetic unit cell (Birgeneau et al. (1970)). Figure (4.2.1) shows the relationship between the crystallographic and magnetic unit cells. In this chapter reciprocal lattice vectors will be with respect to the magnetic unit cell rather than the crystallographic unit cell. The c-axes of the two cells are identical but the magnetic a_m and b_m - axes are rotated by 45° relative to the a and b-axes of the crystallographic unit cell and are larger by a factor of $\sqrt{2}$.

4.2 (ii) K_2CoF_4

Hund's rules indicate that the ground state of the free Co^{2+} ion is $^4F_{9/2}$. In a cubic field, some of the degeneracy is lifted so that the ground state becomes an orbital triplet. The tetragonal

FIGURE (4.2.1): Relationship between the crystallographic (dashed line) and magnetic (solid line) unit cells in the K_2NiF_4 structure.
Note that only the magnetic ion sites are indicated.

Figure (4.2.1)

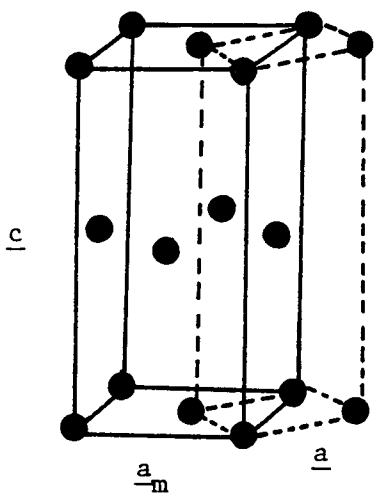

component of the crystal field combined with spin orbit coupling, split the orbital triplet into six Kramers doublets so that the ground state of the Co^{2+} ion in the K_2CoF_4 structure is a doublet and the magnetic properties of K_2CoF_4 at the sample temperatures and neutron energy transfer values of concern in this thesis, can be described in terms of a pseudospin $S = {}^1/2$. The magnetic susceptibility measurements of Breed et al. (1969) have shown that in the critical region, K_2CoF_4 behaves like a $d = 2$ Ising Antiferromagnet. When the model Hamiltonian of equation (4.2.1) with pseudospin $S = {}^1/2$ is used to describe the spin interactions, then $J_{ij}/I_{ij} = 0.3$.

$$\hat{H} = \sum_{<ij>} I_{ij} S_i^z S_j^z + J_{ij}(S_i^x S_j^x + S_i^y S_j^y) \quad . \qquad (4.2.1)$$

$<ij>$ indicates summation over nearest neighbours in the basal (a-b) plane. (The ratio of the interplanar to intraplanar exchange interactions was estimated to be less than 10^{-3} and so only the intraplanar exchange interactions I_{ij} and J_{ij} are required in the Hamiltonian). The paramagnetic to antiferromagnetic phase transition at $T_N = 107.85K$ (Ikeda and Hirakawa (1974)) can occur in this $d = 2$ system because of the Ising asymmetry in the exchange interaction and below T_N the spins acquire long range order with alignment along the c-axis. The ordered phase is thus Uniaxial Antiferromagnetic.

The neutron diffraction experiments of Ikeda and Hirakawa (1974) obtained critical exponents β, ν, γ and η which coincided exactly (within experimental error) with the values obtained in the exact theoretical solution of the $d = 2$ Ising model

(Onsager (1944)).

4.2.(iii) $\underline{K_2FeF_4}$

The ground state of the free Fe^{2+} ion is $^5D_4$. In the system K_2FeF_4 (Thurlings et al. (1977)) the crystal field combined with spin-orbit coupling causes a single-ion anisotropy. The crystal field Hamiltonian of the Fe^{2+} ion in K_2FeF_4 can be separated into a cubic field term and two other terms which represent the tetragonal distortion (Thurlings et al. (1978)). The effect of the cubic crystal field term is to lift the degeneracy of the ground state orbital levels (there are $2L+1 = 5$ of them) to give a Γ_3 triplet and a Γ_5 doublet. The tetragonal distortion separates Γ_3 into a ground state singlet and a doublet. The magnetic properties of interest in this thesis can be described in terms of a pseudospin $S = 2$.

Thurlings et al. (1978) show that if the in-layer and out-of-layer single ion anisotropy terms are decoupled, then up to quadratic terms in the spin components, the spin Hamiltonian of K_2FeF_4 can be modelled by equation (4.2.2)

$$\hat{H} = \sum_{<ij>} J_{ij} \underline{S}_i \underline{S}_j + \sum_i [D S_i^{z2} + E(S_i^{x2} - S_i^{y2})] \qquad (4.2.2)$$

where $<ij>$ indicates a sum over nearest neighbour spins in the basal plane. In contrast to the case of K_2CoF_4, the exchange interaction, J_{ij}, is isotropic. Below the Néel transition temperature ($T_N = 63.0K$) long range order occurs with the spins antiferromagnetically aligned in two domains. In one type of domain, the spins

are aligned along the $\underline{a}_m$ direction, and in the other domain, the spins align along the $\underline{b}_m$ direction. In terms of equation (4.2.2) the first domain corresponds to D negative and E positive and the second to D negative and E negative. By symmetry it is expected that both domains are equally populated and this has been found to be true experimentally. The ordered phase of K_2FeF_4 is planar antiferromagnetic. The in-plane anisotropy represented by the third term in equation (4.2.2) is much smaller than the out-of-plane anisotropy represented by the second term.

4.2(iv) The Pure Systems (Concluding Remarks)

As discussed in Chapter 1, the fact that the two pure systems K_2CoF_4 and K_2FeF_4 both have the K_2NiF_4 structure, the lattice parameters are close and the magnetic ions Co^{2+} and Fe^{2+} are transition metal, means that single crystal samples of the mixed system $K_2Co_xFe_{1-x}F_4$ can be formed over the entire concentration range $(0 < x < 1)$. From the point of view of forming a mixed magnetic system with competing spin anisotropies, the anisotropies are significantly large in each of the pure systems but of comparable size, so that the OAF phase should extend over a range of concentrations and temperatures which are easily accessible experimentally. Fendler and von Eynatten (1984) estimate that at $T \sim 6K$ the OAF in $K_2Co_xFe_{1-x}F_4$ extends across the concentration range $0.16 < x < 0.32$. This makes $K_2Co_xFe_{1-x}F_4$ a more suitable system on which to study mixed systems with competing anisotropies than

FIGURE (4.2.2): Proposed magnetic phase diagram for $K_2Co_xFe_xF_4$. x is the Co^{2+} concentration and T_c indicates transition temperature. The solid lines indicate the phase boundaries calculated from mean-field theory and scaled so that the values of T_c at $x = 0$ and $x = 1$ fitted the Néel temperatures for the pure systems K_2FeF_4 and K_2CoF_4 (Fendler and von Eynatten (1984)).
P indicates the paramagnetic phase, Pℓ indicates the Planar antiferromagnetic phase, U indicates the uniaxial antiferromagnetic phase and O indicates the Oblique antiferromagnetic phase.

fig 4·2·2

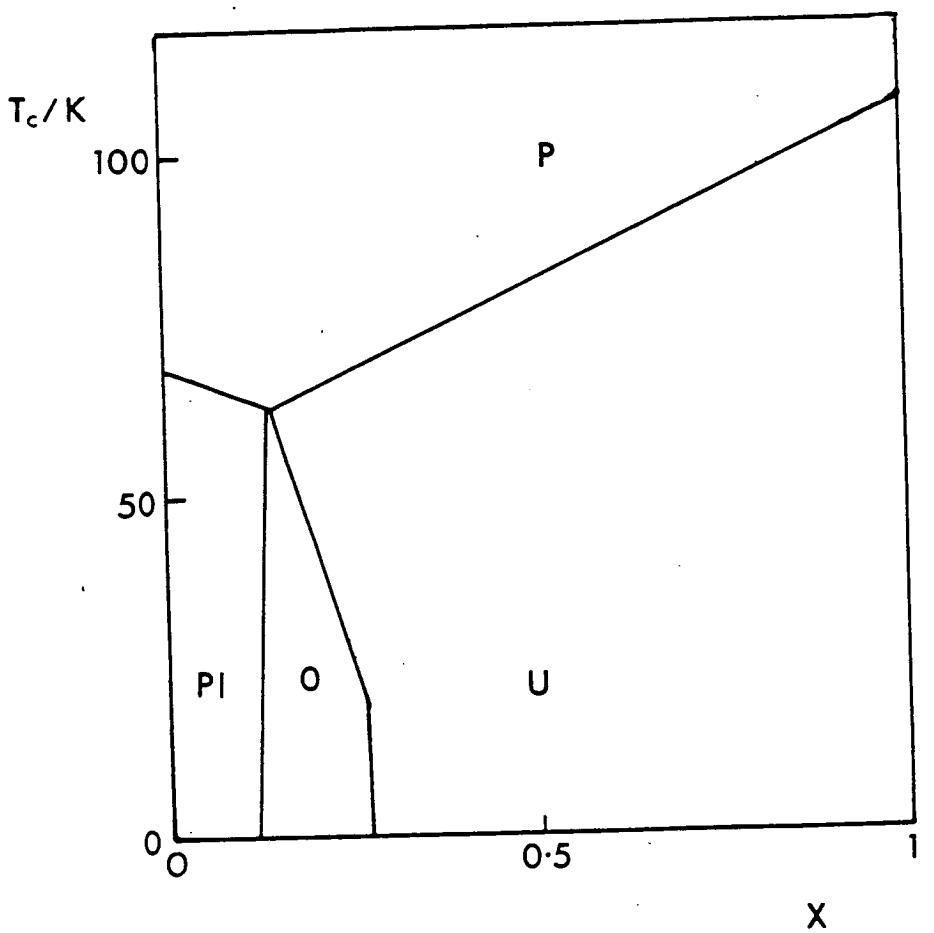

$K_2Fe_xMn_{1-x}F_4$ (Bevaart et al. (1978)), in which the OAF phase extended over the approximate range $0.02 < x < 0.03$ at $T = 0$. Figure (4.2.2) shows a proposed phase diagram for the system $K_2Co_xFe_{1-x}F_4$ (Fendler and von Eynnatten (1984)).

4.3 The Magnetic Structure of $K_2Co_xFe_{1-x}F_4$

This section reports neutron scattering experiments to study the magnetic phase transitions and the magnetic structure of two samples of $K_2Co_xFe_{1-x}F_4$; one with $x = 0.6$ and the other with $x = 0.2$.

4.3.(i) Experimental Details

The neutron scattering measurements reported in this section and in Section 4.4 were performed on triple-axis neutron spectrometers at the National Laboratory, Risø, Denmark and at the Pluto reactor, A.E.R.E. Harwell, U.K. The nominally $x = 0.2$ sample was plate-like with dimensions of 10mm × 10mm × 2mm, while the $x = 0.6$ sample was approximately 1 cm^3 in volume. Both samples consisted of large grains of single crystal, but unfortunately these grains were mis-orientated by about 5° to each other. The multicrystal character limited the accuracy of some of the experimental results presented in this section. The crystals showed no signs of any chemical ordering of the Co^{2+} and Fe^{2+} ions, i.e. the samples seemed to be randomly mixed.

The crystals were mounted in variable-temperature cryostats

with the magnetic a_m^* and c_m^* axes in the scattering plane. The elastic measurements at Risø were performed using a pyrolytic graphite monochromator and an incident neutron energy of 14 meV with a pyrolytic graphite filter to suppress higher order contaminant neutrons in the incident beam. A pyrolytic graphite analyser was used and the horizontal collimation from reactor to counter was 30' - 30' - 30' - 60'. In this configuration, the energy resolution was 0.8 meV. The inelastic experiments performed at Risø (Section 4.4) used a similar instrumental configuration, but with an incident neutron energy of 5 meV and a cooled beryllium filter rather than a graphite filter.

The experiments at Harwell were performed with a pyrolytic graphite analyser and a fixed final neutron energy E_f of 13 or 24 meV. The horizontal collimations were 100' - 30' - 30' - 60' and a pyrolytic graphite filter was used before the analyser in the measurements with fixed E_f = 13 meV.

4.3.(ii) The Magnetic Structure

The intensity of the (1,0,0) magnetic Bragg reflection which is proportional to the square of the sublattice magnetisation, was measured as a function of temperature for both the $x = 0.6$ and the $x = 0.2$ samples and the results are shown in Figures (4.3.1(a)) and (4.3.2(b)) respectively. In the former case, the intensity rises rapidly below $T = 90K$ and becomes constant below $T = 50K$. This indicates the ordering of the c-components of the spins below T_N confirming that the $X = 0.6$ sample exhibits Uniaxial Antiferromagnetic order below T_N as predicted by the phase diagram in

FIGURE (4.3.1) (a) The intensity of the (1,0,0) magnetic Bragg peak I(1,0,0) as a function of temperature for the nominally x = 0.6 sample.
The solid curve indicates the best fit to the expression given in equation (4.3.2).
(Note that the Intensity axis should be multiplied by factor of 200 to give the number of counts per second).

(b) The diffuse scattering intensity I(1.035,0,0) at $\underline{Q}$ = (1.035,0,0) as a function of temperature for the nominally x = 0.6 sample. The solid curve is a guide to the eye.
(Note that the intensity axis should be multiplied by a factor of 100 to give the number of counts per minute.)

fig 4·3·1

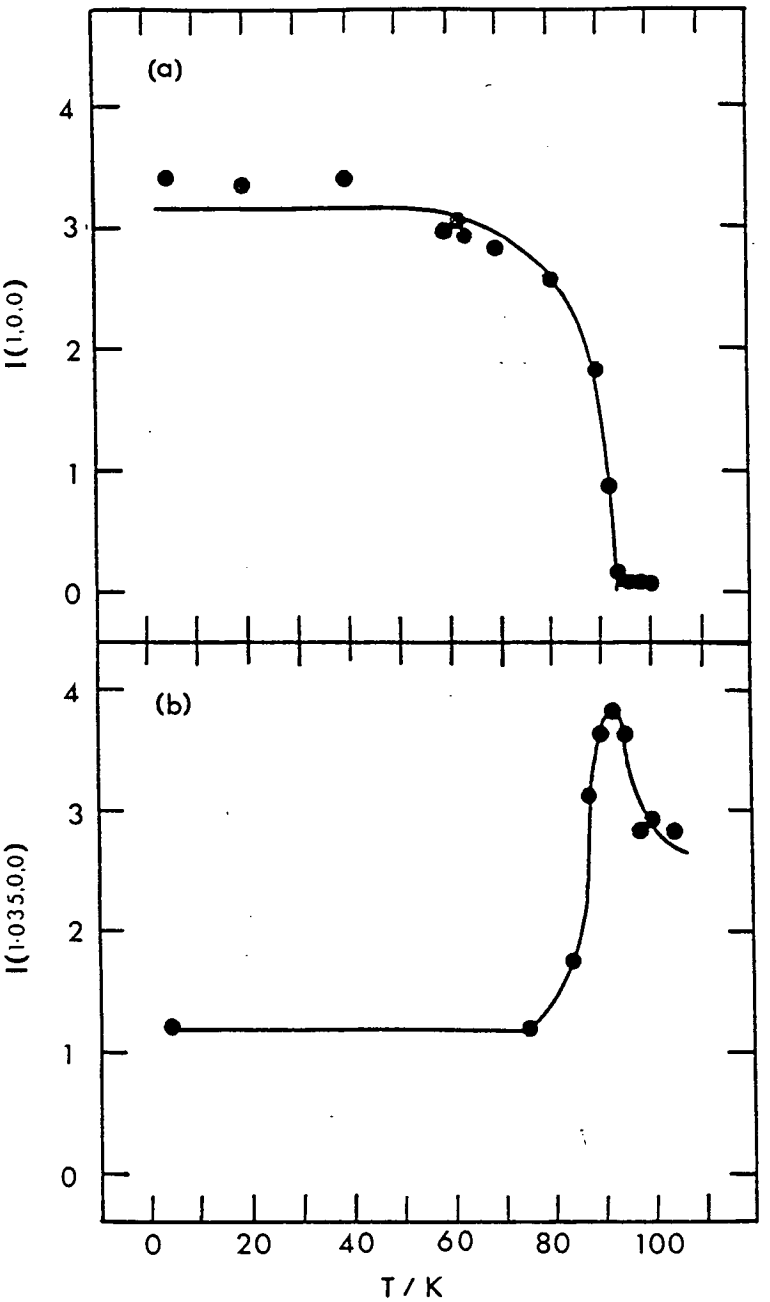

FIGURE (4.3.2): (a) The full circles indicate the intensity of the (1,0,0) magnetic Bragg peak I(1,0,0) as a function of temperature for the nominally x = 0.2 sample. The open circles indicate the (1,0,6) magnetic Bragg peak intensity (scaled). (The intensity axis for I(1,0,0) should be multiplied by 10^4 to give the number of counts per minute.)

(b) The diffuse scattering intensity I(1,0,-0.4) at $\underline{Q}$ = (1,0,-0.4) as a function of temperature for the nominally x = 0.2 sample. (The intensity axis should be multiplied by a factor of 100 to give the number of counts per minute.

fig 4.3.2

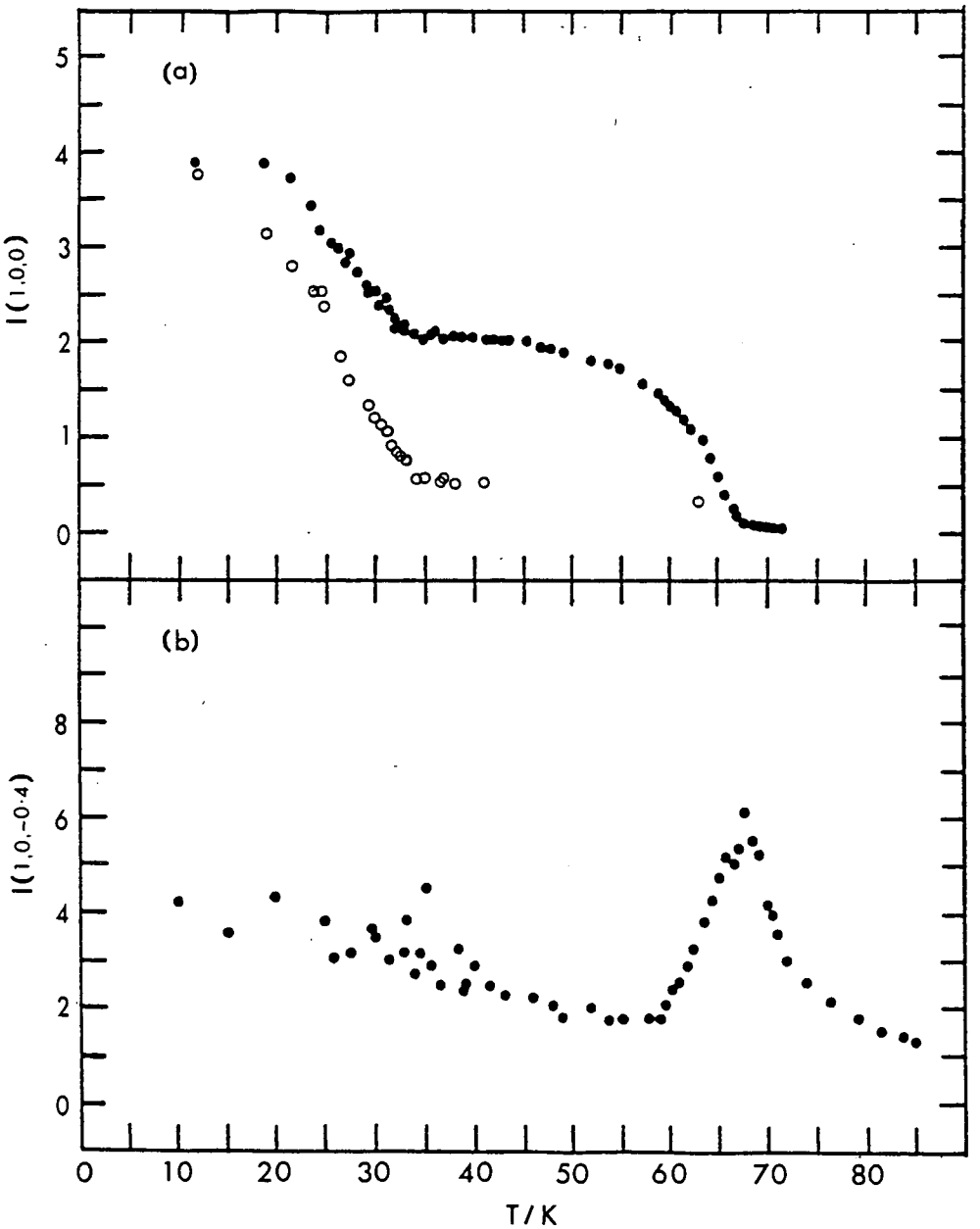

Figure (4.3). Measurements through the (1,0,0) Bragg reflection along the line (1,0,η) showed that the width of the Bragg reflection is not limited by resolution and that it corresponds to the ordering of about four two-dimensional sheets. The intensity of the scattering in Figure (4.3.1(b)) does not decrease to zero below T_N, most probably because it contains a residual Bragg component corresponding to the lack of full three-dimensional ordering, even at the lowest temperatures.

The exact theoretical solution of the $d = 2$ Ising model (Onsager (1944)) predicts that the sublattice magnetisation as a function of temperature should be given by equation (4.3.1).

$$M(T)/M(0) = [1 - \sinh^{-4}(2J/k_BT)]^{\beta} \quad . \qquad (4.3.1)$$

Using the fact that $M(T)$ is zero at the transition temperature so that $T_N = 2J/k_B$ and that $M(T)^2$ is proportional to $I_{100}(T)$ (the intensity of the (1,0,0) Bragg reflection at temperature T) the data of Figure (4.3.1(a)) was fitted to the form given in equation (4.3.2).

$$I_{100}(T)/I_{100} = [1 - \sinh^{-4}(T_N/T)]^{2\beta} \quad . \qquad (4.3.2)$$

The least squares fit gave $\beta = 0.14$. This value is consistent with the exact solution of the $d = 2$ Ising model which gives $\beta = 0.125$. The fit also gave the transition temperature $T_N = 92.2 \pm 0.1$K.

The temperature dependence of the (1,0,0) magnetic Bragg reflection for the sample with $x = 0.2$ is shown in Figure (4.3.2(b)). On cooling, it increases from zero at a temperature $T_N = 66 \pm 1$K,

flattens off, then increases again at a lower temperature $T_L = 32 \pm 2K$. This strongly suggests that between T_N and T_L there is long range order in one spin component, while below T_L the other component orders so that the system has the OAF structure below T_L. The data shown in Figure (4.3.2(a)) between $T = 35K$ and $T = 67K$ was fitted to the form given in equation (4.3.2) and gave a good fit with $\beta = 0.19 \pm 0.02$. That this is significantly larger than the exponent obtained for the $x = 0.6$ sample, and that expected for a $d = 2$ Ising model, may be due to a rounding of the transition due to concentration fluctuations.

In an attempt to determine the magnetic structure of the nominally $x = 0.2$ sample as a function of temperature measurements were made of the integrated intensities of the (1,0,L) Bragg reflections with $|L| < 8$ and the (3,0,L) reflections with $|L| < 4$ at various temperatures between $T = 12K$ and $T = 63K$ but mostly close to $T = 30K$. The observed intensities for $T = 12K$ and $T = 35K$ are listed in Table (4.3.1). The relative intensities of certain Bragg reflections are clearly different at the two temperatures. The Bragg peak intensity data was used to determine the magnetic structure at each of the temperatures in the range $T = 12K$ to $T = 63K$ by fitting three parameters to the experimental results. These parameters were an overall scale factor, proportional to the square of the ordered moment, the angle between the direction and the c-axis, θ_c, and the relative proportion of the domains that give rise to the (1,0,0) and (1.0,1) Bragg reflections (see e.g. Thurlings et al. (1982)). The results for θ_c and the

TABLE (4.3.1): Integral Intensity Values for Magnetic Bragg Peaks at T = 12K and T = 35K.

(H,K,L)	T = 12K Experimental	T = 12K Calculated	T = 35K Experimental	T = 35K Calculated
(1,0,0)	668	685	355	342
(1,0,$\bar{1}$)	374	367	344	342
(1,0,1)	402	367	357	342
(1,0,$\bar{2}$)	321	309	127	128
(1,0,2)	327	309	128	128
(1,0,$\bar{3}$)	100	118	63	80
(1,0,3)	120	118	83	80
(1,0,$\bar{4}$)	98	101	24	28
(1,0,4)	103	101	25	28
(1,0,$\bar{5}$)	29	42	14	18
(1,0,5)	38	42	17	18
(1,0,$\bar{6}$)	55	39	8	7
(1,0,6)	56	39	7	7
(1,0,$\bar{7}$)	14	18	11	5
(1,0,7)	15	18	9	5
(1,0,$\bar{8}$)	19	18	6	2
(1,0,8)	21	18	7	2
(3,0,0)	90	105	64	52
(3,0,$\bar{1}$)	82	69	74	67
(3,0,1)	86	69	73	67
(3,0,$\bar{2}$)	78	89	40	44
(3,0,2)	79	89	43	44
(3,0,$\bar{3}$)	41	50	46	47
(3,0,3)	44	50	46	47
(3,0,$\bar{4}$)	37	56	21	26
(3,0,4)	41	56	21	26

square root of the overall scale factor which is proportional to the average ordered spin moment, are shown in Figures (4.3.3(a)) and (4.3.3(c)). The c-component of the spin, S cos θ_c as a function of temperature is shown in Figure (4.3.3(b)). The results show that θ_c is zero above T_L but that it increases rapidly below T_L. The c-component of the spin varies only slowly with temperature near T = 30K, whereas the total spin distinctly increases. These results show that for this sample the c-component of spin orders at T_N but that the perpendicular components order only below T_L.

The results for the angle θ_c were fitted to the power law given in equation (4.3.3), treating θ_c as an order parameter.

$$\theta_c(T)/\theta_c(0) = (1 - T/T_L)^{\beta'} \quad . \qquad (4.3.3)$$

The best fit parameters were $\beta' = 0.32 \pm 0.04$, $\theta_c = 33 \pm 1°$ and $T_L = 32 \pm 1L$. The exponent β' is characteristic of three-dimensional ordering, unlike the exponent β found for the transition at T_N. The results for θ_c shown in Figure (4.3.3(c)) suggest that T_L is sharp as a function of temperature. This was also tested by measuring the temperature dependence of the (1,0,6) magnetic Bragg reflection which is shown in Figure (4.3.2(a)). This reflection is relatively weak in the upper (uniaxial antiferromagnetic) phase but increases rapidly in intensity on cooling below T_L. These results also suggest that T_L is sharp and that any smearing is over a temperature range of around 2K which is comparable with the smearing of the (1,0,0) reflection in this sample at T_N. This smearing is most likely

FIGURE (4.3.3): Results from fits to magnetic Bragg peak intensities described in the text.

(a) Average spin S (arbitrary units) against temperature.

(b) Average c-component of spin S_c (arbitrary units) against temperature $\left[S_c = S \cos \theta_c\right]$.

(c) The average cant angle θ_c against temperature.

Fig. (4.3.3)

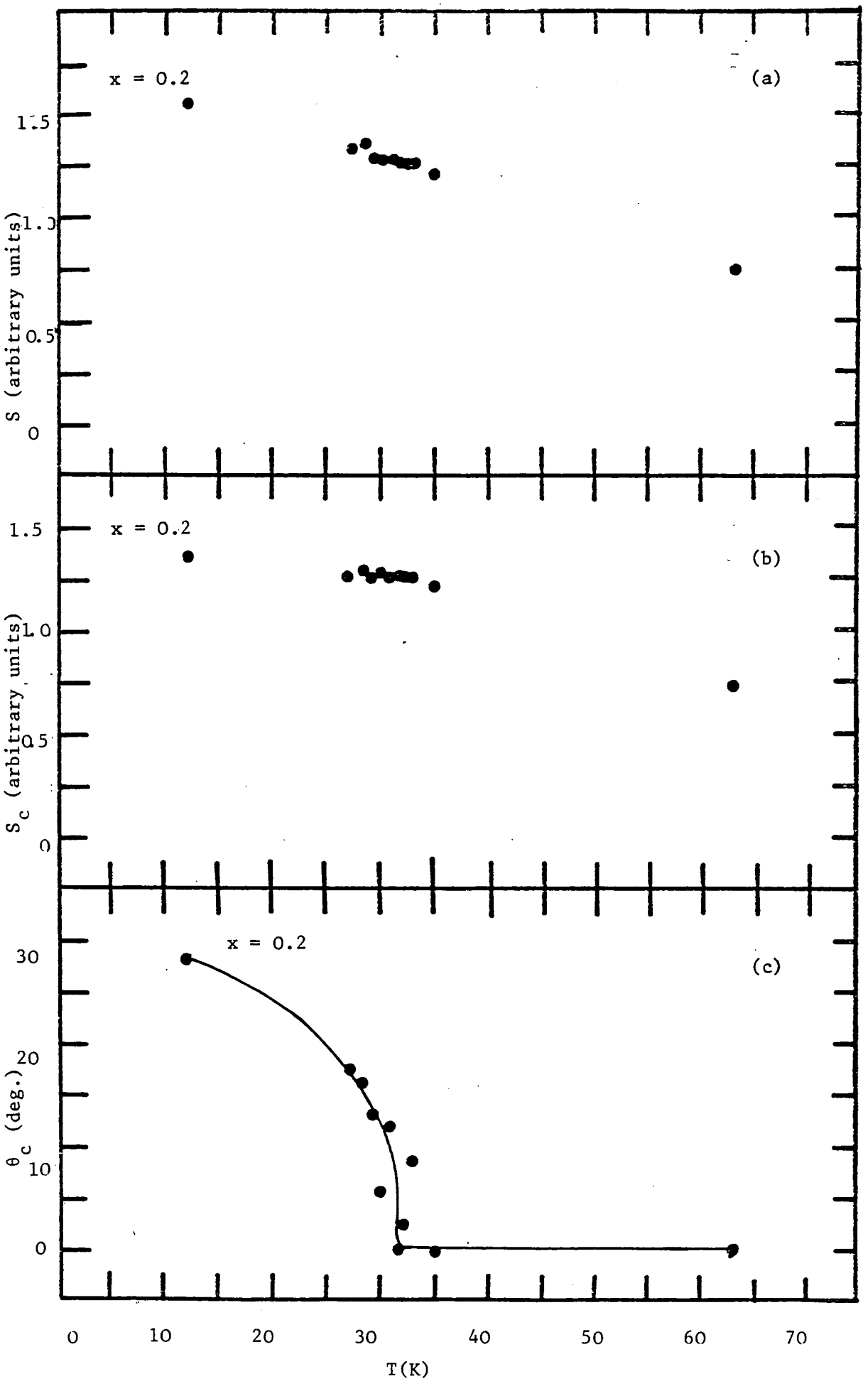
x = 0.2
(a)
S (arbitrary units)
1.5
1.0
0.5
0
x = 0.2
(b)
S_c (arbitrary units)
1.5
1.0
0.5
0
x = 0.2
(c)
θ_c (deg.)
30
20
10
0
0
10
20
30
40
50
60
70
T(K)

to arise from concentration fluctuations and the conclusion is drawn that, within the limitations of the experiments, both magnetic phase transitions (at T_L and T_N) are well defined, unlike the results for $Co_xFe_{1-x}C\ell_2$ (Wong et al. (1983)). As was found with the x = 0.6 sample, the Bragg peaks for the nominally x = 0.2 sample were not limited by resolution in scans along the line (1,0,η), showing that full three dimensional order was not established.

Due to both samples consisting of large grains of single crystal, which were slightly misorientated relative to each other, measurements of the diffuse scattering are less reliable than measurements of the Bragg reflection intensities, which were made on a single large grain of crystal. Neverheless, the diffuse scattering was measured in scans of the form (ξ,0,-0.4) and the width in ξ was found to decrease as T approached T_N. At and below T_N, the width of the scattering in these scans was limited by resolution. The intensity of the scattering at the reciprocal space coordinate (1.035,0,0) for the x = 0.6 sample and at (1,0,-0.4) for the x = 0.2 sample are shown in Figure (4.3.1(b)) and (4.3.2(b)) respectively. The results for both samples show a fairly symmetric peak at T_N but at low temperatures the scattering does not decrease to zero. For the nominally x = 0.2 sample, the scattering intensity slowly increases on further cooling (below T_N). Figure (4.3.2(b)) shows that there is no significant sign of any two dimensional critical scattering around T_L.

FIGURE (4.4.1): (a) A scan through the higher energy branch of spin waves, dispersion related for the nominally x = 0.6 sample. For this scan, the fixed wavevector transfer $\underline{Q}$ = (3.2,0,0) and the fixed final neutron energy was E_f = 24 meV. The sample temperature was T = 4.5K.
The counting time per data point was around 16 minutes.

(b) A scan through the lower energy branch of the spin wave dispersion relation for the nominally x = 0.6 sample. For this scan, the fixed wavevector transfer was $\underline{Q}$ = (1.4,0,0), the fixed final neutron energy was E_f = 13.408 meV and the sample temperature was T = 4.5K.
The counting time per data point was around 20 minutes.

Figure (4.4.1)(a).

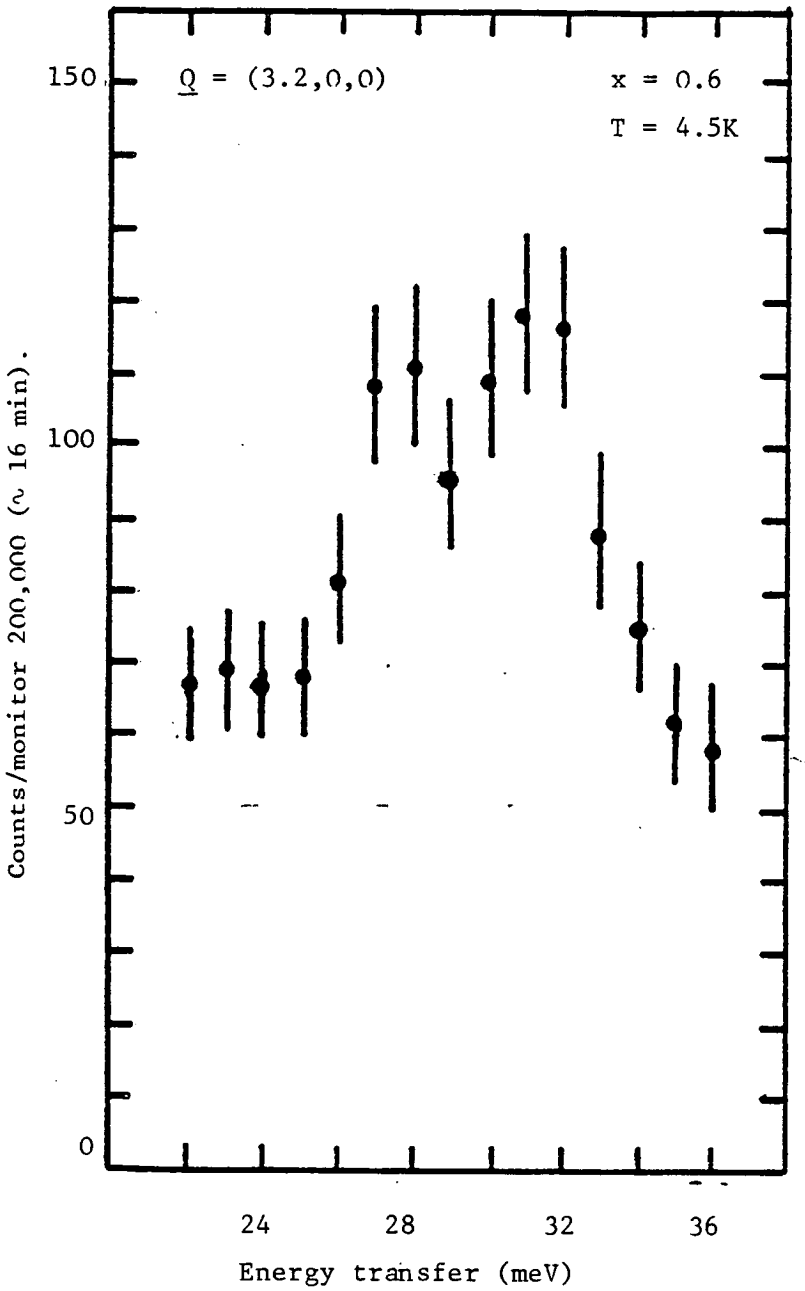
Q = (3.2,0,0)
x = 0.6
T = 4.5K
150
100
50
0
Counts/monitor 200,000 (∿ 16 min).
24
28
32
36
Energy transfer (meV)

Figure (4.4.1)(b)

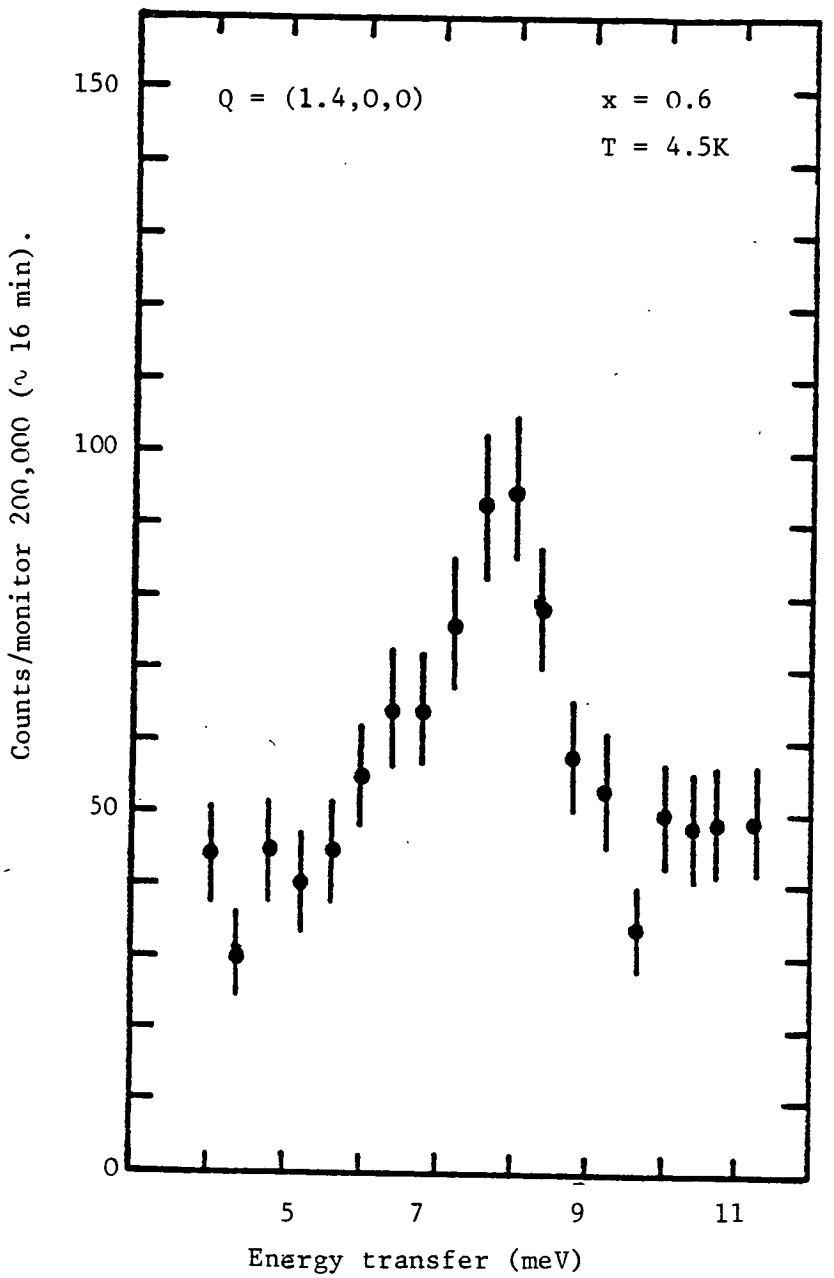
Q = (1.4,0,0)
x = 0.6
T = 4.5K
150
100
50
0
5
7
9
11
Counts/monitor 200,000 (∿ 16 min).
Energy transfer (meV)

FIGURE (4.4.2): The experimentally determined higher- and lower-energy branches of the spin wave dispersion relation for the nominally $x = 0.6$ sample at $T = 4.5K$. The arrows at the Brillouin zone boundary indicate calculated Ising 'spin-flip' frequencies. (See text).

ξ is the reduced wavevector in units of a_m^*.

Figure (4.4.2)

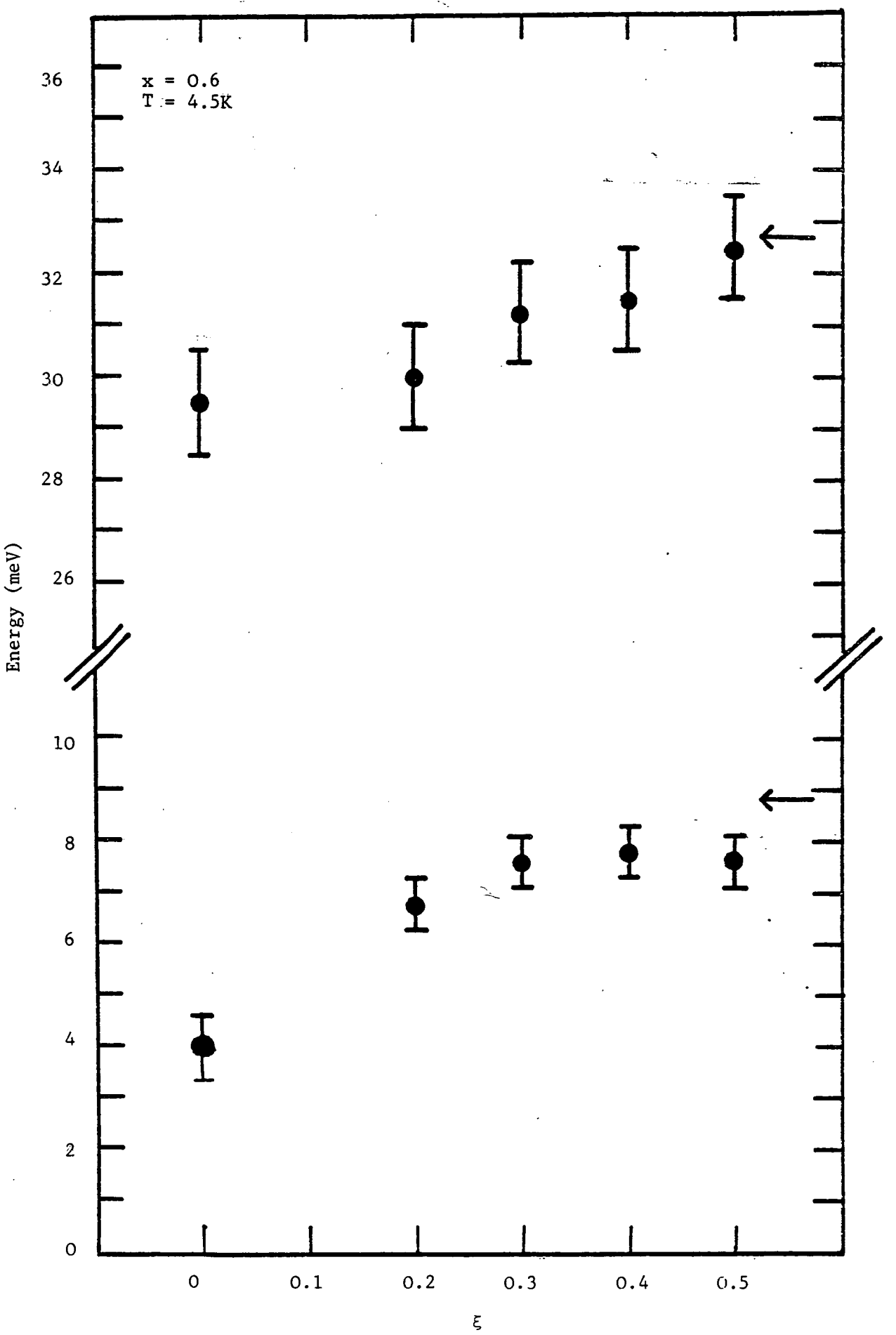

FIGURE (4.4.3): A scan through the lower-energy branch of the dispersion relation for the nominally x = 0.2 sample. The fixed wavevector transfer was $\underline{Q}$ = (1.2,0,0), fixed neutron energy was E_f = 13.408 meV and the sample temperature was T= 4.5K. The counting time per data point was around 20 minutes.

Figure (4.4.3)

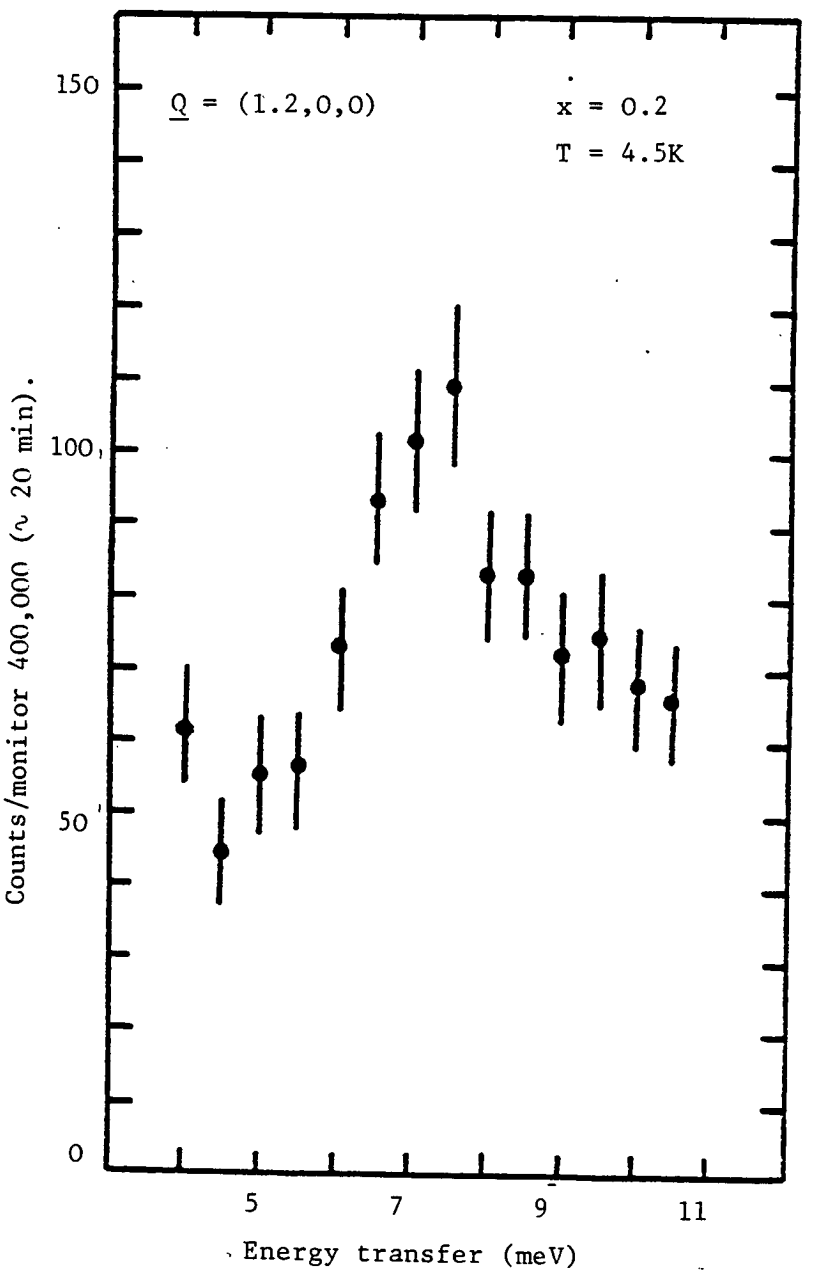
Q = (1.2,0,0)
x = 0.2
T = 4.5K
150
100
50
0
Counts/monitor 400,000 (∿ 20 min).
5
7
9
11
Energy transfer (meV)

FIGURE (4.4.4): The experimentally determined lower energy branch of the spin wave dispersion relation for x = 0.2 at T = 4.5K. The arrow at the zone boundary indicates the calculated Ising "spin-flip" energy (see text).
ξ is the reduced wavevector in units of a_m^*.

Figure (4.4.4)

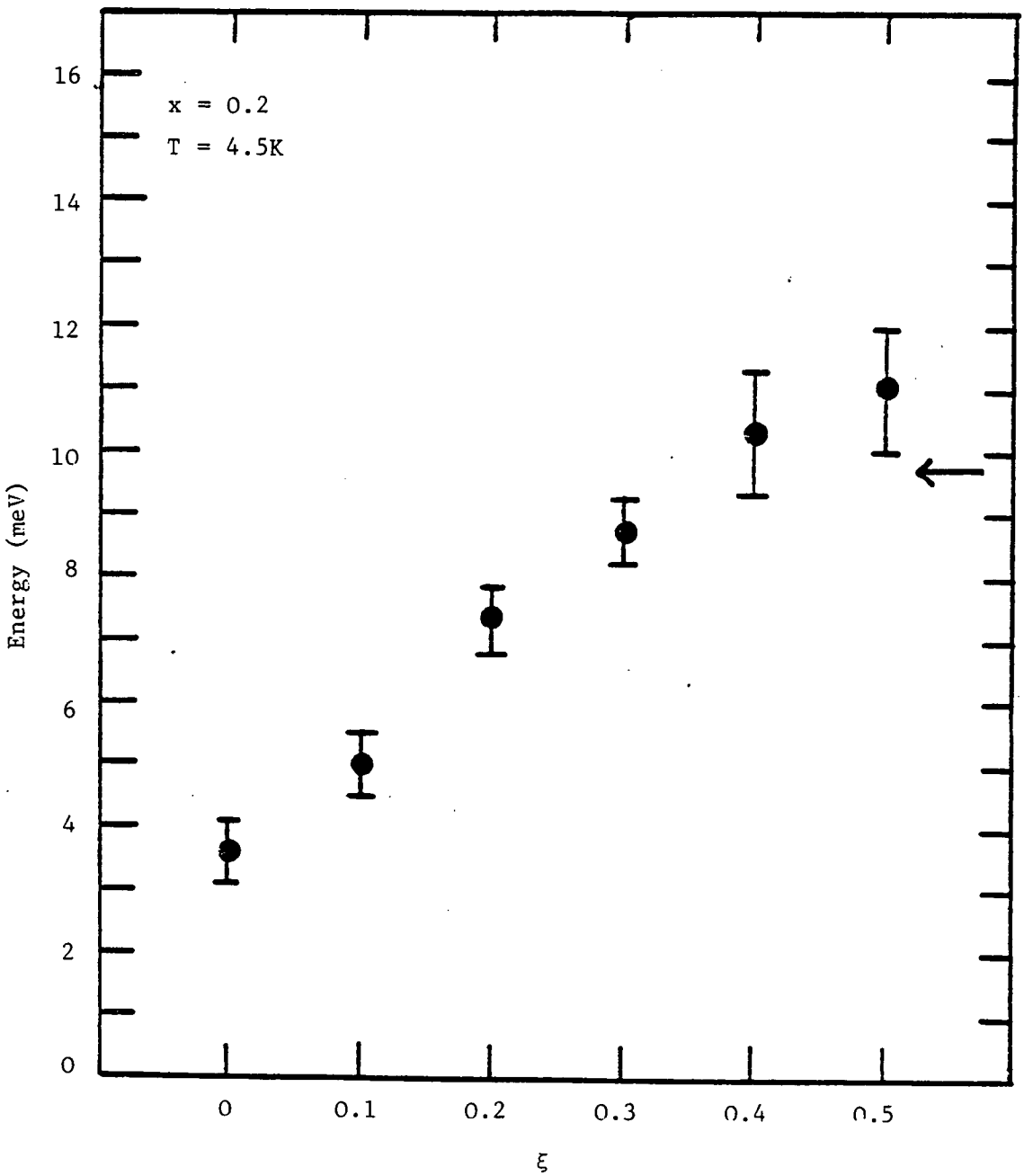

4.4 Experimental Determination of The Spin Waves in $K_2Co_xFe_{1-x}F_4$ at Low Temperatures for Samples with x = 0.6 and x = 0.2

The experiments discussed in this section were performed along with the experiments discussed in Section (4.3) and so the experimental details discussed in Section (4.3) are not repeated here. The inelastic neutron scattering measurements were made on both the x = 0.6 sample and on the nominally x = 0.2 sample to determine the dispersion of the low temperature spin waves, but a more detailed study was made for the larger sample with x = 0.6. In the x = 0.6 sample, two branches of spin waves were observed with fairly well-defined neutron groups, as shown in Figures (4.4.1(a)) and (4.4.1(b)). The upper branch was almost dispersionless and the peak positions for constant $\underline{Q}$ scans were in the range 29.5 meV to 32.5 meV, whilst the lower branch showed relatively more dispersion with a Brillouin zone centre energy of just over 4 meV and a zone boundary energy of just under 8 meV (see Figure (4.4.2)). These results are qualitatively similar to the results found in other mixed systems without competing anisotropy such as $Rb_2Mn_{0.5}Ni_{0.5}F_4$, $Mn_xCo_{1-x}F_2$ and $KMn_xCo_{1-x}F_3$ (as reviewed by Cowley (1982)).

Measurements of the spin waves in the nominally x = 0.2 sample were restricted to only the lower branch because of the smaller sample volume. The intensity as a function of energy transfer for a constant $\underline{Q}$ scan at $\underline{Q}$ = (1.2,0,0), is shown in Figure (4.4.3), to illustrate the typical quality of the data. The dispersion relation for the nominally x = 0.2 sample is shown in Figure (4.4.4).

Measurements were also made under instrumental conditions giving higher resolution (these were the measurements with fixed E_f = 5 meV) to examine whether the low-energy, small-wavevector spectrum was different in the uniaxial phase from that in the OAF phase. The results are illustrated in Figure (4.4.5) and in both phases only overdamped low-energy scattering was observed at small wavevectors, close to T_L. However, since these measurements were made difficult by the mosaic structure of the nominally x = 0.2 sample, a more detailed study of the low energy spin waves, particularly in the OAF phase, obviously required a better sample. When a sample with x = 0.27 became available later, more experiments were carried out, and these are discussed in Section (4.5).

An Ising model for the mean excitation energy of the Co^{2+} spins and the Fe^{2+} spins has been used to calculate zone boundary energies for the spin waves assuming that the spins are aligned along the $\underline{c}$ axis. For the Co^{2+} spins, this energy is given by equation (4.4.1) and for the Fe^{2+} spins by equation (4.4.2).

$$E_{Co} = 4[x(2I_{CoCo})\Delta S^z_{Co}\, S^z_{Co} + (1-x)(2I_{CoFe})\Delta S^z_{Co}\, S^z_{Fe}] \qquad (4.4.1)$$

$$E_{Fe} = 4[x(2I_{CoFe})\Delta S^z_{Fe}\, S^z_{Co} + (1-x)(2I_{FeFe})\Delta S^z_{Fe}\, S^z_{Fe}] + D[(S^z_{Fe})^2_f - (S^z_{Fe})^2_i] \quad . \qquad (4.4.2)$$

In equations (4.4.1) and (4.4.2), S^z_{Co} and S^z_{Fe} refer to the ground state values of S^z for the Co^{2+} and Fe^{2+} spins ($\frac{1}{2}$ and 2 respectively). In the case of an Fe^{2+}/Co^{2+} spin being excited, $(S^z_{Fe/Co})_i$ and $(S^z_{Fe/Co})_f$ are the initial and final $S^z_{Fe/Co}$ values

FIGURE (4.4.5): High resolution scans made at

(a) Q = (1.1,0,-0.4)

(b) Q = (1.05,0,-0.4)

(c) Q = (1,0,-0.4)

for the nominally x = 0.2 sample.

Full circles indicate T = 36K and

open circles indicate T = 24K.

Figure (4.4.5)

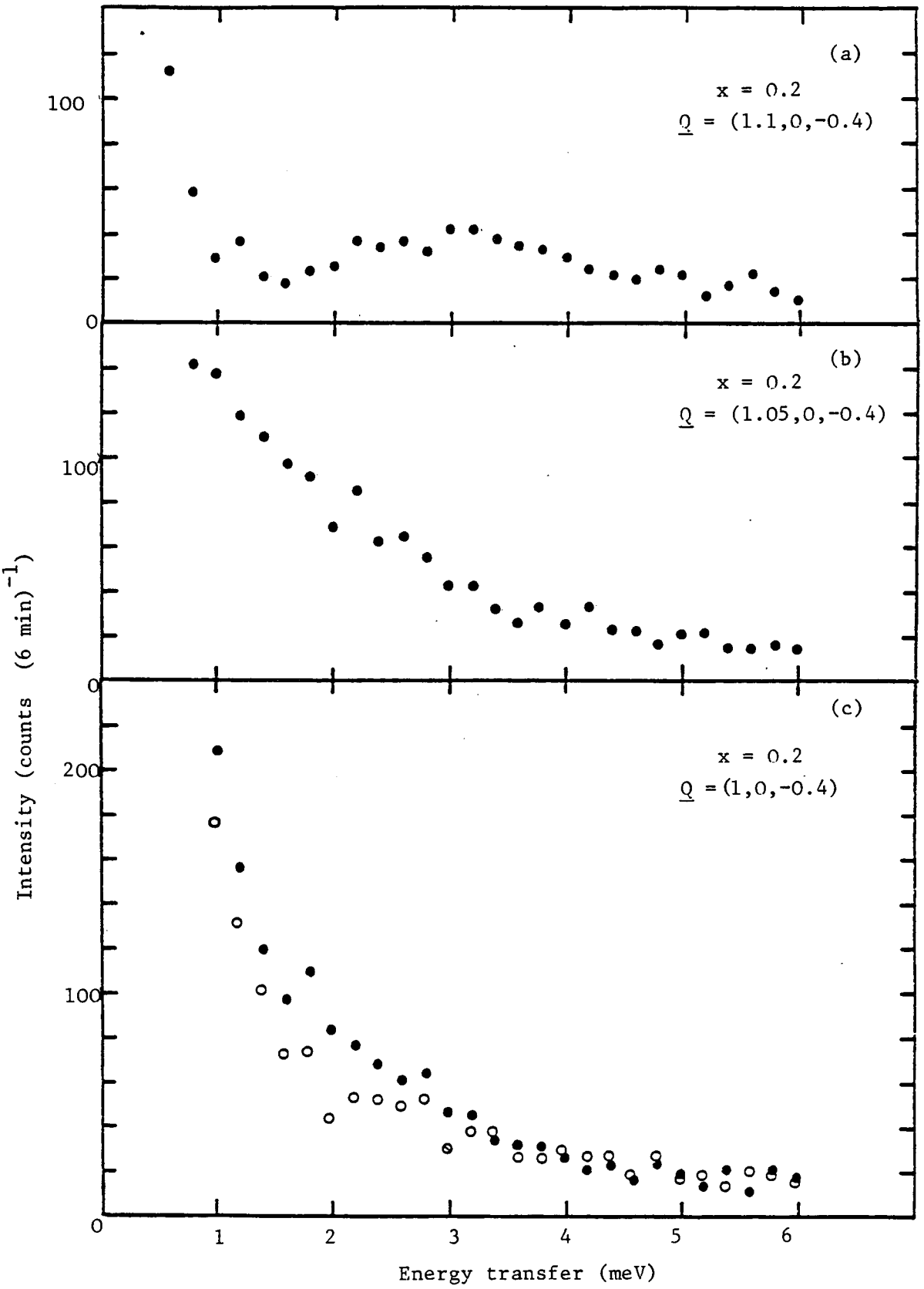
(a)
x = 0.2
Q = (1.1,0,-0.4)
100
0
(b)
x = 0.2
Q = (1.05,0,-0.4)
100
0
(c)
x = 0.2
Q = (1,0,-0.4)
200
100
0
1
2
3
4
5
6
Energy transfer (meV)
Intensity (counts (6 min)$^{-1}$)

and $\Delta S^z_{Fe/Co} = (S^z_{fe/Co})_f - (S^z_{Fe/Co})_i$. In this calculation, the exchange parameters I_{CoCo}, I_{FeFe} and I_{CoFe} were taken to be $I_{CoCo} = 7.48$ meV, $I_{FeFe} = 0.709$ meV (both from Macco et al. (1979)) and $I_{CoFe} = (I_{CoCo}I_{FeFe})^{\frac{1}{2}} = 2.30$ meV. The out-of-plane single-ion anisotropy $D = 0.398$ meV (Macco et al. (1978)). The energies obtained are shown by the arrows in Figures (4.4.2) and (4.4.4) and clearly this model gives a very reasonable description of the zone-boundary energies, showing that these are not greatly affected by the competing anisotropy. The data obtained from the inelastic measurements on the $x = 0.6$ and $x = 0.2$ samples is compared with calculated spectra in Section (4.7) of this chapter.

4.5 More Detailed Measurements of the Spin Waves in the Oblique Antiferromagnetic Phase of $K_2Co_xFe_{1-x}F_4$

In Section (4.4) spin wave measurements on a nominally $x = 0.2$ sample, in the OAF phase, were reported and from the results it was clear that to gain more detailed information on the spin waves in the OAF phase, particularly at low energy/small wavevector transfer, further experiments with higher instrumental resolution and a better quality sample were required. The measurements reported in this section were performed on a sample with nominally $x = 0.27$. Previous neutron diffraction measurements (Vlak et al. (1983)) using a two-axis neutron diffractor, showed that the sample exhibited two phase transitions on cooling from the paramagnetic phase. At $T_N = 64.4 \pm 0.6$K the system underwent a continuous phase transition to a state with two-dimensional uniaxial long-range order and at $T_L = 27 \pm 2$K, a second phase transition occurred in which the planar components established long-range order and the OAF phase was entered.

In many ways, the behaviour of the x = 0.27 sample had been similar to that of the nominally x = 0.2 sample for which $T_N = 66 \pm 1K$ and $T_L = 32 \pm 2K$ (Section (4.4)). One difference was that a rounded hump in the diffuse scattering around T_L was observed in the x = 0.27 sample using a two axis neutron spectrometer, but no such scattering was observed at T_L in the nominally x = 0.2 sample (cf. Figure 4.3.3(b)) for which the measurements were made with a triple axis neutron spectrometer set to record the elastic intensity. For the inelastic measurements on the x = 0.2 sample, only the lower region of the spin wave spectrum, up to around 12 meV was measured. In this range, scans at fixed wavevector transfer revealed single peaks in the energy spectrum, apparently indicating only a spin wave branch. This corresponds to excitation propagating mainly on the Fe^{2+} sites. However, by symmetry arguments, two branches of the excitations might have been expected and this may not have been observed because of problems (discussed earlier) with the sample quality, which only allowed relatively low resolution measurements to be made.

Because of the recent interest in the magnetic excitations in the OAF phase and the nature of the phase transition at T_L, inelastic neutron scattering measurements were performed on the nominally x = 0.27 sample, firstly to establish the form of the dispersion relation at low temperatures, for the excitations in the energy range up to about 12 meV and secondly, to obtain an insight into the temperature dependence of these excitations as the phase transition at temperature T_L is approached from below.

4.5(i) Experimental Details

The neutron scattering measurements were performed at the Institut Laue-Langevin, Grenoble, France. The single crystal $x = 0.27$ sample was mounted in a variable-temperature Helium flow cryostat with the magnetic $\underline{a}_m^*$ and $\underline{c}_m^*$ directions in the scattering plane. The IN3 triple-axis spectrometer was used for most of the measurements but some supplementary work to gain information about the magnetic excitations near the Brillouin zone boundary was carried out on the IN8 triple-axis spectrometer. In all the measurements reported here both the monochromator and the analyser utilised the pyrolytic graphite (0,0,2) Bragg reflections. The high resolution measurements on the low energy, small wavevector spin waves were performed using a Beryllium filter, cooled by liquid nitrogen, before the analyser, a fixed final wavevector of $k_f = 1.571\ \text{Å}^{-1}$ and 60' - 60' - 60' horizontal collimation from monochromator to detector. For the other measurements, the instruments had a pyrolytic graphite filter fitted before the analyser, a fixed $k_f = 2.662\ \text{Å}^{-1}$ and 40' - 40' - 60' collimation from monochromator to detector. Due to the quasi two-dimensional nature of the magnetic interactions, there is no spin wave dispersion along the $\underline{c}_m^*$ direction and it is the spin wave dispersion along the magnetic $\underline{a}_m^*$ direction which is of interest. Labelling the magnetic $\underline{a}_m^*$ direction as [1,0,0] and the $\underline{c}_m^*$ direction as [0,0,1], it was decided to make constant wavevector transfer scans with $\underline{Q} + (-(1+\xi), 0, 0.4)$ to determine the spin wave dispersion along the [1,0,0] direction. The wavevector (-1,0,0.4) corresponded to the quasi elastic position (Birgeneau et al. (1971)).

4.5(ii) Experimental Results

Initial measurements characterised the dispersion of the low energy spin waves at T = 5K. A typical scan is shown in Figure (4.5.1). The data sets from the constant wavevector (constant - $\underline{Q}$) scans were fitted to Gaussian envelopes at each of the $\underline{Q}$ values and the peak positions are shown in Figure (4.5.2). Two branches of excitations can clearly be distinguished. The energy difference between these branches is largest at the Brillouin zone centre and decreases as the reduced wavevector transfer increases. The two branches seem to meet at the zone boundary. Two branches of excitations also occur in K_2FeF_4 (Thurlings et al. (1982)) and in a classical model these were attributed to spins precessing on ellipsoidal cones with the long axes of the ellipses mutually perpendicular. The energies of the excitations in the present x = 0.27 sample are lower at corresponding $\underline{Q}$ - values than those in pure K_2FeF_4. This is presumably due to the effects of disorder and that the x = 0.27 sample has the OAF structure, whereas K_2FeF_4 has a planar antiferromagnetic structure at low temperatures.

The behaviour of the lower branch of the spin wave dispersion at the phase boundary between the OAF phase and the higher symmetry uniaxial phase is of theoretical interest. The phase boundary between the OAF phase and the uniaxial phase for the x = 0.27 sample occurs at $T_L = 27 \pm 2K$ and spin wave measurements were made at T = 5K, T = 19K, T = 25K (all below T_L) and at T = 32K (above T_L) with particular emphasis on high resolution measurements on the low energy branch of the excitations near q = 0.

In constant $\underline{Q}$ scans at T = 5K, the energy width was greater

FIGURE (4.5.1): Constant wavevector transfer scan with $Q = (-1.05, 0, 0.4)$ at $T = 5K$. Fixed $k_f = 2.662\text{Å}^{-1}$ and 40-40-60 collimation from monochromator to detector. Monitor 200,000 corresponded to a counting time of approximately 10 minutes per point.

Fig (4.5.1)

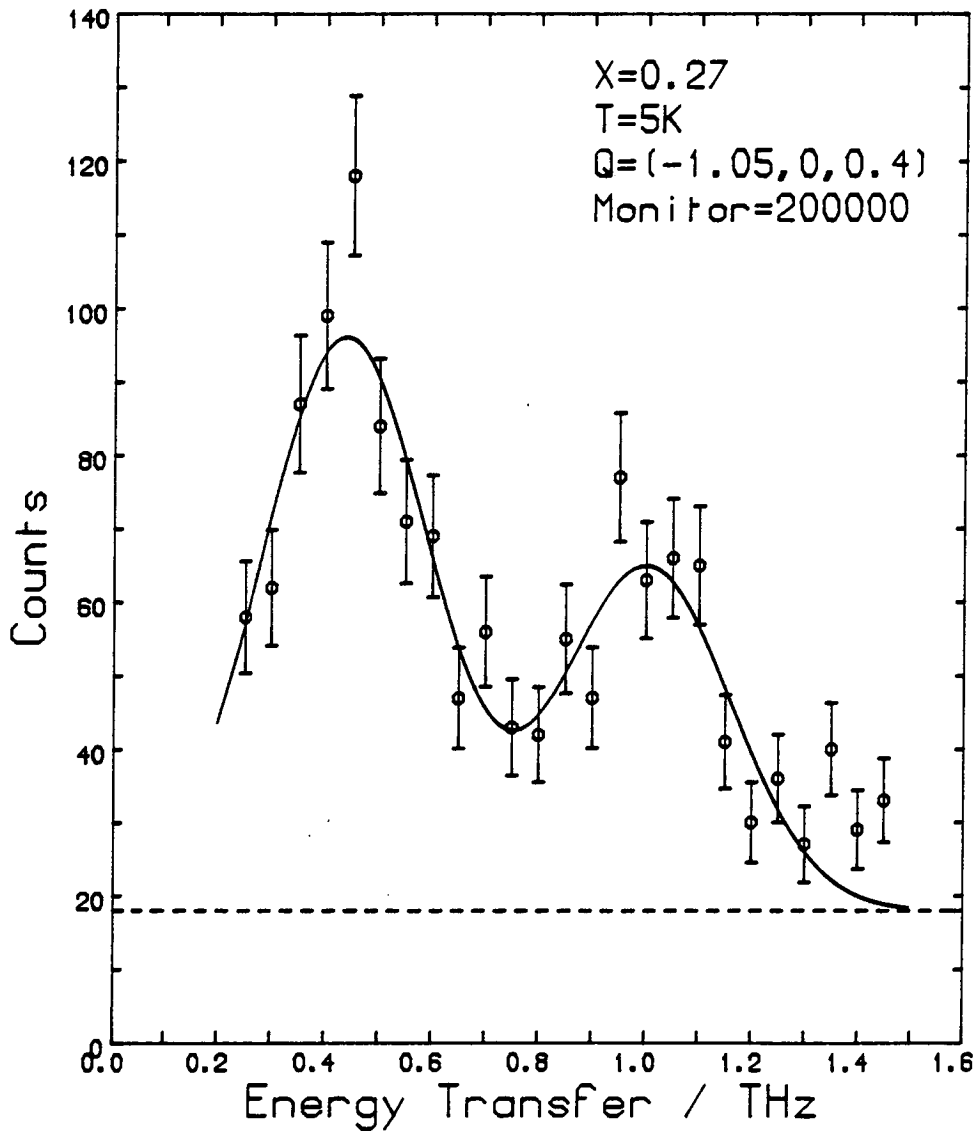
X=0.27
T=5K
Q=(-1.05,0,0.4)
Monitor=200000
Counts
Energy Transfer / THz
0
20
40
60
80
100
120
140
0.0
0.2
0.4
0.6
0.8
1.0
1.2
1.4
1.6

FIGURE (4.5.2): Spin wave dispersion relation at T = 5K for $K_2Co_xFe_{1-x}F_4$ with x = 0.27. The points indicate the peak positions obtained by simply fitting the constant wavevector transfer scans to Gaussian envelopes. The solid lines are a guide to the eye. ξ is the reduced wavevector in units of a_m^*.

Fig (4.5.2)

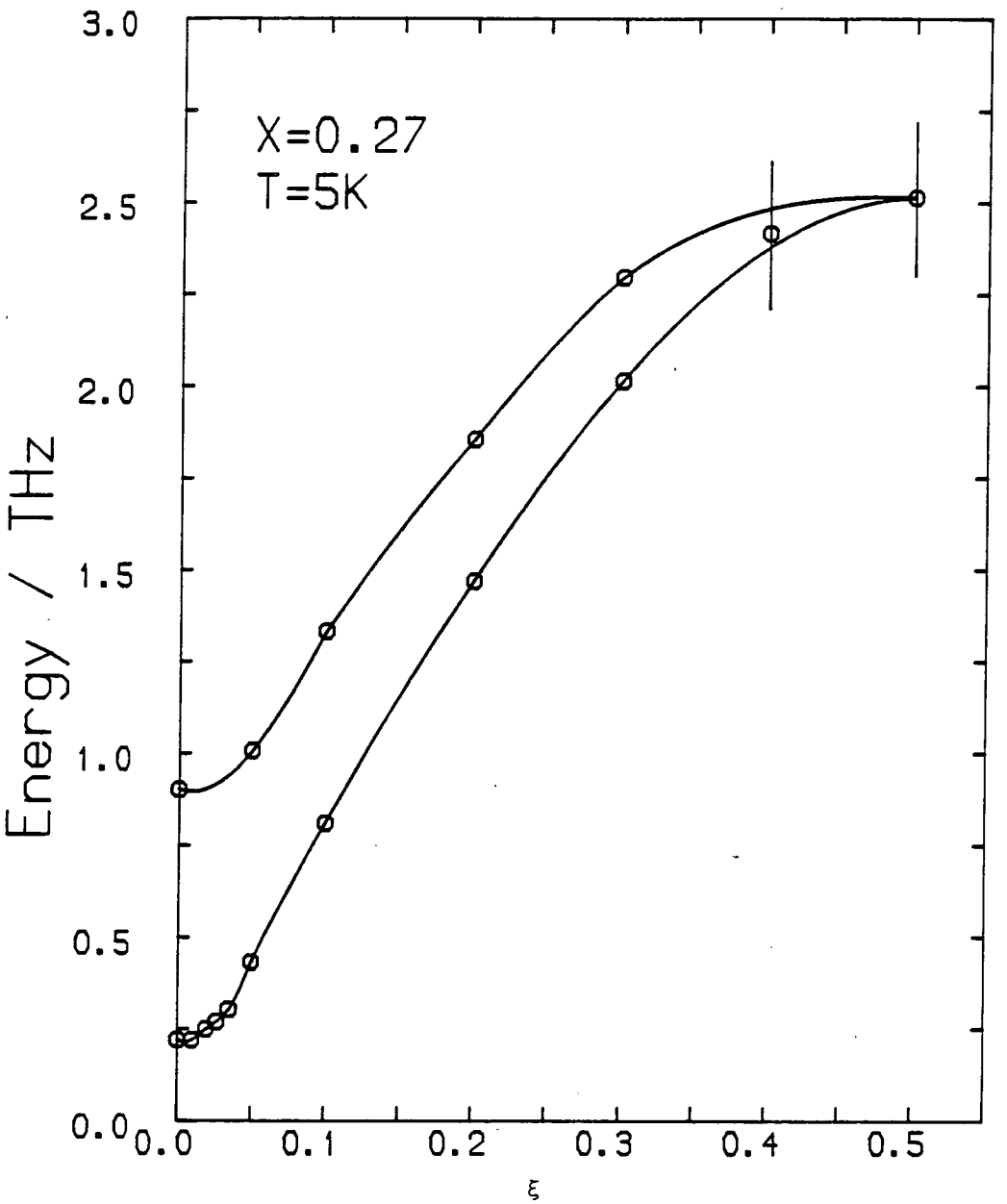

than the instrumental resolution width. Moreover, the intrinsic width of the excitations apparently increased as the temperature approached T_L from below. The effects of instrumental resolution are important in interpreting the data collected at low energy and small reduced wavevector transfer. These effects were accounted for by simultaneously fitting the scans in the range $0 \leq \xi \leq 0.035$ to the form for $S(q,\omega)$ given in equation (4.5.1), folded with the 4-dimensional resolution function of the three axis neutron spectrometer (Cooper and Nathans (1967)). This folding with the resolution function was performed using a unique fitting program (Mitchell and Dove (1985)), which utilizes the parallel architecture of the I.C.L. D.A.P. computer to perform the normally time consuming numerical integration in a greatly reduced time. The chosen form for $S(q,\omega)$ was that of a damped harmonic oscillator, given by:-

$$S(q,\omega) = A(n(\omega) + 1) \frac{\omega\Gamma}{(\omega^2 - \omega_o^2(q))^2 + \omega^2\Gamma^2} \qquad (4.5.1)$$

where A is an overall scale factor, $n(\nu)$ is the Bose-Einstein population factor, Γ is an intrinsic energy width and $\omega_o(q)$ is given by the model dispersion relation of equation (4.5.2):

$$\omega_o(q) = (\varepsilon_g^2 + (D_s q_a)^2)^{\frac{1}{2}} \qquad (4.5.2)$$

where ε_g is the spin wave energy gap for the lower branch, q_a is the reduced wavevector transfer (ξa_m^*) and D_s is the spin wave stiffness for the lower branch. Included in the fits were a flat background parameter and a Gaussian centred near zero energy to account for incoherent elastic scattering.

Figure (4.5.3) shows the result of a single fit to 5 scans with wavevector transfer $\underline{Q} = (-(1+\xi), 0, 0.4)$ in the range $0 < \xi < 0.035$ at $T = 5K$. Figure (4.5.4) compares scans at $\xi = 0$ for $T = 5K$, $T = 19K$ and $T = 25K$ and shows that the inelastic scattering signal moves to lower energies as the temperature increases.

Table (4.5.1) shows the values for ε_g, D_s, Γ and A obtained at the three chosen temperatures below T_L. The number of scans fitted to obtain the values shown in Table (4.5.1) were 5, 4 and 3. at $T = 5K$, $T = 19K$, and $T = 25K$ respectively.

The small amount of dispersion in the wavevector range $0 < \xi < 0.035$ leads to the large error bar on the values of D_s and the most that can be stated about the spin wave stiffness is that it seems to decrease slightly as the temperature increases towards T_L. However, the values of ε_g and Γ obtained for the fits confirm the result obtained directly from the experimental data that the energy of the spin wave gap decreases and the intrinsic energy width of the excitations increases as the temperature tends towards T_L from below.

Scans were made at $T = 32K$ to study the low energy, small wavevector transfer inelastic scattering above T_L. These scans however did not reveal any spin wave "peaks" (Figure (4.5.5)) and any spin wave scattering present can only be described as over-damped.

In summary, it has been shown that the low temperature ($T = 5K$) spin wave dispersion relation for an $x = 0.27$ sample of $K_2Co_xFe_{1-x}F_4$ consists of two distinct branches which appear to come together at the Brillouin zone boundary. Previous experiments on the planar

FIGURE (4.5.3): The data at T = 5K obtained under high resolution conditions: fixed $k_f = 1.571 \text{Å}^{-1}$ and 60-60-60 collimation from monochromator to detector.

(a) Q = (-1,0,0.4)

(b) Q = (-1.01,0,0.4)

(c) Q = (-1.02,0,0.4)

(d) Q = (-1.027,0,0.4)

(e) Q = (-1.035,0,0.4)

Solid lines indicate the results of a single fit to the data described in the text.

Monitor 100,000 corresponds to a counting time of approximately 10 mins. per point.

Fig (4.5.3(a))

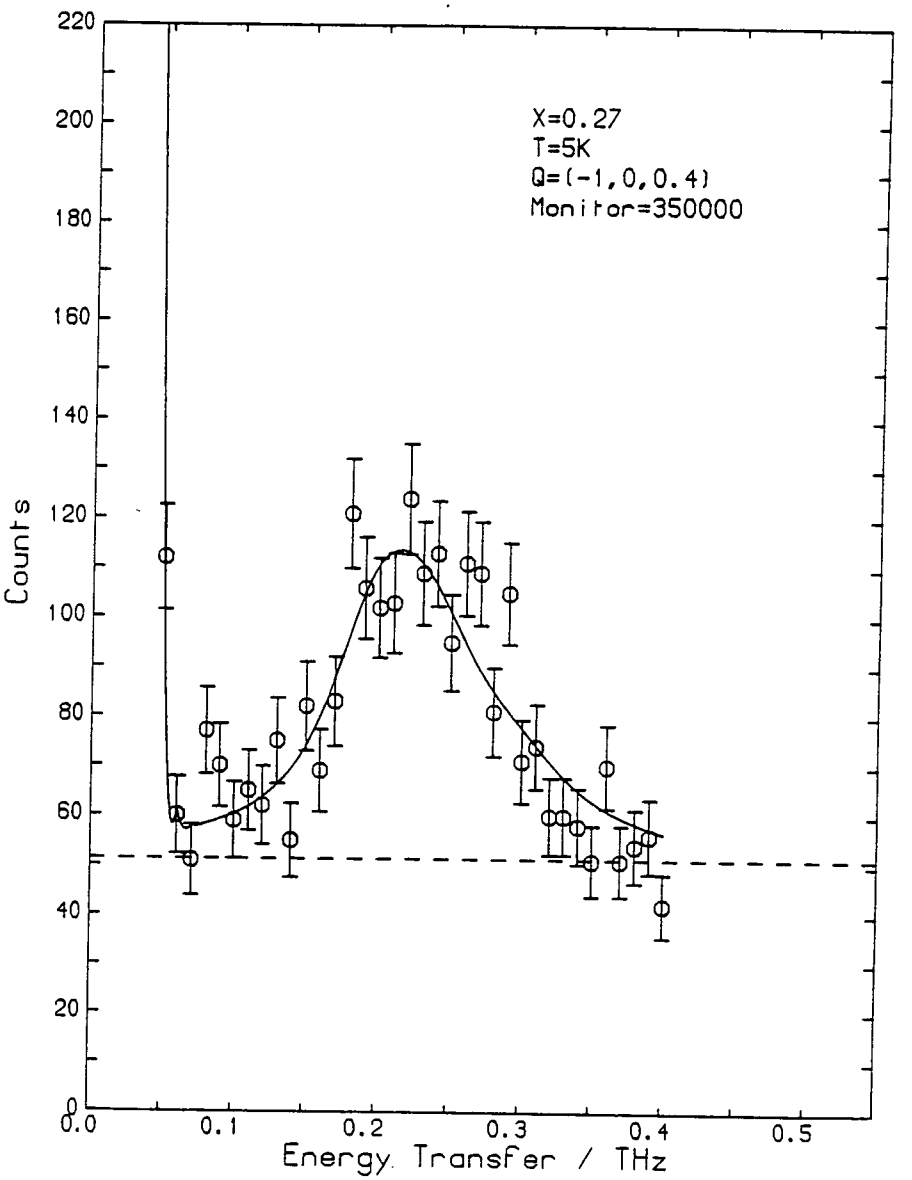
X=0.27
T=5K
Q=(-1,0,0.4)
Monitor=350000
Counts
Energy Transfer / THz
0
20
40
60
80
100
120
140
160
180
200
220
0.0
0.1
0.2
0.3
0.4
0.5

Fig (4.5.3(b))

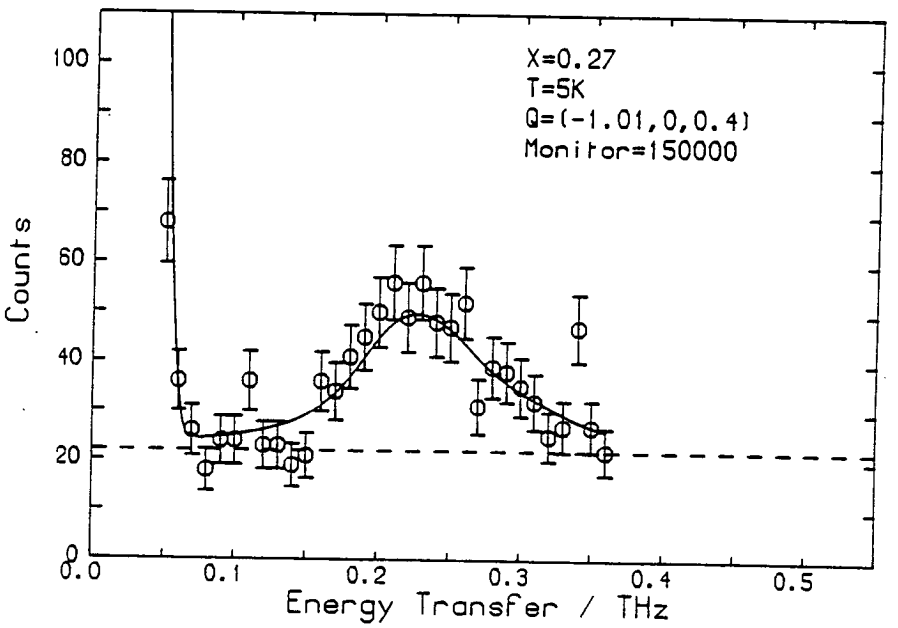

Fig(4.5.3(c))

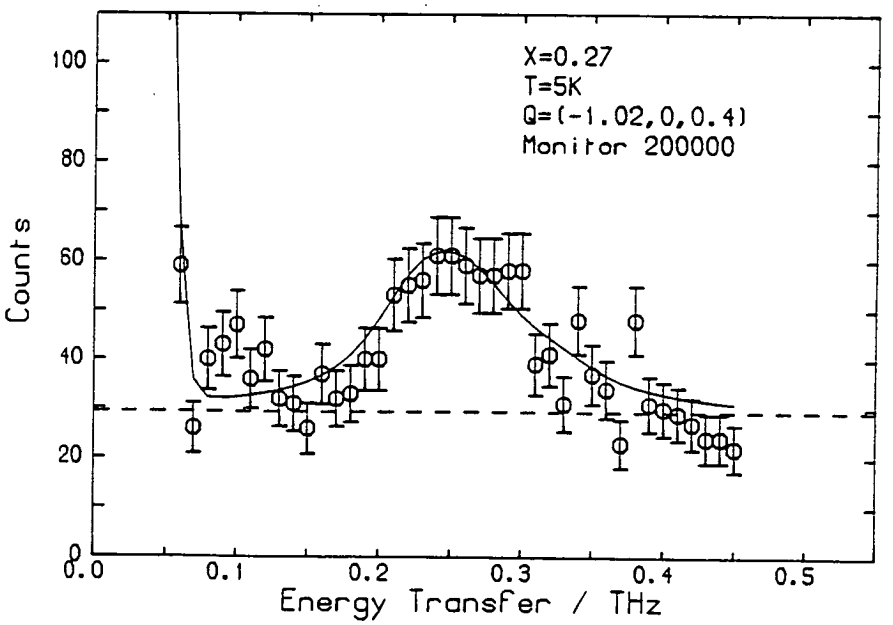

Fig (4.5.3(d))

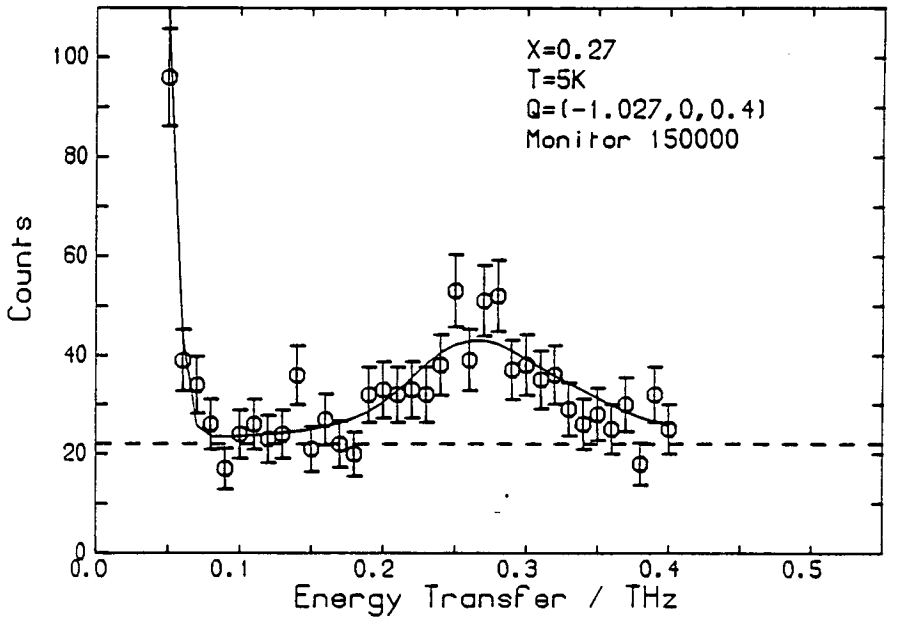

Fig (4.5.3(e))

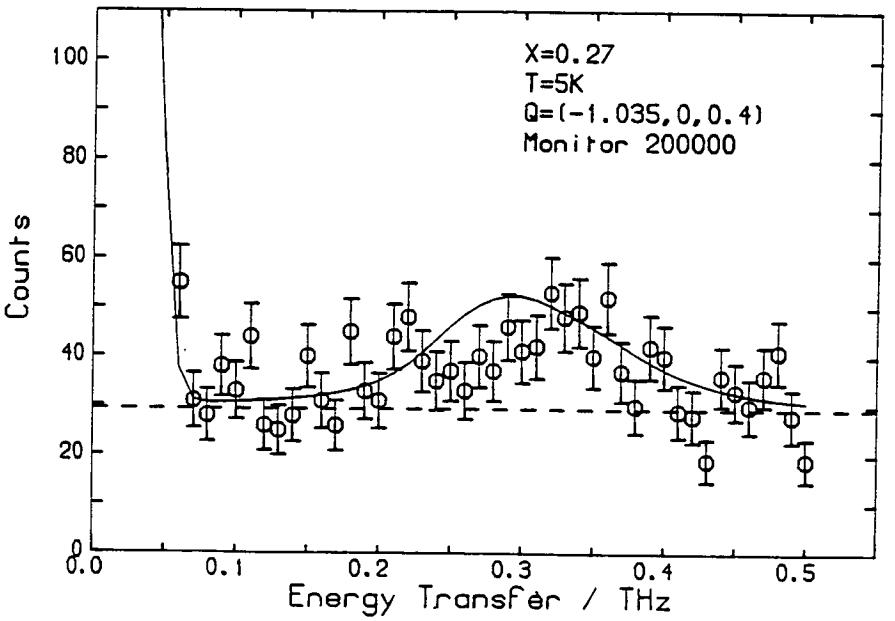

FIGURE (4.5.4): Data collected at

(a) T = 5K

(b) T = 19K

(c) T = 25K

under high resolution conditions: fixed $k_f = 1.571 \text{Å}^{-1}$ and 60-60-60 collimation from monochromator to to detector. Solid lines are from the fit to the data described in the text.

Monitor 100,000 corresponds to a counting time of approximately 10 mins. per point.

Fig (4.5.4(a))

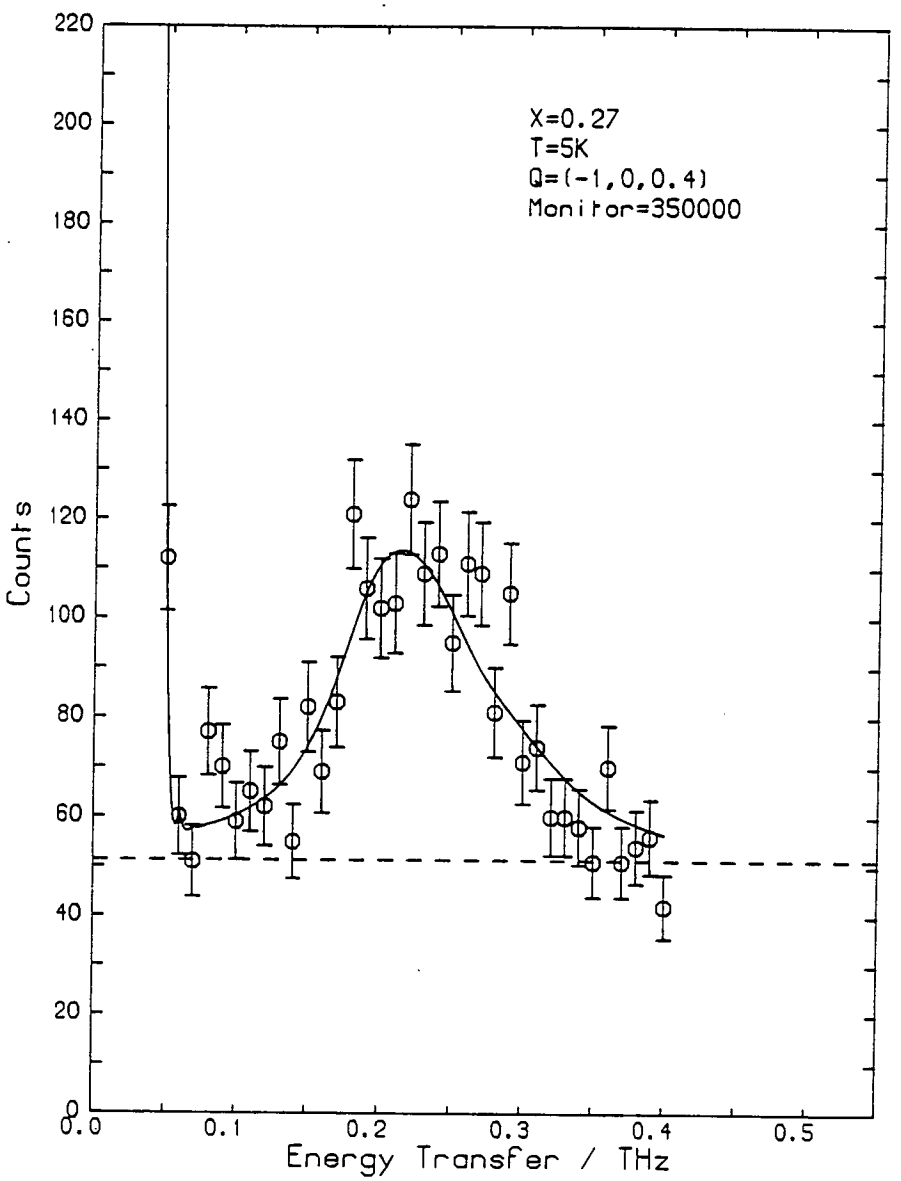
X=0.27
T=5K
Q=(-1,0,0.4)
Monitor=350000
Counts
Energy Transfer / THz
0
20
40
60
80
100
120
140
160
180
200
220
0.0
0.1
0.2
0.3
0.4
0.5

Fig (4.5.4(b))

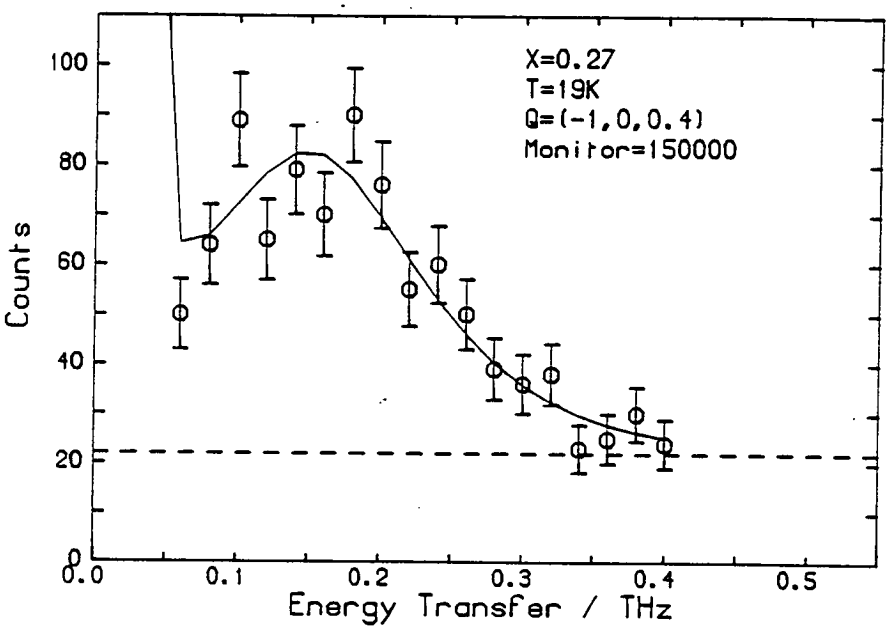

Fig (4.5.4(c))

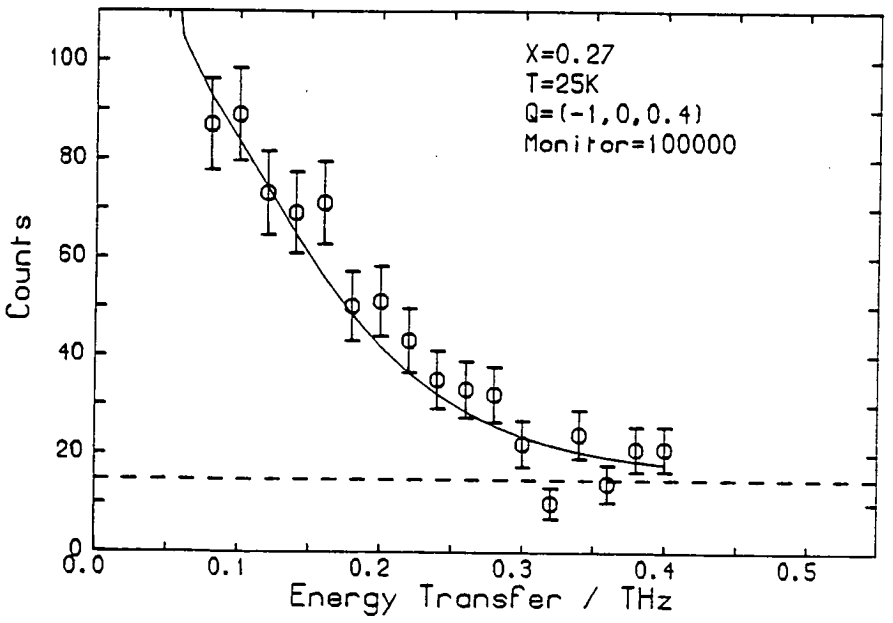

T/K	ε_g/THz	D_s/THz Å	Γ/THz	A/THz^2	Agreement Factor
5	0.196 ± 0.025	5.6 ± 1.4	0.068 ± 0.043	0.16 ± 0.04	1.16
19	0.158 ± 0.037	5.0 ± 1.8	0.145 ± 0.055	0.18 ± 0.04	1.16
25	0.130 ± 0.049	4.4 ± 1.5	0.238 ± 0.127	0.18 ± 0.08	1.18

TABLE (4.5.1): Values of ε_g, D_s, Γ and A obtained from fitting the data taken under high resolution conditions described in the text.
The agreement factor is a goodness of fit parameter and is defined by

$$\text{Agreement Factor} = (\chi^2/N)^{\frac{1}{2}}$$

where N is the number of degrees of freedom and

$$\chi^2 = \sum_{i=1}^{n} \frac{(I_{calc} - I_{obs})^2}{\sigma^2_{calc}}$$

where n is the number of data points, I_{calc} is the calculated value and I_{obs} is the experimental value for a particular data point. $\sigma_{calc} = (I_{calc})^{\frac{1}{2}}$ here.

FIGURE (4.5.5): Constant wavevector scan with Q = (-1.05,0,0.4) at T = 32K. Fixed $k_f = 2.662 \text{Å}^{-1}$ and 40-40-60 collimation from monochromator to detector. Solid line indicates fit to a Gaussian envelope.

Fig (4.5.5)

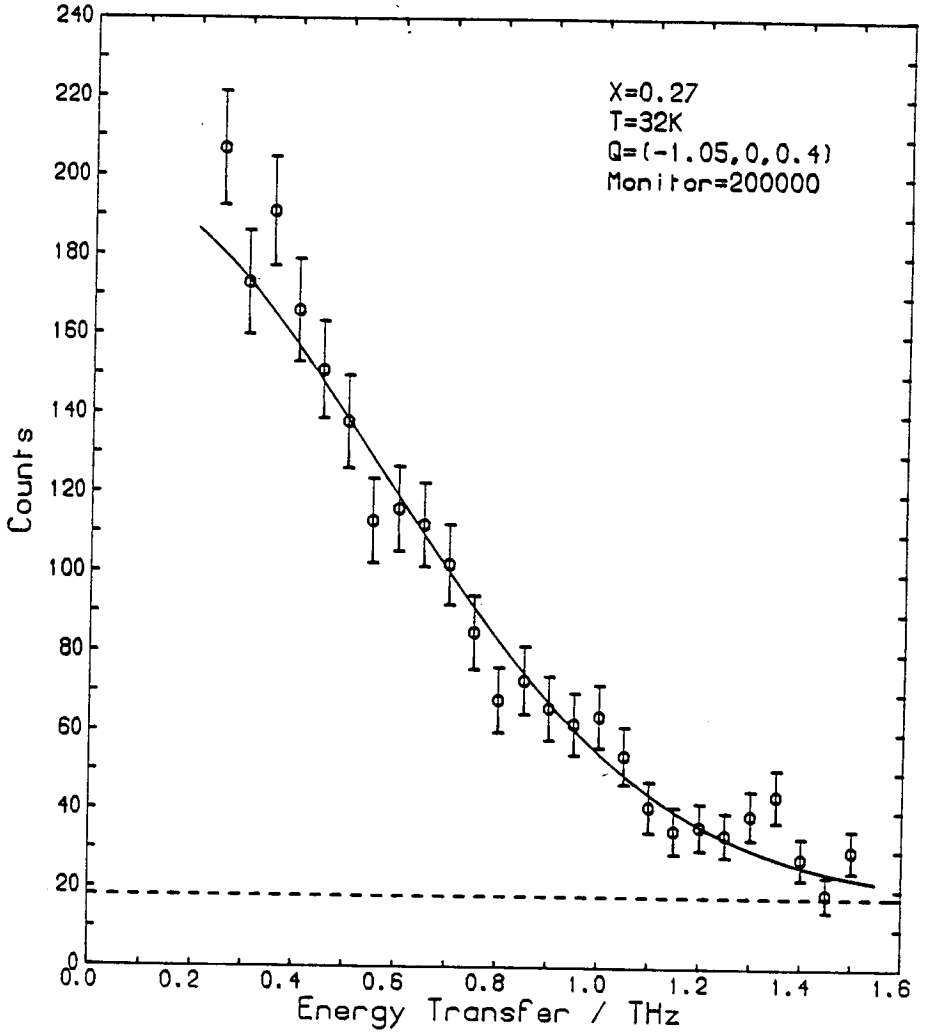
X=0.27
T=32K
Q=(-1.05,0,0.4)
Monitor=200000
Counts
Energy Transfer / THz
0
20
40
60
80
100
120
140
160
180
200
220
240
0.0
0.2
0.4
0.6
0.8
1.0
1.2
1.4
1.6

antiferromagnet K_2FeF_4 had indicated two branches in the pure system; however, as expected, the energies at a given wavevector transfer were different (in fact lower) in the mixed system due to the disorder and that the mixed system has the OAF structure below T_L.

Measurements to investigate the changes in the lower branch of the spin wave dispersion relation as the temperature increased towards T_L, revealed that the energy of the spin wave gap, ε_g, decreases and that the intrinsic width of the excitations increases as T_L is approached from below. Mean field calculations at $T = 0$ by Matsubara (1981) predicted that, as a function of concentration, the spin wave energy gap should go to zero at the phase boundaries between the OAF phase and the other two ordered phases. Although in this experiment, the temperature was being varied, not the concentration, the results are consistent with a zero energy gap for the lower spin wave branch at the boundary between the OAF and Uniaxial Antiferromagnetic phases.

It is now believed that these results resolve an apparent discrepancy between the results of two previous experiments. Measurements, using a two-axis neutron spectrometer, of the diffuse scattering at $Q = (1,0,0.4)$ in the same $x = 0.27$ sample (Vlak et al. (1983)) revealed a rounded hump in the diffuse scattering around T_L. Similar measurements, but using a three axis neutron spectrometer with high resolution on a sample with nominally $x = 0.2$ (Higgins et al. (1984)) revealed no increase in the intensity at or near T_L. In the former case the integrated intensity most probably included a contribution from the spin waves

near T_L whereas in the second case only "quasi-elastic" diffuse scattering was being observed.

4.6 Calculations to Determine the Ground State in $K_2Co_xFe_{1-x}F_4$

As discussed in Chapter 1 of this thesis one of the most difficult problems encountered in interpreting experimental data or calculating excitation spectra for systems with competing spin anisotropy is that the details of the ground state, especially for the mixed (or OAF phase) are largely unknown. Mean field calculations (see, for example, Matsubara (1977)) assume that each of the magnetic species is in the same average environment and so can only predict an average spin direction for each of the two magnetic species, as a function of concentration and temperature. However, in practice the spin at a particular site will have an orientation which depends on its local environment and intuitively a distribution of spin orientation angles would be expected at a particular concentration. This section describes the details of and results from a computer program NEWSQR which was written to calculate the T = OK ground state configurations in $K_2Co_xFe_{1-x}F_4$ by minimising the internal energy U, of each spin in its local environment. Minimising the internal energy at T = OK is equivalent to minimising the Gibbs free energy, G, because $G = U - TS$, where S is the entropy. The purpose of the NEWSQR work was twofold. Firstly, calculation of the ground state characteristics should give a better insight into the magnetic structure at T = OK, which is physically interesting in itself. Secondly, the ground state has

to be known before the equation-of-motion technique can be used to calculate the low temperature spin wave spectra. Calculation of the low temperature spin wave spectra is discussed in Section (4.7).

It was assumed that the system could be modelled by the following Hamiltonian:

$$H = \sum_i D_i (S_i^z)^2 + \sum_i E_i \{(S_i^x)^2 - (S_i^y)^2\} + \sum_{ij} I_{ij} S_i^z S_j^z + J_{ij}(S_i^x S_j^x + S_i^y S_j^y) \qquad (4.6.1)$$

where I_{ij} and J_{ij} depend on the species of the nearest neighbours and D_i and E_i are non-zero only for Fe spins. The coordinates (x,y,z) refer to the crystallographic frame of reference. However, in general the axis of quantisation of a particular spin will not lie along the x, y or z directions. With $E_i < 0$ in the Hamiltonian of equation (4.6.1) the spin is confined to the x-z plane and it can be assumed that the local axis of quantisation labelled z' lies at an angle θ_i to the z-axis. The operators in the crystallographic frame of reference can then be related to the operators in the local frame of reference through a rotation matrix:

$$\begin{pmatrix} S_i^x \\ S_i^y \\ S_i^z \end{pmatrix} = \begin{pmatrix} \cos\theta_i & 0 & \sin\theta_i \\ 0 & 1 & 0 \\ -\sin\theta_i & 0 & \cos\theta_i \end{pmatrix} \begin{pmatrix} S_i^{x'} \\ S_i^{y'} \\ S_i^{z'} \end{pmatrix} \qquad (4.6.2)$$

This relationship can be written as:

$$\underline{S}_i = \underline{\underline{U}}_i \cdot \underline{S}_i \qquad (4.6.3)$$

where $\underline{\underline{U}}_i$ is the rotation matrix whose elements are given by

$U_i^{\alpha\beta}$ (where $\alpha, \beta = x,y,z$). The local spin operators can then be related to the spin deviation operators a_i and a_i^* by:

$$S_i^{z'} = S_i - a_i^* a_i \qquad (4.6.4(a))$$

$$S_i^{x'} = \sqrt{\frac{S_i}{2}}\,(a_i + a_i^*) \qquad (4.6.4(b))$$

$$S_i^{y'} = \sqrt{\frac{S_i}{2}}\,(a_i - a_i^*) \quad . \qquad (4.6.4(c))$$

Using equations (4.6.4) to substitute for $S_i^{x'}$, $S_i^{y'}$ and $S_i^{z'}$ in equation (4.6.3) then the operators in the crystallographic frame of reference can be related to the creation and annihilation operators. As an example:

$$S_i^x = U_i^{xz'}(S_i - a_i^* a_i) + U_i^{xx'}\sqrt{\frac{S_i}{2}}\,(a_i + a_i^*) + U^{xy'}\left(-i\sqrt{\frac{S_i}{2}}\,(a_i - a_i^*)\right) \qquad (4.6.5)$$

This can be rewritten as:

$$S_i^x = U_i^{xz'}(S_i - a_i^* a_i) + U_i^x a_i + (U_i^x a_i)^* \qquad (4.6.6)$$

where U_i^x is given by:

$$U_i^x = \sqrt{\frac{S_i}{2}}\,(U_i^{xx'} - i\,U_i^{xy'}) \qquad (4.6.7)$$

The y and z components are obtained similarly. After some algebraic manipulation the Hamiltonian can be written as:

$$H = H_o + H_1 + H_2 + \ldots\ldots \qquad (4.6.8)$$

where H_n is the n^{th} order term in the spin deviation operators. The zeroth order term is given by

$$H_o = \Delta + \sum_i (D_i - E_i) S_i (S_i - \tfrac{1}{2}) \cos^2\theta_i$$

$$+ \sum_{ij} \{ I_{ij} \cos\theta_i \cos\theta_i + J_{ij} \sin\theta_i \sin\theta_j \} S_i S_j \qquad (4.6.9)$$

where

$$\Delta = \sum_i \frac{D_i S_i}{2} + E_i S_i (S_i - \tfrac{1}{2}) \; . \qquad (4.6.10)$$

Δ is independent of θ_i. The program NEWSQR finds the angles θ_{i_m} at each site which minimise the H_o term of the Hamiltonian. The first order term H_1 can be written as:

$$H_1 = \sum \frac{1}{\sqrt{2S_i}} \frac{\partial H_o}{\partial \theta_i} (a_i + a_j^*) \quad . \qquad (4.6.11)$$

Because the program minimises the zeroth order term H_o then at each site $\partial H_o / \partial \theta_i = 0$ and so the first order term drops out of the Hamiltonian leaving the ground state term H_o and the second order spin wave term H_2 which is given by:

$$H_2 = \sum_i A_i a_i^* a_i + B_i a_i a_i + C_i a_i^* a_i$$

$$\sum_{ij} W_{ij} a_i a_j + X_{ij} a_i a_j^* + Y_{ij} a_i^* a_j + Z_{ij} a_i^* a_j^* \qquad (4.6.12)$$

where A_i, B_i, C_i, W_{ij}, X_{ij}, Y_{ij} and Z_{ij} are defined in Table (4.6.1). In NEWSQR a random $L \times L$ lattice is set up corresponding to a concentration x of Co^{2+} ions and $(1-x)$ of Fe^{2+} ions in $K_2Co_xFe_{1-x}F_4$. The internal energy at each site is calculated for the initial angles given to the program. The internal energies corresponding to the individual sites are then summed to give the total internal energy for the model system. Moving sequentially through the sites the angles are changed by an amount $\delta\theta_i$ so that

TABLE (4.6.1): Definition of Coefficients in Equation (4.6.12)

$$A_i = (-2)\{D_i (U_i^{zz'})^2 + E_i [(U_i^{xz'})^2 - (U_i^{yz'})^2](S_i - \tfrac{1}{2})$$

$$+ D_i |U_i^z|^2 + E_i(|U_i^x|^2 - |U_i^y|^2)$$

$$+ \sum_{ij} I_{ij} S_j U_i^{zz'} + U_j^{zz'} + J_{ij} S_j (U_i^{xz'} U_j^{xz'} + U_i^{yz'} U_j^{yz'})\}$$

$$B_i = D_i (U_i^z)^2 + E_i [(U_i^x)^2 - (U_i^y)^2]$$

$$C_i = B_i^*$$

$$W_{ij} = I_{ij} U_i^z U_j^z + J_{ij}(U_i^x U_j^x + U_i^y U_j^y)$$

$$X_{ij} = I_{ij} U_i^z U_j^{z*} + J_{ij}(U_i^x U_j^{x*} + U_i^y U_j^{y*})$$

$$Y = X_{ij}^*$$

$$Z_{ij} = W_{ij}^*$$

* indicates the complex conjugate

E_i, D_i, I_{ij} and J_{ij} are the paremeters defined in the Hamiltonian of equation (4.6.1).

$U_i^{\alpha\beta'}$ (α = x, y, z) are the elements of the matrix $\underline{\underline{U}}_i$ defined by equations (4.6.2) and (4.6.3), and $U_i^{\propto}$ are defined by

$$U_i^{\alpha} = \sqrt{\frac{S_i}{2}} (U_i^{\alpha x'} - i\, U_i^{\alpha y'}).$$

the internal energy for that site is minimised in the local potential. The total internal energy is calculated again, as is the difference ΔU between the new total internal energy, U_{new}, and the total internal energy at the previous step, U_{old}. The minimisation procedure is iterated until ΔU becomes less than a specified value at which point it is considered that the model system has reached its ground state. To ensure that the results were independent of the particular randomly mixed finite system (configuration) used, the program was run for n different configurations at each chosen value of x and the results averaged over the n configurations. For each configuration the Co spins were initially set at $\theta_i = 0°$ and the Fe spins were initially set at $\theta_i = 90°$, corresponding to the values of θ_i in the pure systems.

Parameters used in NEWSQR and in NEWSIM (discussed in Section (4.7)) are listed in Table (4.6.2). To test for finite lattice size effects the program was run with $x = 0.27$ and the results averaged over 5 configurations for various values of L. Figure (4.6.1) shows the Internal Energy per spin as a function of L for the Co and Fe spins. Beyond $L = 40$ the values of Internal Energy are effectively constant. Figure (4.6.2) shows the mean angle between the spin direction and the c-direction for both Co and Fe spins. Again, for $L > 40$ the results seem to be independent of L. In addition, the distribution functions for the internal energy per spin, the angles θ_i, $\cos\theta_i$ and $\sin\theta_i$ were independent of L for $L > 40$ as were spin wave spectra for $x = 0.2$ and $x = 0.6$. It was therefore assumed that beyond $L = 40$, the results from NEWSQR and from NEWSIM (which are discussed in

Values of Parameters Used in NEWSQR and NEWSIM

Exchange Parameters

I_{CoCo} = 7.48 meV

$I_{FeFe} = J_{FeFe}$ = 0.709 meV

I_{CoFe} = $(I_{CoCo} I_{FeFe})^{\frac{1}{2}}$ = 2.30 meV

J_{CoCo} = 3.84 meV

J_{CoFe} = $(J_{CoCo} J_{FeFe})^{\frac{1}{2}}$ = 1.65 meV

Single Ion Anisotropies (Applicable only to Fe spins).

D_{Fe} = 0.49 meV

E_{Fe} = -0.04 meV

g-factors

$g^x_{Fe} = g^y_{Fe} = g^z_{Fe} = 2.5$

$g^x_{Co} = g^y_{Co} = 3.13$

$g^z_{Co} = 6.30$

(Values were derived from the work of Thurlings et al. (1978), Macco et al. (1978) and Macco et al. (1979)).

FIGURE (4.6.1): Internal energy per spin as a function of the length of the lattice side L for both Co and Fe spins. The concentration of Co spins was x = 0.27.

Fig (4.6.1)

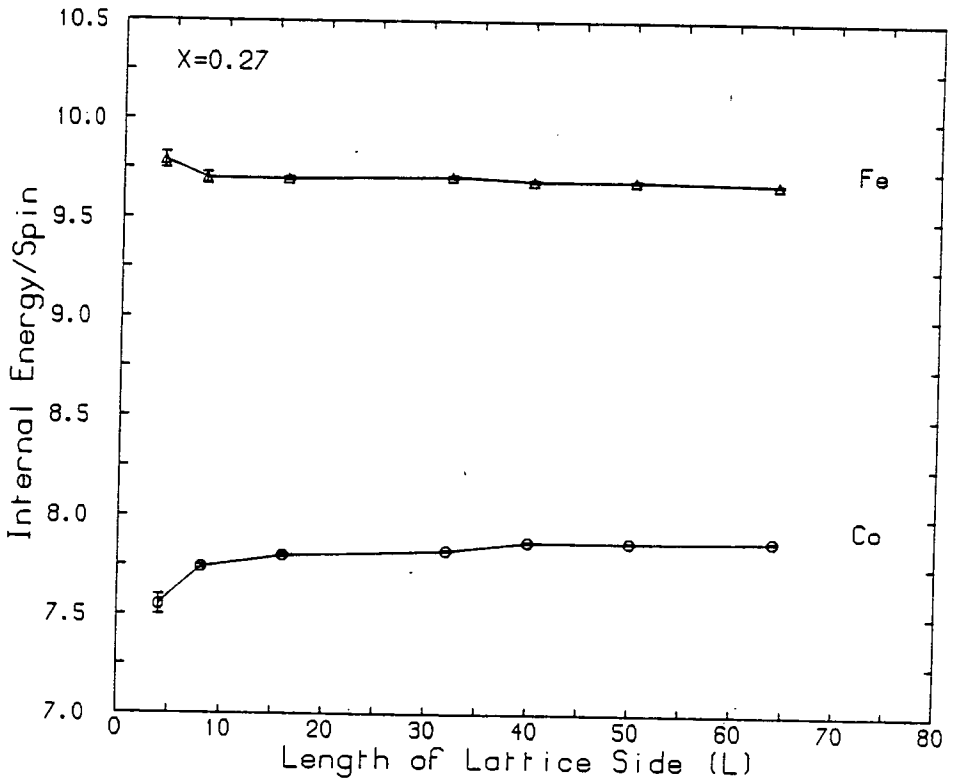
X=0.27
Fe
Co
Internal Energy/Spin
Length of Lattice Side (L)
10.5
10.0
9.5
9.0
8.5
8.0
7.5
7.0
0
10
20
30
40
50
60
70
80

FIGURE (4.6.2): Mean angle between the spin-direction and the c-direction $\overline{\theta}_c$ as a function of the length of the lattice side L for both Co and Fe spins. The concentration of Co spins was $x = 0.27$.

Fig (4.6.2)

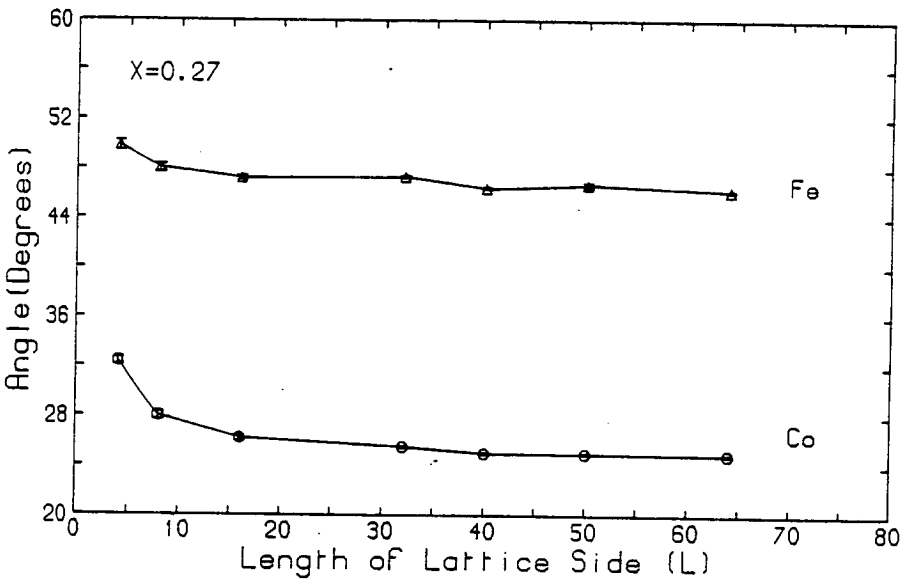
X=0.27
Fe
Co
Angle (Degrees)
Length of Lattice Side (L)
60
52
44
36
28
20
0
10
20
30
40
50
60
70
80

Section (4.7)) are independent of the size of the finite lattice.

To study the ground state of $K_2Co_xFe_{1-x}F_4$ as a function of concentration, NEWSQR was run for a 64×64 lattice averaging over 20 configurations at each of the chosen concentration values. Figure (4.6.3) shows the distribution of cant angles for both Co and Fe spins at $x = 0.25$. It has been expected that this concentration would correspond to the OAF phase, and the figure confirms this. It shows that both the distributions have weight across a wide range of angles between $\theta = 0°$ and $\theta = 90°$. In Figure (4.6.4) the average angles are shown as a function of concentration for both Co and Fe spins. For $0 < x < 0.1$ both the Co and Fe cant angles are 90°, indicating that the system exists in the planar phase. In the concentration range $0.5 < x < 1.0$ the average cant angle $\bar{\theta}_c$ is 0° for both species, which shows that the system has the uniaxial antiferromagnetic structure. For the intermediate concentration range $0.1 < x < 0.5$ the $\bar{\theta}_c$ values are different for Co and Fe spins with the specific $\bar{\theta}_c$ values depending on x. This concentration range therefore corresponds to the OAF phase at $T = 0K$.

Table (4.6.3) compares available experimental values for the cant angles with $\bar{\theta}_c$ values calculated by NEWSQR. The agreement between the calculated values and the experimental values obtained by Mössbauer Spectroscopy and Nuclear Magnetic Resonance (NMR) is reasonable, especially when the fact that the values of x for the experimental samples are nominal values and that none of the measurements were performed at temperatures with $T < \sim 8K$, is taken into consideration. The effect of uncertainty in the actual concentration

FIGURE (4.6.3): Distribution of cant angles θ_c as a function of Co concentration x for both Co and Fe spins, for L = 64 and x = 0.25. The results were obtained by averaging over 20 configurations. The NEWSQR run which produced these results took around 13 hours of VAX11/750 C.P.U. time.

Fig (4.6.3)

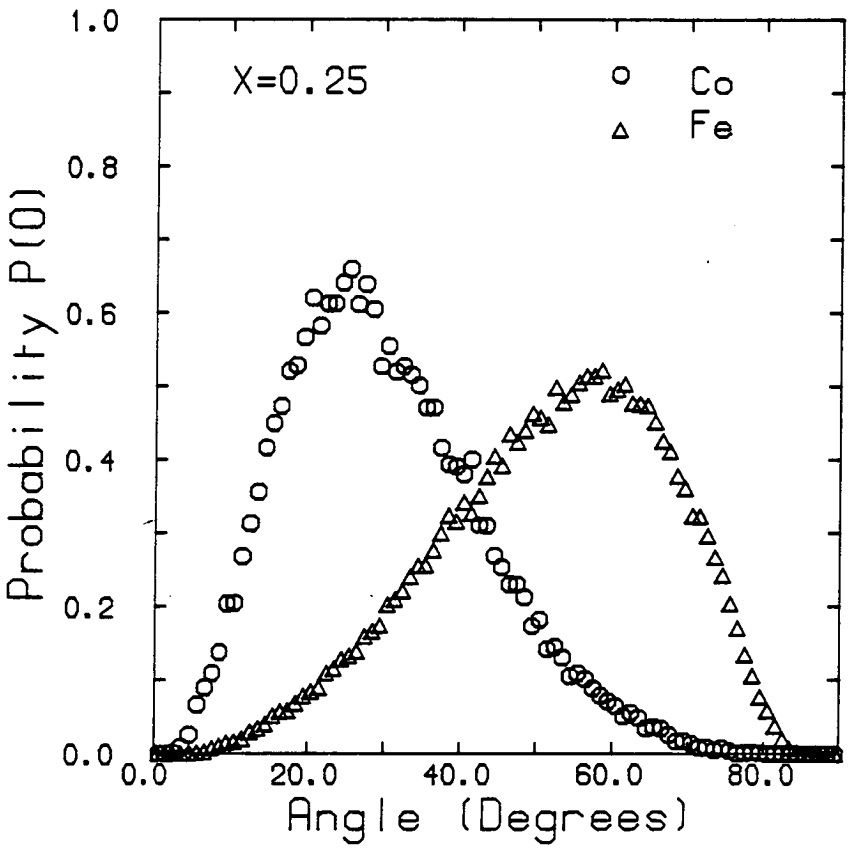
X=0.25
Co
Fe
Probability P(θ)
Angle (Degrees)
1.0
0.8
0.6
0.4
0.2
0.0
0.0
20.0
40.0
60.0
80.0

FIGURE (4.6.4): Average cant angles θ_c for both Co and Fe spins as a function of Co concentration x. The results were obtained by averaging over 20 configurations with L = 64.

Fig (4.6.4)

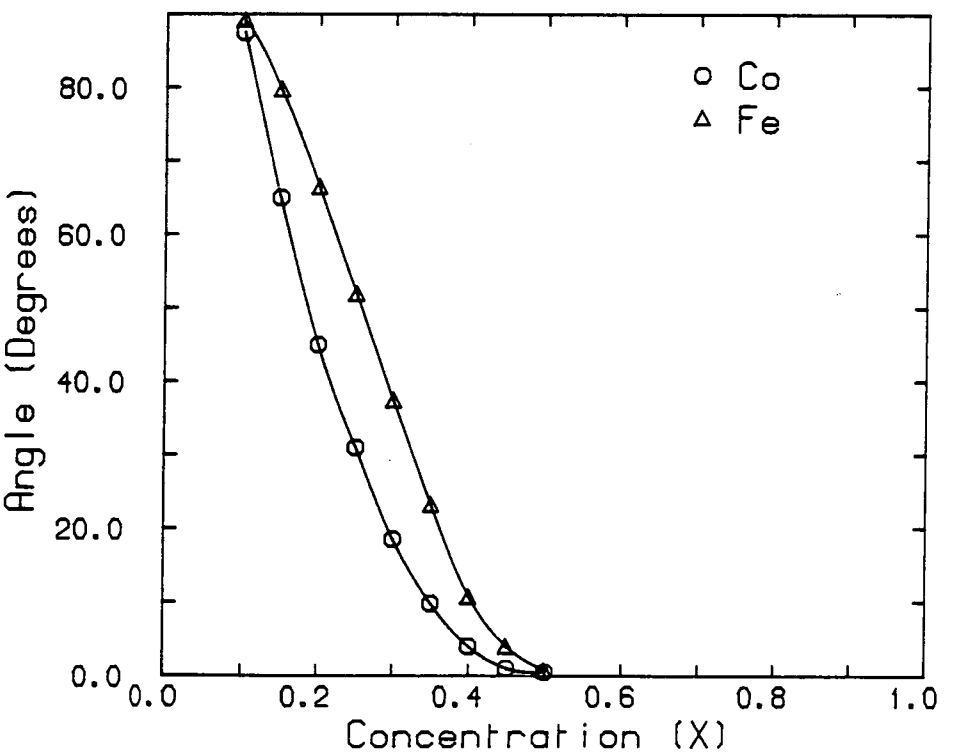
Co
Fe
Angle (Degrees)
80.0
60.0
40.0
20.0
0.0
0.0
0.2
0.4
0.6
0.8
1.0
Concentration (X)

TABLE (4.6.3): Comparison of calculated and experimental values for the average cant angle in $K_2Co_xFe_{1-x}F_4$. The calculated values are given in parenthesis beneath the experimental values. ($\bar{\theta}_{Co/Fe}$ labels the average cant angle for Co/Fe).

Nominal Concentration (x)	$\bar{\theta}_{Fe}$	$\bar{\theta}_{Co}$	Technique	Source
0.06	90 ± 2 (90)	- (90)	1	1
0.12	90 ± 5 (86)	90 ± 5 (74)	1,2	2
0.16	82 ± 3 (79)	- (60)	1,2	2
0.18	90 ± 5 (72)	90 ± 5 (51)	1	1
0.2	55 ± 2 (66)	- (45)	1	1
0.27	52 ± 5 (46)			
	42 ± 5 (46)	23 ± 6 (25)	2	2
0.55	0 ± 5	0 ± 5	1,2	2

Key: Techniques 1: Mossbauer Spectroscopy.
2: Nuclear Magnetic Resonance.

Source of Experimental Data 1: Fendler et al. (1984)
2: Vlak et al. (1985).

Neutron Diffraction Results

x = 0.27	θ_c = 27 ± 2 (40)	Vlak et al. (1983)
x = 0.2	θ_c = 33 ± 1 (63)	Higgins et al. (1984)

of the sample would be greatest in the OAF phase where small differences in concentration lead to significant changes in $\overline{\theta}_c$. Except for the $x = 0.18$ results, which are anomalous in the sense that $\theta_c^{Fe}(x = 0.16) < \theta_c^{Fe}(x = 0.18)$, which is not what would be expected, the predictions from the NEWSQR result that the OAF phase extends between $x = 0.1$ and $x = 0.5$ at $T = 0K$ are reasonably consistent with the experimental results. Neutron diffraction measurements measure the cant angle for the average magnetic moment. The values obtained by neutron diffraction measurements for the cant angles in $x = 0.2$ and $x = 0.27$ samples are not in as good agreement with the NEWSQR results.

4.7 Calculation of the Low Temperature Magnetic Excitation Spectra in $K_2Co_xFe_{1-x}F_4$

In this section, results from calculations of the low temperature magnetic excitation spectra in $K_2Co_xFe_{1-x}F_4$ are presented. The technique chosen was the "Equation-of-Motion" method which had been used in the past to calculate the dynamic structure factor $S(\underline{Q},\omega)$ in $d = 2$ mixed antiferromagnetic systems such as $Rb_2Mn_xNi_{1-x}F_4$ (Thorpe and Alben (1976)). For $Rb_2Mn_xNi_{1-x}F_4$ application of the "Equation-of-Motion" method was straightforward because the spins of both the Mn and Ni ions favoured alignment along the c-axis of the magnetic unit cell so that the ground state was conceptually known. Labelling the ordering direction by $\underline{z}$ then only $S^{xx}(\underline{Q},\omega)$ had to be calculated since, by symmetry considerations, $S^{xx}(\underline{Q},\omega) = S^{yy}(\underline{Q},\omega)$ for that system. Good agreement was obtained between the calculated spectra and the spectra from inelastic neutron scattering experiments on $Rb_2Mn_xNi_{1-x}F_4$ with $x = 0.5$ (Birgeneau et al. (1975), Als Nielsen et al. (1975)). Application of the technique to $K_2Co_xFe_{1-x}F_4$ was a considerably more difficult problem because the results from the program NEWSQR (discussed in Section (4.6)) showed that in the OAF phase, the spins of both the Co and Fe ions have a distribution of cant angles θ_i. It was shown in Section (4.6) that the second order (spin wave) term of the Hamiltonian, H_2, (given by equation (4.6.12)) was a function not only of the spin deviation operators a_i, a_i^* and the spins S_i but also of the cant angles θ_i. Consequently, details of the ground state of the system, obtained

by minimising the zeroth order term H_o (given by equation (4.6.9)), were required as a starting point for the calculations of the magnetic excitation spectra by the program NEWSIM.

At T = 0K, the dynamic structure factor is related to the imaginary part of the magnetic susceptibility by:

$$S(\underline{Q},\omega) = \sum_{\alpha\beta} (\delta_{\alpha\beta} - \hat{Q}^{\alpha}\hat{Q}^{\beta}) S^{\alpha\beta}(\underline{Q},\omega)$$

$$= \mathrm{Im}\left(\sum_{\alpha\beta} (\delta_{\alpha\beta} - \hat{Q}^{\alpha}\hat{Q}^{\beta}) \chi^{\alpha\beta}(\underline{Q},\omega) \right) \qquad (4.7.1)$$

where the indices α,β can take the values x, y and z. (x labels the a-direction and z labels the c-direction in the magnetic unit cell for this case). The susceptibility $\chi^{\alpha\beta}(\underline{Q},\omega)$ is given by

$$\chi^{\alpha\beta}(\underline{Q},\omega) = \sum_{ij} e^{i\underline{Q}.\underline{R}_{ij}} \int_0^{\infty} \chi_{ij}{}^{\alpha\beta}(t) e^{i\omega t}\, dt \qquad (4.7.2)$$

where

$$\chi_{ij}^{\alpha\beta}(t) = g_i{}^{\alpha} g_j{}^{\beta}\, i\langle 0 | [S_i{}^{\alpha}(t),\, S_j{}^{\beta}(0)] | 0\rangle \,. \qquad (4.7.3)$$

In this notation $|0\rangle$ represents the ground state. It was shown in Section (4.6) that for the α-component of the spin at the site labelled by the index i then:

$$S_i{}^{\alpha} = U_i{}^{\alpha z'} (S_i - a_i{}^{*} a_i) + U_i^{\alpha}\, a_i^{+} (U_i^{\alpha}\, a_i)^{*} \qquad (4.7.4)$$

Substituting for the $S_i{}^{\alpha}$ in equation (4.7.3) gives:

$$\chi_{ij}^{\alpha\beta}(t)/(ig_i^{\alpha}g_j^{\beta})$$

$$= \langle 0|[\{U_i^{\alpha}a_i(t) + (U_i^{\alpha})^* a_i^*(t)\}, \{U_j^{\beta}a_j(0) + (U_j^{\beta})^* a_j^*(0)\}]|0\rangle$$

$$+ \text{ higher order terms in } a \text{ and } a^* . \qquad (4.7.5)$$

The higher order terms in equation (4.7.5) are dropped in the linear spin wave approximation. By expansion of the commutators, equation (4.7.5) can be written as:

$$\chi_{ij}^{\alpha\beta}(t)|(ig_i^{\alpha}g_j^{\beta}) = U_i^{\alpha}(U_j^{\beta})^*\langle 0|[a_i(t), a_j^*(0)]]|0\rangle$$

$$+ (U_i^{\alpha}U_j^{\beta})^*\langle 0|[a_i^*(t), a_j^*(0)]|0\rangle$$

$$+ (U_i^{\alpha})^*U_j^{\beta}\langle 0|[a_i^*(t), a_j(0)]|0\rangle$$

$$+ U_i^{\alpha}U_j^{\beta}\langle 0|[a_i(t), a_j(0)]|0\rangle \quad . \qquad (4.7.6)$$

The energy loss part of the spectrum is then given by:

$$\chi_{ij}^{\alpha\beta}(t) = i\, g_i^{\alpha}g_j^{\beta}U_i^{\alpha}(U_j^{\beta})^*\langle 0|[a_i(t), a_j^*(0)]|0\rangle$$

$$+ i\, g_i^{\alpha}g_j^{\beta}(U_i^{\alpha}\, U_j^{\beta})^*\langle 0|[a_i^*(t), a_j^*(0)]|0\rangle \; . \qquad (4.7.7)$$

If two functions $K_{i\underline{q}}^{\beta}(t)$ and $L_{i\underline{q}}^{\beta}(t)$ are given by:

$$K_{i\underline{q}}^{\beta} = \sum_j i\, e^{-i\underline{q}.\underline{r}_j}\, g_j^{\beta}(U_j^{\beta})^*\langle 0|[a_i(t), a_j^*(0)]|0\rangle \qquad (4.7.8)$$

and

$$L_{i\underline{q}}^{\beta} = \sum_j i\, e^{-i\underline{q}.\underline{r}_j}\, g_j^{\beta}(U_j^{\beta})^*\langle 0|[a_i^*(t), a_j^*(0)]|0\rangle \qquad (4.7.9)$$

then $\chi^{\alpha\beta}(\underline{q},t)$ can be written as:

$$\chi^{\alpha\beta}(\underline{q},t) = \sum_i e^{i\underline{q}.\underline{r}_i} g_i{}^{\alpha}[U_i{}^{\alpha} K_{i\underline{q}}{}^{\beta}(t) + (U_i{}^{\alpha})^* L_{i\underline{q}}^{\beta}(t)] . \quad (4.7.10)$$

To calculate the time transform of $\chi^{\alpha\beta}(\underline{q},t)$ an equation-of-motion for $K_{i\underline{q}}{}^{\beta}(t)$ and $L_{i\underline{q}}{}^{\beta}(t)$ has to be used to give $K_{i\underline{q}}^{\beta}(t)$ and $L_{i\underline{q}}^{\beta}(t)$ at successive time steps. To calculate the equations of motion the commutators $[a_i,H]$ and $[a_i{}^*,H]$ need to be known. With H given by H_2 defined in equation (4.6.12) then:

$$[a_i,H] = A_i a_i + 2C_i a_i{}^* + \sum_j 2Z_{ij} a_j{}^* + (X_{ij} + Y_{ij})a_j \quad (4.7.11)$$

and

$$[a_i{}^*,H] = -A_i a_i{}^* - 2B_i a_i - \sum_j 2W_{ij} a_j + (X_{ij} + Y_{ij})a_j{}^* . \quad (4.7.12)$$

The equation-of-motion for a Heisenberg operator $\hat{A}(t)$ is given by (Rae (1981)):

$$\frac{d\hat{A}(t)}{dt} = -\frac{i}{h} \langle O|[\hat{A}_i(t), \hat{H}]|O\rangle \quad (4.7.13)$$

The equations of motion for $K_{i\underline{q}}^{\beta}(t)$ and $L_{i\underline{q}}^{\beta}(t)$ can then be shown to be:

$$i \frac{dK_{i\underline{q}}^{\beta}(t)}{dt} = A_i K_{i\underline{q}}\beta(t) + 2B_i{}^* L_{i\underline{q}}\beta(t) + 2 \sum_j (W_{ij}{}^* L_{i\underline{q}}{}^{\beta}(t) + X_{ij} K_{j\underline{q}}^{\beta}(t)) \quad (4.7.14)$$

and

$$i \frac{dL_{i\underline{q}}^{\beta}(t)}{dt} = -A_i L_{i\underline{q}}{}^{\beta}(t) - 2B_i K_{i\underline{q}}{}^{\beta}(t) - 2 \sum_j (W_{ij} K_{j\underline{q}}{}^{\beta}(t) + X_{ij} L_{i\underline{q}}^{\beta}(t)) . \quad (4.7.15)$$

If equations (4.7.14) and (4.7.15) are converted to difference equations, then the following results are obtained:

$$K_{i\underline{q}}^{\beta}(t+\Delta t) = K_{i\underline{q}}^{\beta}(t-\Delta t) + (-2i\Delta t)\{A_i K_{i\underline{q}}^{\beta}(t) + 2B_i^{*} L_{i\underline{q}}^{\beta}(t) + 2 \sum_{ij} (W_{ij}^{*} L_{j\underline{q}}^{\beta}(t) + X_{ij}^{*} K_{i\underline{q}}^{\beta}(t))\} \qquad (4.7.16)$$

and

$$L_{i\underline{q}}^{\beta}(t+\Delta t) = L_{i\underline{q}}^{\beta}(t-\Delta t) - (-2i\Delta t) \times \{A_i L_{i\underline{q}}^{\beta}(t) + 2B_i K_{i\underline{q}}^{\beta}(t) + 2 \sum_{j}(W_{ij} K_{j\underline{q}}^{\beta}(t) + X_{ij} L_{j\underline{q}}^{\beta}(t))\} \quad . \qquad (4.7.17)$$

To be able to start the iterative process in which $K_{i\underline{q}}^{\beta}(t)$ and $L_{i\underline{q}}^{\beta}(t)$ are calculated at successive time steps then the values of these functions at times $t = 0$ and $t = \Delta t$ have to be known. At $t = 0$ the functions are given by:

$$K_{i\underline{q}}^{\beta}(t=0) = i\, e^{-i\underline{q}.\underline{r}_i}\, g_i^{\beta}(u_i^{\beta})^{*} \qquad (4.7.18)$$

and

$$L_{i\underline{q}}^{\beta}(t=0) = 0 \quad . \qquad (4.7.19)$$

The values of $K_{i\underline{q}}^{\beta}(t=\Delta t)$ and $L_{i\underline{q}}^{\beta}(t=\Delta t)$ must be obtained approximately by a Taylor expansion:

$$K_{i\underline{q}}^{\beta}(t=\Delta t) = \sum_{n} \frac{(\Delta t)^n}{n!} \frac{d^n}{dt^n} (K_{i\underline{q}}^{\beta}(t))\Big|_{t=0} \qquad (4.7.20)$$

and

$$L_{i\underline{q}}^{\beta}(t=\Delta t) = \sum_{n} \frac{(\Delta t)^n}{n!} \frac{d^n}{dt^n} (L_{i\underline{q}}^{\beta}(t)) \Big|_{t=0} . \qquad (4.7.21)$$

The derivatives with respect to time in equations (4.7.20) and (4.7.21) were obtained by iteration from the values of $K_{i\underline{q}}^{\beta}(t=0)$ and $L_{i\underline{q}}^{\beta}(t=0)$ respectively. The number of derivatives in the Taylor series expansion used to calculate $K_{i\underline{q}}^{\beta}(t=\Delta t)$ and $L_{i\underline{q}}^{\beta}(t=\Delta t)$ was 4 for the results presented in this section.

The computer program NEWSIM calculated the $K_{i\underline{q}}^{\beta}(t)$, $L_{i\underline{q}}^{\beta}(t)$ and hence $\chi^{\alpha\beta}(\underline{q},t)$ at successive time steps Δt, for t in the range $0 < t < t_{max}$ (where t_{max} is determined by the highest energy resolution required.) After the $\chi^{\alpha\beta}(\underline{q},t)$ were calculated, a program SQWCAL was used to perform the time Fourier transform which gave $\chi^{\alpha\beta}(\underline{q},\omega)$ and hence $S^{\alpha\beta}(\underline{q},\omega)$. (A damping factor $e^{-\lambda t^2}$ was included in the integrand before the Fourier transform with respect to time was performed, so that the energy resolution for the calculated spectra could be chosen according to requirements.) All the results presented in this section were calculated for an $L \times L$ lattice with $L = 60$.

Calculated $S^{\alpha\beta}(\underline{Q},\omega)$ spectra with $\underline{Q}$ at the Brillouin zone centre are shown in Figure (4.7.1) for the concentration values $x = 0.9$ and $x = 0.8$. Both values of x correspond to the uni-axial antiferromagnetic phase in which the ordered spin component is along the z-direction. As a result, there is no intensity in the calculated $S^{zz}(\underline{Q},\omega)$ spectra and also $S^{xx}(\underline{Q},\omega) = S^{yy}(\underline{Q},\omega)$, so that only the $S^{xx}(\underline{Q},\omega)$ spectra are shown in the figure. In

K_2CoF_4, at $\underline{Q} = (1,0,0)$ there was a single resolution limited peak in the $S^{xx}(\underline{Q},\omega)$ spectrum at $E \sim 26$ meV; Figure (4.7.1) shows that the effect of bringing Fe^{2+} "defects" into the system was to introduce a peak in the $S^{xx}(\underline{Q},\omega)$ spectrum corresponding to excitations propagating mainly on the Fe^{2+} ions and to produce a distribution of intensity corresponding to excitations propagating mainly on the Co^{2+} ions. The effect of decreasing x was to reduce the peak energy for the lower energy excitations and to introduce more broadening in the intensity corresponding to the higher energy excitations. Also, the intensity of the lower energy peak increased relative to the intensity at higher energies. Figure (4.7.2) shows $S^{xx}(\underline{Q},\omega)$, $S^{yy}(\underline{Q},\omega)$ and $S^{zz}(\underline{Q},\omega)$ spectra at $\underline{Q} = (1,0,0)$ for the concentration range $0.1 < x < 0.5$. For $x = 0.5$, which corresponds approximately to the phase boundary between the uniaxial and OAF phases, there appeared to be 5 peaks merged together at higher energies. The energies of these peaks correspond to the energy required to change the Co spin value by 1 unit in the 5 possible nearest neighbour environments. (The 5 possible nearest neighbour environments correspond to 0, 1, 2, 3 and 4 Fe nearest neighbours.) Similar "cluster modes" have been observed in other mixed and diluted systems (Cowley (1980)). As x decreases from 0.5 to 0.1, the average cant angle $\bar{\theta}_c$ increases from 0° to 90°, $S^{zz}(\underline{Q},\omega)$ increases in intensity and $S^{xx}(\underline{Q},\omega)$ decreases in intensity, which is what one would intuitively expect since the ordered z-component of spin decreases and the ordered x-component increases. (Note that the spin is confined to the x-z plane corresponding to one of two possible domains, which are equivalent

FIGURE (4.7.1): Calculated $S^{xx}(\underline{Q},\omega)$ spectra at $Q = (1,0,0)$ for $K_2Co_xFe_{1-x}F_4$ with

(a) $x = 0.9$

(b) $x = 0.8$.

Both of these values of x correspond to the Uniaxial antiferromagnetic phase.

As with all spectra presented in this section the chosen energy resolution was 1 meV F.W.H.M. (Any excess broadening of the spectra is due to the disorder.)

Fig (4.7.1(a))

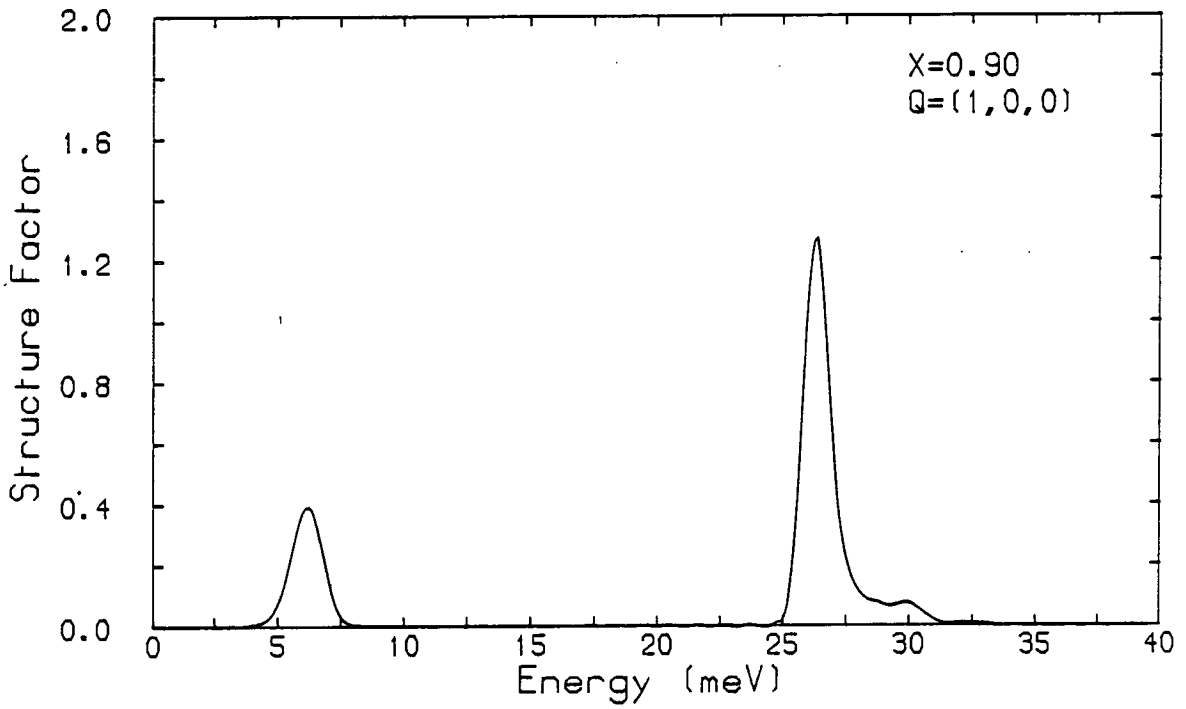

Fig (4.7.1(b))

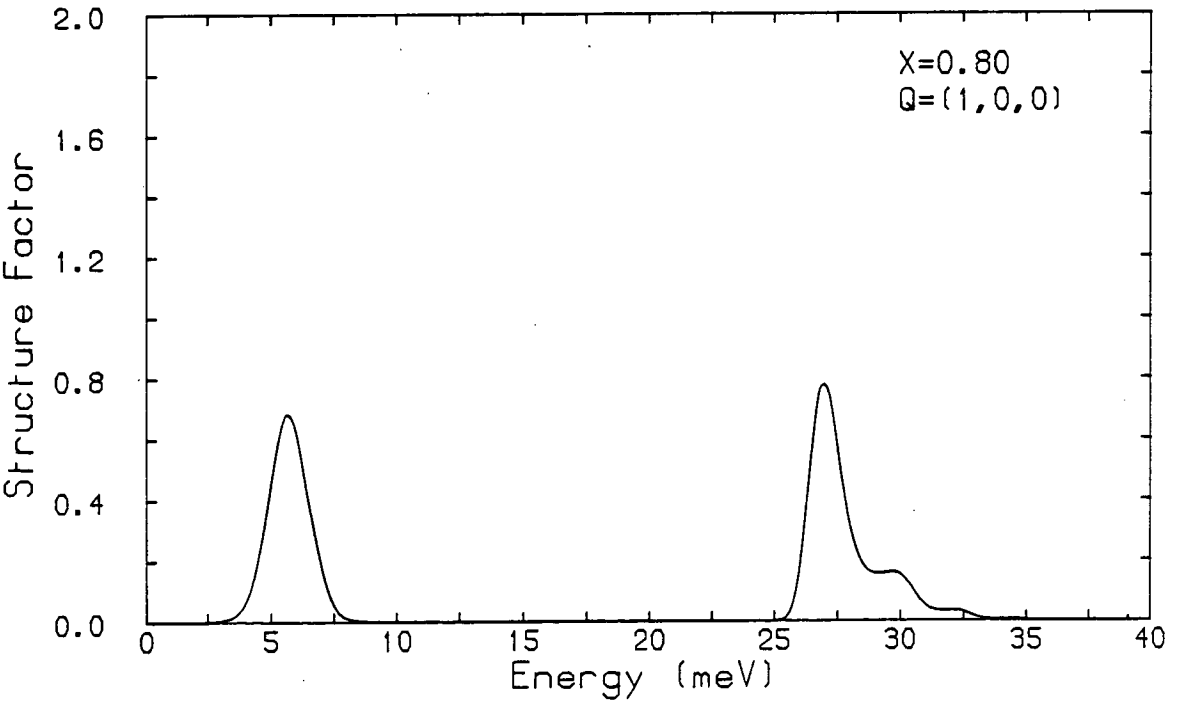

FIGURE (4.7.2): Calculated $S^{\alpha\alpha}(\underline{Q},\omega)$ spectra at Q = (1,0,0) for $K_2Co_xFe_{1-x}F_4$ with

(a) x = 0.5

(b) x = 0.45

(c) x = 0.4

(d) x = 0.35

(e) x = 0.325

(f) x = 0.2

(g) x = 0.15

(h) x = 0.1 .

These values of x span the OAF phase at T = OK. The solid lines indicate $S^{xx}(\underline{Q},\omega)$ spectra. The dashed (larger mark to space ratio) lines indicate $S^{yy}(\underline{Q},\omega)$ spectra and the dotted line (smaller mark to space ratio) lines indicate $S^{zz}(\underline{Q},\omega)$ spectra.

Fig (4.7.2(a))

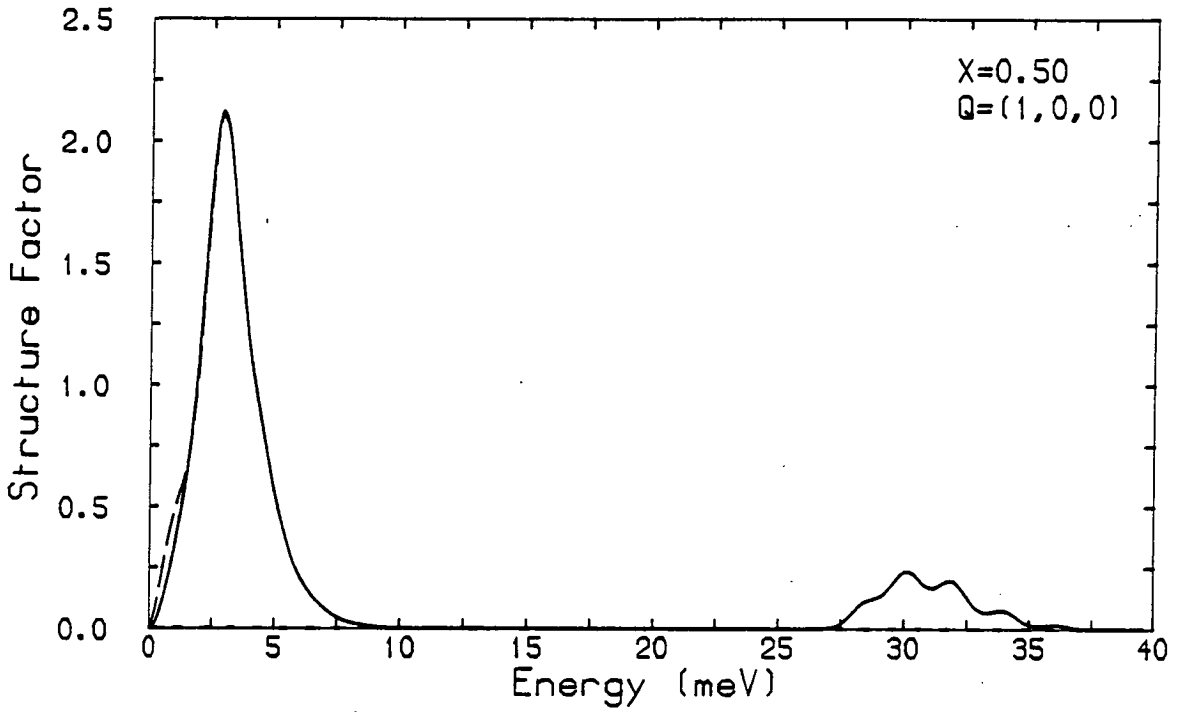

Fig (4.7.2(b))

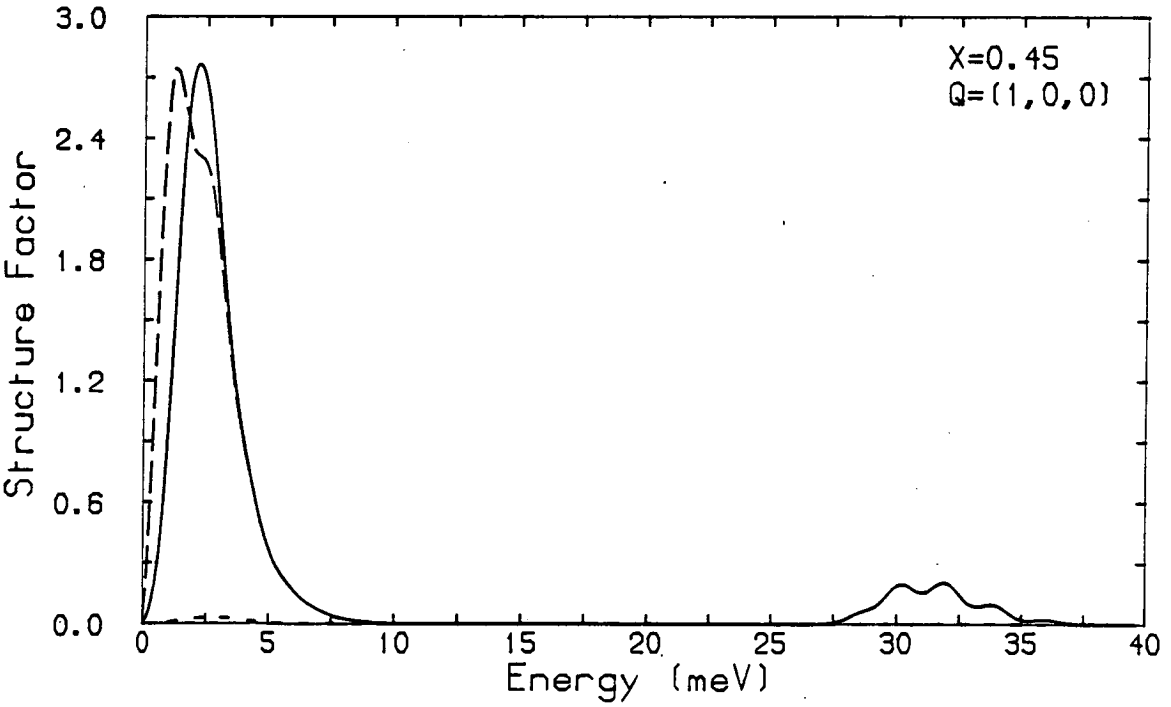

Fig (4.7.2(c))

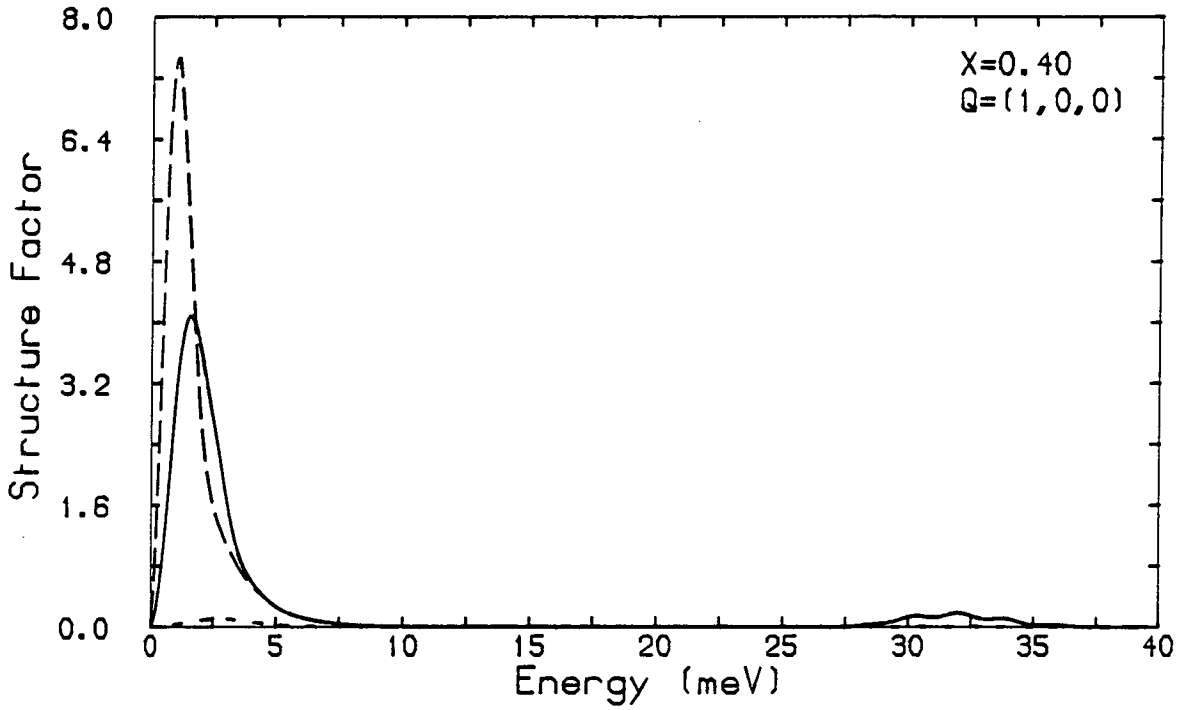

Fig (4.7.2(d))

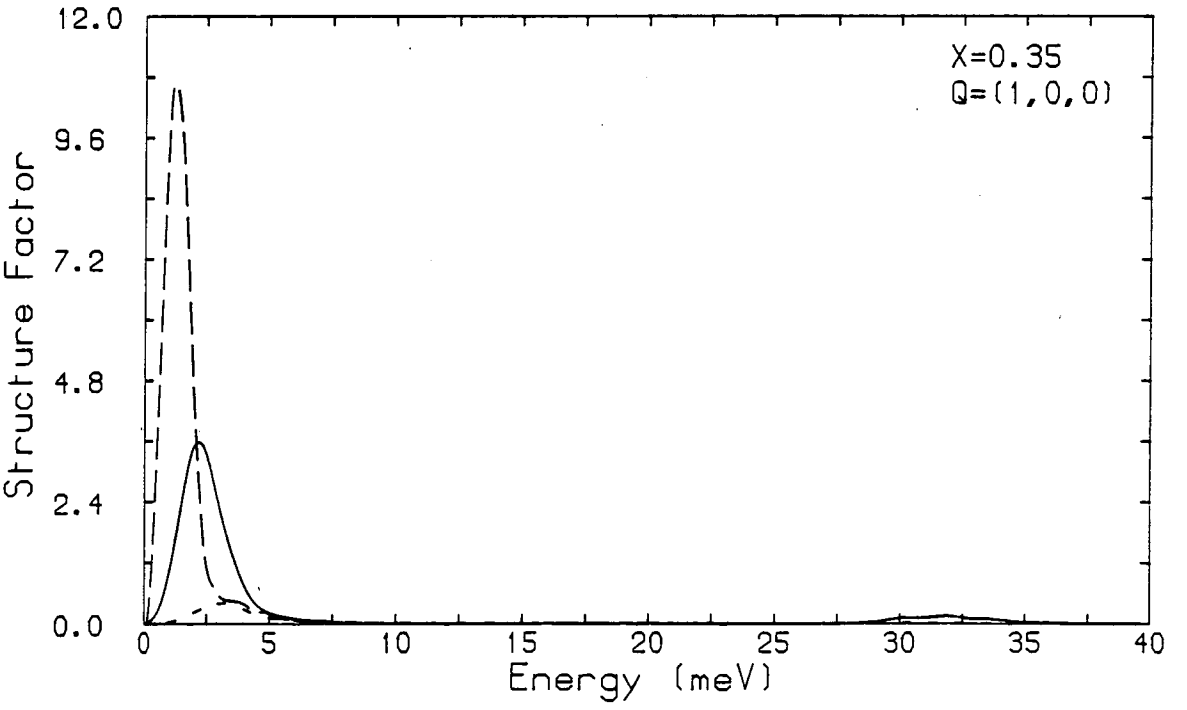

Fig (4.7.2(e))

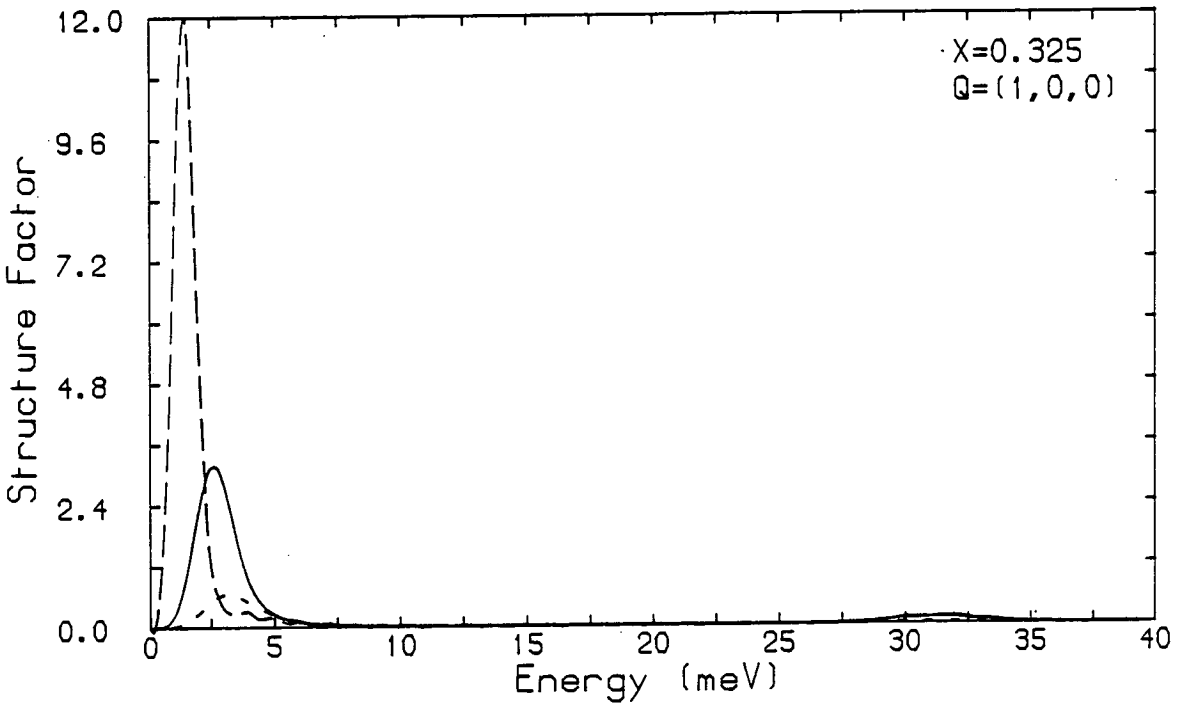

Fig (4.7.2(f))

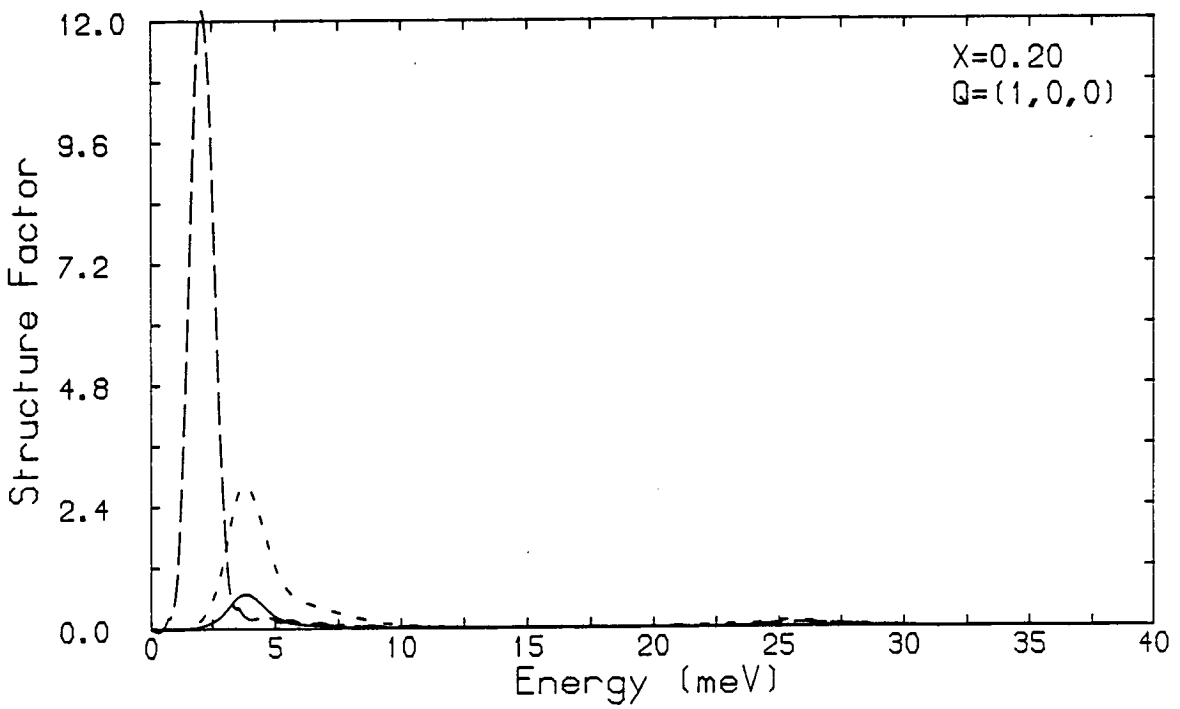

Fig (4.7.2(g))

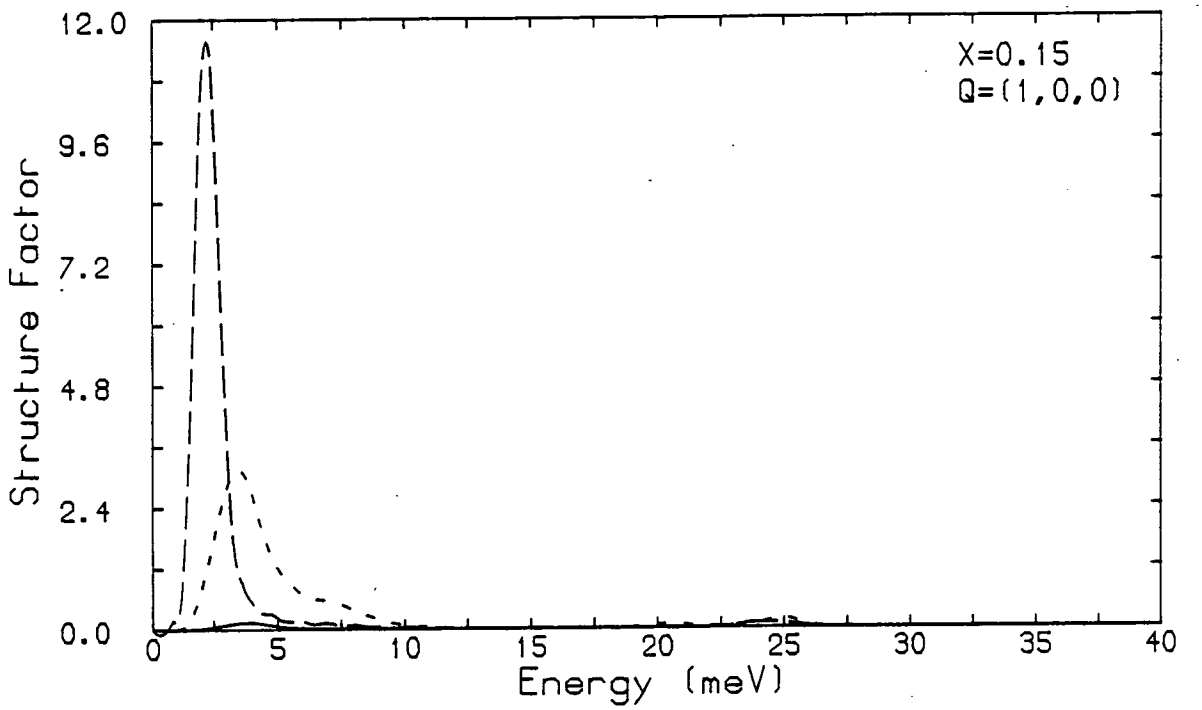

Fig (4.7.2(h))

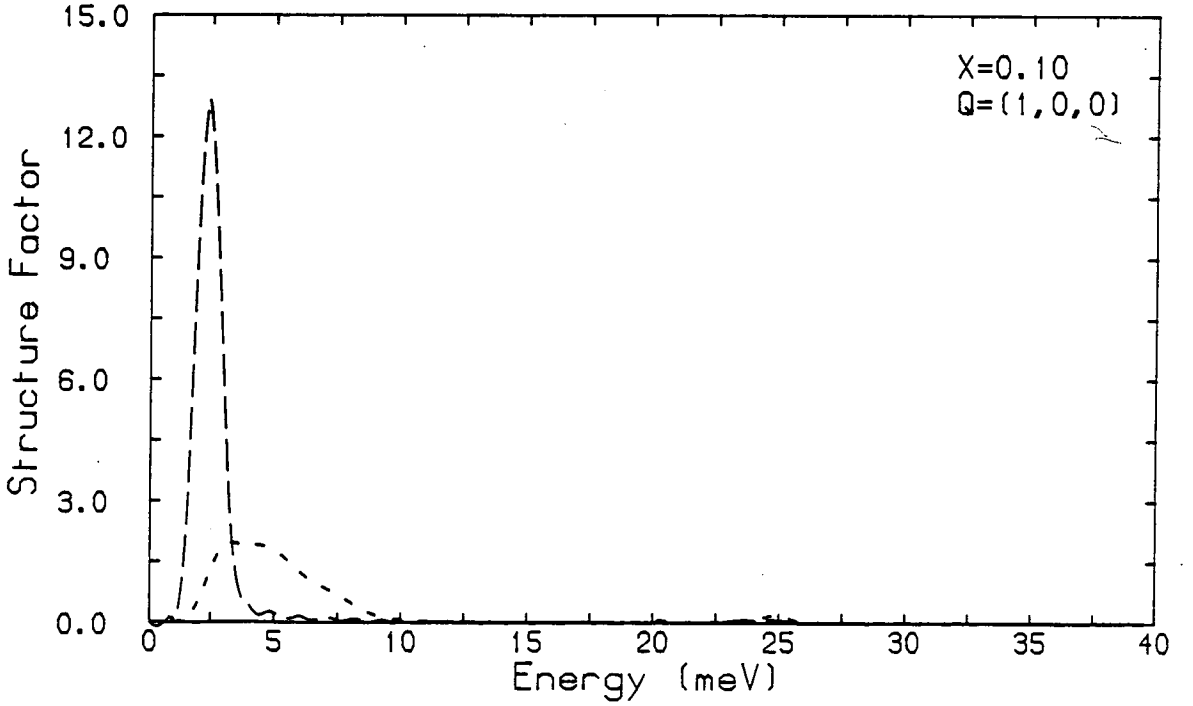

FIGURE (4.7.3): Calculated $S^{yy}(\underline{Q},\omega)$ and $S^{zz}(\underline{Q},\omega)$ spectra at Q = (1,0,0) for $K_2Co_xFe_{1-x}F_4$ with x = 0.05. This value of x corresponds to the planar antiferromagnetic phase.

Fig (4.7.3)

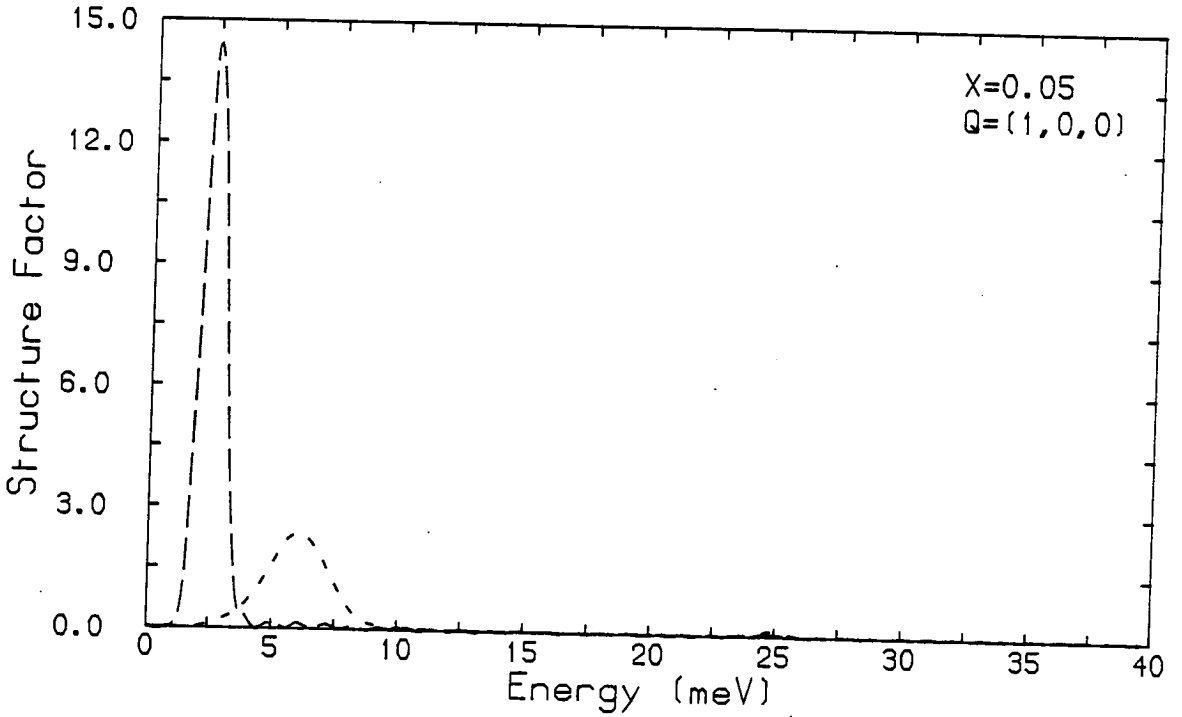
15.0
12.0
9.0
6.0
3.0
0.0
Structure Factor
0
5
10
15
20
25
30
35
40
Energy (meV)
X=0.05
Q=(1,0,0)

FIGURE (4.7.4)(a): The concentration dependence of the Brillouin zone centre ($\underline{Q}$ = (1,0,0)) energy gap for the lower energy band of excitations in $K_2Co_xFe_{1-x}F_4$. The values were obtained from the peak positions in the $S^{\alpha\alpha}(\underline{Q},\omega)$ spectra.

(b): The concentration dependence of the integrated $S^{\alpha\alpha}(\underline{Q},\omega)$ structure factors.

In both (a) and (b) the circles correspond to $\alpha = x$, the crosses correspond to $\alpha = y$ and the triangles correspond to $\alpha = z$.

Fig (4.7.4(a))

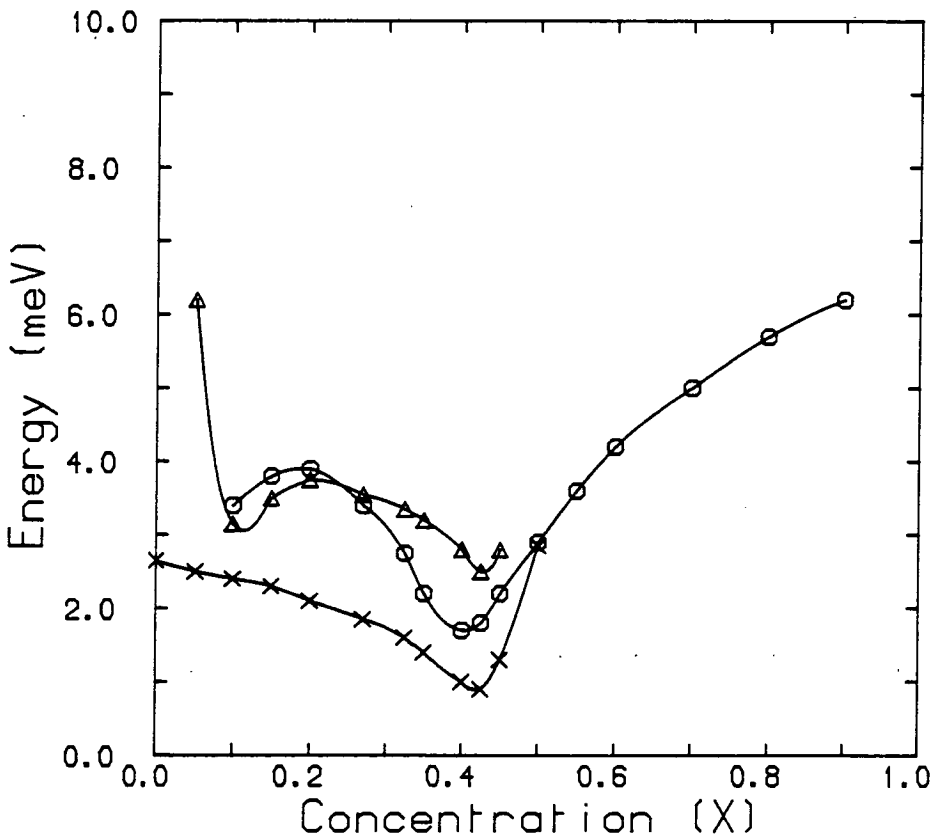

Fig (4.7.4(b))

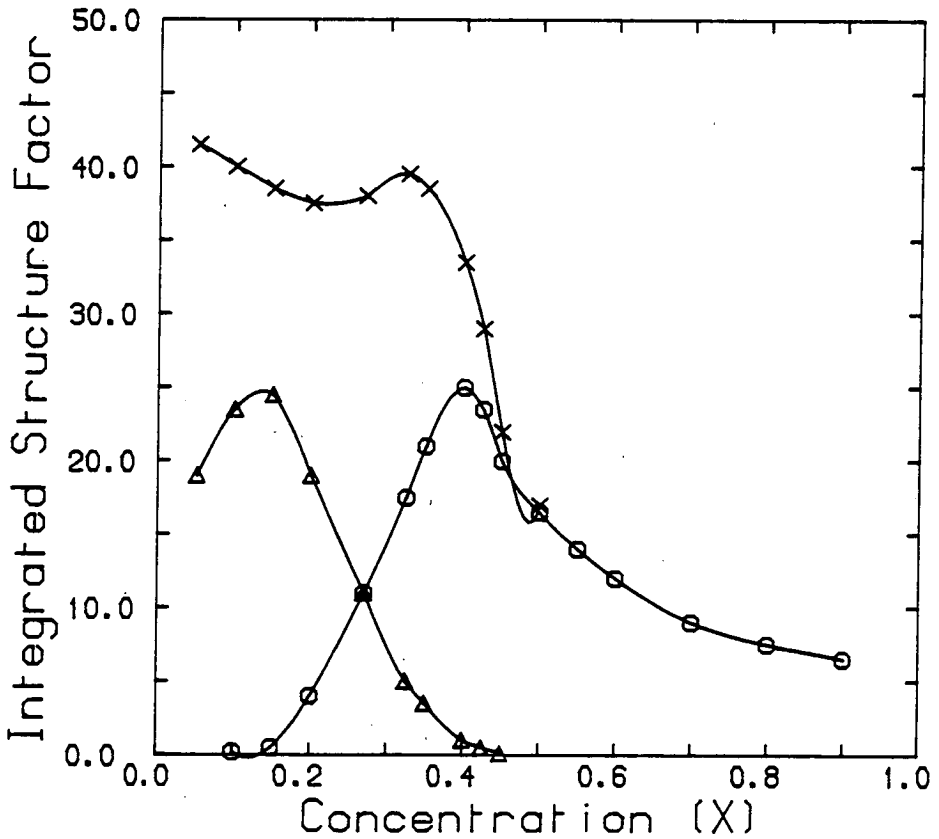
Integrated Structure Factor
50.0
40.0
30.0
20.0
10.0
0.0
0.0
0.2
0.4
0.6
0.8
1.0
Concentration (X)

FIGURE (4.7.5): Calculated $S^{xx}(\underline{Q},\omega)$ spectra for the concentration x = 0.6 at

(a) The Brillouin zone centre (Q = (1,0,0))

(b) The Brillouin zone boundary (Q = (1.5,0,0)).

x = 0.6 corresponds to the nominal concentration of the sample used for some of the experimental measurements described in Section (4.4).

Fig (4.7.5(a))

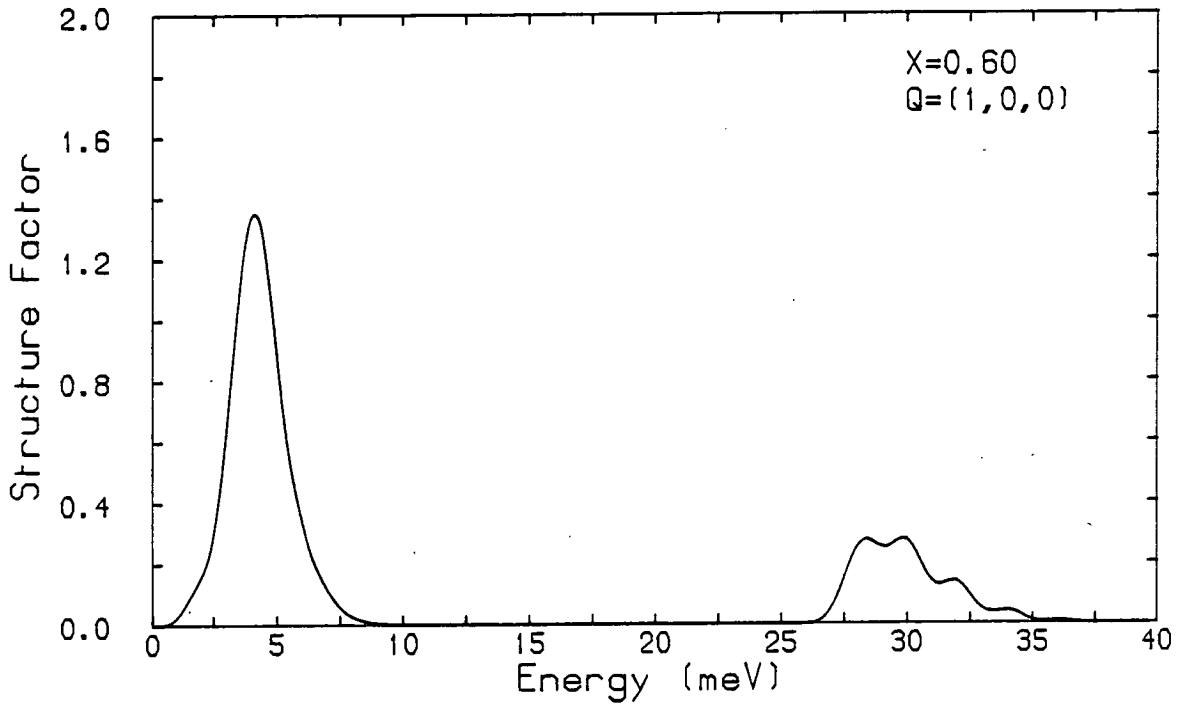

Fig (4.7.5(b))

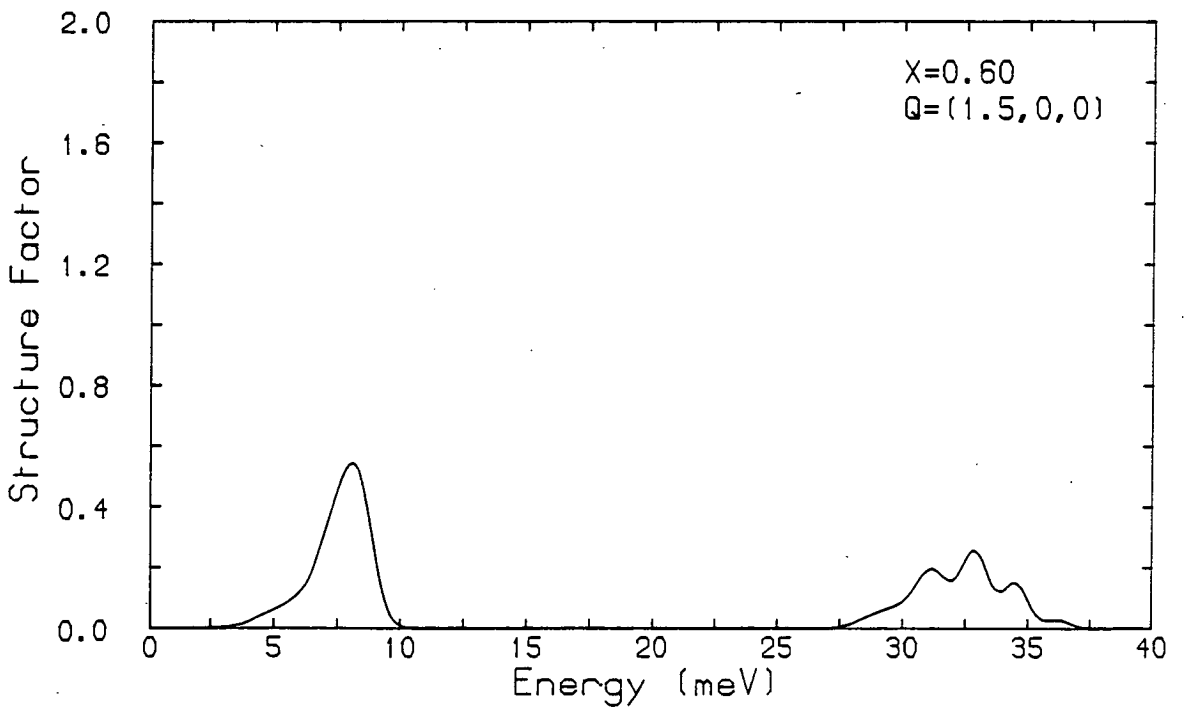

FIGURE (4.7.6): Calculated $S^{\alpha\alpha}(\underline{Q},\omega)$ spectra for the concentration x = 0.27 at

(a) The Brillouin zone centre (Q = (1,0,0))

(b) The Brillouin zone blundary

$\underline{Q}$ = (1.5,0,0)).

The full lines correspond to α = x, the dashed lines to α = y and the dotted lines to α = z.

x = 0.27 corresponds to the nominal concentration of the sample used for the experimental measurements described in Section (4.5).

Fig (4.7.6(a))

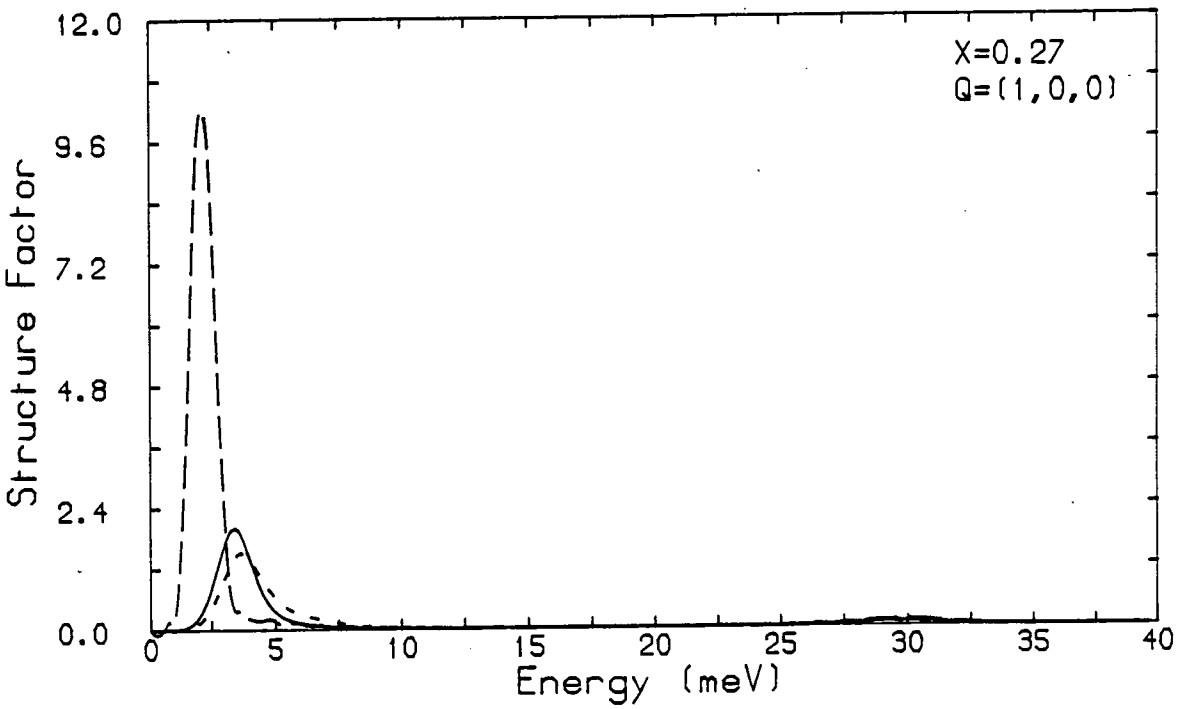

Fig (4.7.6(b))

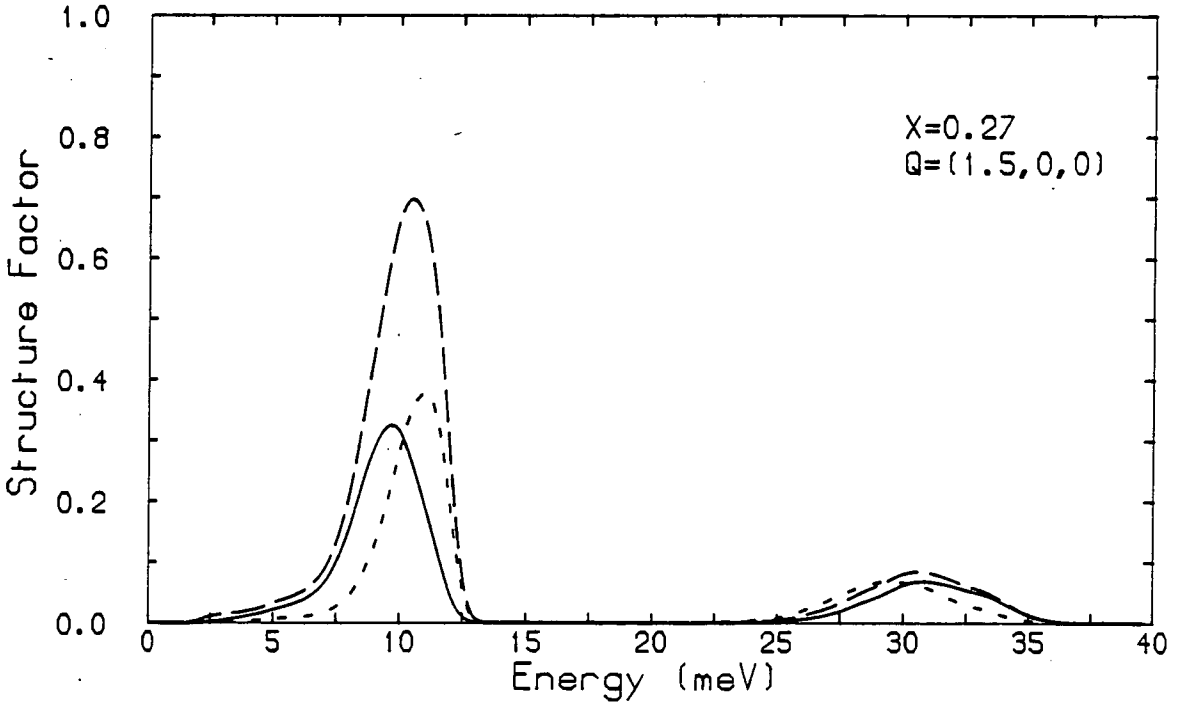

FIGURE (4.7.7): Experimental data obtained from the measurements described in Section (4.4) for a scan through the lower energy branch of magnetic excitations with Q = (1.4,0,0) in the nominally x = 0.6 sample.
The solid line indicates the calculated intensity fitted to the data, as described in the text.

Fig (4.7.7)

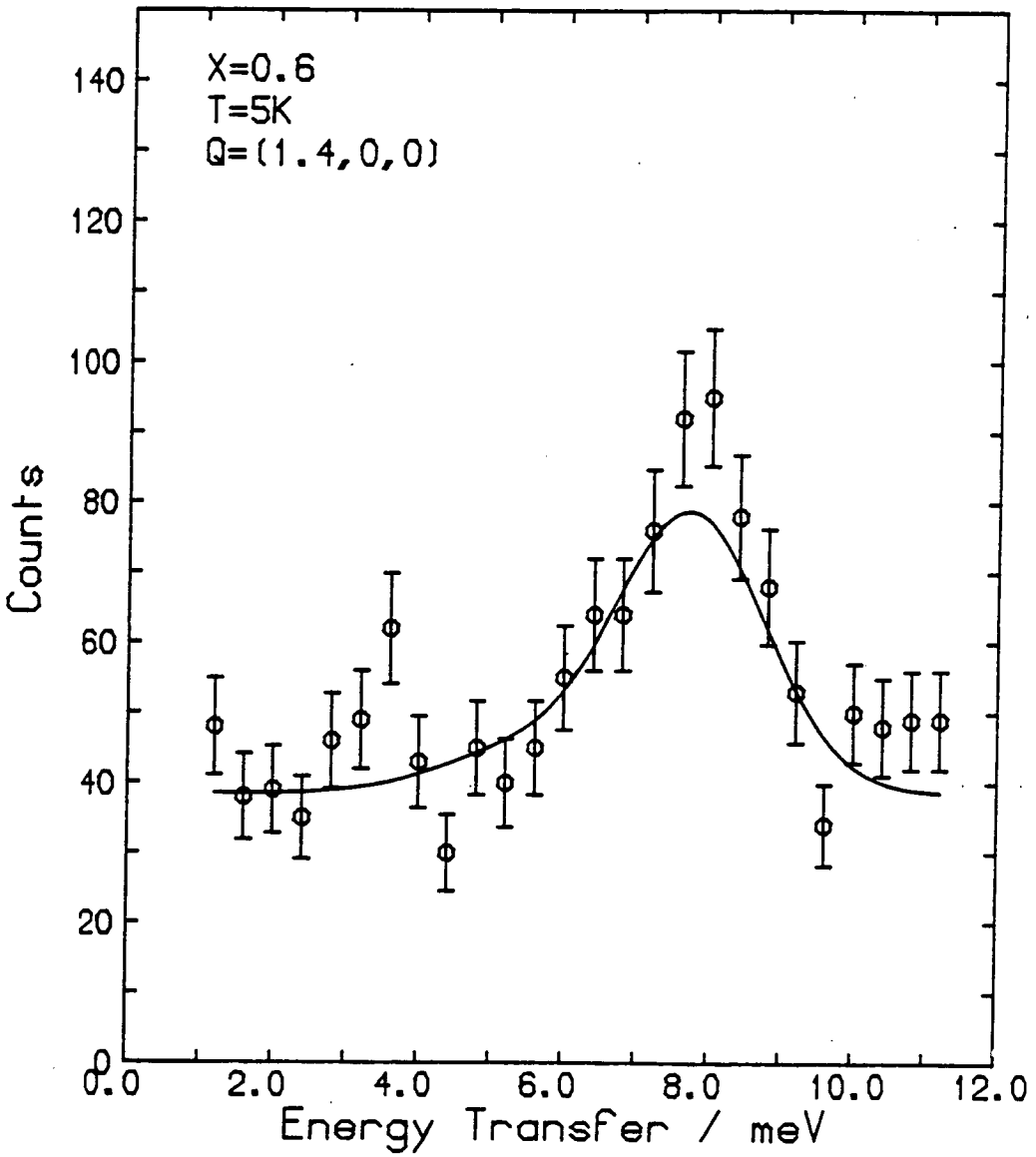
X=0.6
T=5K
Q=(1.4,0,0)
Counts
Energy Transfer / meV
0
20
40
60
80
100
120
140
0.0
2.0
4.0
6.0
8.0
10.0
12.0

FIGURE (4.7.8): Experimental data obtained from the measurements described in Section (4.4) for a scan through the higher energy branch of magnetic excitations with Q = (3.2,0,0) in the nominally x = 0.6 sample.
The solid line indicates the calculated intensity fitted to the data, as described in the text.

Fig (4.7.8)

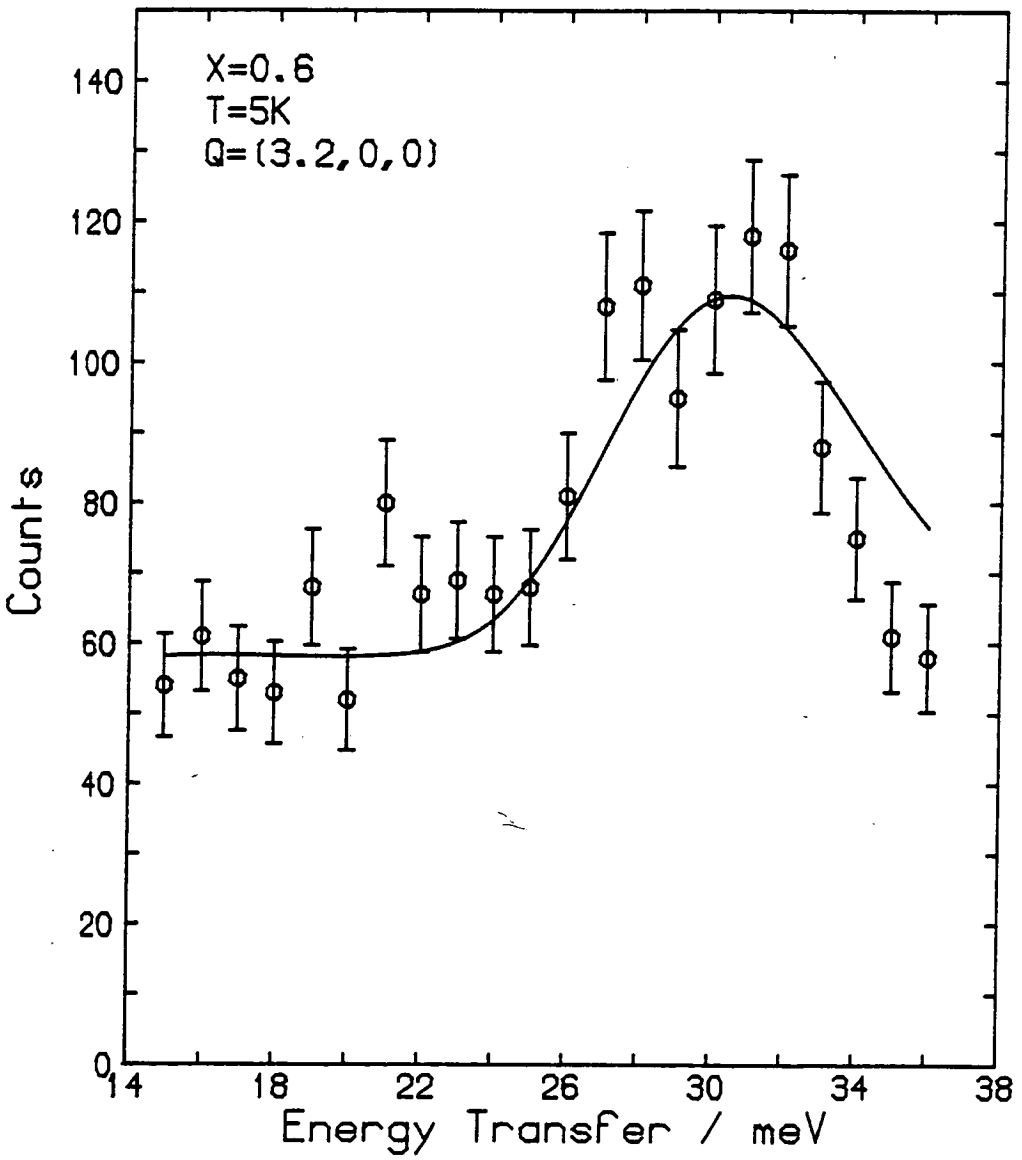
X=0.6
T=5K
Q=(3.2,0,0)
Counts
Energy Transfer / meV
0
20
40
60
80
100
120
140
14
18
22
26
30
34
38

FIGURE (4.7.9): Experimental data obtained from measurements described in Section (4.5) for a scan with Q = (1.2, 0, -0.4) in the nominally x = 0.27 sample. This scan was performed on the IN8 triple-axis neutron spectrometer with fixed $k_f = 2.662 \text{Å}^{-1}$. The solid line indicates the calculated intensity fitted to the data, as described in the text.

Fig (4.7.9)

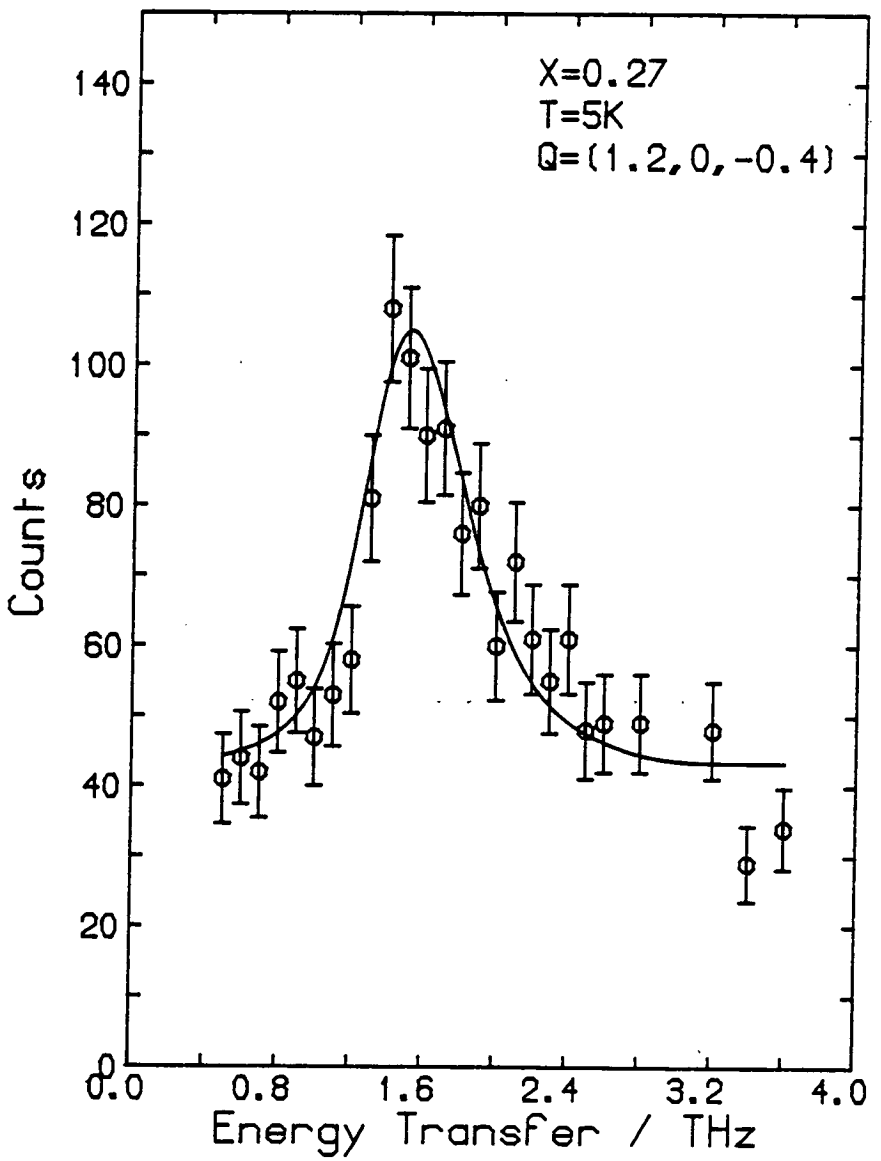
X=0.27
T=5K
Q=(1.2,0,-0.4)
Counts
Energy Transfer / THz
0
20
40
60
80
100
120
140
0.0
0.8
1.6
2.4
3.2
4.0

FIGURE (4.7.10): Experimental data obtained from the measurements described in Section (4.4) for a scan with Q = (1.2, 0, 0) in the nominally x = 0.2 sample. The solid line indicates the calculated intensity fitted to the data, as described in the text.

Fig (4.7.10)

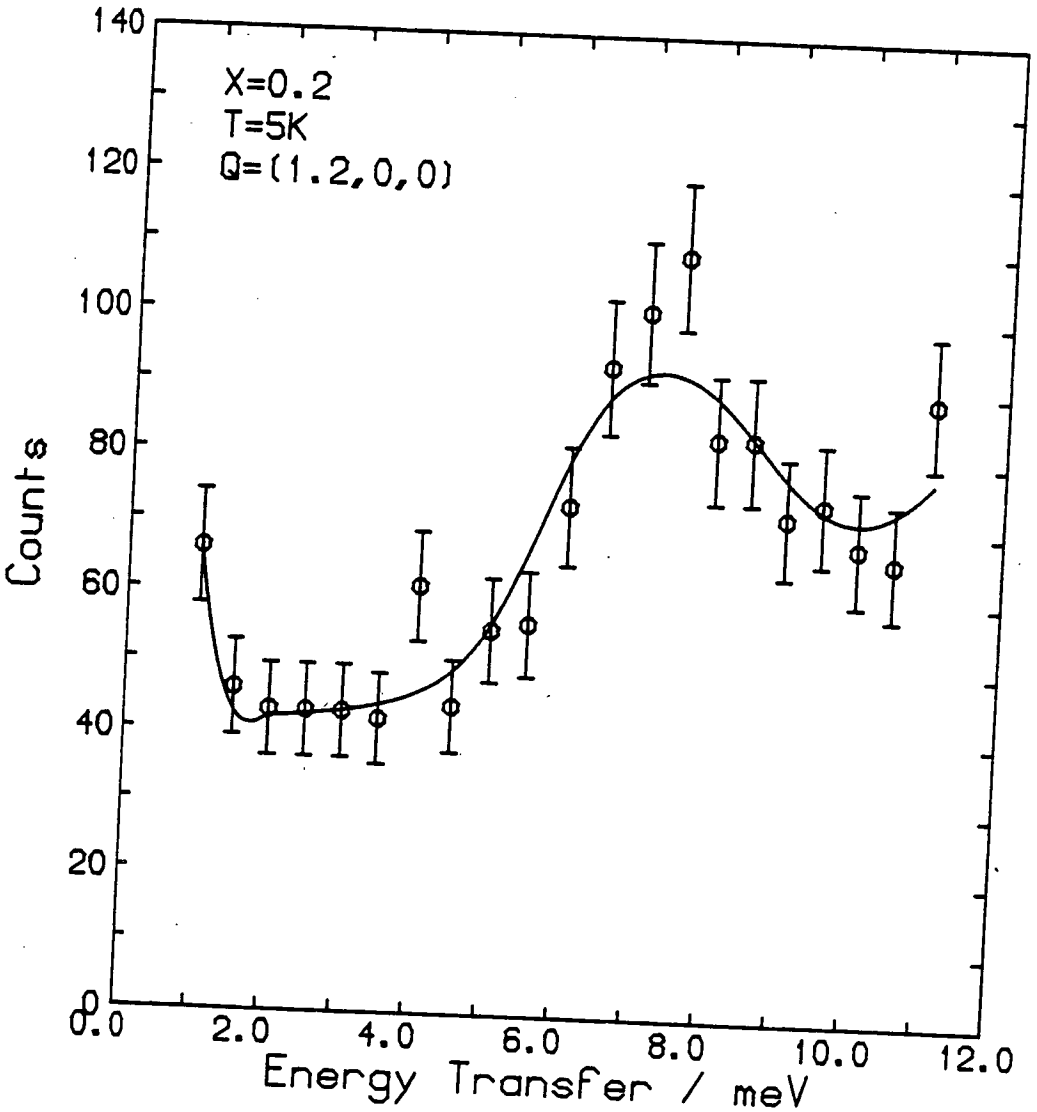
X=0.2
T=5K
Q=(1.2,0,0)
Counts
Energy Transfer / meV
0
20
40
60
80
100
120
140
0.0
2.0
4.0
6.0
8.0
10.0
12.0

FIGURE (4.7.11): Comparison between peak positions in the calculated $S^{xx}(\underline{Q},\omega)$ spectra, calculated with an energy resolution corresponding to the experimental energy resolution, and the experimental data points for the dispersion relations in $K_2Co_xFe_{1-x}F_4$ with x = 0.6 for

(a) The higher energy branch of magnetic excitations, and

(b) The lower energy branch of magnetic excitations.

Fig (4.7.11(a))

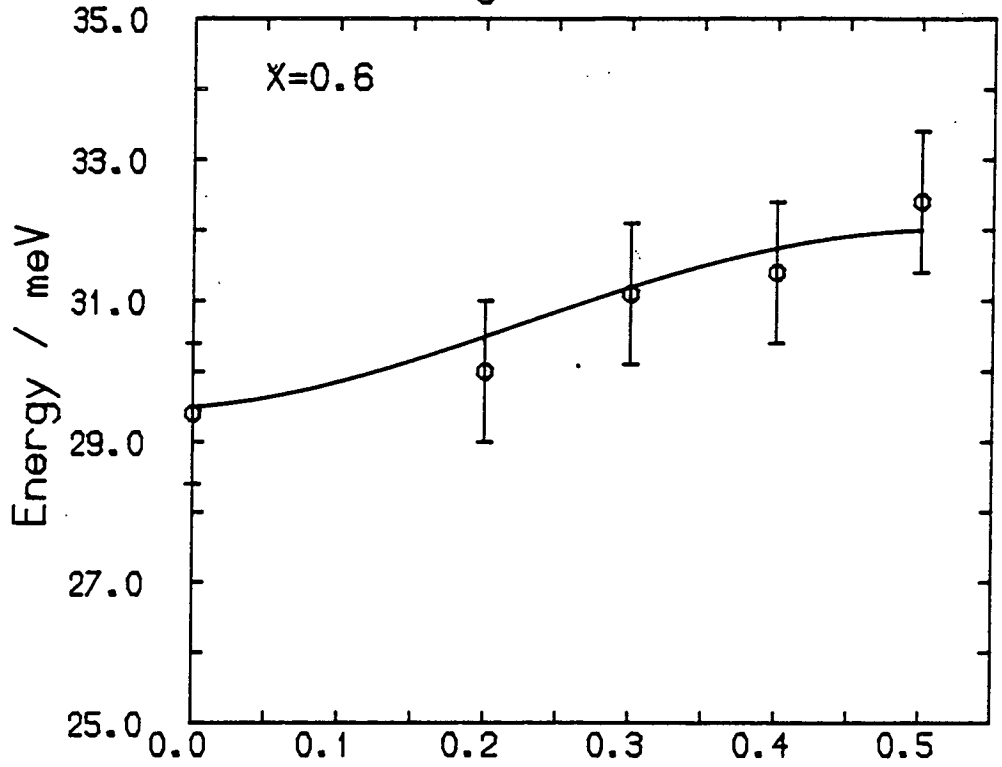

Fig (4.7.11(b))

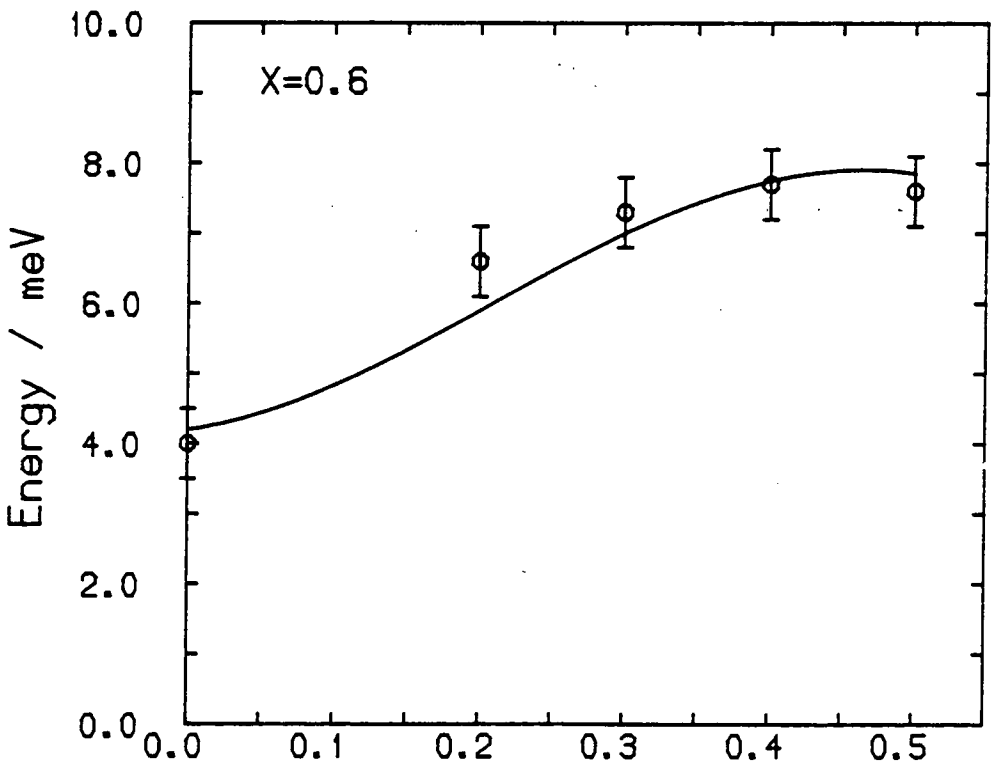

ξ

by symmetry.) Figure (4.7.3) shows the $S^{yy}(Q,\omega)$ and $S^{zz}(Q,\omega)$ spectra at $x = 0.05$, a concentration which corresponds to the planar antiferromagnetic phase. $S^{xx}(Q,\omega)$ is zero in that phase because the ordered component of spin is along the x-direction.

Figure (4.7.4) summarises the concentration dependence of the zone centre energy and the integrated structure factor for the lower energy excitations. There are local minima in the zone centre energies between $x = 0.4$ and $x = 0.5$ for all three of the structure factors shown. There is also a local minimum for the zone centre energy associated with $S^{zz}(Q,\omega)$ just above $x = 0.1$. It is worth comparing these results with the results of Matsubara (1980) who performed mean-field calculations for $K_2Fe_xMn_{1-x}F_4$, which is also a mixed magnetic system with orthogonal competing anisotropies (Bevaart et al. (1978)). The mean field calculations predicted that the gap corresponding to the lowest energy mode should go to zero at the phase boundaries between the OAF and the other antiferromagnetic phrases. $K_2Fe_xMn_{1-x}F_4$ differs from $K_2Co_xFe_{1-x}F_4$ in that the exchange interactions are isotropic in the former system and anisotropic in the latter system; the difference from mean field theory predictions at $x \simeq 0.1$ in $K_2Co_xFe_{1-x}F_4$ might be connected with this. The energy of the peak in $S^{yy}(Q,\omega)$ at the zone centre is sensitive to the value of the in-plane single-ion anisotropy parameter E_i. Consequently the fact that the energy gap for $S^{yy}(Q,\omega)$ does not go to zero at $x \simeq 0.5$ could be due to the value of E_i used in the calculations being slightly wrong. More calculations with a modified in-plane anisotropy might clarify this.

Spectra were also generated for the concentrations $x = 0.6$, $x = 0.27$ and $x = 0.2$, the nominal concentration values of the samples on which the experiments discussed in Sections (4.3), (4.4) and (4.5) were performed. The calculated zone centre and zone boundary spectra are shown for $x = 0.6$ in Figure (4.7.5), and for $x = 0.27$ in Figure (4.7.6). As discussed previously, $x = 0.6$ corresponds to the uniaxial phase, so that $S^{zz}(\underline{Q},\omega)$ is zero and $S^{xx}(\underline{Q},\omega) = S^{yy}(\underline{Q},\omega)$. The concentration $x = 0.27$ corresponds to the OAF phase so that $S^{xx}(Q,\omega)$, $S^{yy}(\underline{Q},\omega)$ and $S^{zz}(\underline{Q},\omega)$ are different.

The partial dynamic structure factors were summed to give the dynamic structure factor for the concentrations $x = 0.6$, $x = 0.27$ and $x = 0.2$ and fits made to the experimental data for $\underline{Q}$-values across the entire Brillouin zone. The fits took into account the two domain structure and used calculated instrumental resolution widths. The free parameters in the fits were a flat background term and an overall scale factor. Figures (4.7.7), (4.7.8), (4.7.9) and (4.7.10) show experimental data with calculated spectra fitted.

In Figures (4.7.11), (4.7.12) and (4.7.13) the measured dispersion relations for $x = 0.6$, $x = 0.2$ and $x = 0.27$ are shown with the peak positions from the calculated $S^{xx}(\underline{Q},\omega)$ $S^{yy}(\underline{Q},\omega)$ and $S^{zz}(\underline{Q},\omega)$ spectra superimposed. For $x = 0.6$ the peak positions from the calculated $S^{xx}(\underline{Q},\omega)$ spectra are in good agreement with the experimental values for both the low energy and high energy excitations. For $x = 0.2$ and $x = 0.27$ only the low energy dispersion relations corresponding to excitations

FIGURE (4.7.12): Comparison between peak positions in the calculated $S^{\alpha\alpha}(\underline{Q},\omega)$ spectra and the experimental data points for the dispersion relation in $K_2Co_xFe_{1-x}F_4$ with nominally $x = 0.2$.

The solid line corresponds to $\alpha = x$, the dashed line corresponds to $\alpha = y$ and the dotted line corresponds to $\alpha = z$.

Fig (4.7.12)

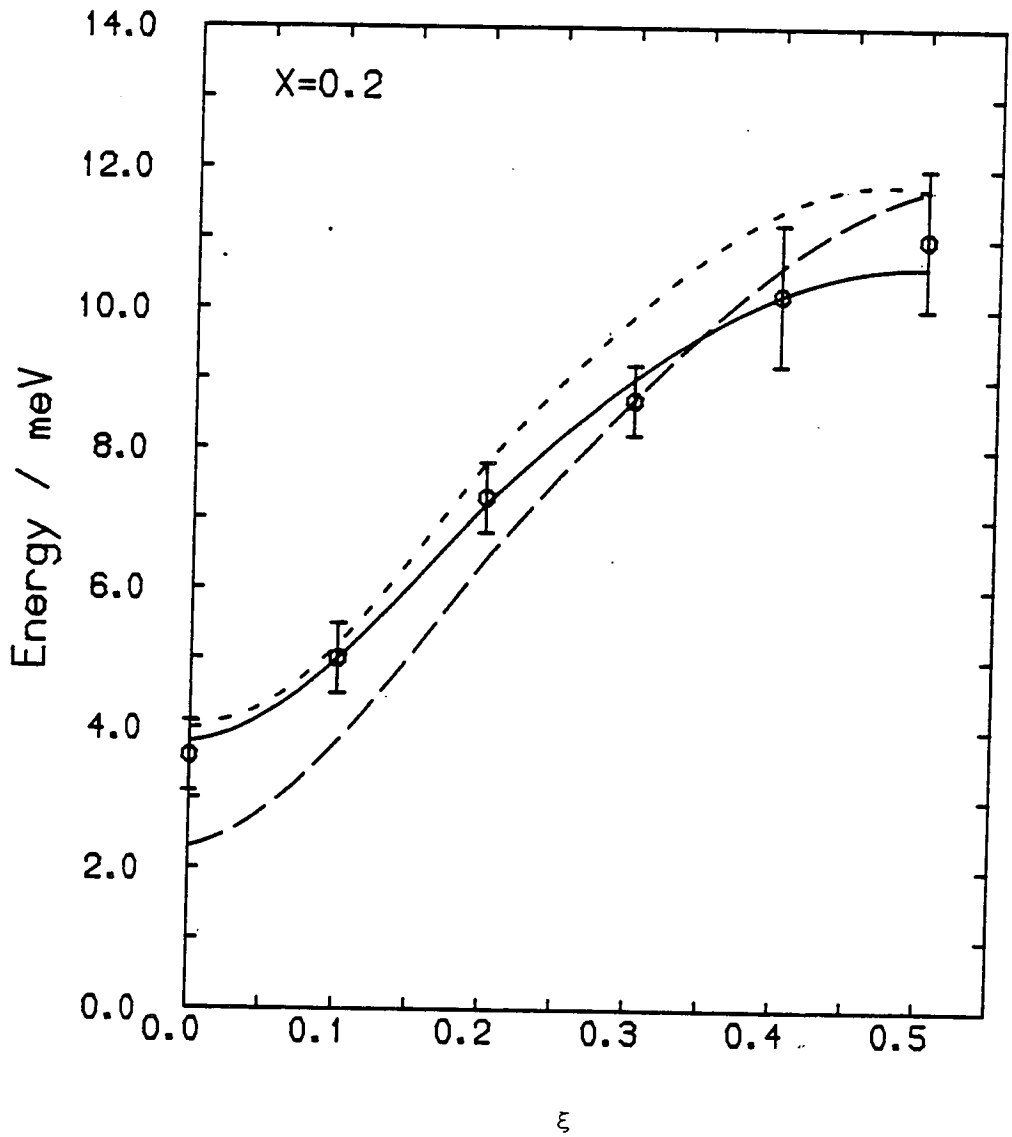

FIGURE (4.7.13): Comparison between peak positions in the calculated $S^{\alpha\alpha}(\underline{Q},\omega)$ spectra and the experimental data points for the dispersion relation in $K_2Co_xFe_{1-x}F_4$ with x = 0.27. The solid line corresponds to $\alpha = x$, the dashed line corresponds to $\alpha = y$ and the dotted line corresponds to $\alpha = z$.

Fig (4.7.13)

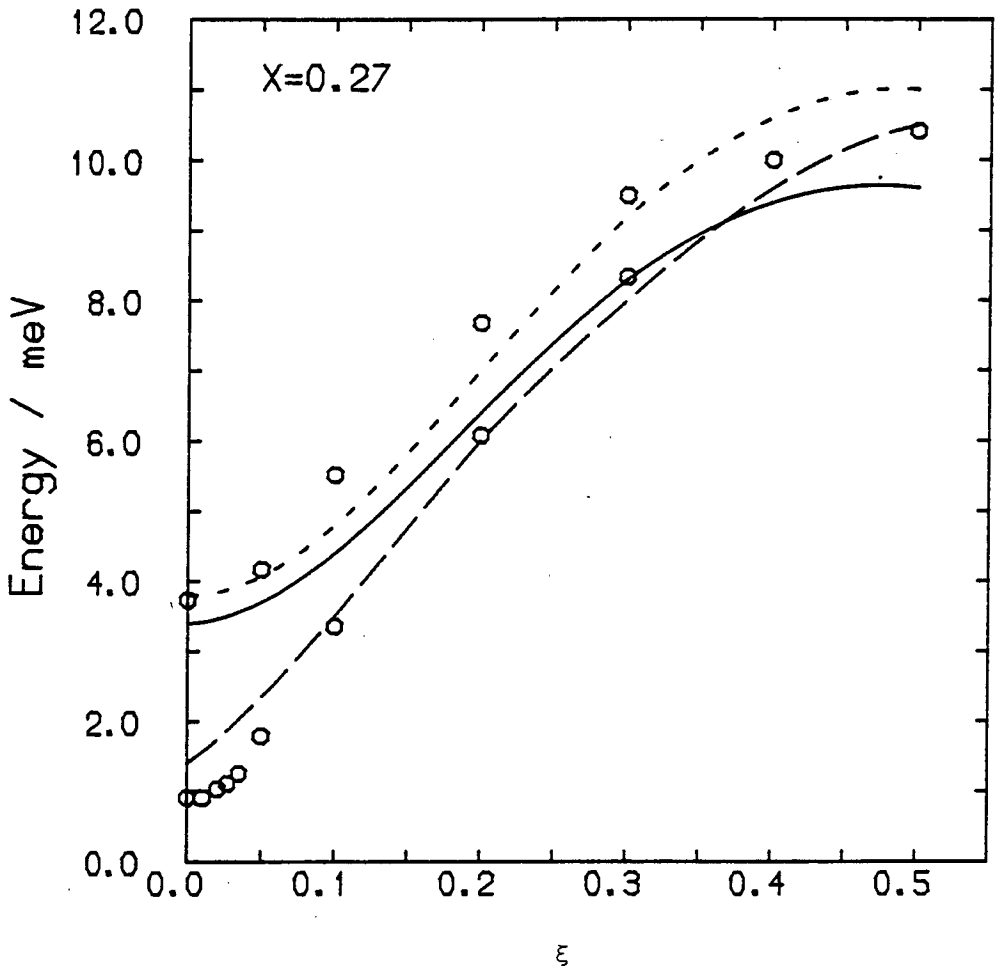

propagating mainly on the Fe^{2+} ions were measured. For x = 0.2 one measured branch was obtained and for x = 0.27 two such branches were deduced from the measurements. However the NEWSIM calculations predict 3 branches of excitations. For both concentrations, $S^{xx}(\underline{Q},\omega)$ and $S^{zz}(\underline{Q},\omega)$ are close to the measured higher energy branch near the zone centre, whilst $S^{yy}(\underline{Q},\omega)$ corresponds to the measured lower energy branch in the x = 0.27 case. The difference between calculated and experimental values for the energy of the excitations at particular reduced wavevector values could be due to uncertainties in the values for the exchange and single-ion anisotropy parameters obtained from the literature. Overall, the calculated results are in reasonable agreement with the results of the experiments.

CHAPTER 5

$Rb_2Mn_xCr_{1-x}C\ell_4$: A MIXED MAGNETIC SYSTEM WITH COMPETING FERROMAGNETIC AND ANTIFERROMAGNETIC EXCHANGE INTERACTIONS

5.1 Introduction

In recent years there has been considerable theoretical and experimental interest in mixed magnetic systems with competing ferromagnetic and antiferromagnetic exchange interactions. Such systems can in theory be formed by randomly mixing an antiferromagnetic system with a ferromagnetic system. Fishman and Aharony (1980) calculated $x - T$ phase diagrams for this type of mixed magnetic system, using both Mean-field Theory and Renormalisation Group Theory. They found that if only nearest neighbour exchange interactions were assumed, then there were four magnetic phases in the $x - T$ plane; a paramagnetic phase, a ferromagnetic phase, an antiferromagnetic phase and a spin glass phase. (In the spin-glass phase the magnetic moments have a local "frozen-in" component but there is no long-range magnetic order.) A schematic phase diagram is shown in Figure (5.1.1). Katsumata (1983) has reviewed some of the recent experimental studies of the system $Rb_2Mn_xCr_{1-x}C\ell_4$, an insulating mixed magnetic system which is a random mixture of the ferromagnetic system $Rb_2CrC\ell_4$ and the antiferromagnetic system $Rb_2MnC\ell_4$. This system is of particular interest because it is the first example of a random mixture of an insulating ferromagnet and an insulating antiferromagnet with nearest neighbour interactions in which a spin-glass phase has been observed (Katsumata et al. (1982), Kohles

FIGURE (5.1.1): Schematic concentration x against temperature T diagram for a mixed magnetic system with competing ferromagnetic-antiferromagnetic exchange interactions.
P indicates the paramagnetic phase,
F indicates the ferromagnetic phase,
AF indicates the antiferromagnetic phase and SG indicates the spin glass phase.

Figure (5.1.1)

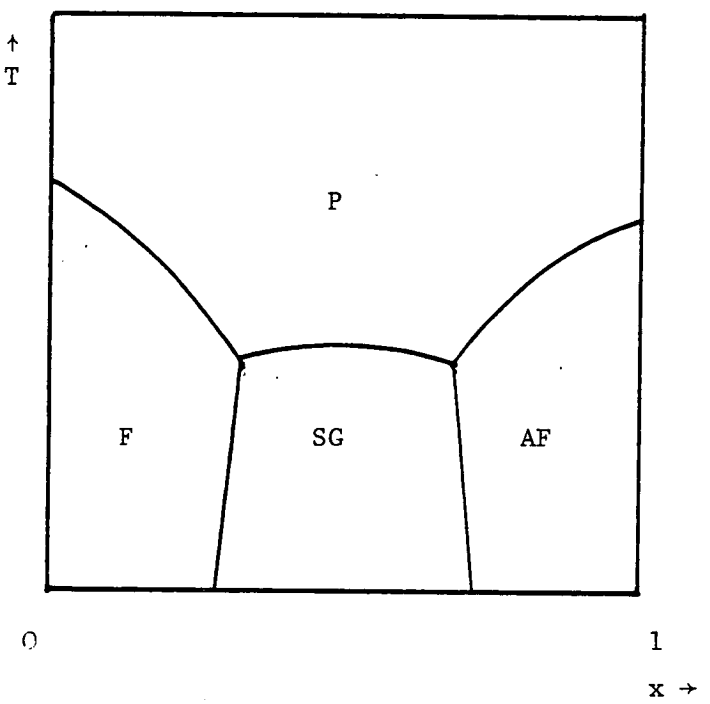

et al. (1982)). It is thus a unique physical representation of the kind of system considered by Fishman and Aharony (1980). There is another system $Eu_xSr_{1-x}S$ which also exhibits a spin-glass phase (Maletta and Felsch (1979)), However, the spin-glass behaviour arises from a different source. $Eu_xSr_{1-x}S$ is formed by dilution of the ferromagnet EuS with diamagnetic SrS. This creates an imbalance between the nearest neighbour ferromagnetic exchange interactions and the next nearest neighbour antiferromagnetic exchange interactions which leads to the spin-glass behaviour.

In this chapter the results of neutron scattering measurements on the system $Rb_2Mn_xCr_{1-x}C\ell_4$, with nominally $x = 0.754$, are reported. The rest of this chapter is set out as follows. In Section (5.2) the pure systems $Rb_2MnC\ell_4$ and $Rb_2CrC\ell_4$ are discussed and in Section (5.3) general details of the experiments are given. The inelastic neutron scattering measurements which were performed in order to investigate the magnetic excitations in the sample are reported in Section (5.4). Section (5.5) discusses experiments which were performed to study the magnetic phase transition for $x = 0.754$, a concentration for which the sample was expected to exhibit antiferromagnetic long-range order below a Néel temperature T_N.

5.2 The Pure Systems

5.2(i) Introductory Remarks

$Rb_2Mn_xCr_{1-x}C\ell_4$ is a random mixture of the systems $Rb_2MnC\ell_4$

and Rb_2CrCl_4, both of which are isomorphous with K_2NiF_4 (Birgeneau et al. (1970)). As discussed earlier in this thesis, for isomorphs of K_2NiF_4, the predominant exchange interactions are between nearest spins in the basal a - b plane, so that the mixed magnetic system is quasi two dimensional.

5.2(ii) $\underline{Rb_2MnCl_4}$

Hunds' rules indicate that the ground state of the free Mn^{2+} ion is $^6S_{5/2}$. The total angular momentum L = 0 for this ion because the 3d shell is half filled by the 5 electrons which occupy it. Consequently, to a good approximation, the ground state of the Mn^{2+} ion is not influenced by the crystal field in Rb_2MnCl_4 or by spin-orbit coupling. The spin Hamiltonian for Rb_2MnCl_4 can therefore be written in terms of a pseudo-spin $S = {}^5/2$, which is equal to the actual spin.

Neutron diffraction studies of Rb_2MnCl_4 by Epstein et al. (1970) showed that the system attains antiferromagnetic long range order below $T_N = 57K$ with the spins aligned along the c-axis of the unit cell. Schröder et al. (1980) determined the spin wave dispersion relation for Rb_2MnCl_4 at T = 8K by inelastic neutron scattering measurements. They also calculated a form for the spin wave dispersion relation and fitted it to their experimental data points. The agreement between the calculated and experimental values was excellent across the entire Brillouin zone. The Hamiltonian for Rb_2MnCl_4 was assumed to be given by:

$$H = \sum_{<ij>} J_{ij}\, \underline{S}_i \cdot \underline{S}_j + g\mu_B\{-H_A \sum_i S_i^z + H_A \sum_j S_j^z\} \qquad (5.2.1)$$

where <ij> indicates a sum over nearest neighbour spins $\underline{S}_i$ and $\underline{S}_j$, J_{ij} is the nearest neighbour exchange interaction and H_A is the magnitude of an anisotropy field. The anisotropy arises from magnetic dipole-dipole interactions.

5.2(iii) $\underline{Rb_2CrCl_4}$

The free Cr^{2+} ion has 4 electrons in the 3d shell and Hunds' rules therefore predict the ground state to be ^5D_o. In Rb_2CrCl_4 the Cr^{2+} ions are attributed a pseudospin S = 2. Single crystal neutron diffraction studies by Day et al. (1979) showed that Rb_2CrCl_4 crystallises effectively in the K_2NiF_4 structure. However, the Cl^- ions in the basal plane are displaced by a small amount from the midpoint of the line joining the Cr^{2+} ions and the ferromagnetic exchange interactions between nearest neighbour Cr^{2+} ions in the a - b plane are attributed to this Jahn-Teller distortion of the $CrCl_6$ octohedra. (With the exception of K_2CuF_4 (T_c = 6.25K) all other known K_2NiF_4 isomorphs exhibit antiferromagnetic ordering.)

Neutron scattering studies of Rb_2CrCl_4 (Fair et al. (1977)) have shown that below $T_c = 57 \pm 2K$ the system orders ferromagnetically with the spins aligned in the basal a - b plane. The spin wave dispersion relation at T = 4.5K was obtained by Hutchings et al. (1976) from inelastic neutron scattering experiments. Their data was well represented by the dispersion relation for a planar ferromagnet with Heisenberg exchange interactions.

5.2(iv) Concluding Remarks

The magnetic properties of Rb_2MnCl_4 and Rb_2CrCl_4 suggest that $Rb_2Mn_xCr_{1-x}Cl_4$ should be a good physical realisation of a $d = 2$ system with nearest neighbour competing ferromagnetic-antiferromagnetic exchange interactions. Figure (5.2.1) illustrates the phase diagram for this system published by Kohles et al. (1982). It predicts that there exists an insulating spin-glass phase for the intermediate concentration range $0.41 < x < 0.59$. AF2 represents a uniaxial antiferromagnetic phase similar to the ordered phase in Rb_2MnCl_4 and AF1 represents an essentially planar antiferromagnetic phase. Single crystal samples with $0.41 < x < 0.59$ were not available to the author and the neutron scattering measurements discussed in the following sections were performed on a sample with $x = 0.754$, which was expected to be in the AF2 phase below a transition temperature T_N. The motivation behind the measurements was to study the effect of a substantial number of Cr^{2+} defects ($\sim$ 25%) on the phase transition and magnetic excitations.

5.3 General Experimental Details

The neutron scattering measurements reported in Sections (5.4) and (5.5) of this chapter were performed, using the IN2 triple-axis neutron spectrometer at the Institut Laue-Langevin, Grenoble, France. A diagram of this instrument is given in Figure (5.3.1). IN2 was fitted with two monochromator crystals both of which utilised the Pyrolytic Graphite (0,0,2) Bragg reflection. The effect of the

FIGURE (5.2.1): Proposed phase diagram for the mixed magnetic system $Rb_2Mn_xCr_{1-x}Cl_4$ (Kohles et al. (1982))

P indicates the paramagnetic phase,

F indicates the planar ferromagnetic phase,

SG indicates the spin glass phase,

AF1 indicates a planar antiferromagnetic phase and AF2 indicates a uniaxial antiferromagnetic phase with the spins aligned along the c-direction.

Figure (5.2.1)

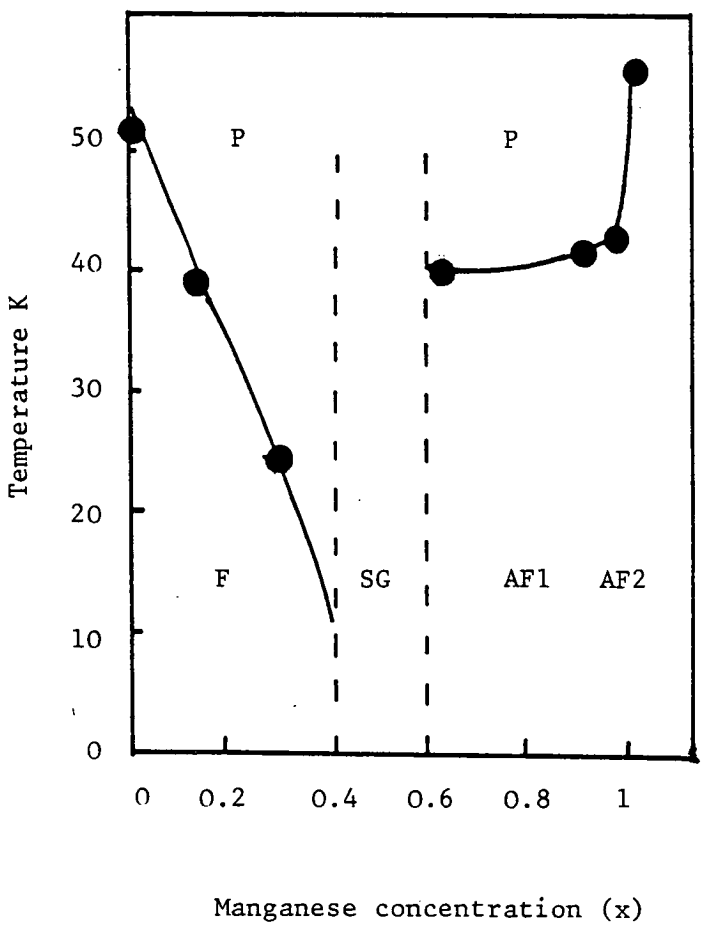
Temperature K
50
40
30
20
10
0
P
P
F
SG
AF1
AF2
0
0.2
0.4
0.6
0.8
1
Manganese concentration (x)

FIGURE (5.3.1): Diagram of IN2 triple axis neutron spectrometer (taken from an I.L.L. User's Guide).
Note the double monochromator arrangement.

fig 5·3·1

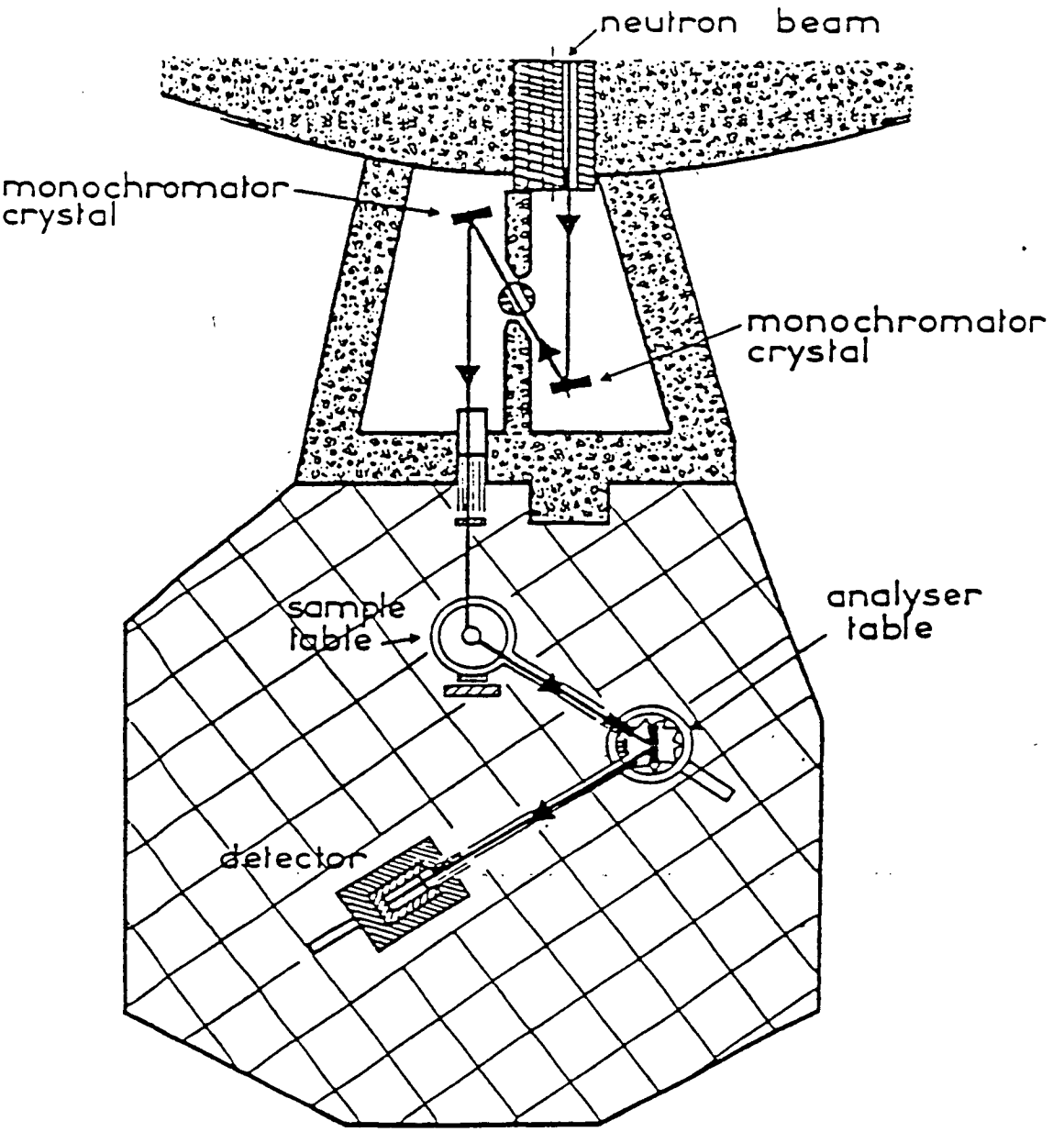

SCHEMATIC DRAWING
OF THE SPECTROMETER IN2

double monochromator is to give improved spectrometer resolution. As shown by Pynn and Passel (1974) the resolution function for the spectrometer can still be calculated, using the Cooper-Nathans formalism, provided that the double monochromator is treated as a single monochromator with an effective horizontal mosaic spread η'_m given by:

$$1/\eta'^2_m = 1/\eta^2_{m_1} + 1/\eta^2_{m_2} \qquad (5.3.1)$$

where η_{m_1} and η_{m_2} are the horizontal mosaic spread values of the individual monochromator crystals.

For the inelastic neutron scattering measurements reported in Section (5.4) the spectrometer was used in a triple-axis mode with a pyrolytic graphite analyser which made use of the (0,0,2) Bragg reflection. The horizontal collimation was chosen to be 60' - 30' - 30' - 60' from reactor to detector and the incident wavevector was fixed at $k_I = 2.662\ \text{Å}^{-1}$ with a pyrolytic graphite filter to eliminate higher order contaminant neutrons.

For the diffuse scattering measurements reported in Section (5.5) the spectrometer was used in a two-axis mode. This was achieved by removing the analyser crystal and aligning arm 2 and arm 3 of the spectrometer so that they were effectively one arm. The collimation for this spectrometer configuration was 60' - 10' - 10' and the wavevector transfer was fixed throughout at 2.662Å^{-1}.

The single crystal sample with manganese concentration nominally $x = 0.754$ was mounted in a variable temperature helium flow cryostat with the magnetic $[1,0,0]$ and $[0,0,1]$ directions in the scattering

plane for both sets of measurements. The dimensions of the sample were approximately $(15 \times 8 \times 4)mm^3$.

5.4 Magnetic Excitation Measurements

In this section an investigation by inelastic neutron scattering measurements of the magnetic excitation spectrum in a sample of $Rb_2Mn_xCr_{1-x}C\ell_4$ with nominally $x = 0.754$ is reported. The measurements consisted of a series of constant wavevector (constant-$\underline{Q}$) and constant energy transfer (constant-E) scans. There is no spin wave dispersion along the c^*-direction $[0,0,\bar{1}]$ in these quasi two dimensional systems and so all measurements were performed with $\underline{Q}$ along the magnetic a_m^* direction $[1,0,0]$. Well-defined spin wave peaks were found for wavevectors up to around two-fifths of the way to the Brillouin zone boundary. Measurements were made for reduced wavevector transfers beyond this but the excitation had become very broad and the scattering intensity had become too weak for any conclusions to be made as to the nature of the excitations near the zone boundary. Beam time has been allocated on the high-flux triple-axis spectrometer IN8 at the Institut Laue-Langevin to make further measurements for wavevectors close to the Brillouin zone boundary and this should enable a complete characterisation of the magnetic excitation spectrum to be obtained.

Figure (5.4.1) illustrates the data collected in one of the constant-$\underline{Q}$ scans and Figure (5.4.2) shows the data from one of the constant-E scans. These figures are representative of the typical quality of the data. The peak positions and the full widths

FIGURE (5.4.1): The data obtained from a scan with constant Q = (1.15,0,0) for the sample of $Rb_2Mn_xCr_{1-x}C\ell_4$ with nominally x = 0.754, indicating a spinwave peak corresponding to an energy of 0.85 THz.

Fig (5.4.1)

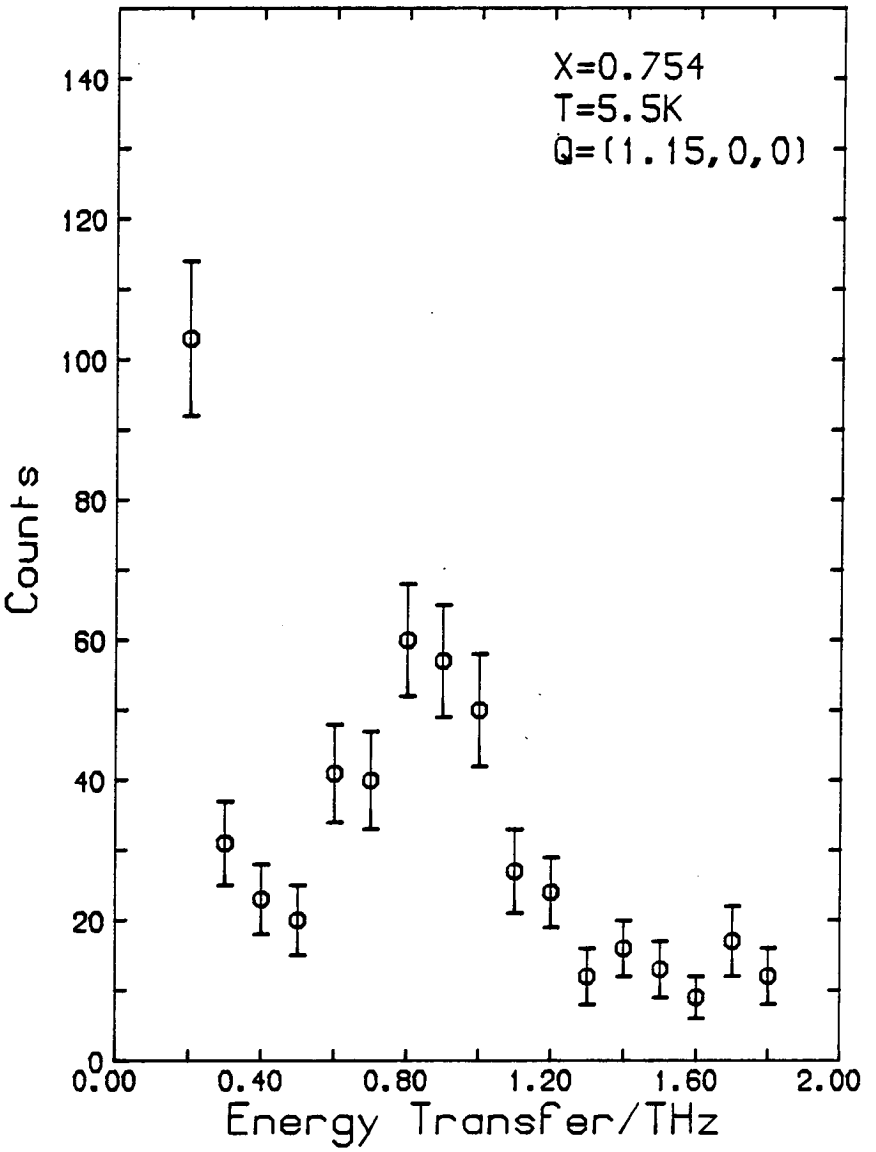
X=0.754
T=5.5K
Q=(1.15,0,0)
Counts
Energy Transfer/THz
0
20
40
60
80
100
120
140
0.00
0.40
0.80
1.20
1.60
2.00

FIGURE (5.4.2): The data obtained from a scan with constant energy transfer E = 0.7 THz. The peaks at QX = 0.9 and QX = 1.1 correspond to spin wave peaks with reduced wavevectors ξ = 0.1 (where ξ is the reduced wavevector expressed in units of a^*).

Fig (5.4.2)

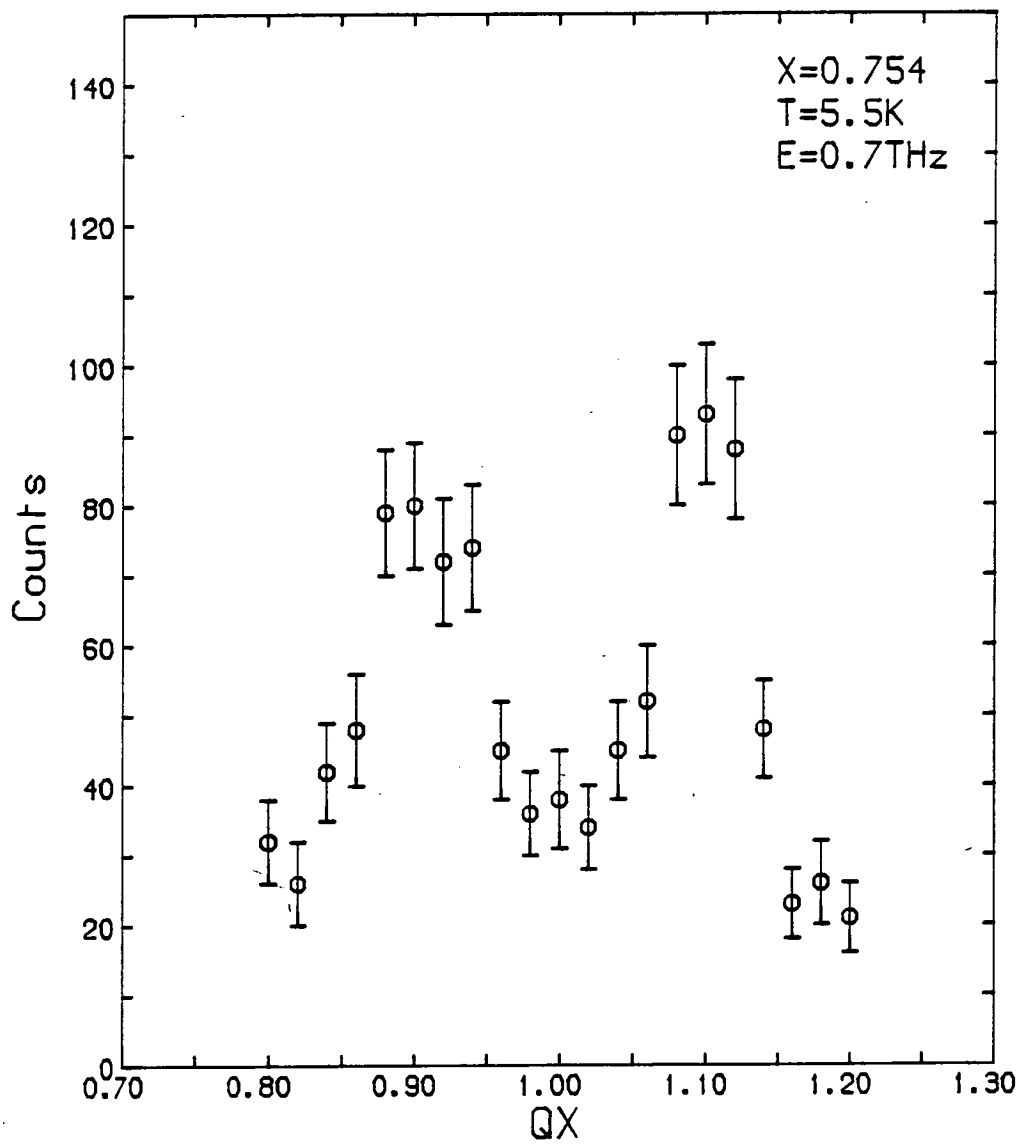
X=0.754
T=5.5K
E=0.7THz
Counts
QX
0
20
40
60
80
100
120
140
0.70
0.80
0.90
1.00
1.10
1.20
1.30

at half-maxima obtained from those scans, in which a peak in the scattering intensity could be distinguished, are indicated in Figure (5.4.3) along with the spin wave dispersion relation for the pure system Rb_2MnCl_4. The Rb_2MnCl_4 dispersion curve passes through the experimental points, to a good approximation, for reduced wavevectors up to one-fifth of the Brillouin zone boundary value. At given reduced wavevectors between one-fifth and two-fifths of the Brillouin zone boundary value, the data points are at lower energy values than those given by the Rb_2MnCl_4 dispersion relation. The experimental evidence thus suggests that for the $x = 0.754$ sample there is a single branch of the spin wave dispersion relation corresponding to excitations propagating mainly on the Mn^{2+} ions. This branch is modified relative to that in the pure system Rb_2MnCl_4 by the presence of $\sim$ 25% Cr^{2+} defects.

Further inelastic neutron scattering measurements will be required before a complete picture can be obtained for the magnetic excitation spectrum in $Rb_2Mn_xCr_{1-x}Cl_4$ with $x = 0.754$. The zone centre energy gap ε_g has to be determined at $T = 5K$, along with its dependence on temperature up to $T = T_N$. The temperature dependence of ε_g is of particular interest because it is believed that spin wave scattering may have contributed to the observed intensity in the diffuse scattering measurements reported in Section (5.5) of this chapter. The measurements to determine ε_g as a function of T may require high resolution measurements similar to those reported in Section (4.5) of Chapter 4 for $K_2Co_xFe_{1-x}F_4$ with $x = 0.27$. The measurements to be made during the scheduled beam time on IN8 discussed previously shall make

FIGURE (5.4.3): The full circles indicate the spin wave peak positions obtained from the inelastic neutron scattering measurements on the $x = 0.754$ sample described in the text. The solid line corresponds to the dispersion relation for the pure antiferromagnetic system Rb_2MnCl_4.

fig 5·4·3

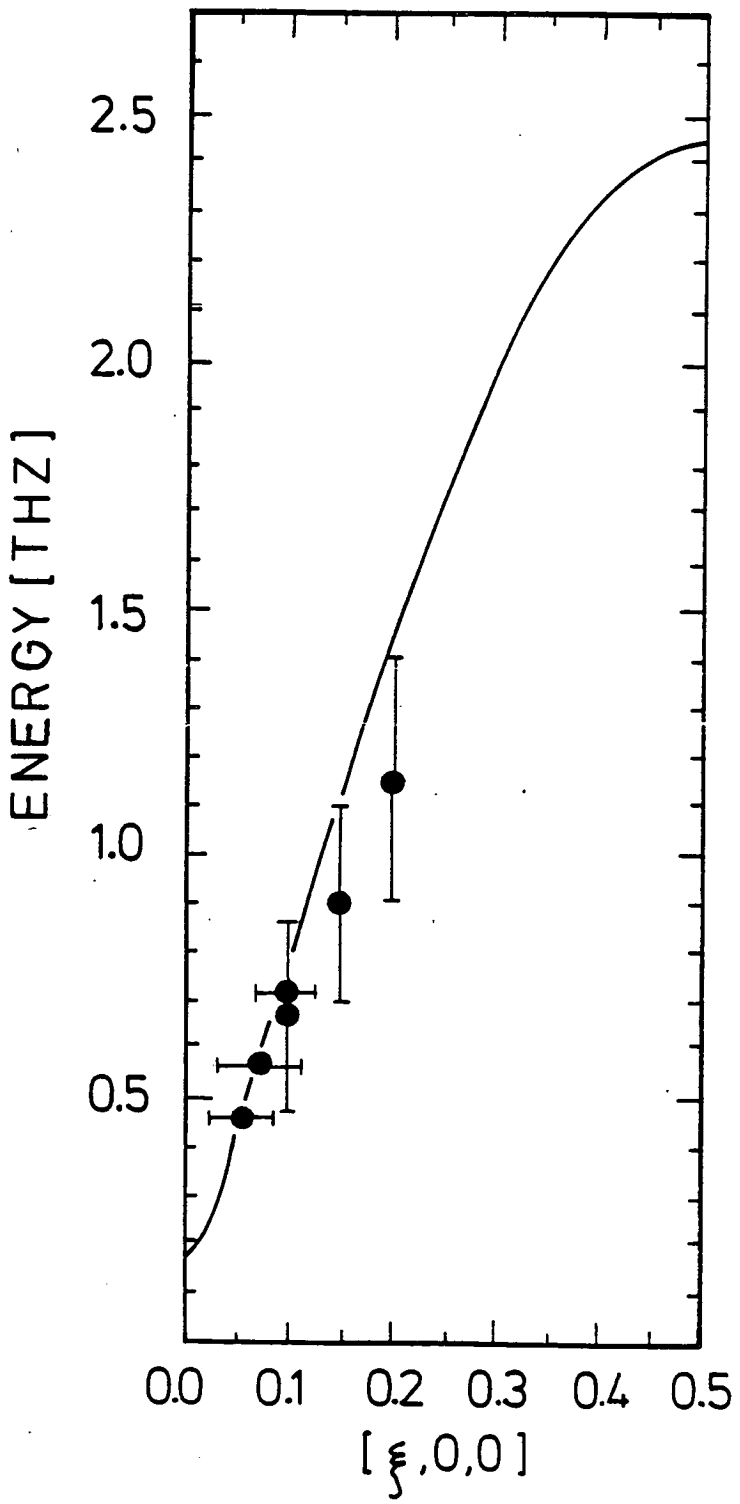

use of the higher neutron flux, compared with IN2, to investigate the magnetic excitation spectrum over the remaining three-fifths of the Brillouin zone where the excitations have so far been too weak to observe.

5.5 The Magnetic Phase Transition

This section reports the results of neutron scattering measurements which were performed to investigate the magnetic phase transition in $Rb_2Mn_xCr_{1-x}Cl_4$ with $x = 0.754$. All measurements were performed with the spectrometer in the two-axis configuration discussed in Section (5.3).

5.5(i) The Order Parameter

Below $T = 35K$ a resolution limited Bragg peak was observed at $Q = (1,0,0)$. Peaks at $Q = (1,0,L)$ and $Q = (3,0,L)$ for $-8 \lesssim L \lesssim 8$ were also observed. This suggested antiferromagnetic long range order existed below $T_N \simeq 35K$ in this system. The intensity of the (1,0,0) Bragg reflection, which is then proportional to the square of the sublattice magnetisation, was measured as a function of temperature and the results are shown in Figure (5.5.1). Two features of this were surprising. Firstly, the intensity, relative say to $K_2Co_xFe_{1-x}F_4$ with $x = 0.6$, rises very slowly as T is lowered from T_N. Secondly, the intensity continues to rise all the way down to the lowest temperature at which measurements could be made. In anticipation of the results from the diffuse

FIGURE (5.5.1): The intensity of the (1,0,0) antiferromagnetic Bragg peak as a function of temperature for $Rb_2Mn_xCr_{1-x}Cl_4$ with nominally x = 0.754.

Fig (5.5.1)

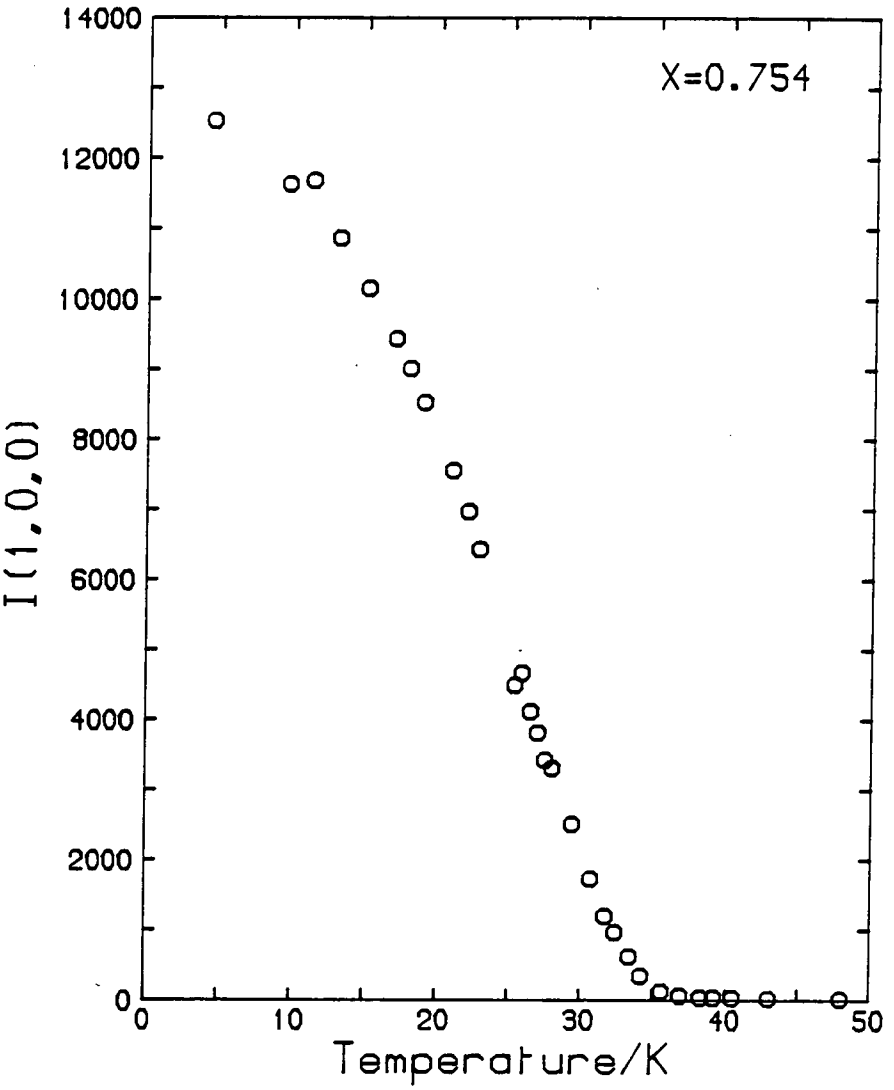
X=0.754
I(1,0,0)
Temperature/K
14000
12000
10000
8000
6000
4000
2000
0
0
10
20
30
40
50

scattering measurements to be presented, further discussion of the temperature dependence of the sublattice magnetisation is delayed until the diffuse scattering measurements are discussed.

5.5(ii) Diffuse Scattering

5.5(ii)(a) Theoretical Background

It was shown in Chapter 2 that for scattering of unpolarised neutrons from N localised spins the magnetic partial differential cross-section is related to the partial dynamic structure factors by:

$$\frac{d^2\sigma}{d\Omega dE} \propto \sum_{\alpha\beta} (\delta_{\alpha\beta} - \tilde{Q}^{\alpha} \tilde{Q}^{\beta}) S^{\alpha\beta}(\underline{Q},\omega) \quad . \tag{5.5.1}$$

As discussed by Birgeneau et al. (1977) the partial dynamic structure factors are related to the wavevector dependent susceptibility $\chi^{\alpha\beta}(\underline{Q})$ and the normalised spectral shape function $F^{\alpha\beta}(\underline{Q},\omega)$ by:

$$S^{\alpha\beta}(\underline{Q},\omega) = \frac{\chi^{\alpha\beta}(\underline{Q})}{\chi^{o}} \frac{\hbar\omega\beta}{1 - e^{\hbar\omega\beta}} F^{\alpha\beta}(\underline{Q},\omega) \tag{5.5.2}$$

where for any $\underline{Q}$:

$$\int_{-\infty}^{\infty} F^{\alpha\beta}(\underline{Q},\omega)d\omega = 1 \tag{5.5.3}$$

and χ^{o} is the Curie susceptibility for non-interacting magnetic moments. Making use of the normalisation condition on $F^{\alpha\beta}(\underline{Q},\omega)$ equation (5.5.2) may be rewritten:

$$\int_{-\infty}^{\infty} d\omega \left(\frac{1 - e^{-\hbar\omega\beta}}{\hbar\omega\beta}\right) S^{\alpha\beta}(\underline{Q},\omega) = \frac{\chi^{\alpha\beta}(\underline{Q})}{\chi^{o}} \quad . \tag{5.5.4}$$

Providing that for the critical fluctuations $\hbar\omega << k_B T$ then:

$$(1 - e^{-\hbar\omega\beta})/\hbar\omega\beta \simeq 1 \qquad (5.5.5)$$

and equation (5.5.4) can be written as:

$$\int_{-\infty}^{\infty} d\omega\ S^{\alpha\beta}(\underline{Q},\omega) \simeq \frac{\chi^{\alpha\beta}(\underline{Q})}{\chi^{o}} \cdot \qquad (5.5.6)$$

Thus in theory, $\chi^{\alpha\beta}(\underline{Q})$ could be obtained by measuring $S^{\alpha\beta}(\underline{Q},\omega)$ and then integrating the measured values with respect to ω. In most cases, however, this proves to be impossible in practice. Instead, the instrument is used to perform the integral directly. This is achieved by removing the analyser from the triple-axis neutron spectrometer and using the instrument in a two-axis mode. All neutrons emerging at a given scattering angle $2\theta_S$ are then accepted by the detector. If $A(k_i, k_f)$ is the proportionality constant in equation (5.5.1), then in that spectrometer configuration the measured quantity is $\int dk_f\ A(k_i,k_f)S(\underline{Q},\omega)$ which is proportional to the integral on the left hand side of equation (5.5.6) provided that:

$$\left[\left(\frac{m_N}{\hbar}\right)\Gamma/k_i\kappa\right] << 1 \qquad (5.5.7)$$

where Γ is a characteristic frequency and κ is the inverse correlation length. As discussed by Birgeneau et al. (1971) this imposes the requirement that the change in k_f, required to integrate over ω, is much smaller than κ.

In magnetic systems with the K_2NiF_4 structure, the spins in adjacent basal planes are only weakly coupled and the dynamics and

phase transitions are effectively those of a two dimensional (d = 2) system so that the diffuse scattering builds up in ridges along the $(1,0,\eta)$ direction as opposed to only around the Bragg peak position at $Q = (1,0,0)$ as it would if the phase transition was three dimensional (d = 3). Whereas for a d = 3 system the susceptibility $\chi^{\alpha\beta}(\underline{Q})$ would be dependent on the reduced wavevector q measured from the (1,0,0) position, for these d = 2 systems, $\chi^{\alpha\beta}(\underline{Q})$ is dependent only on the reduced wavevector q measured from the nearest point on the $(1,0,\eta)$ ridge. That is to say, $\chi^{\alpha\beta}(\underline{Q})$ is independent of q_c in these systems. It can be shown that for these systems equation (5.5.7) then becomes:

$$\left[\left(\frac{m_N}{\hbar}\right)\Gamma/k_i K\right] \sin\theta_f \ll 1 \quad . \tag{5.5.8}$$

where θ_f is the angle between the vector $\underline{k}_f$ and the $(1,0,\eta)$ ridge. Birgeneau et al. (1971) then point out that if the scattering geometry with $\underline{Q} = \underline{k}_i - \underline{k}_f$ is arranged so that $\underline{k}_f$ is parallel to the $(1,0,\ell)$ ridge, then the condition given in equation (5.5.8) is met. It is clear that with k_f parallel to the $(1,0,\ell)$ ridge, then the wavevector transfer within the planes does not change for the range of k_f's accepted by the detector and so the integration with respect to energy is performed correctly by the instrument at each point in the scan. The wavevector transfer $\underline{Q}$ for which $\underline{k}_f$ is exactly along the $(1,0,\eta)$ ridge is called the "Quasi-elastic" position.

Figure (5.5.2) shows a reciprocal space diagram for magnetic systems with the K_2NiF_4 structure with the scattering geometry at the quasi-elastic position superimposed. The value of η for this

FIGURE (5.5.2): Reciprocal space diagram for the K_2NiF_4 structure. The circles indicate the antiferromagnetic Bragg peaks and the crosses indicate the nuclear Bragg peaks. The scattering geometry for $\underline{Q}$ at the "Quasi-elastic" position is superimposed.

Figure (5.5.2)

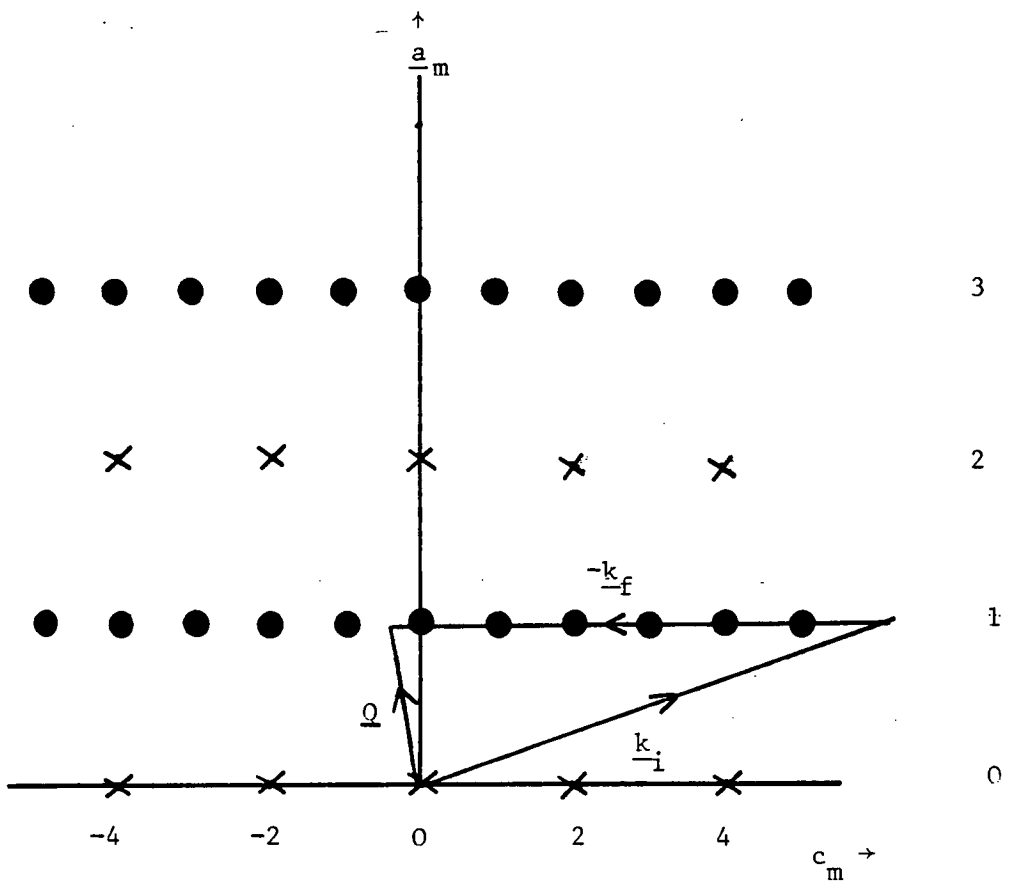
$\underline{a}_m$
3
2
1
0
$-\underline{k}_f$
$\underline{Q}$
$\underline{k}_i$
-4
-2
0
2
4
c_m

wavevector transfer can be calculated straightforwardly. By Bragg's Law:

$$Q = 2 k_f \sin \theta_s \quad . \tag{5.5.9}$$

But also from Figure (5.5.2) it is clear that:

$$Q = ((a_m^*)^2 + (\eta\, c_m^*)^2)^{\frac{1}{2}} \tag{5.5.10}$$

where a_m^* and c_m^* are the reciprocal lattice vectors along the $\underline{a}_m$ and $\underline{c}_m$ directions of the magnetic unit cell. Equating the right-hand sides of equations (5.5.9) and (5.5.10), and rearranging gives:

$$\eta = \left[(4k^2\sin^2\theta_s - (a_m^*)^2)/(c_m^*)^2\right]^{\frac{1}{2}} \tag{5.5.11}$$

where:

$$\theta_s = \tfrac{1}{2} \sin^{-1}(a_m^*/k_f) \quad . \tag{5.5.12}$$

5.5(ii)(b) Specific Details of Diffuse Scattering Measurements

For the lattice parameters of the nominally x = 0.754 sample of $Rb_2Mn_xCr_{1-x}C\ell_4$ and fixed neutron wavevector of $k = 2.662\text{Å}^{-1}$ the quasi-elastic position was calculated to be at $Q = (1,0,-0.392)$. Scans were performed in which the scattering intensity was recorded as a function of q_a along the direction $(1+q_a,0,-0.392)$ with q_a in the range $-0.5 < q_a < 0.5$. Even though the observed scattering intensity attributable to the magnetic susceptibility never extended beyond $|q_a| = 0.25$ the purpose of extending the scans out to $|q_a| = 0.5$ was to ensure a proper determination of the flat background at each of the 26 chosen temperatures in the range

$4.42K < T < 71.5K$. For all scans except those at $T = 63.2K$ and $T = 71.5K$ the step in q_a was $\Delta q_a = 0.05$ for $0.2 \lesssim |q_a| \lesssim 0.5$, $\Delta q_a = 0.01$ for $0.08 < |q_a| < 0.18$ and $\Delta q_a = 0.005$ for $0 \lesssim |q_a| \lesssim 0.075$. These step sizes were chosen (after a preliminary survey) in order that small steps could be made in the small q_a region where the scattering is expected to be sharply peaked near T_N. The number of counts in the detector was recorded over a period of just under 3 minutes for each point in a scan. Since there were 67 points per scan, then a single scan lasted around 3 hours. Allowing up to half-an-hour to change and stabilise the temperature (which had to be done manually) it is worth emphasizing that a large portion of the allocated beam time had to be spent solely on these 26 scans. (In fact this prevented more spin wave measurements from taking place during the allocated beam time.) After these measurements had been completed, the vertical resolution of the spectrometer was measured by tilting the goniometer arcs manually and recording the intensity as a function of tilt angle with the instrument set to record the intensity at a $\underline{Q}$ corresponding to a resolution limited Bragg peak. This effectively scans a delta function through the resolution ellipsoid along the vertical direction and so gives the vertical resolution width. The importance of a correct treatment of the spectrometer resolution, both horizontal and vertical, will be discussed alongside the data analysis.

5.5(ii)(c) Diffuse Scattering Data Analysis

It was initially assumed that only the longitudinal spin fluctuations contributed to the observed diffuse scattering intensity. In the quasi-elastic approximation, the longitudinal susceptibility is related to the partial dynamic structure factor for the spin ordering direction $S''(\underline{Q},\omega)$ by:

$$\int_{-\infty}^{\infty} d\omega\ S''(\underline{Q},\omega) \simeq \frac{\chi''(\underline{Q})}{\chi^{o}} \quad . \tag{5.5.13}$$

It was assumed that $\chi''(\underline{Q})/\chi^{o}$ had the Lorentzian form:

$$\frac{\chi''(\underline{Q})}{\chi^{o}} = \frac{A''K''^{2}}{q_a^{2} + q_b^{2} + K''^{2}} = \sigma(\underline{Q}) \quad . \tag{5.5.14}$$

That is, the longitudinal susceptibility was assumed to be a Lorentzian function of the reduced wavevector $q = q_a^{2} + q_b^{2}$ (where q_a is the reduced wavevector along the $\underline{a}_m$-direction and q_b is the reduced wavevector along the $\underline{b}_m$-direction. The susceptibility is independent of q_c, the reduced wavevector along the $\underline{c}$-direction, because of the quasi two-dimensional nature of the magnetic interactions. (The Lorentzian approximation has been shown to hold in $d = 2$ Ising systems for $q < 10K$ by Tracy and McCoy (1975)).

To interpret the data for a scan at a particular temperature, the cross-section of equation (5.5.14) was folded with the resolution of the spectrometer and the resultant calculated intensity fitted to the data in a least squares routine. The calculated intensity at a particular wavevector $\underline{Q}_o$ was:

$$I(\underline{Q}_o) = |\overline{f(Q_o)}|^{2} \int_{-\infty}^{\infty} R(\underline{Q}_o + \delta\underline{Q})\sigma(\underline{Q}_o + \delta Q)\delta Q \tag{5.5.15}$$

where $R(\underline{Q})$ was the resolution function and $f(\underline{Q}_o)$ was the average form factor. (The form factors given by Watson and Freeman (1961) for the Mn^{2+} and Cr^{2+} ions were weighted according to their concentrations x and (1-x) to obtain $\overline{f(\underline{Q}_o)}$).

In this particular case the cross-section varies only along the (horizontal) a_m-direction and the vertical b_m-direction. Further, because the horizontal and vertical resolution of the spectrometer are decoupled, then equation (5.5.15) reduces to

$$I(\underline{Q}_o) = \int_{-\infty}^{\infty} R_H(\delta Q_a) R_V(\delta Q_b) \sigma(\underline{Q}_o + \delta Q_a + \delta Q_b) \delta Q_a \, \delta Q_b \qquad (5.5.16)$$

where $R_H(\delta Q_a)$ and $R_V(\delta Q_b)$ are the horizontal and vertical components of the resolution function. Hagen (1982) has shown that for the cross-section given in equation (5.5.14) the integration over the vertical resolution could be performed analytically if a triangular vertical resolution function was assumed, so that:

$$I(\underline{Q}_o) = I_H(\underline{Q}_o) I_V(\underline{Q}_o) \qquad (5.5.17)$$

with $I_V(\underline{Q}_o)$ calculated analytically and $I_H(\underline{Q}_o)$ calculated numerically from:

$$I_H(\underline{Q}_o) = I_H(Q_{ao}) = \int_{-\infty}^{\infty} \frac{A'' \, K''}{(Q_a - Q_c)^2 + K''^2} \, e^{\frac{-\delta Q_a^2}{2\sigma_H^2}} \, \delta Q_a \qquad (5.5.18)$$

where $\delta Q_a = (Q_a - Q_{ao})$ and $q_a = (Q_{ao} - Q_c)$. Q_c allowed for any offset in the value of Q_a for which the scan (and hence the diffuse scattering) was centred. The integral of equation (5.5.18) was performed numerically by the Trapezium Rule, with 300 trapezoids between $-3\sigma_H$ and $+3\sigma_H$.

FIGURE (5.5.3): Scans through the ridge of diffuse scattering centred at Q = (1,0,-0.392) for x = 0.754 at

(a) T = 4.42K

(b) T = 29.4K

(c) T = 32.4K

(d) T = 34.2K

(e) T = 40.5K

(f) T = 55.8K.

The dotted line indicates the constant background term of 119 counts. The solid line indicates the calculated intensity obtained from the fitting procedure described in the text. Note, by comparing Figures (5.5.3) (b), (c) and (d), that there is little change in the width or intensity of the diffuse scattering over a temperature range of 5K.

Fig (5.5.3(a))

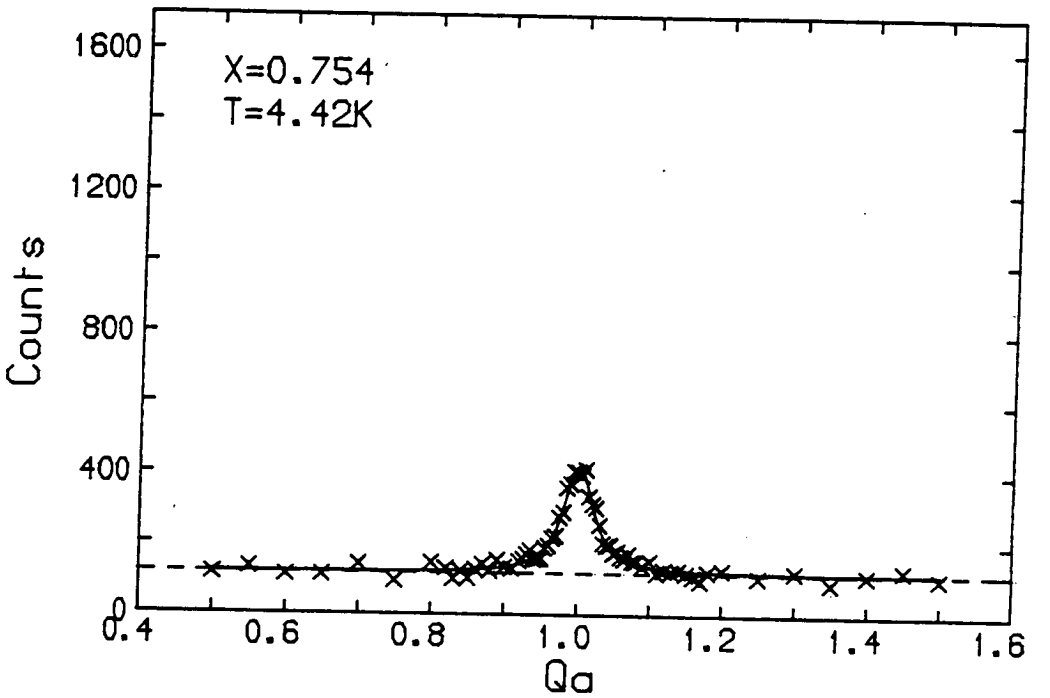

Fig (5.5.3(b))

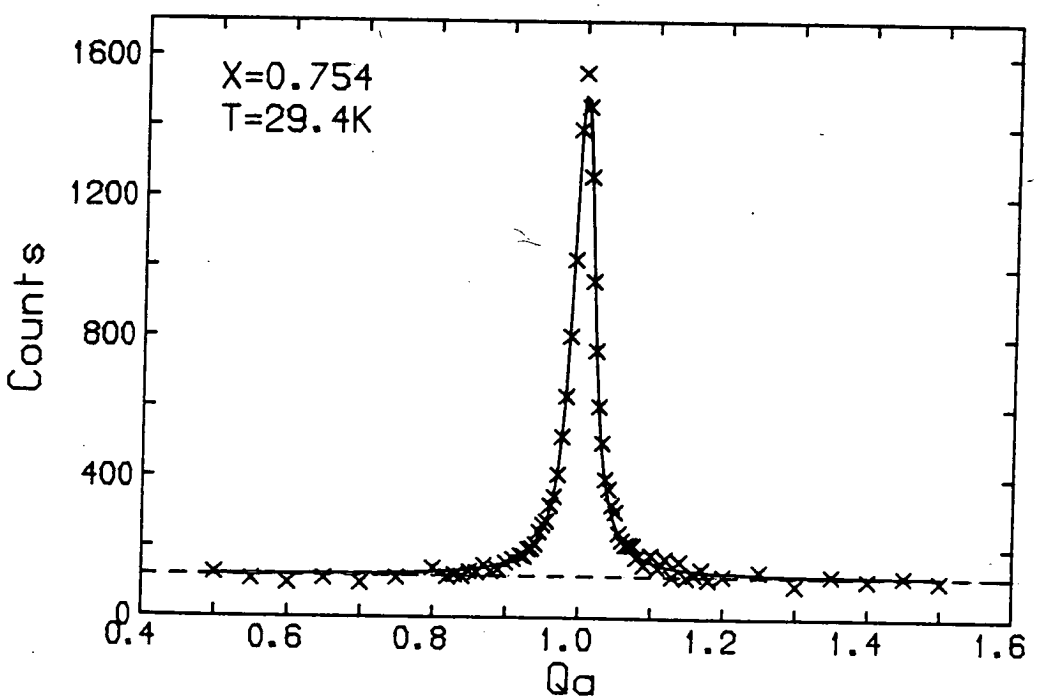

Fig (5.5.3(c))

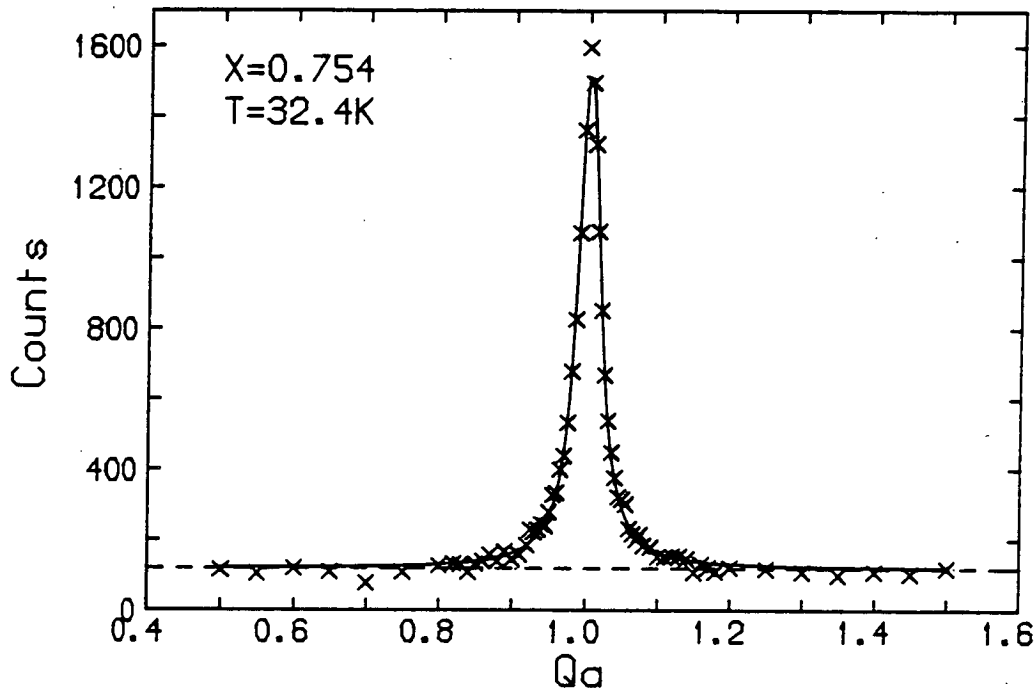

Fig (5.5.3(d))

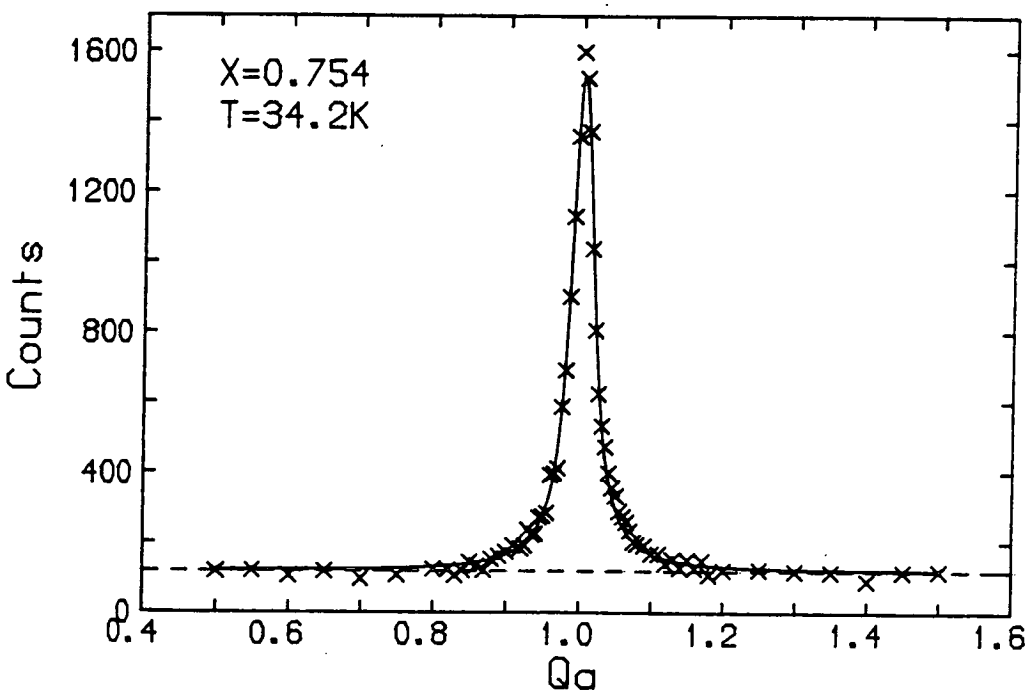

Fig (5.5.3(e))

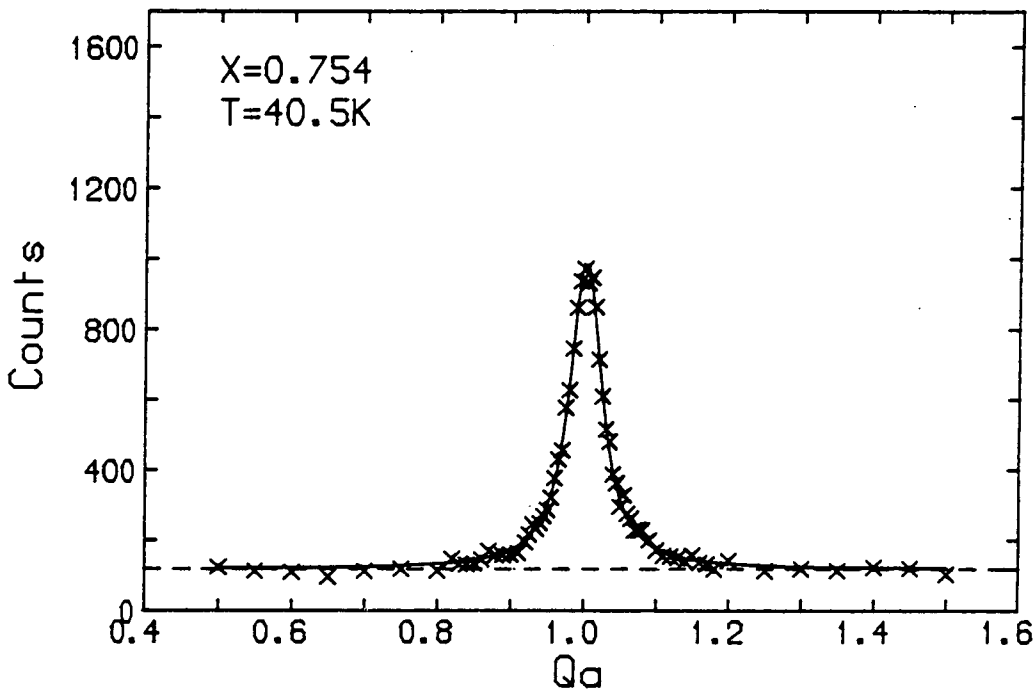

Fig (5.5.3(f))

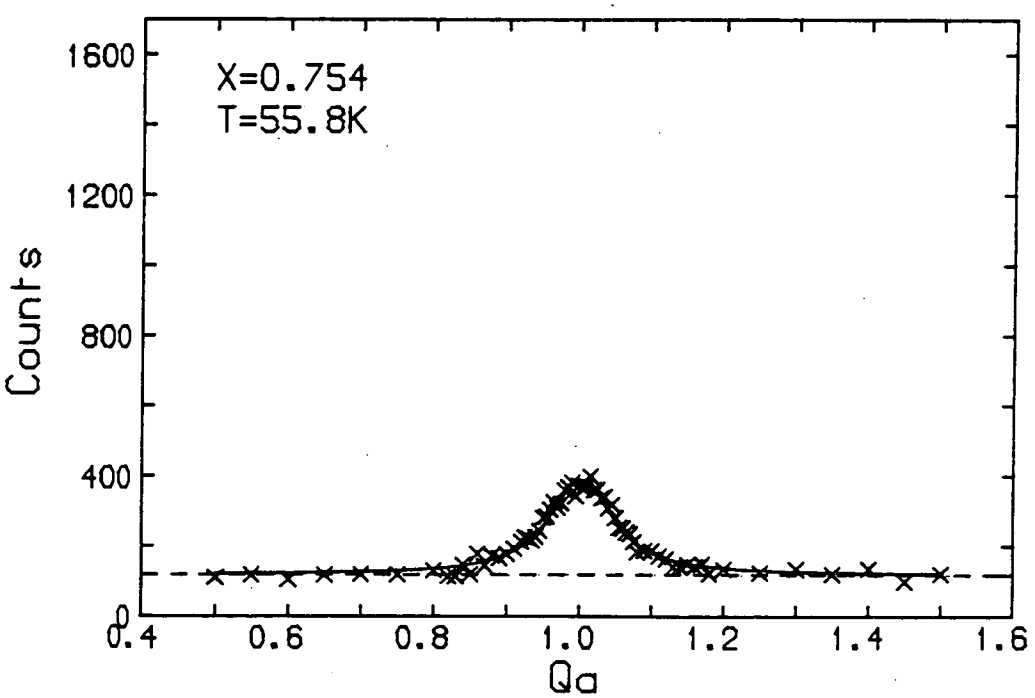

The entire fitting procedure was performed using the computer program K2FIT which incorporated a least squares fitting program LSOFIT. Each of the 26 scans were fitted separately but in each case the same flat background value was used. There were three adjustable parameters for each fit corresponding to Q_c, A'' and κ''. Since the scans were nominally centred on $Q = (1,0,-0.392)$ then $Q_c \simeq 1$ for all of the scans. The parameter κ'' was expected to be the inverse correlation length and A'' proportional to the staggered susceptibility:

$$A'' \propto \frac{\chi''(q=0)}{\chi^o} \quad . \tag{5.5.19}$$

At the (L,0,0) Bragg peak the resolution ellipse has its major axis almost along $[1,0,0]$. At $Q = (1,0,-0.392)$ the long axis of the resolution function in the scattering plane is still almost parallel to the $[1,0,0]$ direction and so the full width half maximum ΔQ_H for the (Gaussian) horizontal part of the resolution function was taken to be the value obtained from a scan through the (1,0,0) Bragg peak along the $[1,0,0]$ direction. The full width half maximum ΔQ_V for the vertical part of the resolution function was measured by the method discussed in the experimental section. The values used were $\Delta Q_H = 0.0181 a_m^*$ and $\Delta Q_V = 0.0678 b_m^*$ (note that $a_m^* = 2\pi/a_m$, $b_m^* = 2\pi/b_m$ and $a_m = b_m = 7.0956\text{Å}$ for $Rb_2Mn_xCr_{1-x}Cl_4$ with $x = 0.754$.

Figure (5.5.3) shows the experimental data with the calculated intensity from the best fit superimposed at several temperatures.

The agreement between the calculated intensity and the experimental data was good at all 26 temperatures for which scans were performed.

Figure (5.5.4) shows a graph of κ'' as a function of temperature and Figure (5.5.5) shows a graph of A'' as a function of temperature over the entire temperature range. The behaviour of κ'' and A'' is not that which might be expected. A $d=2$ system with purely Heisenberg interactions is not expected to undergo a phase transition. However in $d=2$ systems with Heisenberg interactions and a small single ion anisotropy it has been shown that a phase transition occurs and that the staggered susceptibility and correlation length have lower law divergences with exponents close to those of the $d=2$ Ising model (Birgeneau et al. (1977)).

The expected power laws for κ'' and $\chi''(q=0)/\chi^{o}$ were given by:

$$\kappa'' = F(T/T_N - 1)^{\nu} \tag{5.5.19}$$

and

$$\frac{\chi''(q=0)}{\chi^{o}} = C(1 - \frac{T_N}{T})^{-\gamma} \quad . \tag{5.5.20}$$

The results from the experiments on pure antiferromagnetic systems such as K_2NiF_4, K_2MnF_4 and mixed antiferromagnetic systems such as $Rb_2Mn_{0.5}Ni_{0.5}F_4$ (Birgeneau et al. (1977)) showed that the susceptibility decreased and κ'' increased so rapidly below T_N that scattering intensity was observable only down to a few degrees below T_N. The experimental data for $Rb_2Mn_xCr_{1-x}C\ell_4$ with $x = 0.754$ and the parameters obtained from it do not indicate that behaviour.

Thorough checks were made in order to ensure that the correct resolution parameters had been used, particularly with regard to the horizontal resolution. A program TWOAXIS was written to calculate

FIGURE (5.5.4): Inverse correlation length κ'' as a function of temperature obtained by fitting a single Lorentzian function for the diffuse scattering as described in the text. The values of K" obtained from the graph should be divided by a factor of 1000 to obtain the value of K" expressed in terms of the reciprocal lattice units along the [1,0,0] direction.

Fig (5.5.4)

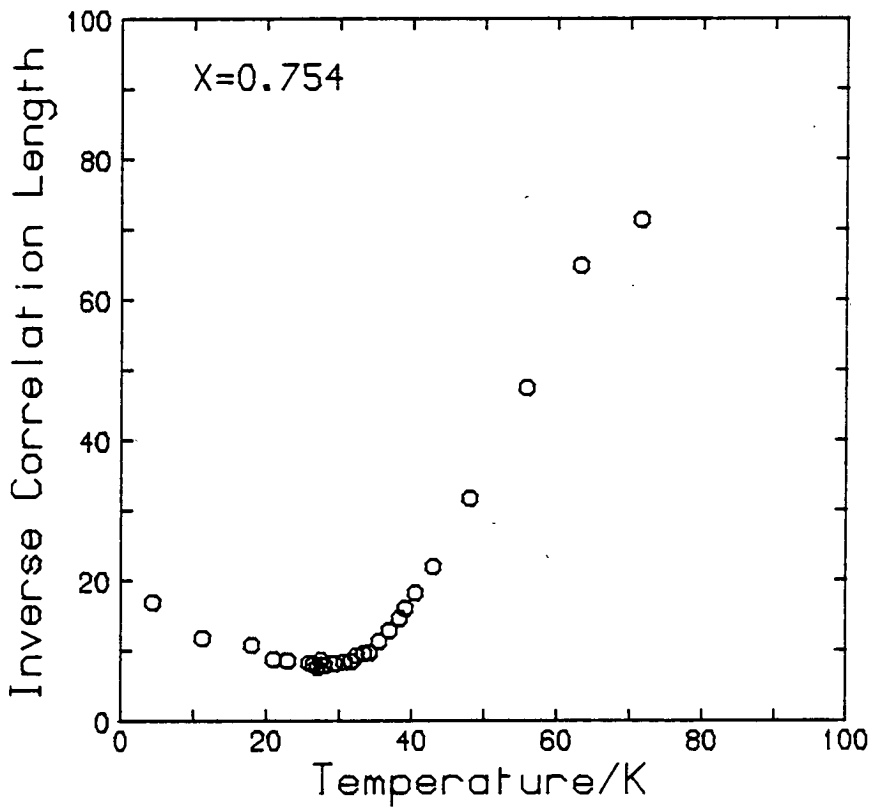
X=0.754
Inverse Correlation Length
Temperature/K
0
20
40
60
80
100

FIGURE (5.5.5): The staggered Susceptibility $\chi''(q=0)/\chi^{o} \propto A''$ as a function of temperature obtained by fitting a single Lorentzian function for the diffuse scattering, as described in the text. The intensity is given in arbitrary units.

Fig (5.5.5)

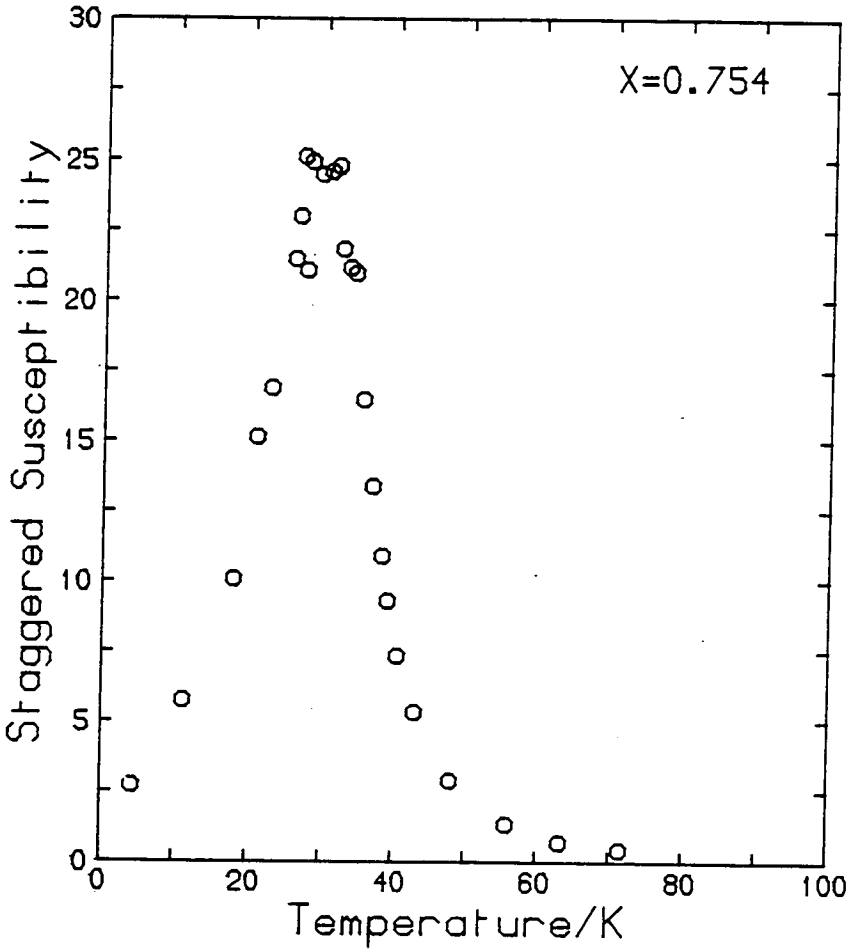
X=0.754
Staggered Susceptibility
Temperature/K
0
5
10
15
20
25
30
0
20
40
60
80
100

the resolution widths both along the length of the wavevector transfer and at right angles to it in the scattering plane. The program used the Cooper-Nathans formalism for the resolution function of a two-axis spectrometer (Cooper and Nathans (1968)). Assuming an effective horizontal mosaic spread for the monochromator of $\eta_m' = 0.55^o$ and a horizontal mosaic spread for the sample of $\eta_s = 0.332^o$, excellent agreement was obtained between the calculated Bragg peak widths and the experimental values for both longitudinal and transverse scans through the (0,0,2), (0,0,4), (0,0,6), (0,0,8), (2,0,0) and (4,0,0) nuclear Bragg peaks. Having established the correct values for η_m' and η_s by comparing calculated and experimental widths for these resolution limited nuclear Bragg peaks, the longitudinal width for the (1,0,0) magnetic Bragg peak was then calculated. This calculated width was $1\frac{3}{4}\%$ higher than the experimental value. This difference was well within the typical differences between the calculated and experimental values for the nuclear Bragg peaks, verifying that the (1,0,0) magnetic Bragg peak was effectively resolution limited. The assumption that the Bragg peak widths for a longitudinal scan through the (1,0,0) Bragg peak was the best estimate of the horizontal resolution width for the scans through $Q = (1,0,-0.392)$ was therefore entirely justified. (The effect of changing the horizontal and vertical resolution widths by small but significant amounts, was to change the absolute values for the parameters derived from the fits but not to change the qualitative features of the staggered susceptibility and inverse correlation length against temperature plots.)

Clearly, either there is an unusual type of magnetic phase transition around $T = 32K$ or there must be some other explanation of the temperature dependence of the scattering around the (1,0,η) ridge. One possibility is that there may have been large concentration fluctuations in the sample. The effect of this would be to smear the transition since the concentrations at different parts of the crystal would correspond to different values of T_N. Secondly, there may have been contributions from the transverse susceptibility (which would not be expected to diverge at $T = T_N$). Birgeneau et al. (1977) were able to fit two Lorentzian functions to their data, one corresponding to the longitudinal wavevector dependent susceptibility and the other corresponding to the transverse wavevector dependent susceptibility. Below the critical temperature region they found the scattering to correspond solely to the transverse susceptibility. They found the transverse susceptibility $\chi^{\perp}(q=0)$ to be constant, (this corresponds to the staggered susceptibility $\chi^{\perp}(q=0)|\chi^{o}$ varying linearly with the temperature) in that temperature region and were able to fix a Lorentzian function for the transverse susceptibility, then fit the additional scattering to a Lorentzian function for the longitudinal susceptibility for temperatures up to and just above T_N.

An attempt was made to fit the $Rb_2Mn_xCr_{1-x}C\ell_4$ (with $x = 0.754$) data using two Lorentzians. The only way this could be achieved was to fix the Lorentzian parameters $K^{\perp}$ and $A^{\perp}$ for the transverse susceptibility for each scan. $A^{\perp}$ was expected to vary linearly with temperature and $K^{\perp}$ was expected to remain constant up to T_N. No attempt was made to fit the data below

$T = 22.9K$ because it was expected that the quasi-elastic approximation that $k_BT >> \hbar\omega$ was not being fulfilled in that temperature region, leading to non-linear behaviour of $A^{\perp}$ with temperature. $A^{\perp}$ and $K^{\perp}$ were set at the values obtained at $T = 22.9K$ in the previous single Lorentzian fit. At higher temperatures $K^{\perp}$ was fixed at this value and $A^{\perp}$ was fixed at a value proportional to the temperature. Unfortunately with the parameters of the fixed Lorentzian set at these values, another Lorentzian could not sensibly be fitted to the additional scattering intensity.

In conclusion, for the sample of $Rb_2Mn_xCr_{1-x}C\ell_4$ with $x = 0.754$, there was a magnetic phase transition at around $T_N = 32K$. The evidence for this lies in the onset of Bragg scattering at the (1,0,0) position below T_N and the decrease in width and increase in intensity of the diffuse scattering in scans through the (1,0,η) ridge, as T_N was approached from either above or below. The data from scans through the (1,0,η) ridge of diffuse scattering could be fitted to a single Lorentzian function for the wavevector dependent susceptibility, with good agreement between the experimental data and the calculated values at all temperatures. However, the parameters A'' and K'' obtained from the fitting do not behave, as a function of temperature, in a similar way to similar parameters obtained in mixed antiferromagnetic systems, such as $Rb_2Mn_{0.5}Ni_{0.5}F_4$ (Birgeneau et al. (1977)). This could be for physical reasons (there are competing exchange interactions in this system) or could be due to effects such as concentration fluctuations in the sample or a contribution to the observed intensity from the transverse susceptibility which cannot be quantified. Finally, it is noted

that the value of T_N = 32K is approximately 8K lower than the value of T_N = 40K implied by the phase diagram of Kohles et al. (1982).

CHAPTER 6

CONCLUSIONS

In Chapter 3 magnetic excitation spectra for a diluted simple cubic ferromagnet with nearest neighbour Heisenberg interactions were calculated by the "equation-of-motion" method. Spectra were obtained with reduced wavevector values along the [1,1,1] direction across the entire Brillouin zone for the magnetic site concentration values $x = 0.9$, $x = 0.5$ and $x = 0.34$. The effects of disorder were expected to become more obvious as the reduced wavevector increased at a given value of x and this proved to be the case. The spectra consisted of broad distributions of intensity with the weight moving to higher energies as the reduced wavevector increased. The effect of decreasing x was to move the weight in the spectra to lower energies at a given reduced wavevector, (except at $q = 0$, where at all three concentrations resolution limited peaks were obtained). A comparison was made between calculated spectra and data from inelastic neutron scattering measurements on the metallic diluted ferromagnet $Cr_{1-x}Fe_x$ with $x = 0.27$. This comparison was of a qualitative nature but nevertheless suggested that the features observed in the inelastic neutron scattering experiments could be attributed mainly to the effects of the dilution-induced disorder. In addition, this work has stimulated more experimental interest in the system $Cr_{1-x}Fe_x$ with $x = 0.27$. A proposal has been submitted to the Institut Laue-Langevin, Grenoble, France (I.L.L.) to test whether a localised mode observed in the calculated spectra also

exists in the $Cr_{1-x}Fe_x$ system. This could give valuable information as to the range of the exchange interactions in the $Cr_{1-x}Fe_x$ system for $x = 0.27$.

In Chapter 4, the results of an investigation into the magnetic structure and magnetic excitations for the $d = 2$ mixed magnetic system with competing spin anisotropies $K_2Co_xFe_{1-x}F_4$ were reported. Neutron scattering experiments for a sample with $x = 0.6$ showed that below a phase transition at $T_N = 92.2 \pm 0.1K$ the system exhibited uniaxial antiferromagnetic long-range order with the spins aligned along the c-axis of the unit cell, and the temperature dependence of the order parameter was well described by the two-dimensional Ising model. Inelastic neutron scattering measurements at $T \sim 5K$ revealed two bands of magnetic excitations. A lower energy band corresponding to excitations propagating mainly on the Fe ions and a higher energy band corresponding to excitations propagating mainly on the Co ions.

Neutron scattering measurements were also performed on a sample with nominally $x = 0.2$. Below a phase transition at $T_N = 66 \pm 1K$ there was antiferromagnetic long-range order for the spin components along the c-axis. The critical exponent β for the order parameter was slightly higher than that for the $d = 2$ Ising model but this was considered to be due to the fact that no account was taken of rounding of the transition due to concentration inhomogeneities in the sample. Below a second phase transition at $T_L = 32 \pm 2K$ components of spin in the basal a-b plane acquired long range order. The details of this lower transition are somewhat obscure since no two-dimensional critical scattering was observed at T_L. Never-

theless, the phase transition at T_L was found to be sharp as a function of temperature, when allowances were made for sample inhomogeneity. This is different from the behaviour found by Wong et al. (1983) in $Co_xFe_{1-x}C\ell_2$, where the lower transition was very smeared. They suggested that the lower transition at T_L in $Co_xFe_{1-x}C\ell_2$ was smeared because the ordering of one spin component generated a random field on the other and this random field inhibited the development of true long-range order. This mechanism could occur in $Co_xFe_{1-x}C\ell_2$ because of a Dzyaloshinsky type of interaction arising from the low local symmetry in the $FeC\ell_2$ structure. The difference between the results at T_L for $Co_xFe_{1-x}C\ell_2$ and $K_2Co_xFe_{1-x}F_4$ with $x = 0.2$ may therefore be attributable to the fact that the local symmetry in the latter structure is much higher. Inelastic neutron scattering measurements at $T \simeq 5K$ for $K_2Co_xFe_{1-x}F_4$ with $x = 0.2$ revealed a single branch of magnetic excitations at energies below $\sim$ 12 meV.

More detailed inelastic neutron scattering measurements of the magnetic excitations in the OAF phase were made on a sample with nominally $x = 0.27$, for which $T_N = 64.4 \pm 0.6K$ and $T_L = 27 \pm 2K$ (Vlak et al. (1983)). These measurements revealed two branches of magnetic excitations which appeared to be degenerate at the Brillouin zone boundary. An investigation of the temperature dependence of the lower branch of the excitations at small reduced wavevector/low energy showed that the spin wave gap $\varepsilon_{g\perp}$ decreased and the intrinsic width of the excitation increased as the temperature approached T_L from below.

Calculations have also been presented of the magnetic structure

of $K_2Co_xFe_{1-x}F_4$ at T = OK. The results of these calculations predict that at T = OK, the OAF phase is in the concentration range $0.1 < x < 0.5$. The results from the calculations of the concentration range of the OAF phase and the average cant angle, between the spin and the c-axis, as a function of concentration are reasonably consistent with the experimental results of other workers (Vlak et al., (1985), Fendler and van Eynatten (1984)).

Magnetic excitation spectra for $K_2Co_xFe_{1-x}F_4$ were calculated by the "equation-of-motion" technique. In the uniaxial antiferromagnetic phase $S^{xx}(\underline{Q},\omega) = S^{yy}(\underline{Q},\omega)$ and $S^{zz}(\underline{Q},\omega) = 0$, as expected by symmetry considerations. However in the OAF phase $S^{xx}(\underline{Q},\omega)$, $S^{yy}(\underline{Q},\omega)$ and $S^{zz}(\underline{Q},\omega)$ are different. There therefore may be three spin wave branches in the OAF phase. These would, however, be difficult to resolve by inelastic neutron scattering experiments on the x = 0.2 and x = 0.27 samples, because they cross in the Brillouin zone and are close together, particularly at the Brillouin zone boundary. The results for x = 0.6, x = 0.27 and x = 0.2 are in reasonable agreement with the experimental results. Calculations of the concentration dependence of the $S^{xx}(\underline{Q},\omega)$, $S^{yy}(\underline{Q},\omega)$ and $S^{xx}(\underline{Q},\omega)$, at the Brillouin zone centre, revealed a minimum in the energy gaps for all three spectra at the phase boundary between the OAF and the uniaxial phases for T = 0.

Finally, in Chapter 5 results were reported of an investigation into the magnetic phase transition and magnetic excitations in $Rb_2Mn_xCr_{1-x}C\ell_4$, with x = 0.754. Measurements of the order parameter and the d = 2 diffuse scattering intensity revealed that there was a phase transition around T_N = 32K below which antiferromagnetic

long-range order existed. The results of fitting a single Lorentzian function for the longitudinal susceptibility convoluted with the spectrometer resolution function, to the data from scans through the $(1,0,\eta)$ ridge of diffuse scattering, gave results which were unusual for both the longitudinal inverse correlation length K'' and the longitudinal staggered susceptibility at $q = 0$. It is believed that a combination of concentration fluctuations in the sample and transverse susceptibility scattering, neither of which could be accounted for quantitatively, may have caused the transition to appear smeared out in temperature. Inelastic neutron scattering measurements on the magnetic excitations in this $x = 0.754$ sample at $T = 5K$ revealed a single branch of excitations at slightly lower energy, compared with the energy of the excitations in Rb_2MnCl_4, at a given reduced wavevector. The observed scattering intensity was very weak for reduced wavevector transfer values beyond two fifths of the way to the Brillouin zone boundary and further measurements are planned, using a higher flux instrument at the I.L.L. to investigate the magnetic excitations near the Brillouin zone boundary.

REFERENCES

Alben, R., Kirkpatrick, S. and Beeman, D. (1977) Phys. Rev. B15, 346.

Aldred, A.T., Rainford, B.D., Konvel, J.S. and Hicks, T.J. (1976) Phys. Rev. B14, 228.

Als-Nielsen, J., Birgeneau, R.J., Guggenheim, H.J. and Shirane, G. (1975) Phys. Rev. B12, 4963.

Bacon, G.E. (1975) 'Neutron Diffraction', 3rd Ed., Clarendon Press, Oxford.

Bevaart, L., Frikee, E., Lebesque, J.Y. and de Jongh (1978) Phys. Rev. B18, 3376.

Birgeneau, R.J., Guggenheim, H.J. and Shirane, G. (1970) Phys. Rev. B1, 2211.

Birgeneau, R.J., Skalyo, Jr. J. and Shirane, G. (1971) Phys. Rev. B3, 1736.

Birgeneau, R.J., Walker, L.R., Guggenheim, H.J., Als-Nielsen, J. and Shirane, G. (1975) J. Phys. C., 8, L328.

Birgeneau, R.J., Als-Nielsen, J. and Shirane, G. (1977) Phys. Rev. B16, 280.

Breed, D.J., Gilijamse, K. and Miedema, A.R. (1969) Physica, 45 (205).

Burke, S.K., Cywinski, R., Davis, J.R. and Rainford, B.D. (1983) J. Phys. F, 13, 451.

Chesser, N.J. and Axe, J.D. (1973) Acta Cryst. A29, 160.

Cooper, M.J. and Nathans, R. (1967) Acta Cryst. 23, 357.

Cooper, M.J. and Nathans, R. (1968) Acta Cryst. A24, 481.

Cowley, R.A. and Buyers, W.J.L. (1972) Rev. Mod. Phys. 44, 406.

Cowley, R.A., Shirane, G., Birgeneau, R.J. and Guggenheim, H.J. (1977) Phys. Rev. B15, 4292.

Cowley, R.A., Birgeneau, R.J., Shirane, G., Guggenheim, H.J. and Ikeda, H. (1980d) Phys. Rev. B21, 4038.

Cowley, R.A. (1982) in 'Excitations in Disordered Systems', ed. M.F. Thorpe, Plenum Press, New York.

Cowley, R.A., Hagen, M. and Belanger, D.P. (1984) J. Phys. C. 17, 3763.

Day, P., Hutchings, M.J. Janke, E. and Walker, P.J. (1979) J. Chem. Soc. Chem. Commun., 711.

Dorner, B. (1972) Acta Cryst. A28, 319.

REFERENCES (Contd.)

Epstein, A., Gurewitz, E., Makowsky, J. and Shaked, H. (1970) Phys. Rev. B2, 3703.

Fair, M.J., Gregson, A.K., Day, P. and Hutchings, M.T. (1977) Physica 86-88B, 657.

Fendler, K. and von Eynatten, E. (1984) Z. Phys. B54, 313.

Fishman, S. and Aharony, A. (1978) Phys. Rev. B18, 3507.

Fishman, S. and Aharony, A. (1980) Phys. Rev. B21, 280.

Hagen, M. (1984) Ph.D. Thesis, University of Edinburgh, unpublished.

Higgins, S.A., Cowley, R.A., Hagen, M. Kjems, J.K., Dürr, U. and Fendler, K. (1984) J. Phys. C 17, 3235.

Hutchings, M.T., Fair, M.J., Day, P. and Walker, P.J. (1976) J. Phys. C, 9, L55.

Ikeda, H. and Hirakawa, K. (1974) Solid State Commun. 14, 529.

Ito, A., Morimoto, S., Someya, Y., Ikeda, H., Syono, Y. and Takei, H. (1982) Solid State Commun. 41, 507.

Ito, A., Morimoto, S., Someya, Y., Syono, Y. and Takei, H. (1982) J. Phys. Soc. Japan 51, 3173.

Katsumata, K., Nire, T., Tanimoto, M. and Yoshizawa, H. (1982) Phys. Rev. B25, 428.

Katsumata, K. (1983) J. Magn. Magn. Mater. 31-34, 1435.

Kittel, C. (1976) 'Introduction to Solid State Physics', 5th Ed., Wiley, New York.

Kohles, N., Theuerkaufer, H., Strobel, K., Geick, R. and Treutmann, W. (1982) J. Phys. C 15, L137.

Lines, M.E. (1967) Phys. Letters 24A, 591.

Macco, F., Lehmann, W., Breitling, W., Slawska-Wariewska, A.E. and Weber, R. (1978) Solid State Commun. 26, 429.

Macco, F., Lehmann, W. and Weber, R. (1979) J. Phys. C 12, L233.

Maletta, H. and Felsch, W. (1979) Phys. Rev. B20, 1245.

Marshall, W. and Lovesey, S.W. (1971) 'Theory of Thermal Neutron Scattering', Oxford University Press, Oxford.

REFERENCES (Contd.)

Matsubara, F. and Inawashiro, S. (1977) J. Phys. Soc. Japan 42, 1529.

Matsubara, F. (1981) J. Phys. Soc. Japan, 50, 1469.

Mitchell, P.W., Cowley, R.A. and Higgins, S.A. (1984) Acta Cryst. A40, 152.

Mitchell, P.W. (1985) Private communication.

Mitchell, P.W. and Dove, M.T. (1985) To be published in J. Appl. Cryst.

Mitchell, P.W., Higgins, S.A. and D.McK. Paul (1985). Paper submitted to Proceedings of Int. Conf. on Neutron Scattering, Santa Fe, New Mexico, August, 1985. To be published in Physica B and C.

Neutron Research Facilities at the I.L.L. High Flux Reactor (1983).

Onsager, L. (1944) Phys. Rev. 65, 117.

Pynn, R. and Passel, L. (1974) B.N.L. Research Memo No. G-19.

Rae, A.I.M. (1981) "Introduction of Quantum Mechanics, McGraw-Hill, London.

Schroder, B., Wagner, V., Lehner, N., Kesharwani, K.M. and Ceick, R. (1980) Phys. Stat. Sal. 97, 501.

Shapiro, S.M., Fincher, C.R., Palumbo, A.C. and Parks, R.D. (1981) Phys. Rev. B24, 6661.

Someya, Y., Ito, A. and Katsumata, K. (1983) J. Phys. Soc. Japan 52, 254.

Squires, G.L. (1976) "Practical Physics 2le", McGraw-Hill, London.

Stephenson, G. (1983) "Mathematical Methods for Science Students", London.

Thorpe, M.F. and Alben, R. (1976) J. Phys. C9, 2555.

Thurlings, M.P.H., van der Pol, A. and de Wijn, H.W. (1977) Solid State Commun. 24, 829.

Thurlings, M.P.H., Frikee, E. and de Wijn, H.W. (1982) Phys. Rev. B25, 4750.

Tracy, C.A. and McCoy, B.M. (1975) Phys. Rev. B12, 368.

Vlak, W.A.H.M., Frikee, E., Arts, A.F.M. and de Wijn, H.W. (1983) J. Phys. C16, L1015.

Vlak, W.A.H.M., Dikken, B.J., Arts, A.F.M. and de Wijn, H.W. (1985) Phys. Rev. B31, 4496.

Vlak, W.A.H.M., van Dort, M.J., Arts, A.F.M. and de Wijn, H.W. (1985) Submitted to Phys. Rev. B.

Watson, R.E. and Freemen, A.J. (1961) Acta Cryst. 14, 27.

REFERENCES (Contd.)

Werner, S.A. and Pynn, R. (1971) J. Appl. Phys. 42, 4736.

Windsor, C.G. (1981) 'Pulsed Neutron Scattering', London.

Wong, P.Z., Horn, P.M., Birgeneau, R.J. and Shirane, G. (1983) Phys. Rev. B27, 428.

Ziman, J.M. (1971) 'Principles of the Theory of Solids', 2nd Ed., Cambridge University Press, Cambridge.

PUBLISHED PAPERS

Acta Cryst. (1984). A40, 152–160

The Resolution Function of Triple-Axis Neutron Spectrometers in the Limit of Small Scattering Angles

BY P. W. MITCHELL, R. A. COWLEY AND S. A. HIGGINS

Department of Physics, University of Edinburgh, Mayfield Road, Edinburgh EH9 3JZ, Scotland

(*Received* 16 *May* 1983; *accepted* 26 *September* 1983)

Abstract

The Cooper–Nathans formulation of the resolution function of a triple-axis crystal spectrometer for neutron-scattering experiments gives a singular resolution matrix when the scattering angle is small. The origin of this singularity is discussed and an alternative derivation of the resolution matrix given which avoids this difficulty. The results are illustrated by numerical calculations for several typical experiments showing that resolution corrections may be large and very significant for experiments at small scattering angles.

1. Introduction

A knowledge of the effects of the experimental resolution in momentum and energy transfer is an important part of any inelastic neutron-scattering experiment. A general formulation of the resolution function of a triple-axis spectrometer was derived by Cooper & Nathans (1967), and discussed by Bjerrum Møller & Nielsen (1970), using a Gaussian approximation for all the contributing transmission functions and crystal mosaic distributions, and the normalisation of this function has been treated at length by Dorner (1972), and Chesser & Axe (1973). Computer programs are widely available for the calculation of this function, and it is known to provide a good representation of the instrumental resolution in many types of triple-axis measurement.

This paper is concerned with one particular limit of the triple-axis resolution function, that of small scattering angle at the sample (small $2\theta_s$ in Fig. 1). Experiments performed at small scattering angles tend to suffer from high background counting rates, and severe restrictions imposed on the energy transfers available by the conservation of momentum requirement (kinematic limits). In the measurement of low-energy magnetic excitations, however, particularly in ferromagnetic materials, such experiments have a number of advantages. Firstly, the magnetic form factor takes its maximum value near (0 0 0), the forward direction. Secondly, scattering from phonons is generally of low intensity, because of the $|\mathbf{Q}|^2$ factor ($\mathbf{Q}$ is the neutron wavevector transfer) in the phonon cross section. Thirdly, the effective resolution near (0 0 0) does not suffer from transverse or longitudinal broadening due to crystal mosaic spreads or lattice-parameter distributions [for the effect of the former on resolution, see Werner & Pynn (1971)], and this allows, under some circumstances, the direct measurement of the magnetic excitations in powdered or polycrystalline materials [*e.g.* Passell, Dietrich & Als-Nielsen (1976), on EuO and EuS] and even amorphous ferromagnetic materials (*e.g.* Axe, Shirane, Mizoguchi & Yamauchi, 1977). For these reasons, many experiments have been performed at small scattering angles in weakly ferromagnetic materials, for which the magnetic scattering may generally be weak compared with the phonon scattering, and large crystals may be difficult to grow.

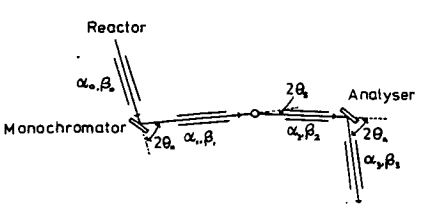

Fig. 1. Plan view of three-axis spectrometer. α, β are horizontal, vertical collimations. ε_M, ε_S, ε_A take the values -1, $+1$ according as scattering at monochromator, sample, analyser is to the right, left. Configuration shown is $\varepsilon_M = +1$, $\varepsilon_S = -1$, $\varepsilon_A = -1$.

As the scattering angle tends to zero, both the efficiency factor and some elements of the resolution matrix diverge, since both contain terms in the reciprocal of the sine of the scattering angle, and extreme care is required to treat the limit correctly. The problem first became apparent to the authors when using a standard computer program to calculate the Cooper–Nathans function at small scattering angles (0·5–1·5°). The resolution matrix itself becomes singular in the limit of the scattering angle tending to zero, and numerical integration over the resolution matrix does not give reliable results unless performed with great care and a high degree of numerical precision.

In the following section, we discuss this limit in the Cooper–Nathans formalism, and then in § 3 we give a more direct formulation of the resolution function, which completely eliminates the problems associated with the Cooper–Nathans function. The results are illustrated by some applications in § 4.

0108-7673/84/020152-09$01.50

2. Small-angle limit of the Cooper–Nathans resolution function

A triple-axis spectrometer (Fig. 1) uses Bragg reflection from a monochromator crystal to define a nominal incident neutron wavevector, $\mathbf{k}_I$,

$$|\mathbf{k}_I| = \frac{\pi}{d_M \sin\theta_M} \tag{2.1}$$

and reflection from an analyser crystal to define a nominal scattered wavevector, $\mathbf{k}_F$,

$$|\mathbf{k}_F| = \frac{\pi}{d_A \sin\theta_A}, \tag{2.2}$$

where $d_{M,A}$ is the appropriate plane spacing and $\theta_{M,A}$ is the appropriate Bragg angle. The directions of incident and scattered beams are defined by the collimators before and after the sample, and the scattered intensity is measured as a function of nominal momentum transfer, $\mathbf{Q}_0$, and nominal energy transfer, $h\nu_0$, where

$$\mathbf{Q}_0 = \mathbf{k}_I - \mathbf{k}_F, \tag{2.3}$$

$$h\nu_0 = \frac{\hbar^2}{2m}(|\mathbf{k}_I|^2 - |\mathbf{k}_F|^2). \tag{2.4}$$

Because of the non-zero angular divergences of the collimators and the mosaic spreads of the monochromator and analyser crystals, neutrons are counted in the detector which have not suffered the nominal momentum and energy changes. The actual changes, $\mathbf{Q}$ and $h\nu$, are related to $\mathbf{Q}_0$ and $h\nu_0$ by

$$\mathbf{Q} = \mathbf{Q}_0 + \delta\mathbf{Q} \tag{2.5}$$

$$h\nu = h\nu_0 + \delta(h\nu). \tag{2.6}$$

It is convenient to write these deviations from the nominal as a four-component vector, $\mathbf{X}$,

$$\mathbf{X} = [\delta\mathbf{Q}, \delta(h\nu)]. \tag{2.7}$$

Cooper & Nathans (1967) showed that the instrumental resolution can be written in the Gaussian approximation as

$$R(\mathbf{X}) = R_0 \exp\{-\tfrac{1}{2}\mathbf{X} \,.\, \mathbf{M} \,.\, \mathbf{X}\}. \tag{2.8}$$

R_0 and $\mathbf{M}$ are complicated functions of the angles defined by the collimators, the crystal mosaics and the nominal $|\mathbf{k}_I|$ and $|\mathbf{k}_F|$ (Chesser & Axe, 1973). R_0 also includes terms due to the detector efficiency and the monochromator and analyser reflectivities, and some of the elements of $\mathbf{M}$ depend upon the senses of scattering (*i.e.* to the left or to the right) at the monochromator, sample and analyser, in addition to the dependence of both R_0 and $\mathbf{M}$ on the scattering angle at the sample.

In detail, R_0 contains the following terms which depend on $2\theta_s$ ($2\theta_s$ is defined in Fig. 1),

$$R_0 \propto \frac{1}{A'^{1/2} \sin 2\theta_s} \tag{2.9}$$

(from Chesser & Axe, equation 6), where A' is as defined by Cooper & Nathans (equation 45*a*) (see also Appendix *A*: *A*.43). In the limit, as $2\theta_s$ goes to zero, the angles between $\mathbf{k}_I$ and $\mathbf{Q}_0$, and between $\mathbf{k}_F$ and $\mathbf{Q}_0$, φ_1 and φ_2, respectively (defined in Fig. 2), tend to the same value, φ, say, since

$$\varphi_1 = \varphi_2 + 2\theta_s \tag{2.10}$$

$$\therefore \quad \varphi_1 \simeq \varphi_2 \equiv \varphi. \tag{2.11}$$

The quantity A' is the sum of six terms, two of which are proportional to

$$\frac{Q_0^2 \cos^2\varphi}{k_F^2 \sin^2 2\theta_s}.$$

For the sake of simplicity, consider two possible cases in whch $2\theta_s$ tends to zero. Firstly, for elastic scattering ($h\nu = 0$, $|\mathbf{k}_I| = |\mathbf{k}_F|$), this quantity decreases as $2\theta_s$ tends to zero ($Q_0 \simeq k_F \sin 2\theta_s$; $\cos^2\varphi \simeq \frac{1}{4}\sin^2 2\theta_s$), A' tends to a constant value and R_0 then diverges as $1/\sin 2\theta_s$. Secondly, for inelastic scattering at constant $\mathbf{Q}_0$, A' behaves like $1/\sin^2 2\theta_s$ as $2\theta_s$ tends to zero, and R_0 tends to a large ($\propto k_F^2/Q_0^2$) constant value.

The behaviour of the elements of the matrix $\mathbf{M}$ in the small $2\theta_s$ limit may be illustrated by considering only the in-plane (x and y) components of $\delta\mathbf{Q}$, because the out-of-plane (z) momentum component is de-coupled from the rest and does not depend on $2\theta_s$. For simplicity, we illustrate the results by choosing $\delta(h\nu) = 0$. This gives the section through the resolution function in the x–y plane (the scattering plane) at zero energy deviation. Rotation by an angle, θ, in this plane diagonalizes this part of the matrix (see Appendix *A* for details), and the result is that

$$\theta = -\varepsilon_s \varphi \tag{2.12}$$

$$M'_{xx} \propto \frac{m_{ij}^2}{A' \sin^2 2\theta_s} \tag{2.13}$$

$$M'_{yy} \propto m_{ij}^2, \tag{2.14}$$

where the new x, y axes are related to the Cooper–Nathans axes (parallel, perpendicular to $\mathbf{Q}_0$) by the angle θ, and the m_{ij} are defined in Appendix *A* (equations *A*.6–*A*.13), and are constant as $2\theta_s \to 0$.

Equation (2.12) shows that the rotation, θ, required from the Cooper–Nathans coordinates $\mathbf{X}$ to the eigenvectors of the section of the resolution matrix in the

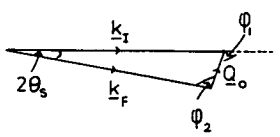

Fig. 2. Scattering triangle (momentum conservation) corresponding to Fig. 1.

scattering plane is just the angle that $\mathbf{Q}_0$ makes with either $\mathbf{k}_I$ or $\mathbf{k}_F$. This means that this section through the resolution function does not change its orientation with respect to $\mathbf{k}_F$, in a constant-Q scan, although it rotates with respect to $\mathbf{Q}_0$. Equations (2.13) and (2.14) show that the component of M in the plane and parallel to $\mathbf{k}_F$ is very much larger than the component perpendicular to $\mathbf{k}_F$. This shows that only one of the eigenvalues of M becomes large as $2\theta_s$ becomes small, and that the resolution function is very thin in the direction parallel to $\mathbf{k}_F$ when $\delta(h\nu)=0$.

It should be emphasized that the above is concerned with a particularly simple case of the four-dimensional resolution function, and illustrates the physical effect of the divergence found in the limit of small scattering angle. It suggests that a different approach to the formulation of the resolution function might eliminate the divergence and this is pursued in the next section.

3. Direct formulation for small-angle limit

As may be seen from the results of § 2 above, that component of momentum deviation which is parallel to $\mathbf{k}_F$ is highly correlated with the energy deviation. So, in the small-scattering-angle limit, simplification may be achieved by working in a frame of reference fixed with respect to $\mathbf{k}_F$, say. (Because the scattering angle is small, we could choose $\mathbf{k}_I$ instead, but $\mathbf{Q}_0$ as chosen by Cooper & Nathans varies in direction with respect to $\mathbf{k}_F$ rapidly as $h\nu_0$ is varied.)

The derivation of the resolution function proceeds as for the Cooper–Nathans form to the point where the instrument transmission is expressed in terms of deviations from the nominal $\mathbf{k}_I$ and $\mathbf{k}_F$, in each of three mutually orthogonal directions, in frames fixed with respect to $\mathbf{k}_I$ and $\mathbf{k}_F$, (x parallel to $\mathbf{k}$, and z out of scattering plane in each case). Cooper & Nathans then transform to the four components of X and two redundant variables, one in-plane and one out-of-plane, which are then integrated out. In the limit considered here, we take $\mathbf{k}_I$ and $\mathbf{k}_F$ to be parallel (Fig. 3), and transform to three components of $\delta\boldsymbol{\kappa}$ (momentum deviations viewed in the frame fixed with respect to $\mathbf{k}_F$), and three redundant variables, which are integrated out.

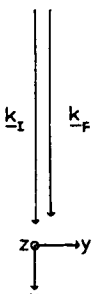

Fig. 3. Coordinates for calculating κ. Note that, when relating to Q, it is still necessary to calculate φ, the angle between $\mathbf{Q}_0$ and $\mathbf{k}_I$ or $\mathbf{k}_F$ (see Fig. 2).

Explicitly, we put

$$\delta\boldsymbol{\kappa} = \delta\mathbf{k}_i - \delta\mathbf{k}_f \tag{3.1}$$

and transform from the space defined by ($\delta\mathbf{k}_i$, $\delta\mathbf{k}_f$) to that defined by ($\delta\mathbf{k}_i$, $\delta\boldsymbol{\kappa}$). The energy deviation is given by

$$\delta(h\nu) = \frac{\hbar^2}{2m}(2|\mathbf{k}_I|\delta k_{ix} - 2|\mathbf{k}_F|\delta k_{fx}) \tag{3.2}$$

or

$$\delta(h\nu) = \frac{\hbar^2}{m}\left[\frac{(|\mathbf{k}_I|+|\mathbf{k}_F|)}{2}(\delta k_{ix} - \delta k_{fx}) + \frac{(|\mathbf{k}_I|-|\mathbf{k}_F|)}{2}(\delta k_{ix} + \delta k_{fx})\right]. \tag{3.3}$$

At small wavevector transfers, the second term in (3.3) is much smaller than the first, so that the energy deviation is linearly dependent on the x component of $\delta\boldsymbol{\kappa}$,

$$\delta(h\nu) = \frac{\hbar^2}{2m}(|\mathbf{k}_I|+|\mathbf{k}_F|)\,\delta\kappa_x. \tag{3.4}$$

This linear dependence of the energy deviation on one of the momentum-deviation components is the origin of the singularity of the Cooper–Nathans matrix in the limits of small $\mathbf{Q}_0$, and the divergence of the Chesser & Axe efficiency terms. By inserting this dependence analytically at this stage in the derivation, the resulting resolution function, now expressed in terms of three rather than four variables, does not have a singularity as $2\theta_s$ goes to zero.

We now have the resolution matrix M expressed in terms of the three components of κ, one of which (z) is not coupled to the other two. It is straightforward to diagonalize M by a simple rotation in the scattering plane by some angle Θ. All the information about the resolution function is contained in the three eigenvalues of M, the angle Θ, and the efficiency factor R_0, all of which are derived in closed form in Appendix *B*. The energy deviation is given by (3.4). We have therefore eliminated the difficulties encountered at small $2\theta_s$ in the conventional approach.

The expressions derived in Appendix *B* show that the slope of the resolution matrix varies rapidly with energy transfer and in particular that it is possible to focus both energy gain and energy loss at small scattering angles (Axe *et al.*, 1977), as can also be seen qualitatively without the use of algebra. It is possible to obtain further simplifications if the dispersion relation is a function of only $|\mathbf{Q}|$, but these are sufficiently complex, as the resolution function is then no longer Gaussian, that quantitative calculations are just as readily performed with the expressions given in Appendix *B*.

4. Applications of the direct formulation

The prediction of excitation line-widths and line-shapes from model scattering laws may be accomplished very simply in many special cases (Cooper & Nathans, 1967; Haywood, 1971). However, when the scattering law varies rapidly or non-linearly over the volume of the resolution function, such predictions necessarily involve the use of numerical integration methods (Werner & Pynn, 1971; Samuelson, 1971).

A typical ferromagnon dispersion law at small $|\mathbf{Q}|$ may be written as

$$h\nu = \varepsilon_g + D|\mathbf{Q}|^2, \tag{4.1}$$

where ε_g is the anisotropy gap, and is usually very small, and D is called the spin wave stiffness. Thus the excitation energy is a rapidly varying function of $|\mathbf{Q}|$ and, because of the population term in the cross section, the intensity of scattering is a function of $|\mathbf{Q}|$. The problem is further accentuated by the design of triple-axis spectrometers, which usually use relaxed out-of-plane collimation to maximize the scattering intensity, but in an experiment where the nominal wavevector transfer, $\mathbf{Q}_0$, is small, the out-of-plane deviations, δQ_z, may be as large as, or larger than, $|\mathbf{Q}_0|$. Since

$$|\mathbf{Q}|^2 = |\mathbf{Q}_0|^2 + (\delta Q_z)^2 + (\delta Q_y)^2 + (\delta Q_x)^2 + 2|\mathbf{Q}_0|\,\delta Q_x, \tag{4.2}$$

the spin wave energies sampled in the resolution volume may be up to several times as large as the spin wave energy at the nominal wavevector. This means that the scattering observed in a constant-Q scan is broad in energy, and the peak of the scattering may be at some energy higher than the energy of the spin wave at the nominal wavevector. These effects are just the same as those observed for excitations near Bragg peaks at scattering angles other than zero (Samuelsen, Hutchings & Shirane, 1970; Hutchings, Als-Nielsen, Lingard & Walker, 1981). It is not difficult to show that, if the in-plane resolution were to be perfectly sharp, the scattering from spin waves in a constant-Q scan would appear as in Fig. 4. The intensity, $I(\nu)$, is given by

$$I(\nu) = \begin{cases} [n(\nu) + \frac{1}{2} \pm \frac{1}{2}] \exp\left\{-\frac{1}{2} M_{zz}\left[\dfrac{|h\nu| - \varepsilon_g}{D} - Q_0^2\right]\right\} \\ \qquad \text{if } |h\nu| \geq \varepsilon_g + DQ_0^2 \\ 0 \qquad \text{otherwise,} \end{cases} \tag{4.3}$$

where $+$, $-$ apply for neutron energy loss, gain and $n(\nu)$ is the Bose–Einstein population factor. That such scattering in practice never takes this form indicates that the in-plane resolution must also be considered, with the effect of rounding the sharp edge at low frequencies, and moving the maximum intensity to higher frequency.

The most satisfactory method of accounting for resolution effects in this case is to use a computer program to generate intensities by integrating an assumed dispersion relation over the calculated resolution function. This has been done, using the direct formulation of § 3, for a number of different data sets, taken under different conditions in small-scattering-angle experiments. Use of this method avoids the difficulties associated with the use of the Cooper–Nathans formulation mentioned in the *Introduction*. Firstly, the resolution matrix is known exactly in diagonal form, and so the problems either of trying to integrate over a sharp function in the crystal coordinates, or of trying to diagonlize a nearly singular matrix to transform to the natural resolution-function coordinates, are avoided. Secondly, the number of dimensions of the numerical integral is reduced by one, enabling a more accurate integral evaluation for a given amount of computing resources.

Fig. 5 shows spin wave scattering intensities generated by numerical integration from the form derived in Appendix *B* (equation *B*.13) utilizing the directly derived resolution matrix (equations *B*.4–*B*.9) and assuming a gapless quadratic spin wave dispersion relation. The figure shows the effects of changing spectrometer configuration and vertical collimation.

Fig. 6 illustrates simulated intensities fitted by non-linear regression analysis to some of the data of Bernhoeft, Lonzarich, Mitchell & Paul (1983) for Ni_3Al. The function form is defined by a flat background term, a Gaussian peak to represent elastic scattering, and the intensity due to spin wave scattering (dispersion defined by equation 4.1). This last term was simulated by performing a numerical integration over the resolution function, as derived in § 3, of a δ-function spin wave scattering law. The importance of an accurate resolution correction for this data becomes clear from the effective shift of the nominal peak frequency by up to ~33%, and an

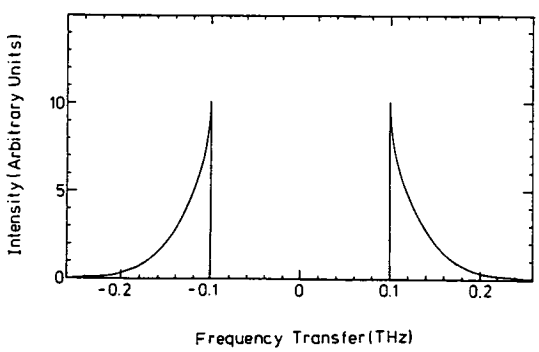

Fig. 4. Intensity of scattering from spin waves which would be observed in a constant-Q scan if the only resolution contribution were the out-of-plane momentum component. Calculations were made using equation (4.3) in the high-temperature limit, so that $n(\nu) + \frac{1}{2} \pm \frac{1}{2} \rightarrow k_B T/h\nu$. Values of parameters used were $M_{zz} = 500$ Å^2, $Q_0 = 0{\cdot}1$ Å^{-1}, $\varepsilon_g = 0$ and $D = 10$ THz Å^2.

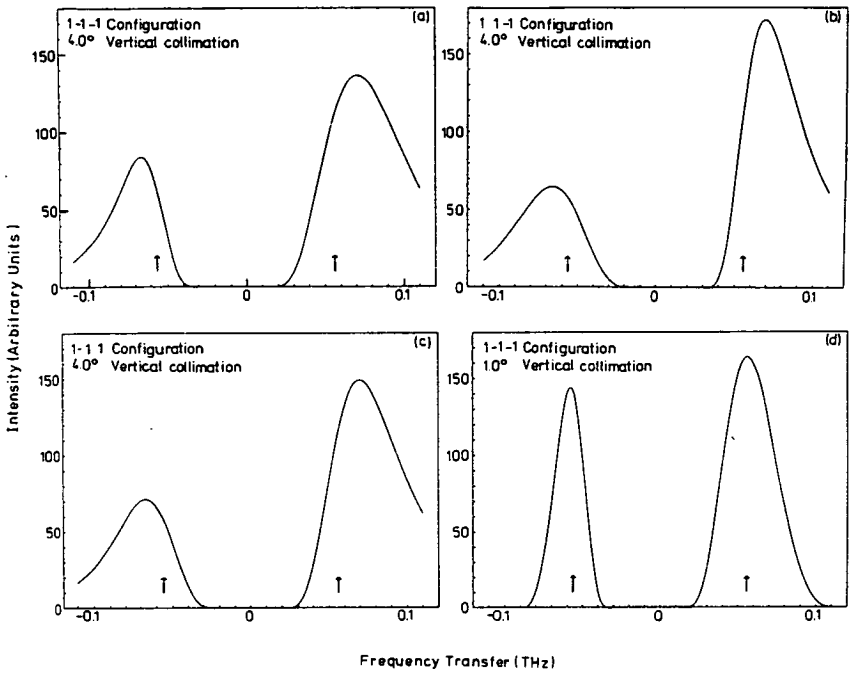

Fig. 5. Pure spin wave scattering generated by the computer program. (*a*), (*b*) and (*c*) differ only in configuration of the spectrometer with the vertical collimation the same for each, namely $\beta_0 = \beta_1 = \beta_2 = \beta_3 = 4{\cdot}0°$. (*a*) and (*d*) differ in vertical collimation, but have the same configuration [the intensity shown for (*d*) has been amplified by a factor of eight]. Note that arrows point to the nominal spin wave energy. In each, $Q = 0{\cdot}075$ Å^{-1}, $\varepsilon_g = 0$ and $D = 10$ THz Å^2. Horizontal collimation is (*a*) 30′, (*b*) 20′, (*c*) 20′, (*d*) 30′. $k_F = 1{\cdot}55$ Å^{-1}, $2\theta_s \leq 2{\cdot}8°$.

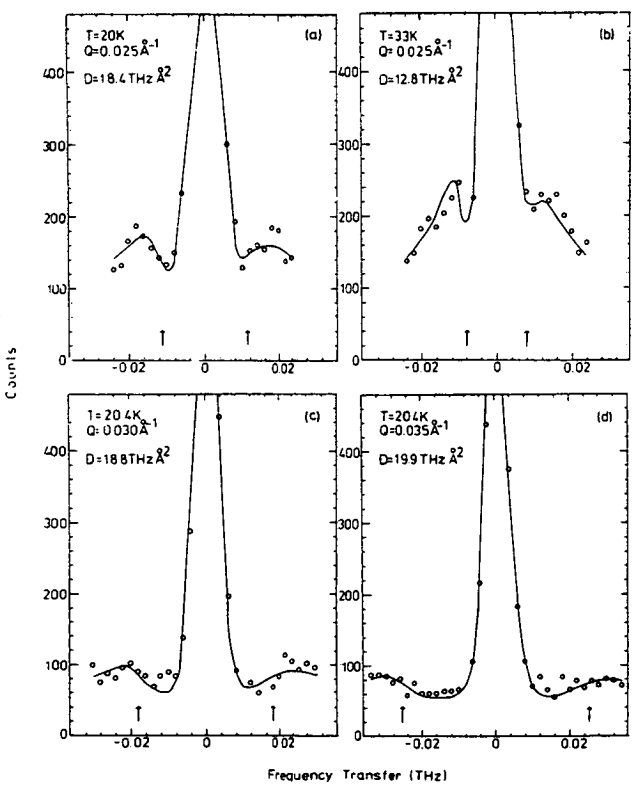

Fig. 6. Experimental data (○) and computer-generated least-squares fit (solid line) showing spin wave scattering from Ni_3Al at various wavevector transfers and temperatures ($T_c \simeq 40$ K). $2\theta_s \leq 1{\cdot}3$, $1{\cdot}6$, $1{\cdot}8°$ for (*a*) and (*b*), (*c*), (*d*), respectively. $k_F = 1{\cdot}1$ Å^{-1}. See text for details.

energy width in the spin wave peak generated by resolution effects which is comparable to the observed peak frequency, and roughly double the energy width observed for Q-independent elastic scattering.

5. Conclusions

We have investigated the Cooper–Nathans resolution function for triple-axis neutron spectrometers in the limit of small scattering angles and found that two of the four deviations from the nominal wavevector (three components) and from the nominal energy become linearly dependent, giving rise to a singular resolution matrix and efficiency factor.

By treating this dependence analytically we have derived a resolution function for the small-scattering-angle limit which is simpler and both easier and faster to compute than the general Cooper–Nathans function. Numerical simulation techniques have been employed which show that this direct formulation allows a detailed analysis of data from small-angle experiments.

We emphasise that the use of standard Cooper–Nathans programs for the calculation of the resolution effects does not give satisfactory results for small scattering angles, unless the resolution matrix is diagonalized and the numerical integrations performed in the diagonlized frame of reference and unless a high degree of numerical precision is used to cope with the singularity of the matrix. The direct

analysis we have given allows the calculations to be performed more accurately and more speedily.

This work was supported by the SERC.

APPENDIX A
Details of Cooper–Nathans at small angles

In the Gaussian approximation, the resolution function may be written

$$R = R_0(\mathbf{X}) \exp\{-\tfrac{1}{2}\mathbf{X} \,.\, \mathsf{M}(\mathbf{X}) \,.\, \mathbf{X}\}, \qquad (A.1)$$

where $\mathbf{X}$ is the space defined by a set of deviations from nominal parameters, $R_0(\mathbf{X})$ is the efficiency factor, and $\mathsf{M}(\mathbf{X})$ is the resolution matrix in the space $\mathbf{X}$.

The Cooper–Nathans function is expressed with

$$\mathbf{X} = [\delta\mathbf{Q}, \delta(h\nu)], \qquad (A.2)$$

where the axes of $\delta\mathbf{Q}$ are fixed with respect to $\mathbf{Q}_0$.

In the space defined by

$$\mathbf{X} = (\delta\mathbf{k}_i, \delta\mathbf{k}_f), \qquad (A.3)$$

where

$$\delta\mathbf{k}_j = \delta k_{jx}, \delta k_{jy}, \delta k_{jz}, \qquad (A.4)$$

the resolution matrix is

$$\mathsf{M}(\delta\mathbf{k}_i, \delta\mathbf{k}_f) = \begin{pmatrix} m_{11} & m_{12} & 0 & 0 & 0 & 0 \\ m_{12} & m_{22} & 0 & 0 & 0 & 0 \\ 0 & 0 & m_{33} & 0 & 0 & 0 \\ 0 & 0 & 0 & m_{44} & m_{45} & 0 \\ 0 & 0 & 0 & m_{45} & m_{55} & 0 \\ 0 & 0 & 0 & 0 & 0 & m_{66} \end{pmatrix}, \qquad (A.5)$$

where

$$m_{11} = (2\tan\theta_M)^2\left(\frac{1}{\alpha_0^2}+\frac{1}{(2\eta_M)^2}\right)\frac{1}{k_I^2} = b_5 \qquad (A.6)$$

$$m_{12} = -2\varepsilon_M \tan\theta_M\left(\frac{1}{\alpha_0^2}+\frac{1}{2\eta_M^2}\right)\frac{1}{k_I^2} = -\varepsilon_M b_0 \qquad (A.7)$$

$$m_{22} = \left(\frac{1}{\alpha_0^2}+\frac{1}{\alpha_1^2}+\frac{1}{\eta_M^2}\right)\frac{1}{k_I^2} = b_1 \qquad (A.8)$$

$$m_{33} = \left(\frac{1}{\beta_1^2}+\frac{1}{(2\sin\theta_M\eta'_M)^2+\beta_0^2}\right)\frac{1}{k_I^2} = a_{11}^2 \qquad (A.9)$$

$$m_{44} = (2\tan\theta_A)^2\left(\frac{1}{\alpha_3^2}+\frac{1}{(2\eta_A)^2}\right)\frac{1}{k_F^2} = b_3 \qquad (A.10)$$

$$m_{45} = 2\varepsilon_A \tan\theta_A\left(\frac{1}{\alpha_3^2}+\frac{1}{2\eta_A^2}\right)\frac{1}{k_F^2} = -\varepsilon_A b_4 \qquad (A.11)$$

$$m_{55} = \left(\frac{1}{\alpha_3^2}+\frac{1}{\alpha_2^2}+\frac{1}{\eta_A^2}\right)\frac{1}{k_F^2} = b_2 \qquad (A.12)$$

$$m_{66} = \left(\frac{1}{\beta_2^2}+\frac{1}{(2\sin\theta_A\eta'_A)^2+\beta_3^2}\right)\frac{1}{k_F^2} = a_{12}^2, \qquad (A.13)$$

where the θ's, ε's, α's and β's are defined in Fig. 1, $\mathbf{k}_I$ and $\mathbf{k}_F$ are defined by (2.1) and (2.2), $\eta_{M,A}$, $\eta'_{M,A}$ are the horizontal and vertical mosaics of monochromator and analyser, and the b's and a's are those defined by Cooper & Nathans (1967), equations (44) and (55) (note the correction given by Dorner, 1972).

The transformation to the space $\mathbf{x}'$, where

$$\mathbf{x}' = [\delta\mathbf{Q}, \delta(h\nu), \delta k_{ix}, \delta k_{iz}], \qquad (A.14)$$

is given by the matrix U, so that

$$\mathbf{x}' = \mathsf{U} \,.\, \mathbf{X}. \qquad (A.15)$$

If the inverse of U is V, then

$$\mathsf{V} = \begin{pmatrix} 0 & 0 & 0 & 0 & v_{15} & 0 \\ v_{21} & v_{22} & 0 & v_{24} & v_{25} & 0 \\ 0 & 0 & 0 & 0 & 0 & v_{36} \\ 0 & 0 & 0 & v_{44} & v_{45} & 0 \\ v_{51} & v_{52} & 0 & v_{54} & v_{55} & 0 \\ 0 & 0 & v_{63} & 0 & 0 & v_{66} \end{pmatrix}, \qquad (A.16)$$

where

$$v_{15} = 1 \qquad (A.17)$$

$$v_{21} = -\varepsilon_s \cos\varphi_2/\sin 2\theta_s \qquad (A.18)$$

$$v_{22} = \sin\varphi_2/\sin 2\theta_s \qquad (A.19)$$

$$v_{24} = -\varepsilon_s/(\gamma \sin 2\theta_s) \qquad (A.20)$$

$$v_{25} = -\varepsilon_s(\cos 2\theta_s - k_I/k_F)/\sin 2\theta_s \qquad (A.21)$$

$$= -\varepsilon_s Q_0 \cos\varphi_1/(k_F \sin 2\theta_s) \qquad (A.22)$$

$$v_{36} = 1 \qquad (A.23)$$

$$v_{44} = -1/\gamma \qquad (A.24)$$

$$v_{45} = k_I/k_F \qquad (A.25)$$

$$v_{51} = -\varepsilon_s \cos\varphi_1/\sin 2\theta_s \qquad (A.26)$$

$$v_{52} = \sin\varphi_1/\sin 2\theta_s \qquad (A.27)$$

$$v_{54} = -\varepsilon_s \cos 2\theta_s/(\gamma \sin 2\theta_s) \qquad (A.28)$$

$$v_{55} = -\varepsilon_s[1-(k_I/k_F)\cos 2\theta_s]/\sin 2\theta_s \qquad (A.29)$$

$$= -\varepsilon_s Q_0 \cos\varphi_2/(k_F \sin 2\theta_s) \qquad (A.30)$$

$$v_{63} = 1 \qquad (A.31)$$

$$v_{66} = 1, \qquad (A.32)$$

where φ_1, φ_2 and $2\theta_s$ are defined in Fig. 2, and

$$\gamma = k_F\hbar^2/m. \qquad (A.33)$$

The dependence on δk_{ix}, δk_{iz} is irrelevant, so these parameters are removed by integrating over all possible values. This leaves the Cooper–Nathans matrix, which has four components, one of which, that in δQ_z, is uncoupled from the other three.

Consider only δQ_x, δQ_y, with $\delta(h\nu)$ set to zero;

$$\mathsf{M} = \begin{pmatrix} M_{xx} & M_{xy} \\ M_{xy} & M_{yy} \end{pmatrix}. \qquad (A.34)$$

The elements are

$$M_{xx} = (\rho v_{21}^2 + \sigma v_{51}^2 - 2\tau v_{21} v_{51})/A' \quad (A.35)$$

$$M_{xy} = [\rho v_{21} v_{22} + \sigma v_{51} v_{52} - \tau(v_{21} v_{52} + v_{22} v_{51})]/A' \quad (A.36)$$

$$M_{yy} = (\rho v_{22}^2 + \sigma v_{52}^2 - 2\tau v_{22} v_{52})/A', \quad (A.37)$$

where

$$\rho = m_{22} m_{55} v_{55}^2 + m_{77}^2 v_{15}^2 + m_{22} m_{44} v_{45}^2 + 2 m_{45} m_{22} v_{45} v_{55} \quad (A.38)$$

$$\sigma = m_{22} m_{55} v_{25}^2 + m_{88}^2 v_{45}^2 + m_{55} m_{11} v_{15}^2 + 2 m_{55} m_{12} v_{15} v_{25} \quad (A.39)$$

$$\tau = m_{22} m_{55} v_{25} v_{55} + m_{45} m_{22} v_{45} v_{25} + m_{55} m_{12} v_{15} v_{55} + m_{45} m_{12} v_{45} v_{15} \quad (A.40)$$

with

$$m_{77}^2 = m_{11} m_{22} - m_{12}^2 \quad (A.41)$$

$$m_{88}^2 = m_{44} m_{55} - m_{45}^2 \quad (A.42)$$

and

$$A' = m_{22} v_{25}^2 + m_{44} v_{45}^2 + m_{55} v_{55}^2 + m_{11} v_{15}^2 + 2 m_{12} v_{15} v_{25} + 2 m_{45} v_{55} v_{45}. \quad (A.43)$$

[Compare (A.43) with Cooper & Nathans' equation (45*a*).]

Diagonalization by rotation in the x–y plane through an angle θ gives

$$\mathsf{M}' = \begin{pmatrix} M'_{xx} & 0 \\ 0 & M'_{yy} \end{pmatrix} \quad (A.44)$$

with

$$M'_{xx} = \tfrac{1}{2}[\omega + (\chi^2 + \psi^2)^{1/2}] \quad (A.45)$$

$$M'_{yy} = \tfrac{1}{2}[\omega - (\chi^2 + \psi^2)^{1/2}], \quad (A.46)$$

where

$$\omega = [\rho + \sigma - 2\tau \cos(\varphi_1 - \varphi_2)]/A' \sin^2 2\theta_s \quad (A.47)$$

$$\chi = [\rho \cos 2\varphi_2 + \sigma \cos 2\varphi_1 - 2\tau \cos(\varphi_1 + \varphi_2)]/A' \sin^2 2\theta_s \quad (A.48)$$

$$\psi = [\rho \sin 2\varphi_2 + \sigma \sin 2\varphi_1 - 2\tau \sin(\varphi_1 + \varphi_2)]/A' \sin^2 2\theta_s \quad (A.49)$$

and

$$\theta = \tfrac{1}{2} \arctan(-\varepsilon_s \psi/\chi). \quad (A.50)$$

This is an exact result from the Cooper–Nathans matrix. Now, the approxiation of (2.11) gives

$$\theta = -\varepsilon_s \varphi \quad (A.51)$$

$$M'_{xx} = (\rho + \sigma - 2\tau)/A' \sin^2 2\theta_s \quad (A.52)$$

$$M'_{yy} = \xi/(\rho + \sigma - 2\tau), \quad (A.53)$$

where

$$\xi = m_{55} m_{77}^2 v_{15}^2 + m_{22} m_{88}^2 v_{45}^2. \quad (A.54)$$

Note that, although ρ, σ and τ independently contain divergent terms as $2\theta_s \to 0$, the combination $(\rho + \sigma - 2\tau)$ does not diverge but tends to the limit

$$\rho + \sigma - 2\tau \to (m_{22} + m_{55})(m_{11} v_{15}^2 + m_{44} v_{45}^2) - (m_{12} v_{15} + m_{45} v_{45})^2. \quad (A.55)$$

The result (A.52) and (A.53) indicates that one of the three diagonal elements arising from the δQ_x, δQ_y, $\delta(h\nu)$ terms in M behaves in the small $2\theta_s$ limit as

$$M_{II} \propto \frac{1}{A \sin^2 2\theta_s}. \quad (A.56)$$

Dorner (1972) showed that the terms in R_0 which depend on scattering at the sample must be derived from the determinant of the resolution matrix, since

$$R_0 = \frac{V_I V_F}{4\pi^2} |\mathsf{M}|^{1/2} \quad (A.57)$$

(Dorner's equation 22), where V_I and V_F are primary and secondary spectrometer resolution volumes and are independent of scattering geometry at the sample. This is consistent with one diagonal element behaving as in (A.56), since $|\mathsf{M}|$ is the product of the diagonal elements, and R_0 behaves as shown in (2.9).

APPENDIX *B*

Resolution matrix and efficiency factor in the direct formulation

The derivation of the resolution function in this form follows that of the Cooper–Nathans form up to the point where the detection probability is expressed in terms of the deviations from the nominal incident and scattered wavevectors (A.3–A.13). We transform to the three components of $\delta\boldsymbol{\kappa}$ (defined in 3.1) and $\delta\mathbf{k}_i$

$$\mathsf{M}(\delta\mathbf{k}_i, \delta\boldsymbol{\kappa}) = \begin{pmatrix} m_{11}+m_{44} & m_{12}+m_{45} & 0 \\ m_{12}+m_{45} & m_{22}+m_{55} & 0 \\ 0 & 0 & m_{33}+m_{66} \\ -m_{44} & -m_{45} & 0 \\ -m_{45} & -m_{55} & 0 \\ 0 & 0 & -m_{66} \end{pmatrix} \begin{pmatrix} -m_{44} & -m_{45} & 0 \\ -m_{45} & -m_{55} & 0 \\ 0 & 0 & -m_{66} \\ m_{44} & m_{45} & 0 \\ m_{45} & m_{55} & 0 \\ 0 & 0 & m_{66} \end{pmatrix} \quad (B.1)$$

Now integrate over the three components of $\delta\mathbf{k}_i$. This gives

$$\mathsf{M}(\delta\boldsymbol{\kappa}) = \begin{pmatrix} (m_{44}m_{77}^2 + m_{11}m_{88}^2)/s & (m_{45}m_{77}^2 + m_{12}m_{88}^2)/s & 0 \\ (m_{45}m_{77}^2 + m_{12}m_{88}^2)/s & (m_{55}m_{77}^2 + m_{22}m_{88}^2)/s & 0 \\ 0 & 0 & m_{33}m_{66}/(m_{33}+m_{66}) \end{pmatrix}, \tag{B.2}$$

where

$$s = (m_{22}+m_{55})(m_{11}+m_{44}) - (m_{12}+m_{45})^2. \tag{B.3}$$

This matrix is diagonalized by a rotation through Θ in the x–y plane,

$$\mathsf{M}(\delta\boldsymbol{\kappa}') = \begin{pmatrix} \tfrac{1}{2}[\Omega + (X^2+\Psi^2)^{1/2}] & 0 & 0 \\ 0 & \tfrac{1}{2}[\Omega - (X^2+\Psi^2)^{1/2}] & 0 \\ 0 & 0 & m_{33}m_{66}/(m_{33}+m_{66}) \end{pmatrix}, \tag{B.4}$$

where

$$\delta\boldsymbol{\kappa}' = \begin{pmatrix} \cos\Theta & -\sin\Theta & 0 \\ \sin\Theta & \cos\Theta & 0 \\ 0 & 0 & 1 \end{pmatrix} \delta\boldsymbol{\kappa} \tag{B.5}$$

with

$$\Theta = \tfrac{1}{2}\arctan(\Psi/X) \tag{B.6}$$

and

$$\Omega = [(m_{44}+m_{55})m_{77}^2 + (m_{11}+m_{22})m_{88}^2]/s \tag{B.7}$$

$$X = [(m_{44}-m_{55})m_{77}^2 + (m_{11}-m_{22})m_{88}^2]/s \tag{B.8}$$

$$\Psi = [2m_{45}m_{77}^2 + 2m_{12}m_{88}^2]/s. \tag{B.9}$$

In order to derive the pre-exponential term in the resolution function, it is necessary to include the factors which arise from the elimination of $\delta\mathbf{k}_i$. To avoid ambiguity, the efficiency factor will be expressed in terms of the ratio of the detector counting rate, Φ_D, to the flux per unit solid angle per unit wavevector from the reactor, $\varphi(k_I)$,

$$\begin{aligned} \frac{\Phi_D}{\varphi(k_I)} = {} & E_D(k_F)\frac{2\pi\hbar}{m}p_M(k_I)p_A(k_I)\frac{1}{k_I^3} \\ & \times\left[1+\left(\frac{2\eta'_M\sin\theta_M}{\beta_0}\right)^2\right]^{-1/2} \\ & \times\left[1+\left(\frac{2\eta'_A\sin\theta_A}{\beta_3}\right)^2\right]^{-1/2} \\ & \times(m_{33}+m_{66})^{-1/2}s^{-1/2} \\ & \times\iiiint S(\mathbf{Q},\nu)\exp\{-\tfrac{1}{2}\delta\boldsymbol{\kappa}'\mathsf{M}(\delta\boldsymbol{\kappa}')\delta\boldsymbol{\kappa}'\} \\ & \times\delta\left(\delta\nu - \frac{\hbar}{4\pi m}(|\mathbf{k}_I|+|\mathbf{k}_F|)\delta\kappa_x\right)\mathrm{d}\nu\,\mathrm{d}(\delta\boldsymbol{\kappa}'), \end{aligned} \tag{B.10}$$

where $E_D(k_F)$ is the detector efficiency at k_F, $p_{M,A}(k_I, k_F)$ is the peak reflectivity of monochromator or analyser at the appropriate wavevector, and other symbols are defined above.

In the same way, we may write the total flux incident on the sample, Φ_s,

$$\begin{aligned} \frac{\Phi_S}{\varphi(k_I)} = {} & (2\pi)^{3/2}p_M(k_I)k_I\cot\theta_M \\ & \times\left[1+\left(\frac{2\eta'_M\sin\theta_M}{\beta_0}\right)^2\right]^{-1/2} \\ & \times\left[\frac{1}{\beta_1^2}+\frac{1}{\beta_0^2+(2\eta'_M\sin\theta_M)^2}\right]^{-1/2} \\ & \times\left[\frac{1}{\alpha_0^2\alpha_1^2}+\frac{1}{\alpha_0^2(2\eta_M)^2}+\frac{1}{\alpha_1^2(2\eta_M)^2}\right]^{-1/2}. \end{aligned} \tag{B.11}$$

Under certain circumstances, it may be desirable to move the fission-chamber monitor, which is usually used to measure the flux incident on the sample, away from the sample to before the monochromator-to-sample collimator, to cut down the background due to small-angle scattering from the monitor. In this case, denote the horizontal, vertical collimation from monochromator to monitor by α_5, β_5. The counting rate of the monitor, Φ_M, is then given by

$$\begin{aligned} \frac{\Phi_M}{\varphi(k_I)} = {} & \frac{E_M}{k_I}(2\pi)^{3/2}p_M(k_I)k_I\cot\theta_M \\ & \times\left[1+\left(\frac{2\eta'_M\sin\theta_M}{\beta_0}\right)^2\right]^{-1/2} \\ & \times\left[\frac{1}{\beta_5^2}+\frac{1}{\beta_0^2+(2\eta'_M\sin\theta_M)^2}\right]^{-1/2} \\ & \times\left[\frac{1}{\alpha_0^2\alpha_5^2}+\frac{1}{\alpha_0^2(2\eta_M)^2}+\frac{1}{\alpha_5^2(2\eta_M)^2}\right]^{-1/2}, \end{aligned} \tag{B.12}$$

where E_M is the monitor efficiency at $K_I = 1$, and the efficiency is assumed to be proportional to $(k_I)^{-1}$.

The experimentally measured quantity is Φ_D/Φ_M,

$$\frac{\Phi_D}{\Phi_M} = \frac{E_D(k_F)}{E_M}\frac{\hbar}{\sqrt{2\pi m}\,k_I^3\cot\theta_M}\frac{p_A(k_F)}{} \times\left[1+\left(\frac{2\eta'_A\sin\theta_A}{\beta_3}\right)^2\right]^{-1/2} \times\left[\frac{1}{\beta_5^2}+\frac{1}{\beta_0^2+(2\eta'_M\sin\theta_M)^2}\right]^{1/2} \times\left[\frac{1}{\alpha_0^2\alpha_5^2}+\frac{1}{\alpha_0^2(2\eta_M)^2}+\frac{1}{\alpha_5^2(2\eta_M)^2}\right]^{1/2} \times(m_{33}+m_{66})^{-1/2}\,s^{-1/2}\iiint S(\mathbf{Q},\nu) \times\exp\{-\tfrac{1}{2}\delta\boldsymbol{\kappa}'\mathrm{M}(\delta\boldsymbol{\kappa}')\delta\boldsymbol{\kappa}'\} \times\delta\left[\delta\nu-\frac{\hbar}{4\pi m}(|\mathbf{k}_I|+|\mathbf{k}_F|)\delta\kappa_x\right]\mathrm{d}\nu\,\mathrm{d}(\delta\boldsymbol{\kappa}'). \tag{B.13}$$

The integral involves three different ways of expressing the deviations from the nominal wavevector transfer (and so, by equation 3.4, from the nominal energy transfer). They are related by (*B*.5) and the following:

$$\delta\mathbf{Q}=\begin{pmatrix}\cos\varphi & -\varepsilon_s\sin\varphi & 0\\ \varepsilon_s\sin\varphi & \cos\varphi & 0\\ 0 & 0 & 1\end{pmatrix}\delta\boldsymbol{\kappa} \tag{B.14}$$

or

$$\delta\mathbf{Q}=\begin{pmatrix}\cos(\Theta-\varepsilon_s\varphi) & \sin(\Theta-\varepsilon_s\varphi) & 0\\ -\sin(\Theta-\varepsilon_s\varphi) & \cos(\Theta-\varepsilon_s\varphi) & 0\\ 0 & 0 & 1\end{pmatrix}\delta\boldsymbol{\kappa}'. \tag{B.15}$$

The effects of sample mosaic have not been incorporated into the resolution function here because, in the limit of small scattering angles, the three-dimensional ferromagnetic systems considered here show isotropic spin wave scattering (equation 4.1). Thus mosaic effects are unimportant, even in powdered or polycrystalline samples. For systems which display anisotropic scattering at small angles, mosaic effects could be incorporated into the transverse momentum components of the resolution function by performing the transformation (*B*.14) on the matrix (*B*.2) and including the terms given by Werner & Pynn (1971).

Note that the spectrometer focusing may be optimized (R_0 maximized) by making s smaller by suitable choice of configuration. In the small $2\theta_s$ limit, this may be achieved with $\varepsilon_A=-\varepsilon_M$.

References

AXE, J. D., SHIRANE, G., MIZOGUCHI, T. & YAMAUCHI, K. (1977). *Phys. Rev. B*, **15**, 2763–2770.

BERNHOEFT, N. R., LONZARICH, G. G., MITCHELL, P. W. & PAUL, D. McK. (1983). *Phys. Rev. B*, **28**, 422–424.

BJERRUM MØLLER, H. & NEILSEN, M. (1970). *Instrumentation for Neutron Inelastic Scattering Research*, pp. 49–70. Vienna: IAEA.

CHESSER, N. J. & AXE, J. D. (1973). *Acta Cryst.* A**29**, 160–169.

COOPER, M. J. & NATHANS, R. (1967). *Acta Cryst.* **23**, 357–367.

DORNER, B. (1972). *Acta Cryst.* A**28**, 319–327.

HAYWOOD, B. C. (1971). *Acta Cryst.* A**27**, 408–410.

HUTCHINGS, M. T., ALS-NIELSEN, J., LINGARD, P. A. & WALKER, P. J. (1981). *J. Phys. C*, **14**, 5327–5345.

PASSELL, L., DIETRICH, O. W. & ALS-NIELSEN, J. (1976). *Phys. Rev. B*, **14**, 4897–4907.

SAMUELSEN, E. J. (1971). In *Structural Phase Transitions and Soft Modes*; edited by E. J. SAMUELSON, E. ANDERSEN & J. FEDER, pp. 189–215, Oslo: Universitetsforlaget Trykningssentral.

SAMUELSEN, E. J., HUTCHINGS, M. T. & SHIRANE, G. (1970). *Physica (Utrecht)*, **48**, 13–42.

WERNER, S. A. & PYNN, R. (1971). *J. Appl. Phys.* **42**, 4736–4749.

J. Phys. C: Solid State Phys., 17 (1984) 3235–3246. Printed in Great Britain

An investigation of the magnetic structure and excitations in $K_2Co_xFe_{1-x}F_4$

S A Higgins†, R A Cowley†, M Hagen†, J K Kjems‡, U Dürr§ and K Fendler‖¶

† Department of Physics, University of Edinburgh, Mayfield Road, Edinburgh EH9 3JZ, UK

‡ Risø National Laboratory, DK-4000 Roskilde, Denmark

§ Physikalisches Institut der Universität Stuttgart, Teil II, 7000 Stuttgart 80, Federal Republic of Germany

‖ Fakultät für Physik, Universität Konstanz, Bücklestrasse 13, 7750 Konstanz, Federal Republic of Germany

Received 25 November 1983

Abstract. Neutron scattering techniques have been used to investigate the magnetic structure of $K_2Co_xFe_{1-x}F_4$ with $x = 0.2$ and $x = 0.6$. The $x = 0.6$ sample exhibits only one magnetic phase transition, at $T_N = 92.2 \pm 0.1$ K. The $x = 0.2$ sample has two magnetic phase transitions; below $T_N = 66 \pm 1$ K the axial spin components order, while below a well defined transition at $T_L = 32 \pm 2$ K the transverse components also order. The spin wave dispersion relations have been measured for both samples using inelastic neutron scattering techniques.

1. Introduction

Magnetic systems with competing anisotropies have recently attracted considerable attention. Mean-field-theory calculations of the phase diagrams of such systems by Matsubara and Inawashiro (1977) predicted four distinct magnetic phases as a function of concentration and temperature with an associated tetracritical point. These were a paramagnetic phase, a phase in which one spin component was ordered and the other disordered, a phase in which only the other component ordered and, finally, a phase in which both spin components ordered.

In mean-field theory the ordering of one spin component affects the ordering of the other with the result that the phase boundaries change slope at the tetracritical point. More recent calculations including the fluctuations, using renormalisation-group theory (see, e.g., Fishman and Aharony 1978) suggest that the ordering of the different spin components is decoupled and that the phase boundaries have a constant slope through a decoupled tetracritical point.

There have been several studies of magnetic systems in which there are competing anisotropies, as reviewed by Katsumata (1983). By far the most detailed study was made by Wong *et al* (1983) on the $Co_xFe_{1-x}Cl_2$ system. They found that although the high-temperature transition was well defined, the one at lower temperature was smeared. They suggested that this was because the ordering of one spin component generated a

¶ Present address: Max-Planck-Institut für Biophysik, 6000 Frankfurt 70, Federal Republic of Germany.

0022-3719/84/183235 + 12 $02.25

random field on the other, and that this random field inhibited the development of true long-range order. This mechanism could occur in $Co_xFe_{1-x}Cl_2$ because of a Dzyaloshinsky type of interaction arising from the low local symmetry of the ions in the $FeCl_2$ structure.

$K_2Co_xFe_{1-x}F_4$ is another system that has competing anisotropies. The end members K_2CoF_4 and K_2FeF_4 have the K_2NiF_4 structure (Birgeneau *et al* 1970) in which the magnetic ions are at the corners and body centre of a tetragonal chemical unit cell. It has become conventional to define a magnetic unit cell in which the magnetic a and b axes are rotated by 45° relative to the a and b axes of the chemical unit cell and are larger by a factor of $2^{1/2}$. The antiferromagnetic exchange interactions for the two systems are predominantly two-dimensional and the planes can stack in two ways relative to each other, leading to a two-domain structure. The competing anisotropy in $K_2Co_xFe_{1-x}F_4$ arises because in K_2CoF_4 the pseudo-spin $S = \frac{1}{2}$ is aligned along the crystallographic c axis owing to the anisotropic exchange (Breed *et al* 1969), while in the K_2FeF_4 the single-ion anisotropy aligns the $S = 2$ spin perpendicular to the c axis (Macco *et al* 1978). Both of these pure materials have been studied in detail and the exchange constants are known. Whilst the magnetic interactions are largely two-dimensional between nearest neighbours the order occurs at least partially in three dimensions at low temperatures.

We have performed neutron scattering measurements on two samples of $K_2Co_xFe_{1-x}F_4$ with $x = 0.6$ and $x = 0.2$ to study the magnetic phase transitions. In $K_2Co_xFe_{1-x}F_4$, the local symmetry is higher than in $Co_xFe_{1-x}Cl_2$, so any random fields generated by the ordering of one spin component are expected to be very much smaller in $K_2Co_xFe_{1-x}F_4$ than in $Co_xFe_{1-x}Cl_2$.

Consequently we have particularly studied the structure and phase transitions of the sample with $x = 0.2$ which shows two transitions and at low temperatures is in the mixed phase shown in figure 1.

Since we made these measurements we have learnt of similar measurements of $K_2Co_xFe_{1-x}F_4$ by Vlak *et al* (1983). Our results and conclusions are similar to theirs, but differ in some important respects.

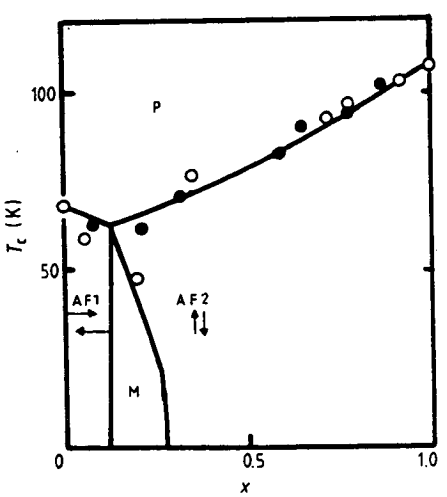

Figure 1. The phase diagram for $K_2Co_xFe_{1-x}F_4$. Points shown indicate results from previous measurements (Fendler 1982). Note: M denotes the mixed antiferromagnetic phase; AF1 denotes the planar antiferromagnetic phase; AF2 denotes the uniaxial antiferromagnetic phase; and P denotes the paramagnetic phase.

The theory of the spin waves in systems with competing anisotropies is not well understood despite the work of Matsubara (1981). We report on preliminary measurements of the spin waves, which show a two-band behaviour very similar to that found in mixed magnetic systems without competing interactions (Cowley 1982). The results also give reasonable accord with the results of Raman scattering experiments (Fendler 1982) and with calculations based on a simple Ising model.

2. Experimental details

The neutron scattering measurements were performed on triple-axis crystal spectrometers at the National Laboratory, Risø, Denmark, and at the PLUTO reactor, AERE, Harwell, UK. The nominally $x = 0.2$ sample was plate-like with dimensions of 10 mm × 10 mm × 2 mm while the nominally $x = 0.6$ sample had a volume of approximately 1 cm^3. Both samples consisted of large grains of single crystal, but unfortunately these grains were misoriented by about 5° with respect to each other. This multicrystal character limited the accuracy of some of the experimental results. The crystals showed no sign of any chemical ordering of the Co and Fe ions.

The crystals were mounted in variable-temperature cryostats with the magnetic a^* and c^* axes in the scattering plane. The elastic measurements at Risø were performed using a pyrolytic graphite monochromator and an incident neutron energy of 14 meV with a graphite filter to suppress unwanted contaminant neutrons in the incident beam. A pyrolytic graphite analyser was used to filter the scattered neutrons and the collimation was chosen to be 30′, 30′, 30′ and 60′ from reactor to counter. The energy resolution in this configuration was 0.8 meV. The inelastic experiments were performed with a similar configuration but with an incident neutron energy of 5 meV.

The experiments at Harwell were performed with a pyrolytic graphite monochromator and a pyrolytic graphite analyser and with a fixed neutron analyser energy of 13 or 24 meV. The collimations were 100′, 30′, 30′, and 60′ and a pyrolytic graphite filter was used before the analyser in the 13 meV measurements.

3. Experimental results

3.1. Measurements of the structure

The intensity of the (1, 0, 0) magnetic Bragg reflection was measured as a function of temperature for $x = 0.6$ and $x = 0.2$ and the results are shown in figures 2 and 3 respectively. In the former case the intensity rises rapidly on cooling below 90 K and then becomes almost constant below 50 K. We believe this indicates the ordering of the components in the c direction of the spin below this temperature, in agreement with the phase diagram shown in figure 1.

Measurements through the (1, 0, 0) Bragg reflection along the line (1, 0, η) showed that the width of the Bragg reflection is not limited by the resolution and that it corresponds to the ordering of around four two-dimensional sheets. The intensity of the scattering in figure 2(b) does not decrease to zero below T_N, most probably because it contains a residual Bragg component corresponding to the lack of full three-dimensional ordering even at the lowest temperatures.

The data shown in figure 2(a) were fitted to the form expected for a two-dimensional

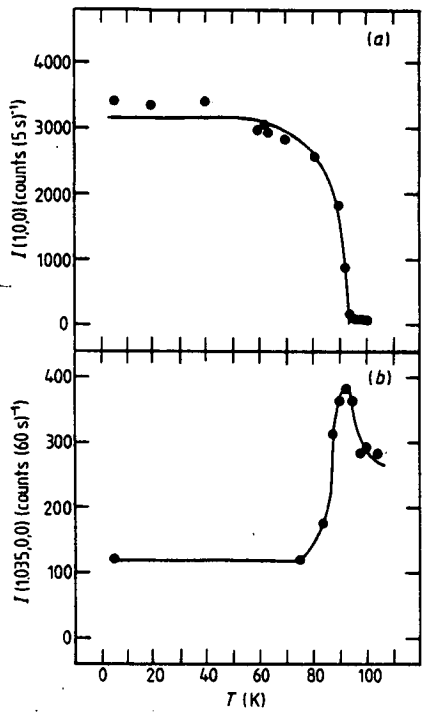

Figure 2. (*a*) The (100) Bragg peak intensity as a function of temperature (for x = 0.6). The full curve indicates the best fit to a $d = 2$ Ising model. (*b*) The diffuse scattering at $Q = (1.035, 0, 0)$ as a function of temperature (for $x = 0.6$).

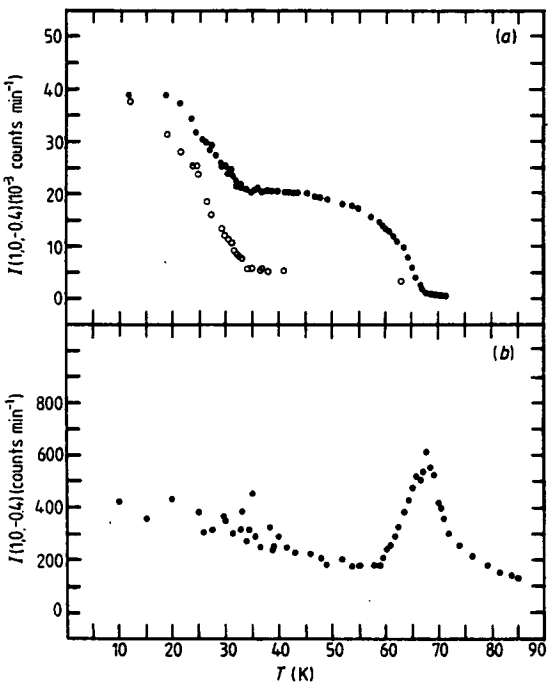

Figure 3. (*a*) Full circles indicate the (1, 0, 0) Bragg peak intensity as a function of temperature ($x = 0.2$). The open circles indicate the (1, 0, 6) Bragg peak intensity (scaled). (*b*) The diffuse scattering at $Q = (1, 0, -0.4)$ as a function of temperature.

Ising model (Onsager 1944):

$$I_{100}(T)/I_{100}(0) = [1 - \sinh^{-4}(2J/k_BT)]^{2\beta} \tag{1}$$

and a least-squares fit gave $\beta = 0.14$. This is consistent with the exact solution of the Ising model, which gives $\beta = 0.125$. The fit also gave the transition temperature $T_N = 92.2 \pm 0.1$ K.

The temperature dependence of the (1, 0, 0) magnetic Bragg reflection for the sample with $x = 0.2$ is shown in figure 3. On cooling it increases from zero at a temperature T_N of 66 ± 1 K and then increases again at a lower temperature T_L of about 32 ± 2 K. We believe that between T_N and T_L only one component of the spin is ordered, while below T_L the other component also orders and the sample is in the mixed phase shown in figure 1. The data shown in figure 3(a) between 35 and 67 K were fitted to the form given as (1) and gave a good fit with $\beta = 0.19 \pm 0.02$. This is significantly larger than the exponent obtained for $x = 0.6$, and that expected for a $d = 2$ Ising model. The difference may well arise because no account has been taken of the rounding of the transition due to concentration fluctuations.

The structure of the $x = 0.2$ system was determined as a function of temperature by measuring the integrated intensities of the (1, 0, L) Bragg reflections with $|L| < 8$ and the (3, 0, L) Bragg reflections with $|L| < 4$ at various temperatures between 12 and 63 K, but mostly close to 30 K. The observed intensities are listed in table 1 for 12 and 35 K.

Table 1. Integrated intensity.

	$T = 12$ K		$T = 35$ K	
(H, K, L)	Experimental	Calculated	Experimental	Calculated
(100)	668	685	355	342
(10$\bar{1}$)	374	367	344	342
(101)	402	367	357	342
(10$\bar{2}$)	321	309	127	128
(102)	327	309	128	128
(10$\bar{3}$)	100	118	63	80
(103)	120	118	83	80
(10$\bar{4}$)	98	101	24	28
(104)	103	101	25	28
(10$\bar{5}$)	29	42	14	18
(105)	38	42	17	18
(10$\bar{6}$)	55	39	8	7
(106)	56	39	7	7
(10$\bar{7}$)	14	18	11	5
(107)	15	18	9	5
(10$\bar{8}$)	19	18	6	2
(108)	21	18	7	2
(300)	90	105	64	52
(30$\bar{1}$)	82	69	74	67
(301)	86	69	73	67
(30$\bar{2}$)	78	89	40	44
(302)	79	89	43	44
(30$\bar{3}$)	41	50	46	47
(303)	44	50	46	47
(30$\bar{4}$)	37	56	21	26
(304)	41	56	21	26

These results were used to determine the structure by fitting three parameters to the experimental results. These parameters were an overall scale factor, which is proportional to the square of the ordered moment, the angle between the spin direction and the c axis, θ_c, and the relative proportion of the domains that give rise to the (1, 0, 0) and (1, 0, 1) Bragg reflections (Thurlings *et al* 1982). The results for θ_c and the square root of the overall scale factor, which is proportional to the average ordered spin moment, are shown in figures 4(a) and (c). The c component of the spin, $s \cos \theta_c$, is shown in figure 4(b). The results show that θ_c is zero above T_L but that it increases rapidly below T_L. The c component of the spin varies only slowly with temperature near 30 K, whereas the total spin increases. These results show that for this sample the c axis spin component orders at T_N but that the perpendicular component only orders at T_L.

The results for the angle θ_c were fitted to the form

$$\theta_c(T)/\theta_c(0) = (1 - T/T_L)\beta' \tag{2}$$

and the results were

$$\beta' = 0.32 \pm 0.04 \qquad \theta_c(0) = 33 \pm 1° \qquad T_L = 32 \pm 1 \text{ K}.$$

The exponent β' is characteristic of three-dimensional ordering, unlike that found for the transition at T_N.

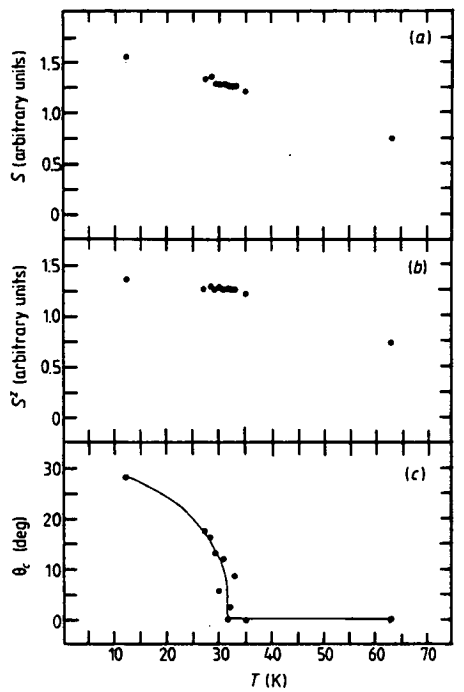

Figure 4. Results from fits to Bragg-peak intensities. (*a*) Average spin S against temperature. (*b*) Average component S^z against temperature. (c) Cant angle θ_c against temperature and a best fit described in the text.

The results for θ_c shown in figure 4(*c*) suggest that the transition at T_L is sharp as a function of temperature. This was also examined by measuring the temperature dependence of the (1, 0, 6) Bragg reflection as shown in figure 3(*a*). This reflection is relatively weak in the upper phase and increases rapidly in intensity on cooling below T_L. These results also suggest that T_L is sharp and that any smearing is only about 2 K which is comparable with the smearing of the (1, 0, 0) reflection at T_N. This smearing is most likely to arise from concentration fluctuations and so we conclude that within the limitations of the experiments both transitions are well defined unlike the results found for $Co_xFe_{1-x}Cl_2$ (Wong *et al* 1983).

As was found with the sample for $x = 0.6$, the Bragg peaks for $x = 0.2$ were not limited by resolution in scans along (1, 0, η) showing that full three-dimensional order was not established.

3.2. *The diffuse scattering*

Due to the mosaic structure of the specimens, measurements of the diffuse scattering are less reliable than measurements of the Bragg reflections, which can be made on a single crystal. Above T_N the diffuse scattering was measured in scans of the form (ζ, 0, −0.4) and the width in ζ was found to decrease as T approached T_N. At and below T_N the width of the scattering in these scans was limited by resolution. The intensity of the scattering at (1.035, 0, 0) for $x = 0.6$ and (1, 0, −0.4) for $x = 0.2$ is shown in figures 2(*b*) and 3(*b*) respectively. The results for both materials show a fairly symmetric peak at T_N but at low temperatures it does not decrease to zero. For $x = 0.2$ the scattering

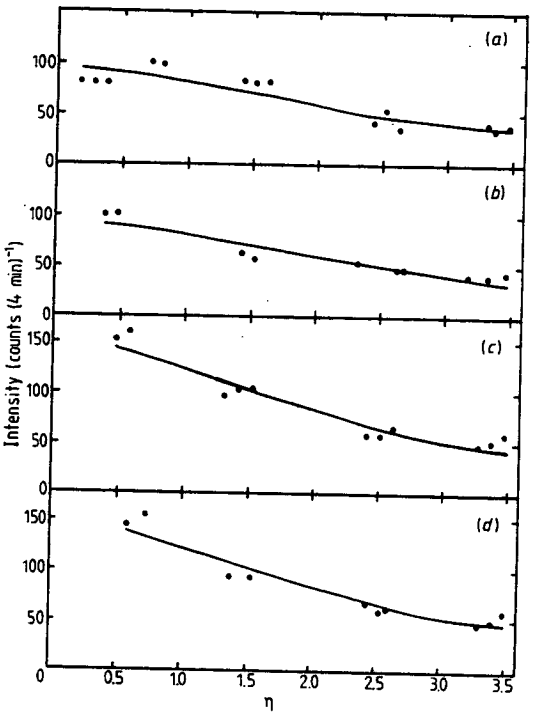

Figure 5. The intensity observed along $(1, 0, \eta)$ as a function of η for $x = 0.2$ at values of T (K) of (*a*) 72, (*b*) 30, (*c*) 45 and (*d*) 12. The full curves are fits to the sums of longitudinal and transverse correlation functions.

slowly increases on further cooling. There is no significant sign of any two-dimensional critical scattering at T_L in figure 3(*b*).

The form of the diffuse scattering for $x = 0.2$ was measured by scans with wavevectors $\boldsymbol{Q}$ along $(1, 0, \eta)$ at four different temperatures; see figure 5. Below T_N there is intense scattering near the integer values from the Bragg peaks and this has been omitted. Since, however, these peaks are wider than the resolution function it is somewhat uncertain how much of the scattering between the peaks is really two-dimensional Bragg scattering from the lack of order from one layer to the next rather than true diffuse scattering. Nevertheless the scattering was analysed into the longitudinal component, along the c axis, which varies as $|f(\boldsymbol{Q})|^2 (1 - \cos^2 \varphi)$ and the transverse component which varies as $|f(\boldsymbol{Q}|^2 \frac{1}{2} (1 + \cos^2 \varphi)$, where φ is the angle between the wavevector transfer, $\boldsymbol{Q}$, and the c axis and $f(\boldsymbol{Q})$ is the average form factor of the ions.

The results of the fitting are shown in figure 5 and suggest that the scattering is largely of longitudinal character at all temperatures. The results gave only (0.15 ± 0.05), (0.14 ± 0.05), (0.26 ± 0.07) and (0.24 ± 0.06) of transverse scattering at 4.5, 30, 45 and 72 K respectively.

3.3. Inelastic scattering

The inelastic scattering was measured in both samples but the more detailed study was made for the larger sample with $x = 0.6$. In this material two branches of the spin waves were observed with fairly well defined neutron groups as shown in figure 6. One of these branches was almost dispersionless with an energy of about 32 meV and the other

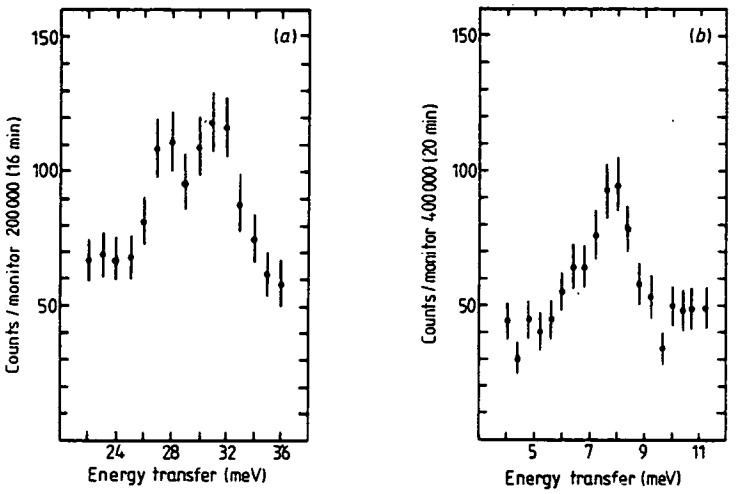

Figure 6. (*a*) A scan through the upper-frequency branch of the dispersion relation for $x = 0.6$. $Q = (3.2, 0, 0)$ and $E_F = 24$ meV while $T = 4.5$ K. (*b*) A scan through the lower-frequency branch of the dispersion relation for $x = 0.6$. $Q = (1.4, 0, 0)$ and $E_F = 13.408$ meV while $T = 4.5$ K.

showed more dispersion but had a zone-boundary energy of about 7.5 meV, as shown in figure 7.

These results are qualitatively similar to the results found in other mixed systems without competing anisotropy such as $Rb_2Mn_{0.5}Ni_{0.5}F_4$, $Mn_xCo_{1-x}F_2$ and $KMn_xCo_{1-x}F_3$ (Cowley 1982). The upper branch corresponds to excitations propagating largely on the Co ions and the lower branch to ones propagating largely on the Fe ions.

The results are in reasonable accord with Raman scattering measurements (Fendler *et al* 1982).

Measurements of the $x = 0.2$ sample were restricted to only the lower branch because of the smaller sample volume. A typical scan is shown in figure 8, and the dispersion relation in figure 9. Measurements were made under conditions giving higher resolution to examine whether the low-frequency/small-wavevector spectrum was different in the Ising phase from that in the mixed phase. The results are shown in figure 10 and in both phases only overdamped low-frequency scattering could be observed at small wavevectors close to T_L. This was surprising because although a gap is expected in the Ising phase it would be absent or much smaller in the mixed phase. Since, however, these results are made very difficult by the mosaic structure, a detailed study of the low-frequency excitations in these phases requires a better sample.

The Ising model for the mean excitation frequency of the Co and Fe atoms has been used to calculate the excitation frequencies assuming that the spins are aligned along the *c* axis.

For the Co ions this frequency is given by

$$E_{Co} = 4[x(2I_{Co})\Delta S^z_{Co}S^z_{Co} + (1-x)(2I_{CoFe})\Delta S^z_{Co}S^z_{Fe}]$$

and for the Fe ions by

$$E_{Fe} = 4[x(2I_{CoFe})\Delta S^z_{Fe}S^z_{Co} + (1-x)(2I_{FeFe})\Delta S^z_{Fe}S^z_{Fe}] + D[(S^z_{Fe})^2_f - (S^z_{Fe})^2_i]$$

where S^z_{Co} and S^z_{Fe} refer to the ground-state values of S^z for Co and Fe neighbours

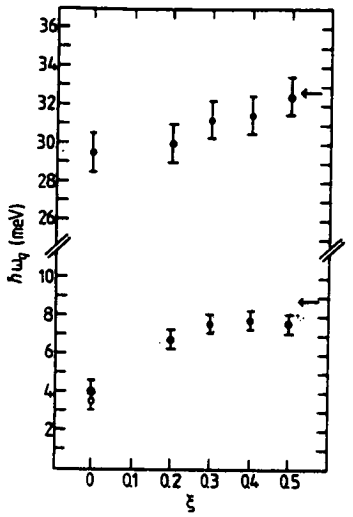

Figure 7. The upper- and lower-frequency branches of the dispersion relation for $x = 0.6$. Full circles indicate points obtained by inelastic neutron scattering. Open circles indicates measurements made previously (Fendler 1982). Arrows at the zone boundary indicate calculated Ising 'spin-flip' frequencies (see the text). Measurements were made at $T = 4.5$ K.

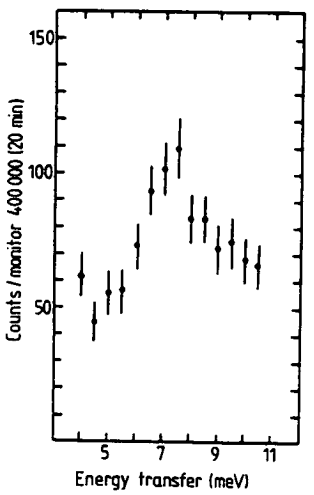

Figure 8. (*a*) A scan through the lower-frequency branch of the dispersion relation for $x = 0.2$. $Q = (1.2, 0, 0)$, $E_F = 13.408$ meV and $T = 4.5$ K.

respectively and $(S^z_{Fe})_f$ and $(S^z_{Fe})_i$ are the final and initial values for the ion that is being excited and $\Delta S^z_{Fe} = (S^z_{Fe})_f - (S^z_{Fe})_i$.

The exchange parameters I_{Co}, I_{Fe} and I_{CoFe} were taken to be $I_{Co} = 7.48$ meV and $I_{Fe} = 0.709$ meV (both from Macco *et al* 1979) and $I_{CoFe} = (I_{Co}I_{Fe})^{1/2} = 2.30$ meV. The single-ion anisotropy is $D = 0.398$ meV (Macco *et al* 1978). The frequencies obtained are shown by the arrows in figures 7 and 9 and this simple model gives a very reasonable

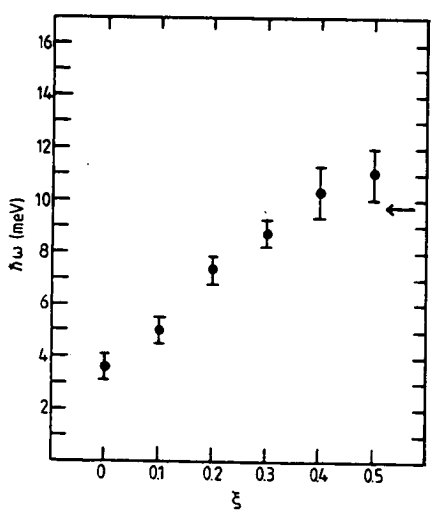

Figure 9. The lower branch of dispersion relation for $x = 0.2$. The arrow at the zone boundary indicates the calculated Ising 'spin-flip' frequency (see the text). Measurements were made at 4.5 K.

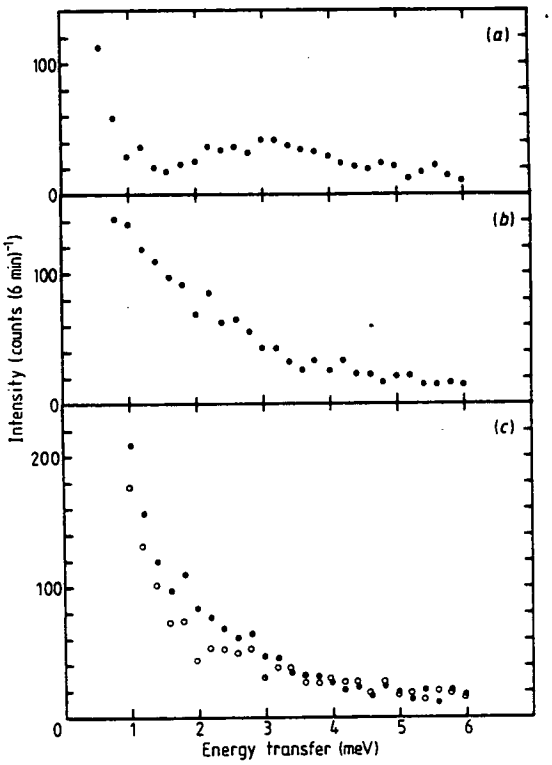

Figure 10. High-resolution inelastic scans made at (*a*) $Q = (1.1, 0, -0.4)$, (*b*) $Q = (1.05, 0, -0.4)$, (*c*) $Q = (1, 0, -0.4)$. Full circles indicate $T = 36.0$ K. Open circles indicate $T = 24.0$ K.

description of the zone-boundary frequencies, showing that these are not greatly affected by the competing anisotropy. This type of model also gave a good account of the Raman scattering results.

4. Conclusions

We have studied the phase transitions and excitations of the system $K_2Co_xFe_{1-x}F_4$ which has competing anisotropies for the two values $x = 0.6$ and $x = 0.2$ using neutron scattering techniques. The results for $x = 0.6$ show that at low temperatures the spins are ordered along the *c* axis and that the phase transition at $T_N = 92 \pm 0.1$ K is well described as a two-dimensional Ising model. The excitations in this sample have been measured and show two bands corresponding to excitations propagating largely on the Co or Fe ions and the frequencies of the bands are in good accord with Raman scattering measurements and with a simple Ising model. No calculations have as yet been performed for the dispersion of these branches.

The results for the sample with $x = 0.2$ are more complex because it undergoes two transitions at $T_N = 66 \pm 1$ K and $T_L = 32 \pm 2$ K. At T_N the *c* component of the spin orders and the transition has essentially two-dimensional fluctuations although there is some ordering of a few of the two-dimensional sheets. The exponent and critical scat-

tering are also consistent with a two-dimensional Ising transition if allowance is made for rounding due to concentration inhomogeneity.

Below the lower transition, T_L, the in-plane spin components order and the mean spin direction deviates from the c axis by about 30° at low temperatures. This transition appeared to be sharp in temperature when allowance is made for the concentration inhomogeneity. This is different from the behaviour found (Wong *et al* 1983) in $Co_xFe_{1-x}Cl_2$ where the lower transition was very smeared. The difference strongly supports the suggestion that the smearing arises from random fields generated by a Dzyaloshinsky type of interaction in $Co_xFe_{1-x}Cl_2$ as this would be expected to be much smaller in the high-symmetry $K_2Co_xFe_{1-x}F_4$. Since this work was performed we have learnt of similar work on $Co_xFe_{1-x}Cl_2 \cdot 2H_2O$ which also shows two sharp transitions and in which the Dzyaloshinsky-type terms are expected to be small.

The details of this lower transition are still somewhat obscure as we failed to observe any two-dimensional critical scattering (see figure 3(*b*)) and the exponent $\beta = 0.32$ is characteristic of a three-dimensional transition. Since a $d = 2$ XY system does not order at non-zero temperature, it is clear that three-dimensional effects must play an important role in this transition. Further theoretical and experimental effort is needed to understand this behaviour.

Since the experimental work described here was completed we have learnt of a similar study with x nominally equal to 0.27 in this system by Vlak *et al* (1983). Despite the difference in the nominal concentrations their results are very similar to ours for $x = 0.2$ giving two transitions: $T_N = 64.4 \pm 0.6$ K and $T_L = 27 \pm 2$ K. Their results are very similar to ours for the structure of the two phases and for the critical scattering except that they observe a broad hump in the intensity for $\boldsymbol{Q} = (1, 0, 0.4)$ close to T_L. Furthermore the wavevector dependence of the diffuse scattering shown in figure 5 is different from that found in their experiment. We do not understand the reason for this difference, but possibly it arises from the extent to which three-dimensional order is developed at T_N, modifying the behaviour close to T_L. We do not understand their argument that at T_L there is a first-order transition as it seems to be a contradiction to our data shown in figure 3 and their own data shown in their figure 3.

Preliminary measurements have been made of the excitations in the sample with $x = 0.2$. The results are similar to the results for $x = 0.6$, for excitations close to the zone boundary. Little difference was observed in the low-frequency spin waves close to T_L, which is surprising. Further experimental and theoretical work is needed to study the spin waves in the mixed phase close to T_L. We hope that this paper will help to stimulate this work.

Acknowledgments

We are grateful for assistance from Dr P W Mitchell with the experiments, and for helpful discussions and preprints from W Vlak and K Katsumata. Financial support was provided by the Science and Engineering Research Council and by the Risø National Laboratory for whose hospitality RAC is grateful. Two of us (SAH and MH) acknowledge the financial support of SERC studentships.

References

Birgeneau R J, Guggenheim H J and Shirane G 1970 *Phys. Rev.* B **1** 2211
Breed D J, Gilijamse K and Miedema A R 1969 *Physica* **45** 205

Cowley R A 1982 *Excitations in Disordered Systems* ed. M F Thorpe (New York: Plenum) p 373
Fendler K 1982 *PhD Thesis* Universität Konstanz
Fendler K, Lehmann W, Weber R and Dürr U 1982 *J. Phys. C: Solid State Phys.* **15** L533
Fishman S and Aharony A 1978 *Phys. Rev.* B **18** 3507
Katsumata K 1983 *J. Magn. Magn. Mater.* **31–34** 1435
Macco F, Lehmann W, Breitling W, Slawska- Wariewska A E and Weber R 1978 *Solid State Commun.* **26** 429
Macco F, Lehmann W and Weber R 1979: *J. Phys. C: Solid State Phys.* **12** L233
Matsubara F 1981 *J. Phys. Soc. Japan* **50** 1469
Matsubara F and Inawashiro S 1977 *J. Phys. Soc. Japan* **42** 1529
Onsager 1944
Thurlings M P H, Frikee E and de Wijn H W 1982 *Phys. Rev.* B **25** 4750
Vlak W A H M, Frikee E, Arts A F M and de Wijn H W 1983 *J. Phys. C: Solid State Phys.* **16** L1015
Wong P Z, Horn P M, Birgeneau R J and Shirane G 1983 *Phys. Rev.* B **27** 428